Simulation et modélisation des écoulements dans les récepteurs solaires à gaz sous-pression

Martin David

THÈSE

Pour obtenir le grade de

Docteur

Délivré par

Université Perpignan Via Domitia

Préparée au sein de l'école doctorale

Énergie et Environnement (ED305)

Et de l'unité de recherche

PROMES-CNRS, UPR 8521

Spécialité : **Science de l'ingénieur**

Présentée par **Martin DAVID**

Simulation et modélisation des écoulements dans les récepteurs solaires à gaz sous-pression

Soutenue **le 26 novembre 2021** devant le jury composée de

Mme. Cathy CASTELAIN, DR, LTEN	Rapportrice
M. Stéphane VINCENT, PR, MSME	Rapporteur
M. Gilles FLAMANT, DR, PROMES	Examinateur
M. Jacques MAGNAUDET, DR, IMFT	Examinateur
M. Alain BASTIDE, PR, PIMENT	Examinateur
Mme. Françoise BATAILLE, PR, PROMES	Directrice de thèse
M. Adrien TOUTANT, MCF-HDR, PROMES	Directeur de thèse

Simulation and modeling of flows in gas-pressurized solar receivers

Simulation et modélisation des écoulements dans les récepteurs solaires à gaz sous-pression

Remerciements

Cette thèse a été rendue possible par l'obtention d'un financement de la région Occitanie. Elle a été préparée au laboratoire PROcédés, Matériaux et Energie Solaire (PROMES), UPR 8521 du CNRS.

Tout d'abord, je souhaite remercier Françoise Bataille et Adrien Toutant pour m'avoir suivi tout au long de ces 3 années. Je vous suis particulièrement reconnaissant pour le temps que vous m'avez accordé et le soutien que vous m'avez apporté. Vos précieux conseils ont rendu possible la réussite de ces travaux et me seront utiles pour la suite. Je vous remercie également pour votre enthousiasme et votre bonne humeur qui ont contribué à rendre ces travaux de thèses agréables.

Je voudrais exprimer ma profonde gratitude à tous les membres du jury constitué pour évaluer cette thèse : Mme Cathy Catelin et M. Stéphane Vincent, pour avoir accepté d'examiner en détail ces travaux de thèse et d'en être les rapporteurs, ainsi que M. Jacques Magnaudet, M. Gilles Flamant et M. Alain Bastide pour l'attention qu'ils ont porté à cette soutenance. Je remercie tous les membres du jury pour leurs questions et remarques.

Je remercie vivement tous les membres du laboratoire qui m'ont toujours aidé avec enthousiasme et efficacité : Sandrine, Armelle, Romie, Naoual et Christelle au niveau administratif et comptable, Faissal et Philippe pour ce qui a concerné l'informatique ainsi que Gilles Hernandez pour le remplacement de la lampe de la douche et ses interventions qui nous ont permis de travailler dans un environnement sain.

Je souhaite remercier l'ensemble des enseignant-chercheurs du laboratoire. Ils m'ont bien accueilli et ont facilité mon intégration au sein du laboratoire.

Je remercie l'ensemble des stagiaires et des doctorants du laboratoire que j'ai croisé et avec qui j'ai partagé des moments inoubliables lors de ces trois années. Particulièrement, je tiens à remercier Dorian qui m'a passé le flambeau et qui m'a beaucoup aidé au début de la thèse. Je remercie également Jean-Marc pour ses discussions scientifiques et Salim pour sa gestion des serveurs locaux et sa bonne humeur.

Ces années de thèse ont aussi été l'occasion de faire briller le laboratoire et l'Université de Perpignan Via Domitia sur le plan sportif. Je remercie les membres de l'équipe PROMES-UPVD : Christian, Shab, Kadar, Youssef, Julien, Antoine , Anis et Diane, qui ont largement contribué à ce beau parcours en championnat : 14 matchs, 14 défaites... Un sans-faute.

Je remercie chaleureusement Mario, pour ses mauvaises ondes responsables de l'élimination de l'équipe de France à l'Euro ~~2020~~ 2021 et son acolyte Edouard, devenu doctorant, pour (grâce à ?) ses réalisations culinaires de qualité.

Les grillades du laboratoire qui se sont tenues en juillet 2021 ont été l'occasion de révéler

certains talents cachés. Je remercie donc Corentin pour sa tarte courgette-chèvre “bien cuite” et Romain pour la cuisson des sushipolatas.

Je n'oublie pas les vétérans : Chloé et Viviane pour les randos, Danielle, Alexis pour m'avoir fait découvrir la pizza aux pâtes, Aubin pour sa recette secrète des frites au four bien croustillantes et Cédric pour les matchs de tennis.

Quelques remerciements en vrac *(et sans emballage)* : merci au captaine Perrigot, le marin du laboratoire, pour ses récits de colocation et d'aventures. Gad pour sa ponctualité, Amine pour ses qualités de dribbleur, Baptiste, le petit prince de *l'ortograf*, Matthieu pour les sessions de surf glassy, Michel, Séb et Philippe pour le padel, ainsi que Christian, Brice, Jean-Marc et Yann pour les doubles de badminton d'anthologie. Je réitère mes remerciements pour Christian qui m'a, enfin, laissé gagné un simple le mardi 19 octobre 2021 (jour férié depuis lors dans le calendrier Davidien).

Je remercie, uniquement parce qu'il le faut, les heureux locataires du ~~bureau Aquarium~~ Lagon. Notamment, Antoine, Kadar, Romain et Alex qui n'ont jamais raté une occasion de me mettre des bâtons dans les roues et de ralentir mes travaux de thèse. Je pense que pour toutes les gênes occasionnées, ils me doivent bien un gâteau, sans noisette bien sûr.

Enfin, je remercie Diane, ma chérie, qui m'a supporté, soutenu et bien aidé durant cette fin de thèse, et avec qui j'ai partagé des moments inoubliables.

Résumé

0.1 Introduction

La réduction des émissions de gaz à effet de serre est d'intérêt mondial. Le cap fixé par l'accord signé en 2015 à la COP21 de Paris par 195 pays vise une limitation de la hausse de la température "bien en deçà de 2°C", en faisant tous les efforts pour la maintenir "en deçà de 1,5°C". D'après l'Agence Internationale de l'Énergie (IEA), pour respecter l'objectif de 2°C, il ne faudra pas exploiter plus d'un tiers des ressources fossiles prouvées d'ici à 2050. Sachant qu'en 2018, 80% de la production énergétique mondiale était d'origine fossile [1], l'objectif est encore loin d'être atteint. La réduction de la dépendance aux énergies fossiles repose à la fois sur la diminution de la consommation énergétique et sur le remplacement progressif de l'utilisation des ressources fossiles au profit des ressources nucléaire et renouvelables. En 2018, la production d'électricité issue de sources renouvelables représentait 25% de la production électrique totale soit 4% de la production énergétique mondiale. La production renouvelable était dominée par l'hydroélectricité (16%), l'éolien (5%) et le solaire photovoltaïque (2%) [1]. Aujourd'hui, le solaire à concentration représente une part marginale de la production d'électricité. Il dispose, néanmoins, d'un avantage significatif par rapport à l'éolien et au solaire photovoltaïque. En effet, les centrales solaires à concentration produisent de la chaleur et peuvent donc facilement être associées à un système de stockage massif permettant de moduler la production en fonction de la demande en électricité. Parmi les différentes technologies de solaire à concentration, les tours solaires sont très prometteuses. La majorité des centrales industrielles actuellement en activité fonctionnent avec des sels fondus qui limitent la température de fluide à environ 850 K. Les travaux de recherche en cours visent à repousser la température de fonctionnement des centrales à celle de résistance des matériaux, permettant ainsi d'atteindre de très hauts niveaux de température de fluide. Ceci permettra l'amélioration du rendement du cycle thermodynamique et conduira à abaisser les coûts de production de l'électricité. Les recherches portent sur l'amélioration de la tenue en température des sels fondus et sur l'utilisation de nouveaux fluides caloporteurs comme les métaux liquides, les particules, les mélanges gaz-particules, les fluides supercritiques et les gaz pressurisés. Le but principal de cette thèse est de favoriser le développement des tours solaires à concentration fonctionnant avec un gaz sous-pression, dont une représentation schématique est donnée par la figure 1. Lors de ces travaux, les simulations sont effectuées dans un canal dont les températures des parois sont fixes. On s'intéresse donc à une tranche de récepteur solaire comme indiqué par les lignes jaunes sur la figure. Le récepteur solaire est un élément critique du système puisqu'il assure le transfert de la chaleur issue du rayonnement concentré vers le fluide.

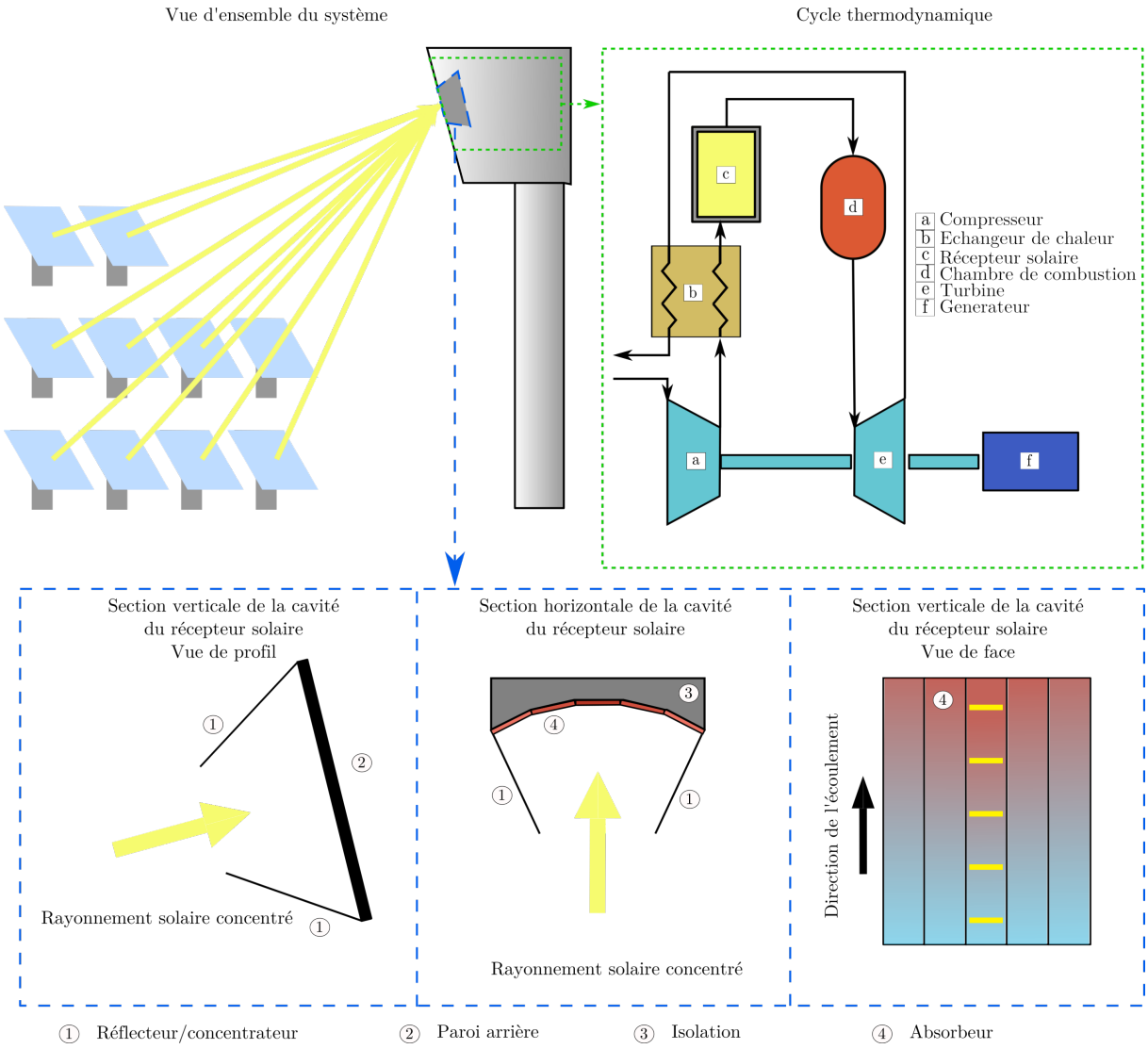

Figure 1 – Représentation schématique d'une tour solaire à concentration et de la cavité du récepteur à gaz sous-pression.

Il est le lieu de phénomènes très complexes liés au fort chauffage asymétrique de l'écoulement qui est turbulent.

Étant donné que les récepteurs solaires sont de taille métrique et qu'ils font intervenir des échelles de turbulence de taille micro-métriques, une étude du système à trois niveaux d'échelle a été menée, voir figure 2. A la connaissance des auteurs, il n'existe pas, dans la littérature, de Simulation Numérique Directe (SND) ni de Simulation des Grandes Échelles (SGE) dans les conditions opératoires des récepteurs solaires à gaz sous-pression. En outre, aucune corrélation ne permet d'estimer les transferts de chaleur en configuration de chauffage asymétrique. Au niveau d'étude le plus fin, il est question de simuler des écoulements grâce à des SND. De ces simulations résultent des données de référence permettant, à la fois d'approfondir la connaissance des phénomènes locaux occurrents dans le récepteur solaire et de tester des simulations moins

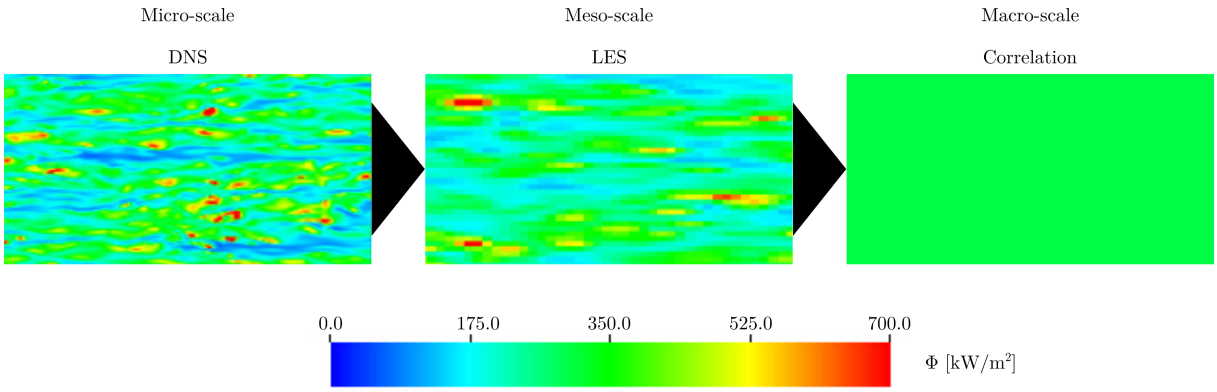

Figure 2 – Estimation des flux de chaleur pariétaux obtenue avec les trois méthodes utilisées dans l'approche par remontée d'échelle.

coûteuses. A fort nombre de Reynolds, et hauts niveaux de flux, les SND nécessitent des grandes ressources de calcul ce qui limite le nombre de simulations réalisable. Au niveau d'étude intermédiaire, des SGE sont effectuées et comparées aux SND par des tests *a posteriori*. En effet, ces simulations consistent à ne résoudre qu'une partie du spectre de la turbulence et à modéliser l'autre. La modélisation des plus petites échelles de turbulence limite la quantité d'information obtenue. Cette approche permet de réduire drastiquement le temps de calcul (quelques dizaines de milliers d'heures) ouvrant ainsi la voie à son optimisation et la réalisation de nombreuses simulations dans des conditions variées. L'étude du récepteur solaire dans son ensemble constitue le dernier niveau d'échelle traité. Une corrélation visant à estimer les transferts de chaleur entre le fluide caloporteur et la paroi du récepteur a été développée grâce aux SGE. Elle permet d'estimer le flux moyen et d'effectuer des analyses macroscopiques du système, facilitant ainsi les études de pré-dimensionnement de tours solaires.

Le résumé, tout comme la thèse, s'articule autour de ces trois niveaux d'échelles. La première section vise à décrire la méthode utilisée pour simuler et modéliser le récepteur solaire. La seconde porte sur les deux premiers niveaux d'échelle : l'analyse des écoulements dans les conditions de fonctionnement des récepteurs solaires grâce aux SND et les tests *a posteriori* des modèles de turbulence des SGE. La troisième section aborde le dernier niveau d'échelle : le développement de la corrélation pour estimer les transferts de chaleur et son utilisation pour étudier la sensibilité des flux de chaleur pariétaux. Une quatrième et dernière section conclut le travail de thèse.

0.2 Méthode

0.2.1 Modélisation de l'écoulement

Les écoulements dans les récepteurs solaires à gaz sous-pression sont caractérisés par un nombre de Reynolds compris entre 50 000 et 100 000, des parois chauffant asymétriquement le fluide et une pression thermodynamique de 10 bar. Les simulations sont effectuées sous l'hypothèse des bas nombres de Mach [2], consistant à négliger les effets purement compressibles. Les équations de Navier-Stokes à bas nombre de Mach sont données par les équations présentées ci-dessous :

- Équation de conservation de la masse

$$\frac{\partial \rho}{\partial t} + \frac{\partial \rho U_j}{\partial x_j} = 0, \tag{1}$$

- Équation de conservation de la quantité de mouvement

$$\frac{\partial \rho U_i}{\partial t} = -\frac{\partial \rho U_j U_i}{\partial x_j} - \frac{\partial P}{\partial x_i} + \frac{\partial \Sigma_{ij}}{\partial x_j}, \tag{2}$$

- Équation de conservation de l'énergie

$$\frac{\partial U_j}{\partial x_j} = -\frac{1}{\gamma P_0}\left[(\gamma - 1)\left(\frac{\partial Q_j}{\partial x_j} - H_s\right) + \frac{\mathrm{d}P_0}{\mathrm{d}t}\right], \tag{3}$$

- Loi des gaz parfaits

$$T = \frac{P_0}{\rho r}, \tag{4}$$

avec ρ la masse volumique, T la température, t le temps, U_k la vitesse du fluide dans la direction k, $\gamma = 1.33$ l'index adiabatique obtenu pour de l'air à 1100 K, r la constante spécifique des gaz parfaits et H_s le terme source introduit dans l'équation d'énergie pour modifier la température de fluide. Notons que la notation indicielle suit la convention de sommation d'Einstein et que δ_{ij} représente le symbole de Kronecker. L'hypothèse des bas nombres de Mach conduit à séparer la pression en deux termes. La pression thermodynamique, notée P_0, est constante en espace et représente la pression moyenne dans le domaine de calcul.

$$\frac{\partial P_0}{\partial x_i} = 0 \tag{5}$$

La pression mécanique, notée P, est liée aux variations de quantité de mouvement et varie spatialement. La convection forcée étant largement prépondérante face à la convection naturelle les effets de la pesanteur sont négligés. Les contraintes visqueuses sont calculées en supposant le fluide newtonien avec l'hypothèse de Stokes,

$$\Sigma_{ij}(\boldsymbol{U}, T) = \mu(T)\left[\left(\frac{\partial U_i}{\partial x_j} + \frac{\partial U_j}{\partial x_i}\right) - \frac{2}{3}\frac{\partial U_k}{\partial x_k}\delta_{ij}\right], \tag{6}$$

où $\mu(T)$ est la viscosité dynamique. La loi de Fourier permet de déterminer le flux de chaleur conductif, Q_j :

$$Q_j(T) = -\lambda(T)\frac{\partial T}{\partial x_j}, \tag{7}$$

où $\lambda(T)$ est la conductivité thermique. Les forts gradients de température nécessitent de tenir compte des variations des propriétés du fluide. La loi de Sutherland est utilisée pour calculer la viscosité dynamique, μ :

$$\mu(T) = \mu_0 \left(\frac{T}{T_0}\right)^{\frac{3}{2}} \frac{T_0 + S_1}{T + S_1}, \tag{8}$$

avec $\mu_0 = 1,716 \times 10^{-5}$ Pa s, $S_1 = 110,4$ K et $T_0 = 273,15$ K. La conductivité thermique est obtenue par l'équation suivante, en supposant la capacité thermique isobare, C_p, et le nombre de Prandtl indépendants de la température :

$$\lambda(T) = \mu(T)\frac{C_p}{Pr}. \tag{9}$$

Les calculs sont effectués grâce au code de calcul TrioCFD [3]. Un solveur multigrille est utilisé pour réduire le temps de résolution du calcul de la pression : la solution de l'équation de Poisson est calculée sur des maillages de plus en plus précis, en utilisant comme condition initiale le résultat du niveau de grille précédent. Les équations sont discrétisées par la méthode des différences finies sur un maillage décalé [4]. Les dérivées temporelles sont approximées par un schéma Runge–Kutta d'ordre trois [5]. Les schémas centré d'ordre deux et Quick d'ordre 3 [6] sont testés pour la discrétisation de la convection de la masse. Les schémas centré d'ordre deux et centré d'ordre quatre sont testés pour la discrétisation de la convection de la quantité de mouvement. La diffusion est approchée au second ordre. La méthode numérique a été validée à des nombres de Reynolds de 180 et 395 par comparaison avec les SND de Moser *et al.* [7], Vreman et Kuerten [8] et Lee et Moser [9]. Lors de cette thèse, une validation à haut nombre de Reynolds ($Re_\tau = 930$) a été effectuée grâce à la SND de référence de Hoyas et Jiménez [10]. Sur la figure 3, qui présente les résultats de cette comparaison, les profils de vitesse longitudinale et fluctuations de vitesse obtenus se superposent.

0.2.2 Modélisation du récepteur

Le récepteur solaire est assimilé à un canal plan dont les directions longitudinale, (x), et transversale, (z), sont bi-périodiques et les températures des parois sont fixes, voir figure 4. Ces conditions limites sont adaptées à l'étude de tranche de récepteur solaire. Des configurations isotherme et anisothermes sont étudiées. Les dimensions du canal sont identiques pour toutes les simulations effectuées durant cette thèse : $L_x \times L_y \times L_z = 4\pi\delta \times 2\delta \times 4/3\pi\delta$, avec $\delta = 3$ mm. Les directions longitudinale et transversale sont discrétisées avec un maillage uniforme. La direction perpendiculaire aux parois est sujette à de forts gradients de vitesse et de température, elle est donc discrétisée avec un maillage suivant une loi en tangente hyperbolique :

$$y_k = L_y\left(1 + \frac{1}{a}\tanh\left[\left(\frac{k-1}{N_y - 1} - 1\right)\tanh^{-1}(a)\right]\right), \tag{10}$$

avec a le paramètre de dilatation du maillage et N_y le nombre de points dans la direction perpendiculaire aux parois. Plusieurs maillages ont été testés pour les tests *a posteriori* des SGE puis le maillage offrant le meilleur compromis coût de calcul - précision des résultats a été sélectionné. Les maillages retenus pour les SND et les SGE sont donnés dans le tableau 1. Notons que les valeurs des tailles adimensionnées des cellules sont dépendantes du nombre de Reynolds de frottement et varient donc très légèrement selon les configurations étudiées. Le lecteur est donc invité à se reporter aux sections concernées pour les valeurs exactes de tailles de mailles adimensionnées.

0.3 Analyse de la physique des écoulements et tests *a posteriori* de simulations des grandes échelles

Cette première section aborde les deux premiers niveaux d'échelles grâce aux SND et aux SGE. On s'intéresse dans un premier temps à la physique de l'écoulement et aux performances des

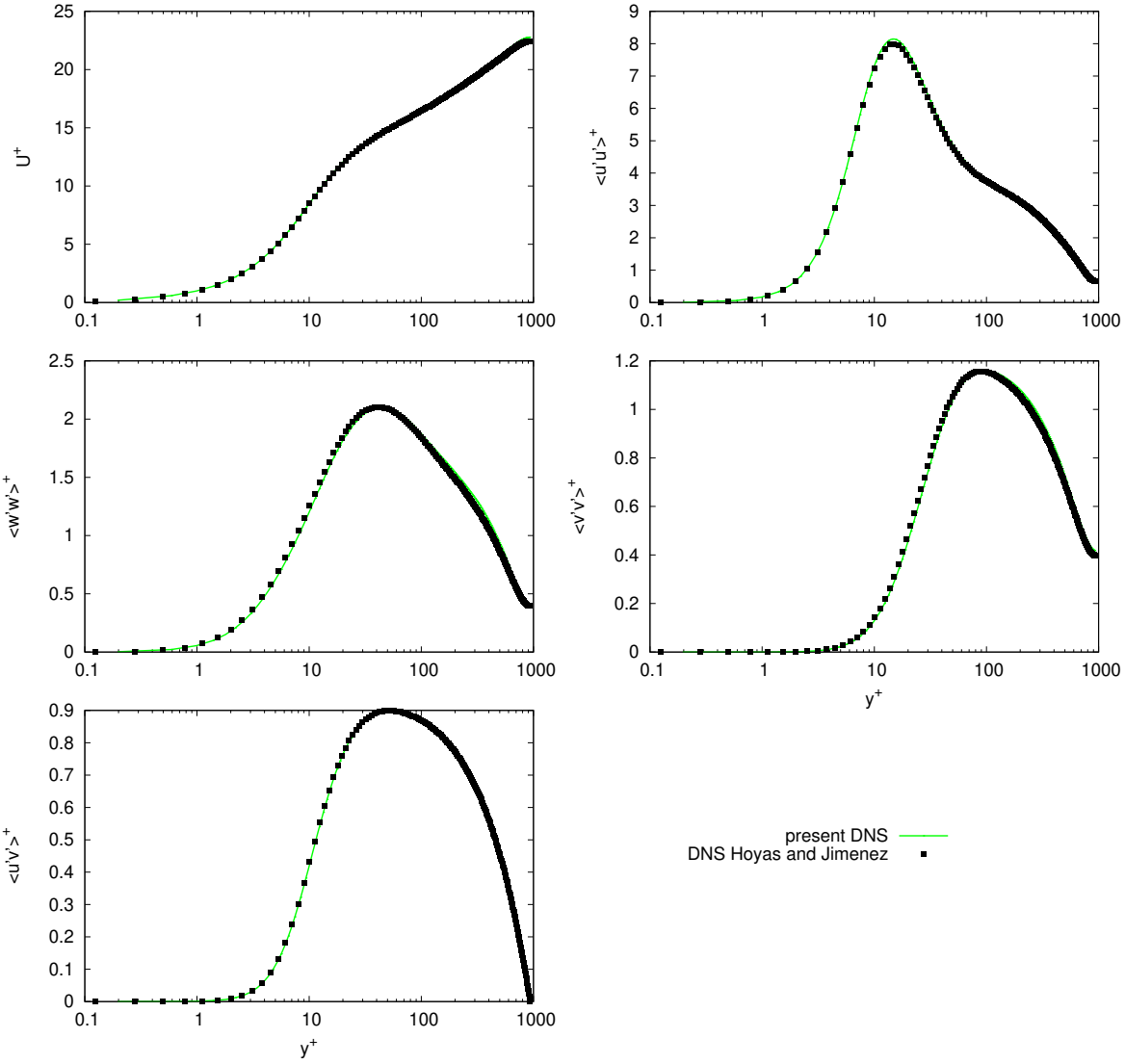

Figure 3 – Comparaison des résultats obtenus avec la SND isotherme réalisée durant cette thèse et celle effectuée par Hoyas et Jiménez [10] à un nombre de Reynolds de frottement de 930.

SGE dans des conditions isothermes, en s'affranchissant des effets de la température. Dans un second temps, deux configurations anisothermes sont étudiées.

Dans cette thèse, un grand nombre de modèles de SGE sont évalués de façon globale puis certains sont selectionnés pour une étude détaillée des statistiques de la turbulence de premier et de second ordre ainsi que des champs instantanés de flux dans les cas anisothermes. Ce résumé ne présente qu'une partie des études détaillées. Les grandeurs observées sont normalisées grâce à l'adimensionnement classique $\langle\cdot\rangle^+$, défini par : $y^+ = yU_\tau/\nu$, $U_i^+ = U_i/U_\tau$, $\langle R_{ij}\rangle^+ = \langle R_{ij}\rangle/U_\tau^2$ avec $R_{ij} = \langle U_iU_j\rangle - \langle U_i\rangle\langle U_j\rangle$. Les modèles fonctionnels étant à trace nulle, seule la partie

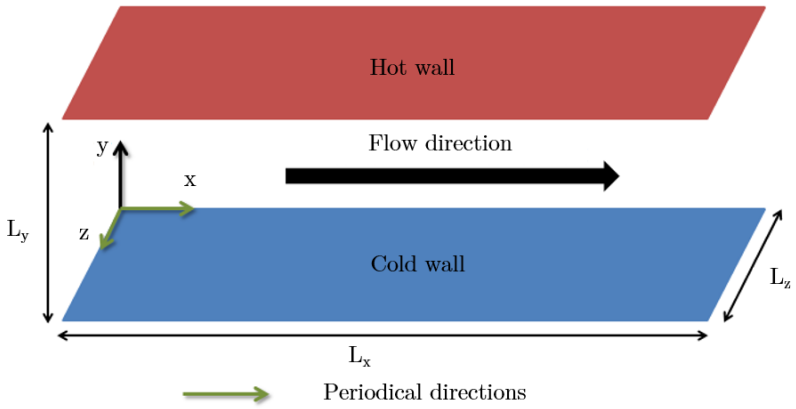

Figure 4 – Canal plan bi-périodique.

Table 1 – Caractéristiques des maillages utilisés en SND et SGE. Les valeurs sont données pour le côté froid de la simulation anisotherme noté [HT] dans la suite. Le côté froid correspond au plus grand nombre de Reynolds de frottement et donc aux tailles de mailles adimensionnées les plus grandes.

Simulation	Nombre de cellules $N_x \times N_y \times N_z$	Taille adimensionnée des cellules Δ_x^+ ; $\Delta_y^+(0)$; $\Delta_y^+(\delta)$; Δ_z^+
SND	$1152 \times 746 \times 768$	10.7 ; 0.41 ; 5.3 ; 5.3
SGE	$160 \times 152 \times 96$	78 ; 1.1 ; 32 ; 43

déviatrice, notée $\langle\cdot\rangle^{dev}$, du tenseur de Reynolds peut être reconstruite et comparée aux résultats de SND non filtrés [11, 12] :

$$R_{ij}^{dev} = R_{ij} - \frac{1}{3}R_{kk}\delta_{ij}. \tag{11}$$

De plus, les termes modélisés en SGE sont ajoutés aux quantités correspondantes afin d'accomplir une comparaison juste avec la SND :

$$R_{ij}^{DNS,dev} = R_{ij}^{LES,dev} + \langle\tau_{ij}^{SGS}(\mathbf{U},\overline{\Delta})\rangle^{dev}, \tag{12}$$

où $R_{ij}^{DNS} = \langle U_iU_j\rangle - \langle U_i\rangle\langle U_j\rangle$ et $R_{ij}^{LES} = \langle\widetilde{U}_i\widetilde{U}_j\rangle - \langle\widetilde{U}_i\rangle\langle\widetilde{U}_j\rangle$.

0.3.1 Cas isotherme

Dans cette section, l'écoulement est analysé et des tests *a posteriori* de SGE sont effectués au même niveau de turbulence que ceux rencontrés dans les récepteurs solaires. L'étude dans le cas isotherme est une étape nécessaire et intéressante car elle permet de valider les résultats de SND avec ceux de la littérature et de comparer à la fois la physique de l'écoulement et les performances des modèles de SGE dans des conditions moins complexes que celles rencontrées dans les récepteurs solaires. En outre, la réalisation de simulations dans le cas isotherme permettra de mettre en exergue les effets de la température lors des simulations anisothermes.

Le terme sous-maille associé à la corrélation vitesse-vitesse est successivement estimé par les modèles AMD [13], WALE [14], gradient [15] (Grd) et similarité d'échelle [16] associé au filtre

Laplacien (SiL). La formulation $H^{(4)}$ du modèle AMD tensoriel proposée par Dupuy *et al.* [17] est également étudiée et notée AMDt. Le terme sous-maille est alors calculé de la façon suivante :

$$\tau_{ij}^{H^{(4)}AMD}\left(\mathbf{U},\overline{\Delta}\right) = H_{ij}^{(4)}\tau_{ij}^{AMD}\left(\mathbf{U},\overline{\Delta}\right), \tag{13}$$

avec

$$H_{ij}^{(4)} = \begin{pmatrix} 0 & 1 & 1 \\ 1 & 0 & 0 \\ 1 & 0 & 0 \end{pmatrix}. \tag{14}$$

Deux simulations sans modèle sont effectuées et notées ILES. La première est menée avec un schéma centré d'ordre 4 pour la discrétisation de la convection de la quantité de mouvement "ILES (c4)" alors que la seconde fait intervenir un schéma centré d'ordre 2 "ILES (c2)".

La figure 5 présente les profils de vitesse longitudinale et des fluctuations de vitesse en fonction de la distance à la paroi. Le profil de vitesse observé suit celui d'une couche limite canonique. Excepté les simulations "AMD (c4)" et "WALE (c4)", toutes les SGE reproduisent bien le profil de vitesse. Les profils de covariances de vitesses longitudinale, transversale et perpendiculaire aux parois sont semblables. Ils font apparaître un pic de fluctuations en $y^+ = 12$. Un quasi-plateau, caractéristique des hauts nombres de Reynolds est observé dans la région $70 < y^+ < 300$ [18, 19, 20]. Les modèles de SGE surestiment les pics de fluctuations et ne reproduisent pas les phénomènes caractéristiques des hauts nombres de Reynolds observés sur les résultats de la SND. Le modèle "AMDt+AMDs" présente des profils différents des autres et, grâce à sa formulation tensorielle qui permet de mieux reproduire l'anisotropie de l'écoulement, offre une meilleure prédiction des profils de covariances de vitesses. L'augmentation de l'ordre du schéma numérique utilisé pour la discrétisation de la conservation de la quantité de mouvement permet de réduire la surestimation des pic de covariances. Enfin, la corrélation entre les vitesses longitudinale et transversale a une forme de cloche avec une amplitude maximale en $y^+ = 500$. Elle est bien reproduite par toutes les SGE. Ainsi, l'étude de l'écoulement en canal isotherme à un nombre de Reynolds de frottement de 930 présente les caractéristiques des écoulements à hauts nombres de Reynolds. Dans la section 0.3.2, l'effet de la température vient modifier les phénomènes observés en conditions isothermes.

0.3.2 Cas anisothermes

Les récepteurs solaires sont caractérisés par des écoulements très complexes couplant une forte turbulence, un chauffage asymétrique du fluide et des hauts niveaux de température et de flux de chaleur. Dans cette thèse, deux conditions de chauffage sont étudiées. Elles sont présentées dans la figure 6 qui décrit l'évolution du profil de température en fonction de la hauteur dans le canal. La première, notée [HT] et obtenue en prenant $H_s = 0$, se caractérise par une température de fluide quasi-égale à la moyenne des températures de paroi et est représentative des conditions qui seraient rencontrées dans un récepteur solaire infiniment long. La seconde, notée [LT] et obtenue en prenant $H_s = 55$ MW/m^3, se caractérise par une température moyenne de fluide inférieure à la température de paroi froide. Ceci se traduit par un chauffage du fluide par les deux parois et une asymétrisation des flux pariétaux. Cette configuration est rencontrée dans les récepteurs solaires.

Les termes sous-maille associées aux corrélations vitesse-vitesse et vitesse-masse volumique sont modélisés, comme recommandé par Dupuy *et al.* [21]. Les modèles AMD [13], AMD tensoriel [17] associé au modèle AMD scalaire [22] (noté AMDt+AMDs) et similarité d'échelle [16]

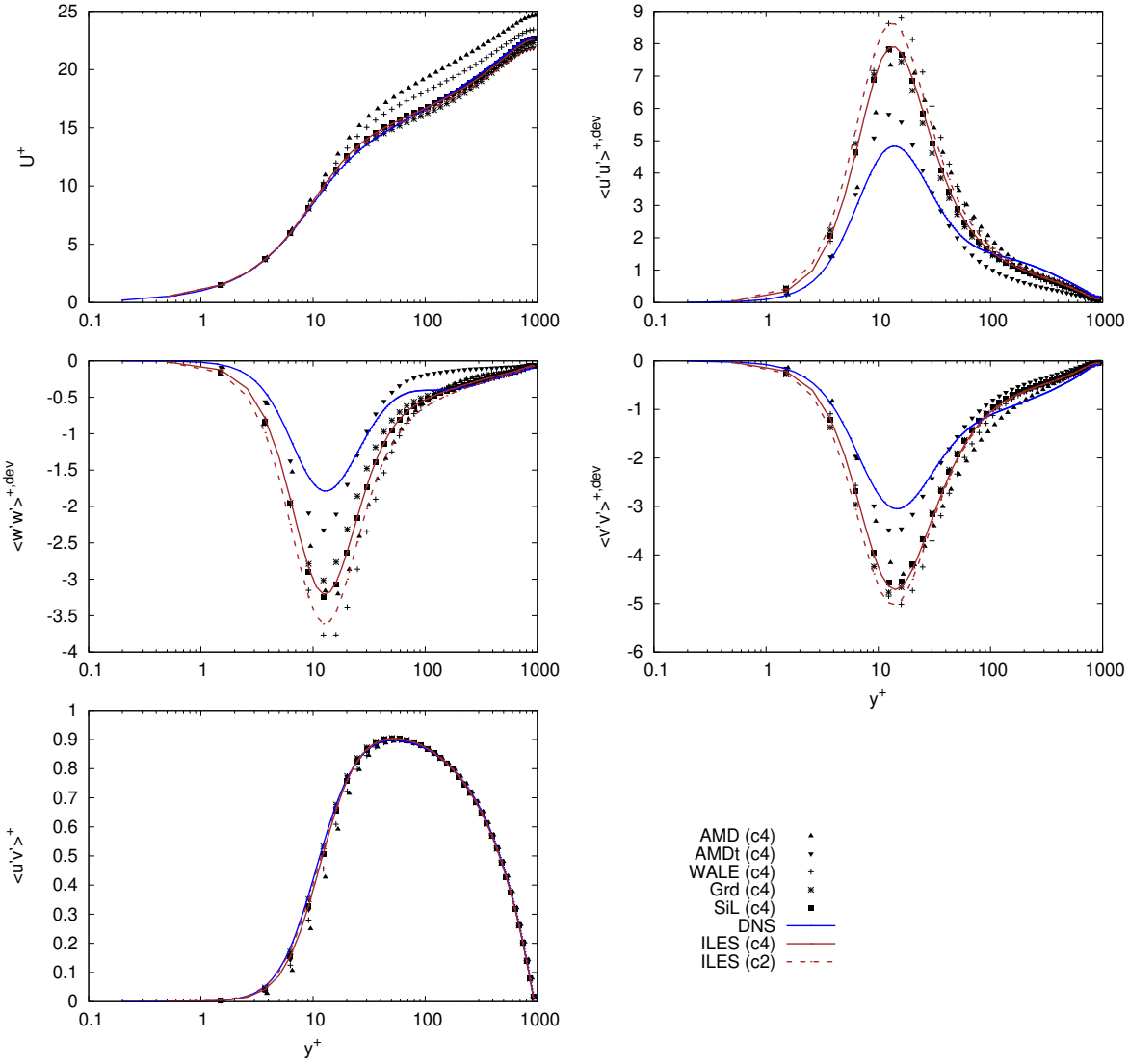

Figure 5 – Comparaison des profils des statistiques obtenues avec les SGE et la SND.

associé au filtre boîte (Sim) ainsi que deux simulations sans modèle, notées ILES sont comparés aux résultats de SND.

La figure 7 décrit l'évolution des vitesses longitudinale et perpendiculaire ainsi que l'évolution de la température en fonction de la distance à la paroi. Les graphiques de gauche correspondent aux résultats associés au côté chaud, ceux de droite représentent les résultats du côté froid. Les profils de la vitesse longitudinale montrent que l'introduction du terme source dans l'équation d'énergie induit une réduction de la vitesse pour un même frottement pariétal. Pour les deux distributions de température, le modèle AMD surestime la vitesse longitudinale des deux côtés du canal, comme pour le cas isotherme. Les autres SGE donnent une bonne estimation du profil de

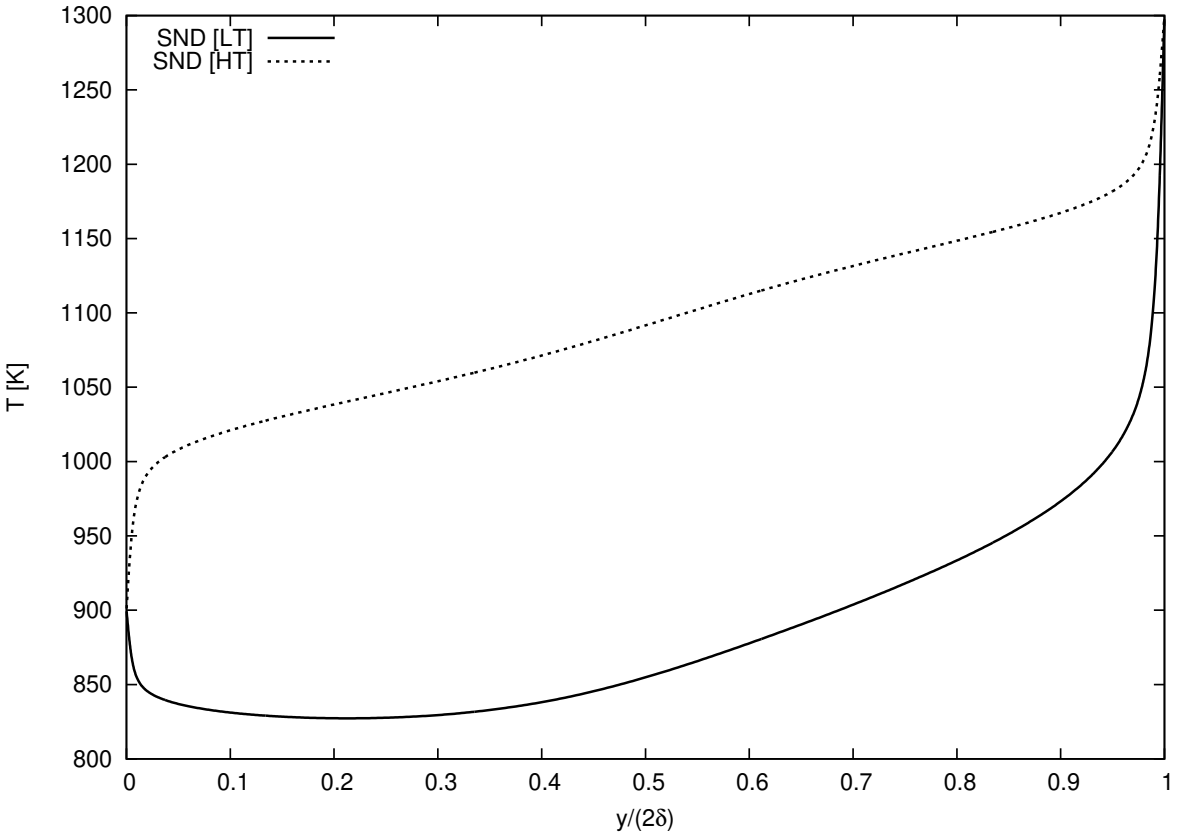

Figure 6 – Profils de température obtenus dans les deux conditions étudiées.

la vitesse longitudinale. Les profils de la vitesse normale aux parois montrent des comportements très différents selon le type de chauffage. Les graphiques de la colonne de gauche sont comparés à ceux de la colonne de droite. Dans le cas [HT], les vitesses normales aux parois sont orientées dans le même sens et présentent des profils très similaires. Dans le cas [LT], les vitesses sont opposées et forment un pic vers $y^+ = 50$. Cette vitesse s'annule autour de $y^+ = 500$ dans le côté froid. Les SGE donnent une bonne représentation du profil [LT] chaud, elles sous-estime la vitesse perpendiculaire aux parois dans le cas [HT] et la surestime dans le côté froid de la configuration [LT]. Il semble donc que les résultats s'améliorent lorsque le gradient de température augmente. Les profils de température adimensionnés se superposent jusqu'à $y^+ = 10$ pour le côté chaud et $y^+ = 6$ pour le côté froid. Le profil [LT] présente un minimum en $y^+ = 500$ qui coïncide avec l'annulation de la vitesse-perpendiculaire aux parois. Les profils de température sont mieux estimés par le modèle AMDt+AMDs. Les performances des modèles sont influencées par la configuration d'étude, mais le classement des performances des modèles les uns vis-à-vis des autres est, quant à lui, faiblement impacté.

Les champs instantanés de flux pariétaux de SND et SGE effectuées les conditions "[LT]" sont présentées sur la figure 8. Ils permettent de visualiser la distribution des flux et offre donc des informations utiles en vue des recherches sur l'intensification des transferts thermiques. Les graphiques de gauche, respectivement droite, décrivent les résultats obtenus à la paroi chaude, respectivement froide. Les flux tracés sont compris dans la gamme $0 - 700$ kW/m^2 pour la paroi chaude et $0 - 172$ kW/m^2 pour la paroi froide. Les motifs révèlent la présence des structures

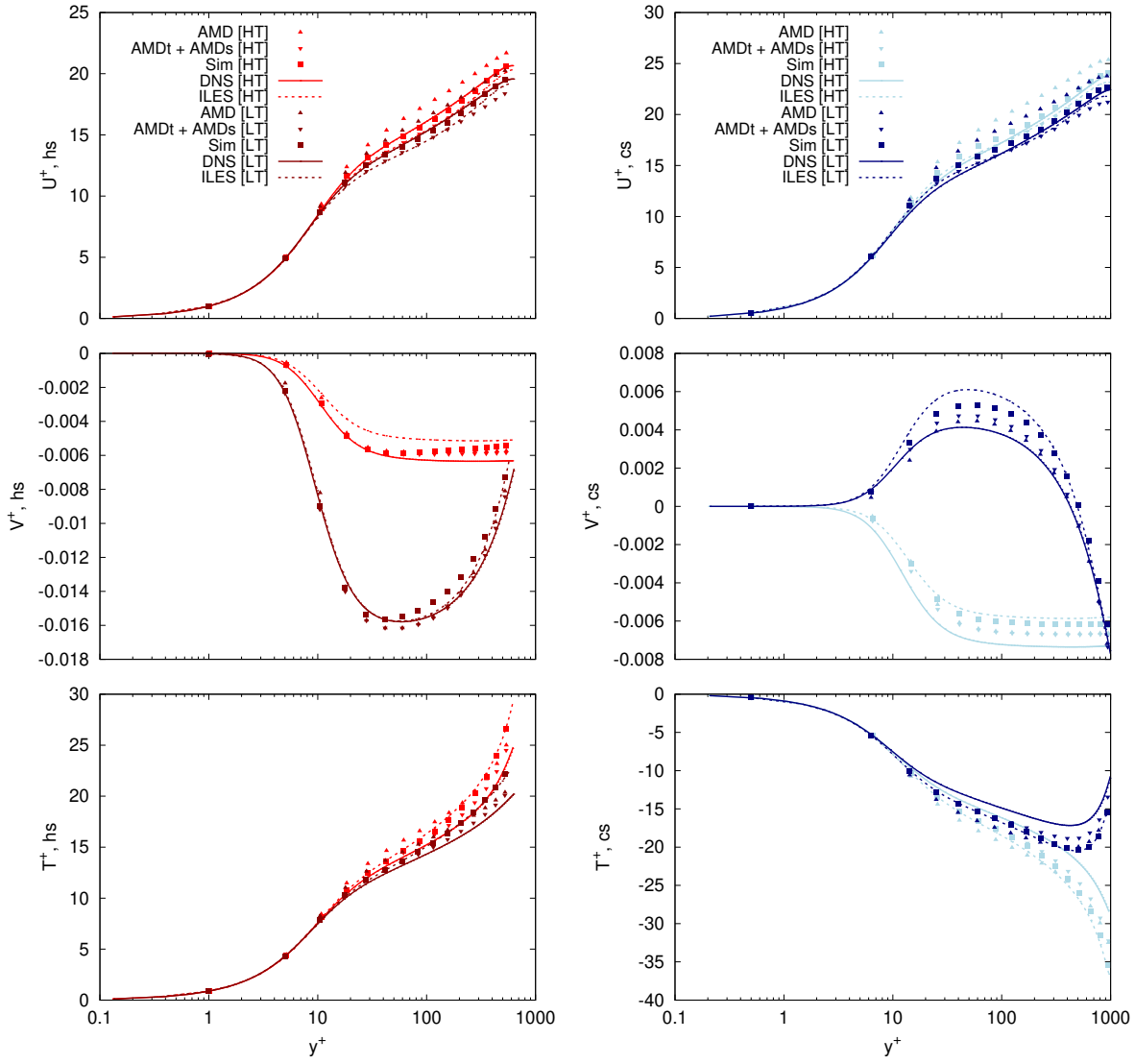

Figure 7 – Profils adimensionnés de vitesses longitudinale et perpendiculaire aux parois ainsi que de température. Les côtés chaud et froid sont respectivement tracés sur les première et deuxième colonnes.

turbulentes en proche paroi. Ils sont similaires aux deux parois, néanmoins, les structures semblent être plus grosses à la paroi chaude. Ceci est lié au fait que les niveaux de turbulence sont plus importants en proche paroi froide, induisant de plus petites structures. Des petites taches rouges sont observées : les zones de forts flux sont donc associées à des échelles de turbulence de haute fréquence. Les zones de faibles flux, représentées en bleu, sont allongées dans la direction de l'écoulement et semblent être associées aux *streaks*. Le maillage utilisé en SGE ne permet pas de reproduire finement les structures turbulentes, mais les résultats obtenus montrent que les phénomènes observés en SND sont globalement reproduits. Les SGE sous-estiment légèrement le flux moyen obtenu à la paroi chaude et surestiment celui obtenu à la paroi froide. La simulation effectuée avec le schéma centré d'ordre 2 pour la discrétisation de la convection de la masse donne une bonne approximation du flux moyen, mais surestime le flux maximal et les fluctuations de flux. De façon générale, les simulations "AMD (Q)" et "AMDt+AMDs (Q)" sont celles qui donnent les meilleures représentations des motifs de flux.

Ainsi, l'étude des écoulements par les SND a permis d'analyser les comportements du fluide et de tester les modèles de SGE en fonction des conditions de chauffage. Dans la section suivante, les écoulements traversant le récepteur solaire sont étudiés au niveau macroscopique.

0.4 Développement et utilisation d'une corrélation pour estimer les transferts de chaleur dans les conditions de fonctionnement des récepteurs solaires

Dans cette section, les SGE sont utilisées pour développer une corrélation permettant d'estimer les transferts thermiques qui est ensuite mise à profit pour étudier la sensibilité des flux de chaleur pariétaux.

0.4.1 Développement de la corrélation

Les conditions rencontrées dans les récepteurs solaires à gaz-pressurisés sont très complexes. Elles sont caractérisées par un écoulement fortement turbulent et un chauffage asymétrique du fluide. Les corrélations de la littérature applicables en canal plan ne considèrent pas les cas de chauffage asymétrique du fluide et les tests effectués montrent qu'il est nécessaire de développer une corrélation dédiée. C'est pourquoi 70 SGE ont été effectuées pour obtenir une base de données fiable et conséquente permettant de proposer une expression reliant le nombre de Nusselt aux différents paramètres de l'écoulement. Les résultats obtenus ont été ajustés pour compenser la sous-estimation du flux observé en SGE et obtenir des flux très proches de ceux donnés par les SND, voir annexe I. L'expression de la corrélation est est donnée par l'équation 15. Elle est inspirée par la forme de la corrélation de Battista et Perkins [23]:

$$Nu = 0.024 Re_b^{0.8} Pr_b^{0.4} \left(\frac{T_w}{T_b}\right)^{-0.9} \left(\frac{T_w}{\mid T_w - T_b \mid}\right)^{1.4\left(1-\frac{T_w}{T_m}\right)\frac{T_b}{T_w}} \tag{15}$$

où T_m est la moyenne des températures de paroi. Le nombre de Reynolds est calculé à partir du diamètre hydraulique du canal. La corrélation est en cohérence avec des expressions de références existantes [23, 24, 25, 26] et fait intervenir un nouveau terme, dédié au chauffage asymétrique : $(T_w/\mid T_w - T_b \mid)^{1.4(1-T_w/T_m)T_b/T_w}$. Ce terme devient neutre en cas de chauffage symétrique du fluide rendant la corrélation également utilisable dans ces conditions. Les domaines d'application

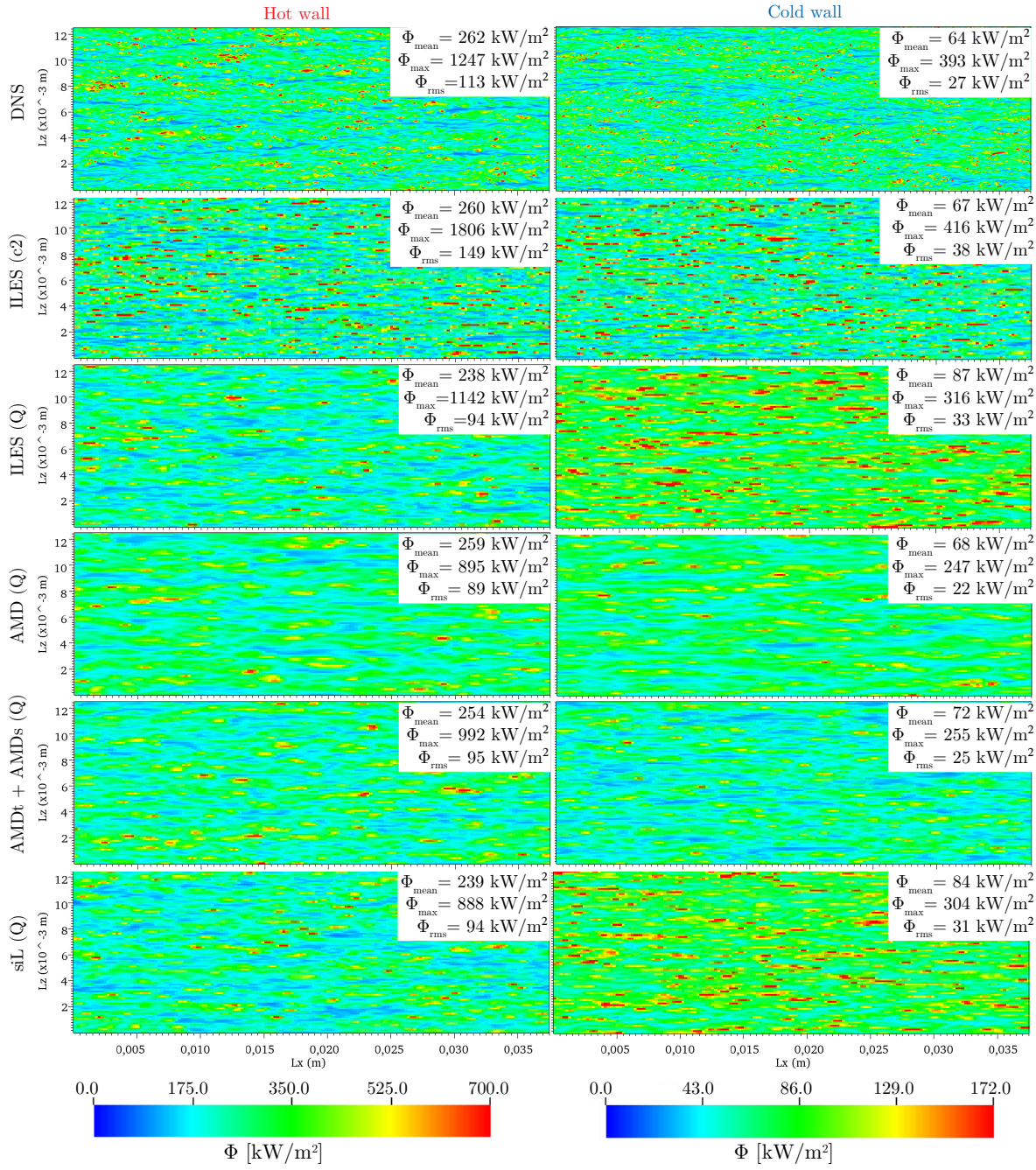

Figure 8 – Champs instantanés de flux pariétaux dans les conditions "[LT]".

Table 2 – Domaine d'application de la corrélation.

Conditions de chauffage symétrique	Conditions de chauffage asymétrique
$12000 < Re_b < 177000$	$10600 < Re_b < 145000$
$0.47 < T_b/T_w < 0.99$	$1.1 < T_h/T_c < 2.0$
	$0.63 < T_b/T_c < 0.95$
	$0.44 < T_b/T_h < 0.85$

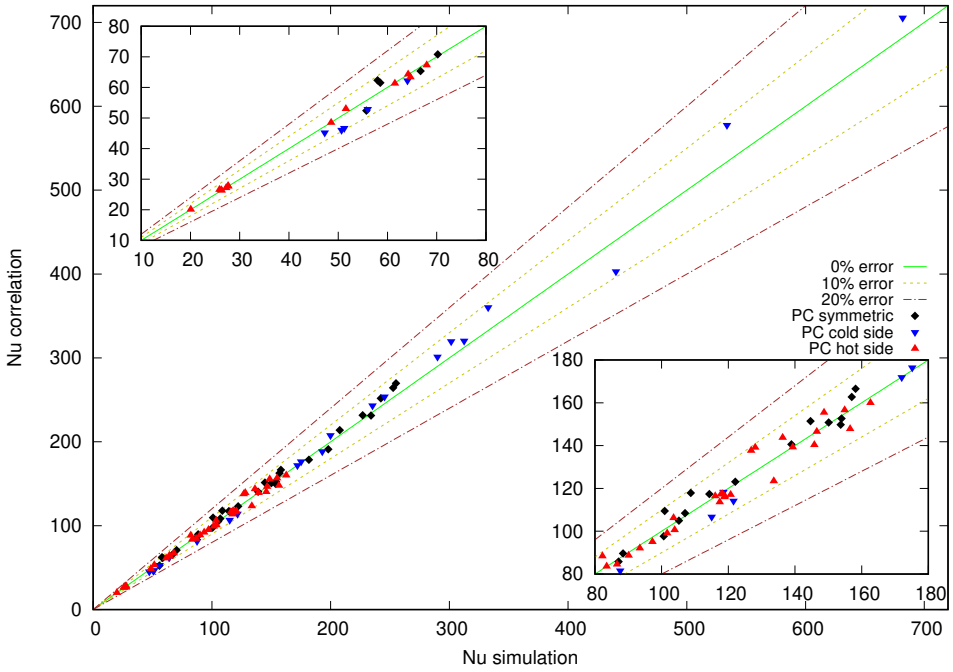

Figure 9 – Nombre de Nusselt obtenu par la corrélation proposée en fonction du nombre de Nusselt obtenu par la simulation des grandes échelles.

de la corrélation pour les deux conditions de chauffage sont donnés par le tableau 2, où T_h et T_c sont respectivement les températures de parois chaude et froide.

La gamme de température de fluide varie de 342 K à 1237 K, le nombre de Prandtl est compris entre 0.76 et 3.18 et les flux de chaleurs sont compris entre 4 kW/m^2 et 578 kW/m^2.

Les nombres de Nusselt obtenus avec la corrélation proposée par David *et al.* [27] sont tracés en fonction des nombres de Nusselt obtenus par les simulations numériques sur la figure 7.4. La gamme de Nusselt étudiée varie de 20 à 680. Les résultats montrent que l'ensemble des points est contenu dans la marge d'erreur de 10%. Le coefficient de détermination de la corrélation est de 0,993. La moyenne des erreurs est de 0.29% et l'écart type des erreurs est de 4,1%.

La corrélation proposée pourra être employée en particulier pour effectuer des pré-dimensionnements de récepteurs solaires. Dans la section 0.4.2, la corrélation est utilisée pour analyser la sensibilité des flux de chaleur aux paramètres de l'écoulement.

Table 3 – Conditions étudiées dans le cas d'un chauffage asymétrique du fluide.

Re_b	Pr_b	T_h [K]	T_c [K]	T_b [K]
60 000	0,87	1300	900	700

0.4.2 Analyse de sensibilité des flux de chaleur

Les incertitudes sur la mesure ou le calcul des grandeurs physiques sont inévitables. La propagation des erreurs commises doit être quantifiée pour estimer leur répercussion. Cette section concrétise l'étude des récepteurs solaires par remontée d'échelle. La corrélation proposée est analysée pour estimer la sensibilité des flux de chaleur pariétaux aux paramètres de l'écoulement. Les conditions de cette étude sont caractéristiques des conditions de fonctionnement des récepteurs solaires à gaz sous-pression des centrales solaires à tour (voir tableau 3). Les travaux effectués présentent des résultats critiques pour la conception de ces derniers. En effet, la quantification de la propagation des incertitudes de mesure est essentielle en vue du dimensionnement des installations.

Les incertitudes sur les flux pariétaux sont exposées sur la figure 10 en fonction de l'incertitude sur les températures de paroi chaude et froide, sur la température de fluide, sur le nombre de Reynolds et sur le nombre de Prandtl. Comme attendu, les résultats montrent que les imprécisions de mesure sur la température de paroi froide (respectivement chaude) sont celles qui ont le plus d'influence sur l'estimation du flux de la paroi froide (respectivement chaude). L'incertitude sur la mesure de la température de fluide est également un facteur important pour la prédiction du flux de la paroi froide. La paroi chaude est, quant à elle, moins impactée. Ces différences sont dues à l'asymétrie du chauffage du fluide : la température de paroi froide est plus proche de la température de fluide que la paroi chaude. Ainsi, une petite variation de la température de fluide aura plus d'influence sur le résultat du flux obtenu à la paroi froide qu'à la paroi chaude. Les températures des parois opposées aux flux concernés ont aussi une influence sur le résultat, même si elle est limitée. La propagation des erreurs liées aux incertitudes sur les nombres de Reynolds et Prandtl est elle aussi moindre. En effet, pour les quatre derniers paramètres abordés, les incertitudes sur les flux sont atténuées. Par exemple, une sous-estimation de la température de paroi chaude de 6% conduit à une sous-estimation du flux de la paroi froide de 5%. Enfin, il est intéressant de noter que la propagation des incertitudes concernant les températures n'est pas symétrique : la surestimation de la température de fluide conduit à une erreur plus importante sur le flux de la paroi froide que la sous-estimation de la température de fluide (pour une incertitude de 10% sur la température, on obtient une incertitude sur le flux de 20% pour la surestimation contre 13% dans le cas de la sous-estimation).

La sensibilité des flux a également été étudiée en fonction de la position axiale dans le récepteur solaire. En effet, à mesure que le fluide progresse dans le récepteur solaire il se réchauffe et l'écart entre les températures de fluide et de paroi diminue. La sensibilité du flux est donc étudier pour une plage de ratio de températures de fluide et de paroi. Deux approches ont été testées. L'erreur commise sur le flux de chaleur est calculée par l'utilisation directe de la corrélation et par l'approximation de la fonction décrivant les incertitudes sur le flux grâce aux développements de Taylor (méthode GUM : Guide for the expression of Uncertainty in Measurement). L'expression des incertitudes sur les flux obtenue par la méthode GUM est, dans des conditions de chauffage

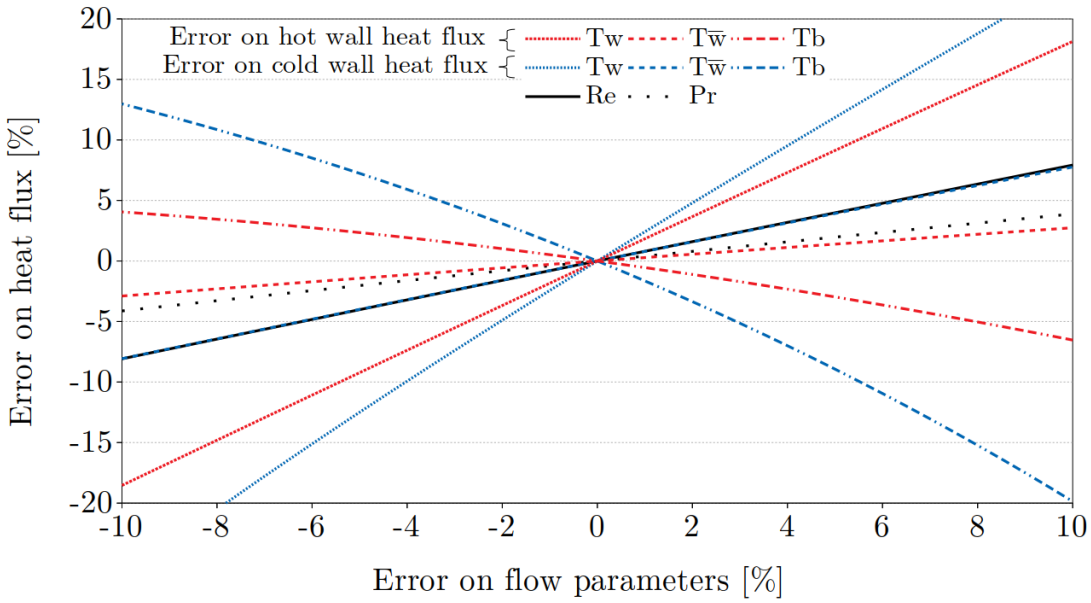

Figure 10 – Erreur commise sur les flux de chaleur pariétaux en fonction de l'erreur commise sur différents paramètres de l'écoulement. Les résultats sont obtenus dans les conditions données par le tableau 3.

asymétrique, la suivante :

$$\frac{\Delta\phi_{asy}}{\phi_{asy}} = \sqrt{A_{asy}^2 + B_{asy}^2 + C_{asy}^2 + D_{asy}^2 + E_{asy}^2}, \tag{16}$$

avec

$$\begin{aligned}
A_{asy} &= \Delta Re_b \left(\frac{0.8}{Re_b}\right), \\
B_{asy} &= \Delta Pr_b \left(\frac{0.4}{Pr_b}\right), \\
C_{asy} &= \Delta T_b \left(\frac{0.9}{T_b} + \frac{1.4}{T_w}\alpha\left(\gamma + \log(\beta)\right) - \frac{1}{T_w - T_b}\right), \\
D_{asy} &= \Delta T_w \left(-\frac{0.9}{T_w}\right) + \Delta T_w \left(-1.4\alpha\frac{T_b}{T_w^2}\left(\gamma + \frac{\log(\beta)}{1 + \frac{1}{\delta} + \frac{\alpha}{\delta}}\right) + \frac{1}{T_w - T_b}\right), \\
E_{asy} &= \Delta T_{\overline{w}} \left(2.8\frac{T_b}{(T_w + T_{\overline{w}})^2}\log(\beta)\right).
\end{aligned}$$

où $\alpha = (T_{\overline{w}} - T_w)\,/\,(T_w + T_{\overline{w}})$, $\beta = T_w/(T_w - T_b)$, $\gamma = T_b/(T_w - T_b)$, $\delta = (T_{\overline{w}} - T_w)/T_w$. Notons que le logarithme utilisé ici est le logarithme naturel.

La figure 11 présente les lignes d'iso-incertitude sur les flux pariétaux en fonction des incertitudes sur les mesures des températures de paroi et du ratio des températures du fluide et de la paroi froide. Les résultats concernant la paroi chaude, respectivement froide, sont tracés sur la première, respectivement seconde, ligne de graphiques. Les résultats issus du calcul direct sont observés sur la première colonne, ceux issus de la méthode GUM sont donnés sur la seconde colonne. La zone noire du graphique située en bas à gauche représente une région en dehors du

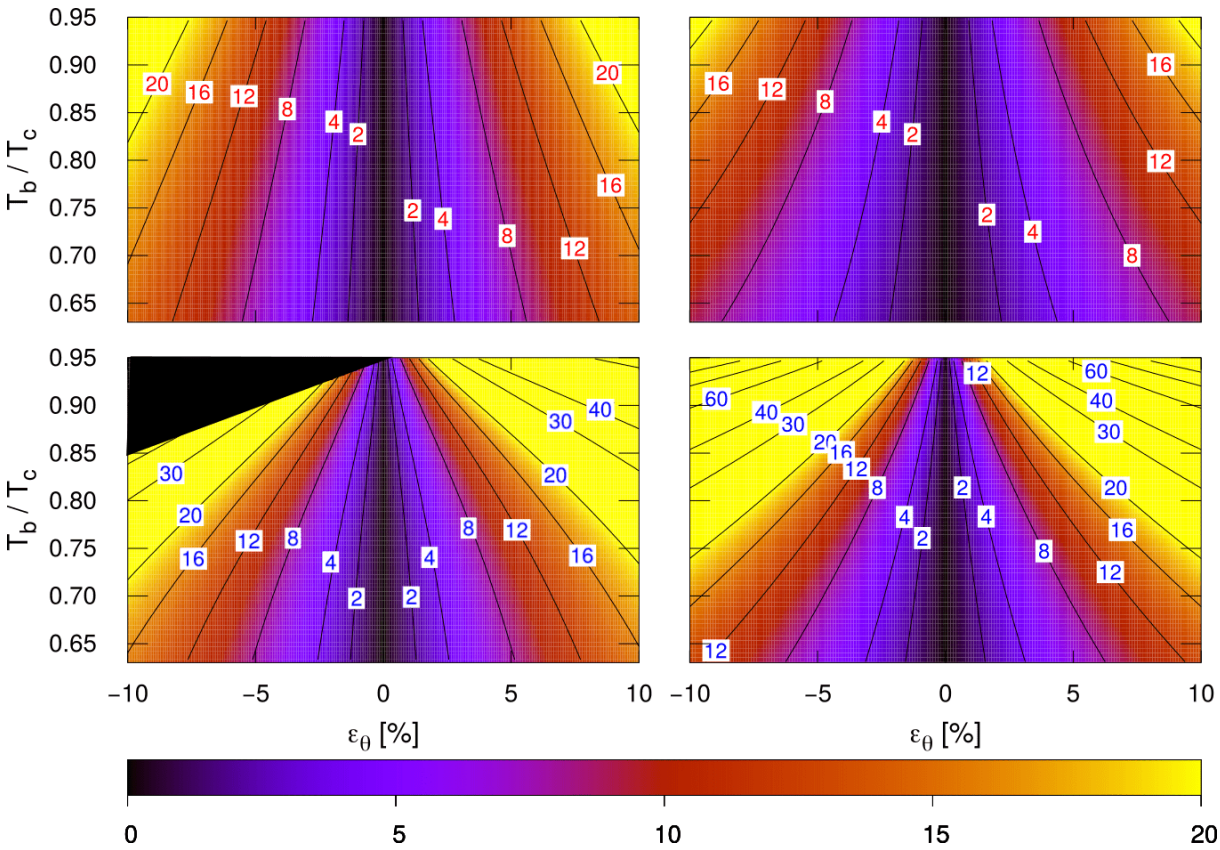

Figure 11 – Incertitude sur les flux pariétaux en fonction du ratio des températures du fluide et de la paroi froide et de l'incertitude de mesure des températures de parois dans un cas de chauffage asymétrique. Les graphiques de gauche montrent les résultats de référence alors que les graphiques de droite représentent ceux issus de la méthode GUM. Les résultats concernant le flux de la paroi chaude sont exposés en haut, ceux concernant la paroi froide sont en dessous. Les lignes indiquent les isovaleurs d'incertitudes sur les flux de 2%, 4%, 8%, 12%, 16%, 20%, 30%, 40%, 60%, 80% et 100%.

domaine de validité de la corrélation. Les résultats du calcul direct montrent que le flux de la paroi froide est plus sensible aux incertitudes sur les paramètres de l'écoulement que celui de la paroi chaude. Une sous-estimation de la température de paroi froide de 10% induit une erreur de 30% sur le flux de la paroi froide, alors que la sous-estimation de 10% de la température de paroi chaude implique une erreur de 19% sur le flux de la paroi chaude. Lorsque la mésestimation de la température de paroi est faible, la position axiale dans le récepteur solaire n'a que peu d'influence sur les résultats. En revanche, lorsque les incertitudes de mesure ou de calcul de la température sont plus élevées, le ratio des températures du fluide et de la paroi froide devient très influent, notamment à la paroi froide. Côté chaud, la propagation des erreurs est quasi-symétrique par rapport à l'axe correspondant à une erreur de mesure de la température nulle. Côté froid, l'asymétrie est plus marquée, surtout pour des fortes mésestimations de la température de paroi et pour des ratio de température relativement élevés. Les résultats de la méthode GUM présentent les mêmes tendances que ceux issus du calcul direct. L'approximation de la fonction par des développements de Taylor montre des meilleurs résultats lorsque (1) le ratio des

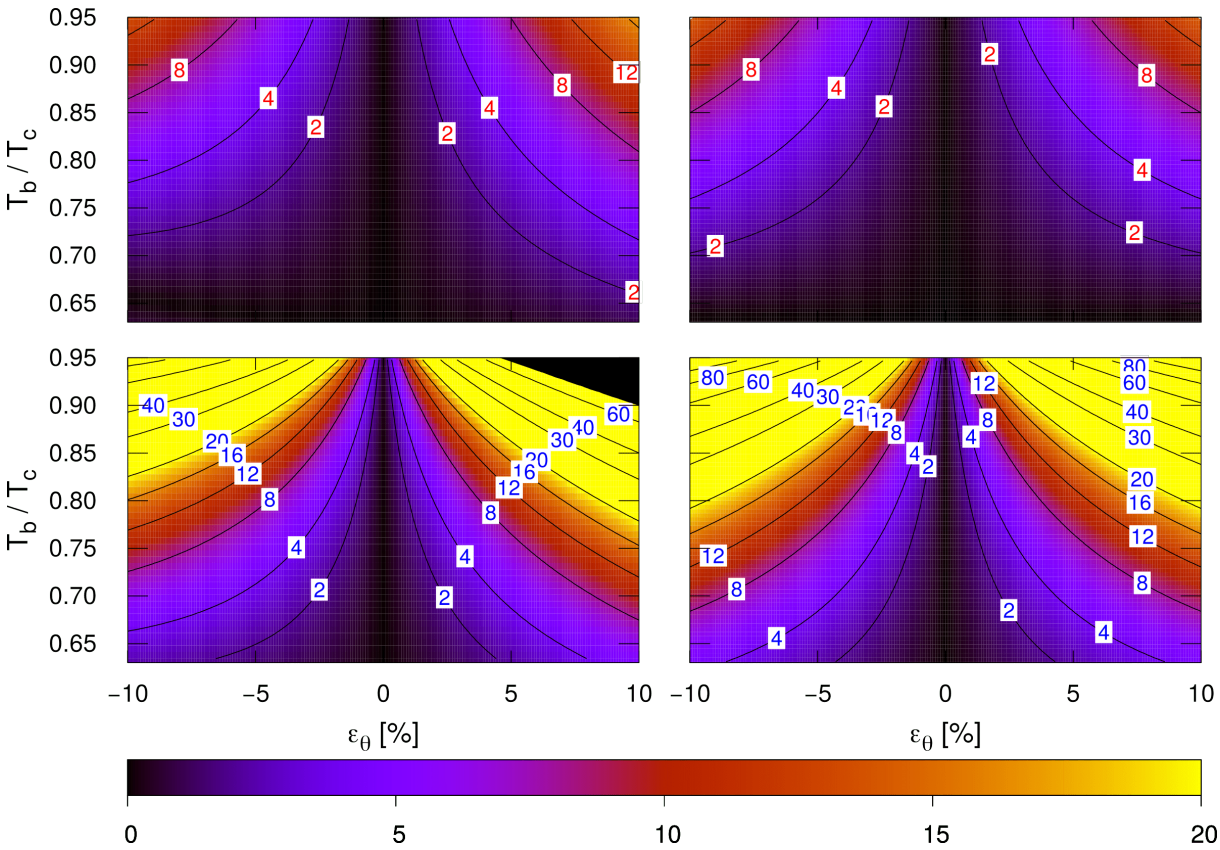

Figure 12 – Incertitude sur les flux pariétaux en fonction du ratio des températures du fluide et de la paroi froide et de l'incertitude de mesure de la température de fluide dans un cas de chauffage asymétrique. Les graphiques de gauche montrent les résultats de référence alors que les graphiques de droite représentent ceux issus de la méthode GUM. Les résultats concernant le flux de la paroi chaude sont exposés en haut, ceux concernant la paroi froide sont en dessous. Les lignes indiquent les isovaleurs d'incertitudes sur les flux de 2%, 4%, 8%, 12%, 16%, 20%, 30%, 40%, 60%, 80% et 100%.

températures est faible : le comportement de la fonction décrivant l'erreur est quasi-linéaire et donc bien décrit par des séries de Taylor ; (2) les incertitudes sur les températures de paroi sont faibles : les non-linéarités sont mieux approchées sur un petit intervalle.

La sensibilité des flux de chaleur à la température de fluide est observée sur la figure 12 en fonction des conditions d'études. Les résultats montrent que la sensibilité des flux s'accroît à mesure que la température de fluide se rapproche de la température de paroi froide de façon encore plus marquée qu'observé sur la figure 11. Le type d'erreur (sous-estimation ou surestimation de la température de fluide) influence significativement l'erreur commise sur les deux flux pariétaux : la surestimation de la température de fluide conduit à des erreurs plus importantes que sa sous-estimation. La paroi chaude est faiblement influencée par la mésestimation de la température de fluide. En effet, l'erreur est atténuée sur la majorité de la plage de ratio de température couverte. Les erreurs commises sur le flux de la paroi froide atteignent de très grandes valeurs lorsque le ratio des températures du fluide et de la paroi froide est proche de l'unité. Cependant, ces erreurs sont associées à des flux faibles puisque le gradient de température entre le fluide et

la paroi est alors réduit. La méthode GUM produit des résultats satisfaisants à la paroi chaude malgré la non prise en compte de l'asymétrie des incertitudes. Ils sont acceptables à la paroi froide pour des faibles valeurs du ratio T_b/T_c et des faibles incertitudes sur la température de fluide.

Dans cette section, la corrélation proposée a été utilisée pour quantifier et analyser la sensibilité des flux de chaleurs aux paramètres de l'écoulement. Les résultats obtenus devraient aider au dimensionnement des récepteurs solaires.

0.5 Conclusion

Les tours solaires fonctionnant à gaz sous-pression offrent de multiples avantages dans le cadre de la transition énergétique. Leur implémentation dans le mix énergétique mondial reste pourtant marginale. Afin de promouvoir cette technologie, nous avons (1) produit des données de référence dans le but d'approfondir la compréhension des écoulements au sein des récepteurs solaires qui sont fortement turbulents, asymétriquement chauffés et qui impliquent des niveaux de flux intenses ; (2) développé des outils permettant proposer des optimisations du récepteur solaire, à savoir la maximisation des transferts thermiques dans le récepteur solaire tout en maintenant des pertes de charges aussi faibles que possible ; (3) déterminé une corrélation applicable dans ces conditions extrêmes afin de faciliter la réalisation d'études de faisabilité. Ces trois niveaux d'études ont été traités durant ces travaux de thèse grâce à une approche par remontée d'échelle. Les résultats issus des études au niveau local (SND) sont analysés et utilisés pour renseigner l'échelle intermédiaire (SGE). De façon analogue, les résultats de l'échelle intermédiaire (SGE) sont analysés et utilisés pour renseigner l'échelle macroscopique (corrélation).

L'étude des phénomènes locaux à conduit à la réalisation de 3 SND pour étudier le comportement de l'écoulement à un nombre de Reynolds de frottement de 950 dans différentes conditions thermiques. L'étude de la turbulence seule a permis la validation de la méthode numérique et a mis en évidence des phénomènes se produisant seulement à hauts nombres de Reynolds. Dans le cas anisotherme, l'analyse des résultats détaillés fournis par ces simulations souligne le fort couplage entre la dynamique et la température. Les résultats de SND quantifient les niveaux de flux obtenus et leur distribution. Ces trois simulations ont été exploitées pour tester des modèles de turbulence de type SGE.

À l'échelle intermédiaire, environ 140 SGE ont été effectuées. Dans chaque condition étudiée, une vingtaine de SGE a été comparée aux résultats de SND grâce à des tests *a posteriori* qui ont permis d'étudier les performances de différents schémas numériques et modèles de turbulence. Les résultats ont montré que les SGE reproduisent les tendances observées en SND. Cependant, les phénomènes liés aux grands nombres de Reynolds et la forte interaction entre la dynamique et la température ne sont pas très bien reproduits par les SGE. Le modèle AMD tensoriel, se différencie des autres, notamment sur les fluctuations de vitesse, et présente les meilleurs résultats. La moitié restante des SGE a été utilisée pour développer un outil simple permettant d'estimer les transferts de chaleur.

Au niveau macroscopique, une corrélation permettant d'estimer les transferts thermiques dans les conditions de fonctionnement des récepteurs solaires a été développée grâce aux résultats de SGE. Elle permet de déterminer les flux de chaleur pariétaux dans un canal traversé par un écoulement fortement turbulent et chauffé asymétriquement, ce qui à la connaissance des auteurs, constitue une première dans la littérature. La corrélation à une précision de 10% et couvre une large gamme de nombres de Reynolds et de Prandtl. Cette expression simple d'utilisation

permet d'effectuer diverses études à l'échelle du récepteur solaire. Les incertitudes de mesure et de calcul étant inhérentes à la recherche et à l'ingénierie, la corrélation a été utilisée pour analyser la sensibilité des flux de chaleur aux paramètres de l'écoulement. Les résultats permettent de quantifier la propagation des erreurs sur l'estimation des flux pariétaux. Il apparaît que la sensibilité des flux est fortement dépendante des conditions d'études. Une expression analytique modélisant la propagation d'incertitude grâce aux développements de Taylor a été proposée et testée. Les résultats obtenus sont satisfaisants pour de faibles incertitudes sur l'estimation des paramètres de l'écoulement et un faible ratio des températures de fluide et de paroi.

Table of contents

List of figures

Figures 1 to 15 are those of the french summary. Then, figures are numeroted X.Y where X is the chapter number and Y is the number of the figure in the chapter. There are no figures in chapters 5 and 6, that respectively correspond to the conclusion of part 1 and the introduction of part 2. For that reason, there are no figures numbered 5.Y and 6.Y.

List of tables

General introduction

In 2015, the COP15 was held in Paris to establish a roadmap of the global energy consumption. When the conference ended, 195 have signed an agreement to limit the increase of the global temperature below 2°C and endeavour to keep it below 1.5°C. According to the International Energy Agency (IEA), no more than one-third of proven reserves of fossil fuels can be consumed prior to 2050 if the world is to achieve the 2°C goal. Knowing that, in 2018, around 80% of the global energy production comes from fossil resources, the goal is far from being achieved [1].

It is interesting to see how well a parallel between the reliance of the current consumer society on the high fossil energy consumption and the relation of an addict with his drugs can be drawn. As a matter of fact, similarly to the addict that takes drugs to forget reality, the fossil energies has offered a dreamed opportunity to scientific progresses and development of society. However, as time goes by, both the drugs for the addict and the fossil energies for the society become necessary for their fulfillment. To stay with a metaphor, when the addict becomes aware of its dependency on the drug, it is often too late for an instantaneous withdrawal and the recovery period takes much time. The current society has come to this conclusion and the weaning process is initiated. The physician's prescriptions are often not pleasant: they consist in the reduction of drug use and the replacement of the most destructive substance, which are often the most liked. The physicist's prescriptions are no more agreeable: the global energy consumption has to plummet sharply and the most detrimental energies for the environment have to be replaced. The first point can partly be achieved thanks to the optimization of engineering systems (better insulation of housing, utilization of the fatal losses in industries, reduction of the energy consumption of the means of transport, and so on). However these technological advances will not be sufficient, the modification of our habits towards energy sobriety is necessary. The second point, which concerns the replacement of the most detrimental energies, is no more simple. The following example illustrates the energetic treasure that represents petrol. One liter of essence contains 10 kWh produces 4 kWh of mechanical energy when used in an average engine. At the same time, the mechanical energy production of a man producing highly physical labor is 0.5 kWh per day at most, this is equivalent to the energy produced by the consumption of 0.125 liters of essence which corresponds to a small glass [28]. Knowing that, it is easy to understand why the replacement of the petrol, and more generally the fossil energy, will be difficult. Renewable energy and nuclear technologies permit converting energy with low greenhouse gas emissions and thus seem interesting to achieve the energy transition. Nuclear power plants allow to produce a huge amount of energy which is necessary to ensure the production basis. However, they suffer from two major drawbacks. Firstly, their inertia complicates the adaptation of the production to

the consumption. Secondly, the period of time between the wish of the construction of a nuclear power plant and its commissioning is often more than 10 years [29] which is long considering the urgency of the situation. The renewable energy production systems are quicker to install and should thus be used simultaneously to meet the challenges of the greenhouse gas reduction. In 2018, the renewable electricity production represented 25% of the global electricity production and 4% of the global energy production. Among the existing renewable energy production, the hydropower plants are very interesting thanks to their storage capacity but they are limited by the geographic possibilities. In 2015, hydroelectricity represented the majority of the global renewable energy production and 16 % of the global electricity production. However, no major increase in hydroelectricity production is expected since the most favorable places are already occupied [30]. The wind power and photovoltaïc technologies are quite well established in the global energy mix (respectively 5% and 2% of the global electricity production [1]) and should pursue their breakthrough. These two technologies directly produce electricity which raises the storage problem. The concentrated solar power plants have a marginal contribution to global energy production but they are promised to a brilliant future [31]. Indeed, they produce heat at a high temperature which signifies heat of very high quality that can be used for manifold applications. Besides, one of the main advantages of concentrated solar power plants lies in their capacity to produce a considerable amount of energy and their beneficial association with energy storage systems, which allow them to achieve remarkable capacity factors. Indeed, with 4 to 8 hours of storage duration, the capacity factor of CSP plants lies between 31% and 45%. If the storage duration is increased to 12 hours, the capacity factor can exceed 60% [32].

The existing CSP systems are listed in Figure 13. There are two main categories of concentrated solar power systems: line concentrators and point concentrators. The linear concentrating collectors are cheaper than the point focusing collectors but the reached temperature is also lower. Indeed, the maximum temperature achievable with linear concentrators is about 750 K [34]. The central receiver can be divided into solar furnace and solar power tower technologies. In the solar furnace technology, the solar radiation is firstly oriented toward a very large parabola thanks to heliostats and then the parabola concentrates the solar radiation on a receiver. The solar furnace permits reaching a very high concentration of sunlight and thus extreme temperatures. For instance, the solar furnace of Odeillo can reach temperatures above 3500 K. The use of a large parabola induces additional cost and complicate the maintenance of the installation. The solar power tower works with heliostats only, reducing the operating costs when compared to the solar furnace. However, they require substantial land areas: the surface of heliostats is generally between 5500 m^2/MW and 8500 m^2/MW installed [35, 36, 37]. Some of the early designed projects utilized water to directly generate steam which ran a turbine. Currently, molten salts are employed because they have high heat capacities and permit storing the energy before using it to boil water to drive turbines. Nevertheless, molten salts limit the maximum fluid temperature to about 850 K. The efficiency of the thermodynamic cycles used in solar power towers is enhanced when the fluid temperature increase. For that reason, researches are performed to higher this maximum temperature. Recent molten salts allow to reach temperature of 950 K [38, 39] but they also have a higher fusion temperature which introduces other issues. In 2015, the Levelized Cost Of Energy (LCOE) of solar power tower was estimated to 0.16 \$/kWh and it is estimated to fall down to 0.09 \$/kWh in 2025 [40, 32]. The third generation of solar power towers operating at higher temperatures is at the research stage. A large number of heat transfer fluids are investigated: the particles [41], the super-critical CO_2 [42], the liquid metals [43], the gas-pressurized [44] and the mixture of fluid and particles [45, 46]. They permit reaching fluid temperature higher than 1200 K [47] and thus obtain high solar-to-power conversion efficiency of

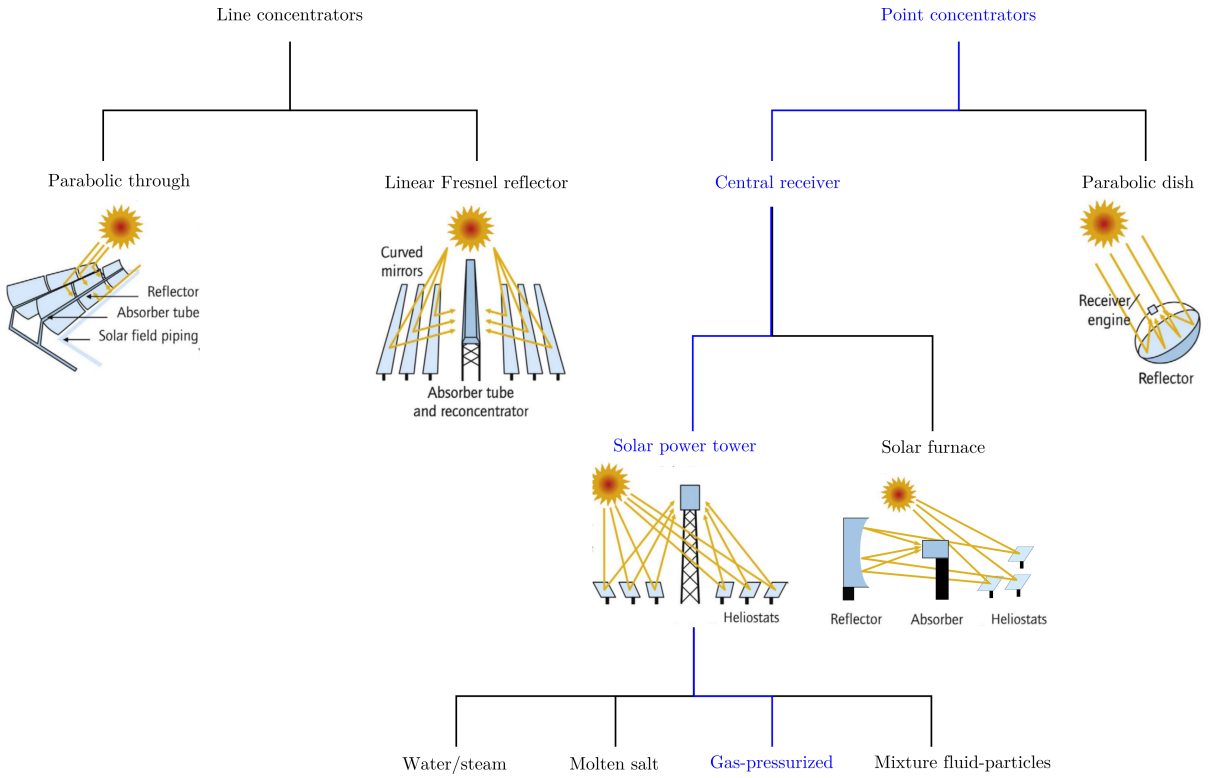

Figure 13 – Organizational chart of the various types of concentrated solar systems. The parabolic through, linear Fresnel reflector, solar power tower and parabolic dish schemes are extracted from Fuqiang *et al.* [33].

about 30% [48]. In those cases, the maximum fluid temperature is constrained by the resistance of the solar receiver materials. Among the usable materials, the ceramics offer the best robustness [49, 50]. The maximum power limit obtained with a single tower is 400 MW [47]. During this thesis, we focus on the gas-pressurized technology of solar power towers. More particularly, the studied heat transfer fluid is air. This heat transfer fluid offers the advantage of being free, available everywhere on Earth, and with no environmental impact. Nevertheless, it complicates the integration of the heat storage system to the solar tower. A schematic view gas-pressurized solar power is proposed in Figure 14. Note that, here, the solar receiver is composed of rectangular channels. This geometry permits maximizing the collected radiation when compared to the tubular shape. The solar receiver is placed at the top of the tower and, in the case of electricity production, is included in a Brayton cycle. The solar receiver, also called absorber, is a built-in cavity in order to minimize the convective and radiative heat losses. The studied technology consists of an assembling of vertical channels of about 10 meters long. The front wall of the channel receives the concentrated solar radiation and the rear wall, which absorbs a significant part of the front wall radiation, is insulated to mitigate the heat losses. These walls are thus at very different temperatures. The gas passes through the channels and is asymmetrically heated from the walls of the receiver. The flow rate is high to increase the turbulence phenomena and thus enhance the heat transfer towards the fluid. Notice that, a balance has to be found since the pressure drops must remain as low as possible.

The gas-pressurized solar receiver has metric dimensions and involves micro-metric turbulent

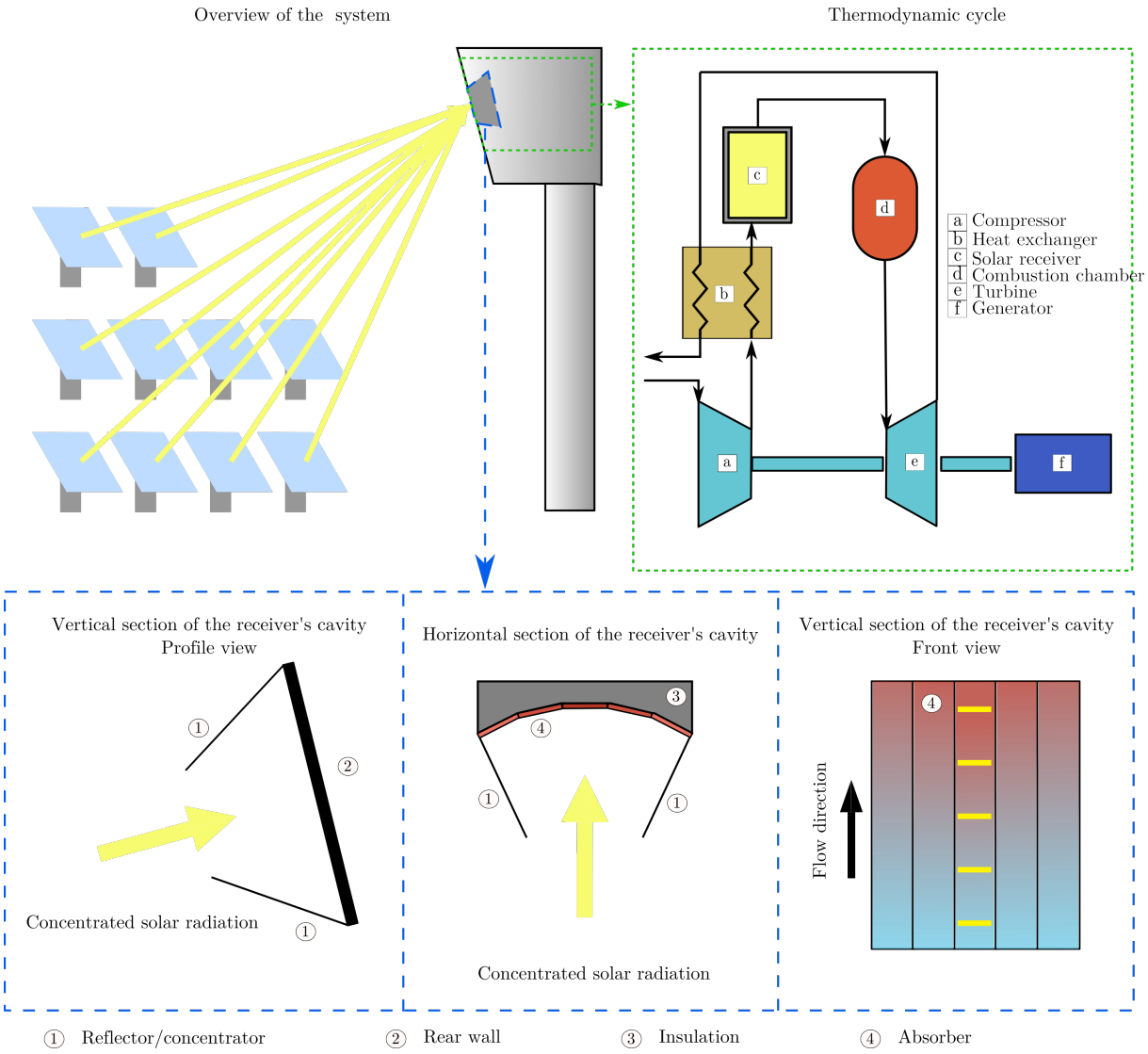

Figure 14 – Schematic view of the gas-pressurized solar power tower.

scales. It is still at the research stage but should be industrialized in few years. To the author's knowledge, there is neither Direct Numerical Simulation (DNS) nor Large Eddy Simulation (LES) performed in the very complex operating conditions of solar receivers (strong heat fluxes and high turbulence level). Moreover, no correlation permitting estimating the solar receiver wall heat flux has been found because of the asymmetrical heating of the fluid. For these reasons, approaches at different levels are needed. This thesis aims to promote the development of the gas-pressurized solar power tower by performing a multi-scale approach to fulfill the gaps of the literature. As the fine simulation of the full solar receiver is not achievable, the computations have been performed in a channel with fixed wall temperatures aiming to get information on slices of a solar receiver (see yellow lines in figure 14). To increase the competitiveness of the technology, the heat transfer should be maximized and the pressure drops have to remain as low as possible. This requires very fine information on the flow behavior and the coupling

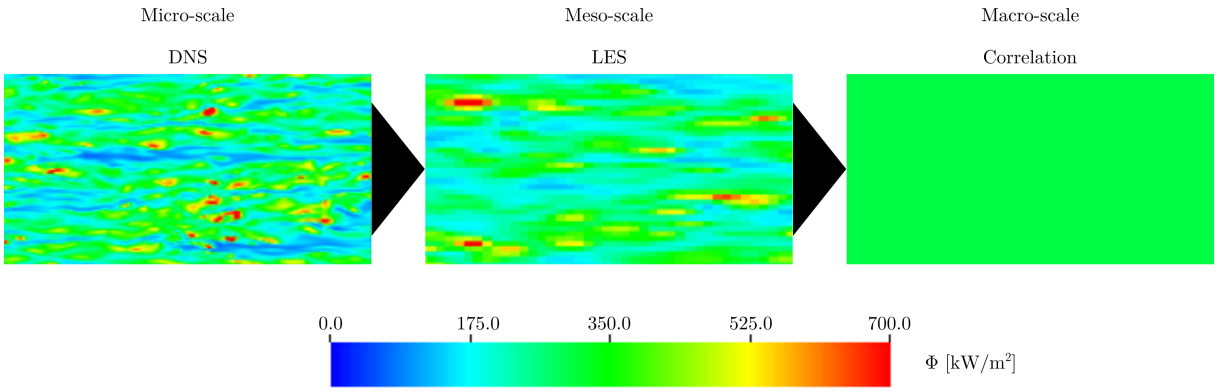

Figure 15 – Wall heat flux estimation obtained with the three methods used in the upscaling approach.

between the dynamic and the temperature. By solving the quasi-integrality of the turbulence spectra, DNS offer very rich and accurate results that could be used to better understand very anisothermal turbulent flows. This type of simulation is only applicable to simple geometries due to its tremendous computational costs. Therefore, more accessible simulations should be used to propose optimizations (heat transfer enhancements). The LES permit obtaining local instantaneous quantities, and thus quantity fluctuations, as the DNS but involve a turbulence model to compensate for their coarser mesh. Tools are also needed to perform a more global evaluation of the system such as feasibility studies. The heat transfer correlations address this point by linking the heat flux to few flow parameters thanks to a simple expression.

The main purpose of this thesis is to facilitate the development of the concentrated solar power towers functioning with gas-pressurized in the medium and long terms. This overall problem is addressed with a upscaling approach consisting in three levels and illustrated in figure 15. The link between the investigated geometry and the slice of solar receiver is detailed in section 1.6. The DNS produce rich and accurate results at the micro-scale level that permit deepening the flow comprehension and providing reference data for the meso-scale studies. However, these simulations are very costly and can only be performed at the local-scale: the DNS of a channel flow at the turbulence level encountered in solar receiver require up to 4.5 million of hours on a supercomputer. In this study, three DNS have been carried out. Two of them have been performed in highly turbulent and asymmetrically heated flow, which is a first in the literature. The DNS are used to assess the LES, that are less costly. To the author's knowledge, the assessment of turbulence models in those extrem conditions is new in the literature. In the LES the biggest turbulence scales are solved and the smallest are modeled. They are able to achieve simulations in more complex configurations and are well adapted to produce data for the development of macro-scale models: the LES performed in the studied conditions needs about 20 000 hours, namely 200 times less than the DNS. During this thesis, the geometry studied with the LES was not more complex than the one studied in DNS but the LES permit investigating a large number of configurations. Indeed, more than 160 LES have been carried out. The results of about 140 LES are presented in the manuscript. Seventy different configurations have been investigated thanks to LES to propose a heat transfer correlation that permits performing studies at the macro-scale by investigating heat transfers in the entire solar receiver. Thanks to its formulation that includes temperature ratios, the proposed heat transfer correlation permits

estimating wall heat flux under asymmetric heating which did not exist in the literature. Heat transfer correlations are simple expressions that instantaneously produce heat transfer estimation within 20 % of error. In this thesis, thousands of wall heat flux have been computed thanks to the proposed correlation in order to study the error propagation.

The outline of the thesis follows this upscaling approach. Chapter 1 presents the methodology applied in this thesis. It explains the multi-scale approach then gives the resolved equations, the hypothesis, and the modeling of the channel.

Part I deals with the micro- and the meso-scale levels. At the local level, the flow is investigated through the analysis of the interactions between the dynamics and the temperature thanks to DNS results. At the intermediate level, LES of the highly turbulent and asymmetrically heated flow are performed. Turbulence models are tested and compared with the DNS. Chapter 2 gives general information on the LES, providing the main principles of this type of simulation and detailing the filtering and the subgrid-scale modeling. Chapter 3 handles the simulation of channel flow in the isothermal case in order to validate the numerical method, study high Reynolds number effects without the temperature influence, and highlight the temperature effects investigated in the next chapter. A large number of turbulence models of LES are investigated. Chapter 4 tackles two anisothermal conditions corresponding to two different heating configurations that reproduce the physic encountered in solar receivers. Turbulence models of LES are tested in those conditions. Chapter 5 concludes on the coupling between the dynamic and the temperature and the LES of highly turbulent channel flows.

Part II deals with the macro-scale level and focuses on more applied studies. Chapter 6 introduces heat transfer correlations. Chapter 7 concerns the development of a heat transfer correlation applicable in the operating conditions of gas-pressurized solar receivers. In chapter 8, the proposed correlation is applied to investigate the wall heat flux sensitivity to the flow parameters. Chapter 9 reminds the main results of the heat transfer correlation and draws conclusions on the wall heat flux sensitivity analysis.

The last chapter concludes on the works achieved during this thesis and gives the perspectives with regard to the LES modeling, the heat transfer correlation, and heat transfer sensitivity analysis.

Section 4.2, chapter 7, section 4.3, and chapter 8 respectively reproduce the following articles published in international peer-reviewed journals:

- M. David, A. Toutant, and F. Bataille. Investigation of Thermal Large-Eddy Simulation approaches in a highly turbulent channel flow submitted to strong asymmetric heating. *Physics of Fluids*, vol. 33, no. 4, p. 045104, 2021.

- M. David, A. Toutant, and F. Bataille. Numerical development of heat transfer correlation in asymmetrically heated turbulent channel flow. *International Journal of Heat and Mass Transfer*, vol. 164, p. 120599, 2021.

- M. David, A. Toutant, and F. Bataille. Thermal Large-Eddy Simulations of a turbulent channel flow asymmetrically heated from both walls. *Physics of Fluids*, vol 33, no. 8, p. 085111, 2021.

- M. David, A. Toutant, and F. Bataille. Impact of asymmetrical heating on the uncertainty propagation of flow parameters on wall heat transfers in solar receivers, *Applied Thermal Engineering*, vol. 199, p. 117547, 2021.

Chapter 1

Methodology

Contents

1.1 Introduction of chapter 1

The works achieved during this thesis aim to promote the development of solar power towers operating with gas-pressurized solar receivers thanks to a heat transfer correlation and to improve the Thermal-Large Eddy Simulation (T-LES) of anisothermal flows. The methodology is

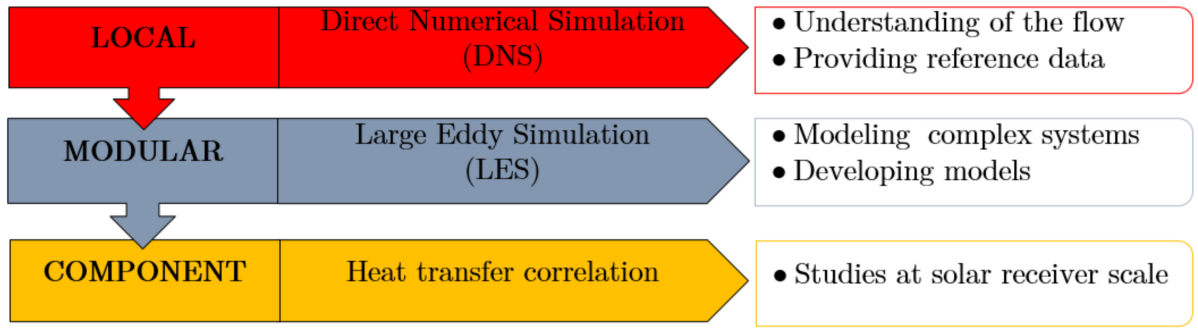

Figure 1.1 – Multi-scale approach.

described in this part. The solar receivers induce physical phenomena ranging from micro-metric to metric scales. Hence, a multi-scale investigation of gas-pressurized solar receivers is performed, fthis approach is explained in section 1.2. The operating conditions of solar receivers are detailed in section 1.3. The understanding of the flow passing through the solar receiver requires the use of accurate numerical simulation. In section 1.4, the resolved governing equations are given. The numerical settings are described in section 1.5. Lastly, the mesh of the computational domain and the data processing are described in section 1.6.

1.2 Multi-scale approach

The gas pressurized solar receiver technology is at the prototype stage. This technology still requires some optimization in order to become competitive with the more mature renewable energy technologies. Furthermore, due to the very complex operating conditions of the solar receiver, the technology needs specifically designed tools for the study at the component scale. This should facilitate the expansion of solar power towers working with gas-pressurized solar receivers. To meet these challenges, a multi-scale investigation of the solar receiver is carried out, see Figure 1.1. Three levels of description are proposed. The local level, also denoted micro-scale level, involves the Direct Numerical Simulation (DNS). The modular level, also denoted intermediate level or meso-scale level, uses the LES. Lastly, the component level, also denoted macro-scale level, is addressed with the heat transfer correlation. A major aim of the current studies is to maximize the heat transfers from the concentrated sunlight to the flow while keeping low-pressure drops. One of the main objectives of this thesis is to enhance the comprehension of coupling between the dynamic of the flow and the temperature to facilitate the solar receiver optimization. This is achieved by using a fine level of description to feed the models of more macroscopic study levels. In the DNS, the quasi-completeness of the turbulent scales is solved. Hence, the obtained data are very accurate and permits deepening the flow understanding. The DNS results are classically used as reference data to assess coarser simulations [51, 52, 53]. The Large Eddy Simulation (LES) is much more accessible in terms of computational cost. Indeed, in these simulations, the smallest turbulence scales, which are the most difficult to compute, are modeled thanks to the addition of a subgrid model. They can simulate more complex and larger geometries than the DNS and provide quite reliable results that can be used to test parts of the solar receiver such as patterns of heat transfer enhancement geometry. Moreover, LES may be used to develop coarser models. During the thesis, a heat transfer correlation has been developed. It is inspired by the gas-pressurized solar receivers and is, thus, well adapted to their

complex flows. The correlation should facilitate the growth of the solar power tower systems by enabling studies at the component scale. For instance, the correlation can be used to size solar receivers or to perform wall heat flux sensitivity analysis.

1.3 Operating conditions of gas-pressurized solar receivers

Most of the present commercial solar receivers of solar power towers operate with molten salt. However, this technology suffers from the price and the environmental cost of the molten salt. Furthermore, solar power tower needs to be placed in very sunny regions which are often remote from the large cities and industries. This complicates the transport of the molten salt. In addition, to enhance the thermodynamical conversion, it is necessary to increase the fluid temperature and thus to change the heat transfer fluid. Contrary to the molten salt technology, which is limited to a fluid temperature of 870 K [54], concentrated solar power towers functioning with gas-pressurized, supercritical fluid, or mixture of gases and particles allow reaching very high fluid temperatures [55]. The maximal fluid temperature is, then, only limited by the material resistance. This is useful for many applications such as evaluation of material behaviors under strong heating, achievement of chemical reactions, and electricity production. In that last case, the solar receiver is included in a Brayton cycle [56], as observed in Figure 14. This thermodynamical cycle allows to reach high power conversion efficiency and its performances are enhanced by the increase of the fluid temperature. In the next, the focus is placed on the gas-pressurized solar receiver.

The actual solar absorbers are built-in cavity in order to minimize the heat loss and allow to reach temperatures of about 1300 K. The reader is referred to Ho [57] for a detailed review of the high-temperature central receiver designs for concentrating solar power. Several geometries of solar receivers are investigated including tubes [58], channels with vortex generators [59, 60], and thin channels [61, 56]. In the present study, we focus on this last type of gas-pressurized solar receivers. Concentrated sunlight is oriented toward the front wall of the channel, denoted "irradiated wall" or "hot wall". The opposed wall of the solar receiver is insulated on the exterior face. This wall does not receive the direct concentrated sunlight, it is heated by the radiation of the hot wall and it is then denoted as "cold wall". For the purpose of improving the heat transfer, micro-channel solar receivers are crossed by gas with a high mass flow. The resulting turbulence permits increasing the heating of the fluid by transferring the hot packet of fluid toward the center of the channel. In those solar absorbers, the bulk Reynolds number is usually between 50 000 and 100 000. These operating conditions conduct to wall heat fluxes between 100 kW/m^2 and 600 kW/m^2. To compensate the low density of the gas when compared to the liquid or the molten salt, the thermodynamical pressure is usually set to 10 bars.

1.4 Flow simulation

The flow simulation requires solving the Navier-Stokes equations. They are non-linear partial differential equations that describe the motion of viscous fluid substances in a continuous domain. In the 1820s, French engineer Claude-Louis Navier introduced the element of viscosity to the Euler equation. Approximately two decades after, British physicist and mathematician Sir George Gabriel Stokes improved on this work, leading to the Navier-Stokes equations.

The studied flows are characterized by strong forced convection that is preponderant in front of the natural convection. The Richardson number, which expresses the ratio of the buoyancy

to the viscous force acting on a fluid, is defined by

$$Ri = \frac{g\beta\Delta T_\star L_\star}{U_\star^2}, \tag{1.1}$$

or

$$Ri = \frac{Gr}{Re^2}, \tag{1.2}$$

with $Gr = g\beta\Delta T_\star L_\star^3 \rho_\star^2/\mu_\star^2$ the Grashof number. In those equations, $\beta = (1/P)(\partial P/\partial T)_v$ is the coefficient of thermal expansion (equal to 1/T, for ideal gases), g is the gravitational constant, $T_\star$ is the characteristic temperature, $U_\star$ is the characteristic streamwise velocity, and $L_\star$ is a characteristic length. In the investigated conditions, the Grashof number is about 10^{-4} at most, highlighting the dominance of the forced convection in front of the natural convection. Hence, the gravity effects are neglected.

In the studied conditions, there is a strong coupling between the turbulence and the thermal effects. For that reason, the thermal dilatation as well as the fluid property variations are taken into account. In the simulations, the Navier-Stokes equations are solved to compute the flow.

1.4.1 Navier-Stokes equations

1.4.1.1 General case

In this section, the general Navier-Stokes equations are described. They consist of a set of three equations. The mass conservation law states that despite chemical reactions or physical transformations, mass is conserved within an isolated system. It cannot be created or destroyed. The mass conservation law derives from the theory of classical mechanics [62]. The momentum conservation equation traduces the balance between the variations of momentum and the sum of external forces [63]. Lastly, the energy conservation equation is obtained from the first law of thermodynamics [64]. It expresses the equality between the variations of total energy and the sum of the external work and the heat flux received. The equations are listed below in index notation, assuming that no volumic force is involved:

- Mass conservation equation

$$\frac{\partial \rho}{\partial t} + \frac{\partial \rho U_j}{\partial x_j} = 0, \tag{1.3}$$

- Momentum conservation equation

$$\frac{\partial \rho U_i}{\partial t} = -\frac{(\partial \rho U_j U_i)}{\partial x_j} + \frac{\partial \Upsilon_{ij}}{\partial x_j}, \tag{1.4}$$

- Total energy conservation

$$\frac{\partial \rho (E+I)}{\partial t} = \frac{\partial \rho U_j (E+I)}{\partial x_j} - \frac{\partial Q_j}{\partial x_j} + \frac{\partial \Upsilon_{ij} U_i}{\partial x_j}, \tag{1.5}$$

with x_i the Cartesian coordinate in the i-th direction, U_i the velocity in the i-th direction, Υ_{ij} the component of the total stress tensor, Q_j the conductive heat flux in the j-th direction, t the time, I the internal energy per unit mass, and $E = U_i U_i/2$ the kinetic energy per unit mass.

The total stress tensor can be decomposed into the sum of the pressure and the viscous stresses:

$$\Upsilon_{ij} = -P\delta_{ij} + \Sigma_{ij}. \tag{1.6}$$

Assuming a Newtonian fluid, the viscous stresses are linearly correlated to the local strain rate,

$$\Sigma_{ij} = 2\mu S_{ij} + \eta S_{kk}\delta_{ij}, \tag{1.7}$$

where μ denotes the dynamic viscosity, η is the second viscosity, and S_{ij} is the rate of deformation tensor, whose expression is given by:

$$S_{ij} = \frac{1}{2}\left(\frac{\partial U_i}{\partial x_j} + \frac{\partial U_j}{\partial x_i}\right). \tag{1.8}$$

The Stokes' hypothesis [65] permits linking the second viscosity to the dynamic viscosity with the following expression:

$$\eta = -\frac{2}{3}\mu, \tag{1.9}$$

equation (1.7) thus becomes:

$$\Sigma_{ij} = 2\mu S_{ij} - \frac{2}{3}\mu S_{kk}\delta_{ij}. \tag{1.10}$$

The conductive heat flux, involved in the energy conservation equation, is obtained thanks to the Fourier's law [66],

$$Q_j = -\lambda\frac{\partial T}{\partial x_j}, \tag{1.11}$$

where λ is the thermal conductivity and T is the temperature.

Note that the energy conservation equation can be written with alternative formulations. The transport equation of kinetic energy, internal energy, enthalpy, entropy, temperature, and pressure are described in Garnier *et al.* [67]. The transport equation of temperature that is classically used is given by:

$$C_v\frac{\partial \rho T}{\partial t} = -C_v\frac{\partial \rho U_j T}{\partial x_j} - \frac{\partial Q_j}{\partial x_j} - \beta P T\frac{\partial U_j}{\partial x_j} + \Sigma_{ij}\frac{\partial U_i}{\partial x_j}, \tag{1.12}$$

where $C_v = (\partial I/\partial T)_v$ is the isochoric heat capacity. The system consists in five equations and involves eight variables $(\rho, U, V, W, T, P, \lambda, \mu)$. Hence, it is necessary to add three equations to close it.

1.4.1.2 Ideal gas law

The ideal gas law was stated by Benoît Paul Émile Clapeyron in 1834 as a combination of the empirical Boyle's law, Charles's law, Avogadro's law, and Gay-Lussac's law [68]. The ideal gas law relies on a series of hypotheses on gas particles. (1) All gas particles are in constant motion and collisions between the gas molecules and the walls of the container cause the pressure of the gas. (2) The particles are so small that their volume is negligible compared with the volume occupied by the gas. (3) The particles do not interact, meaning that there are no attractive or repulsive forces between them. (4) The average kinetic energy of the gas particles is proportional to temperature. The ideal gas law relates the density to pressure and temperature,

$$P = \rho r T, \tag{1.13}$$

where r is the ideal gas-specific constant. In an ideal gas, the heat capacities obey Mayer's relation, defined as $C_p - C_v = r$. They are only dependent on the temperature. Moreover, the isobaric thermal expansion coefficient, α, and the isochoric thermal pressure coefficient, β are equal: $\alpha = \beta = 1/T$. Thus, internal energy and enthalpy only depend on temperature.

1.4.2 Determination of the fluid properties

The system of equations (1.3-1.5) associated with the ideal gas law (1.13) describes the physics of the flow and provides six equations. Two more equations are needed to compute the dynamic viscosity and thermal conductivity.

The studied gas-pressurized solar receivers are those operating with air. The ideal gas specific constant is obtained combining the expression $r = C_p - C_v$ and $\gamma = C_p/C_v$. The adiabatic index, γ is obtained from tables at the mean wall temperature. The Sutherland's law [69] permits computing the dynamic viscosity thanks to the temperature. It is based on the kinetic theory of ideal gases and an idealized intermolecular-force potential. The Sutherland's law is still widely used and gives fairly accurate results over a wide range of temperatures (from 220 K to 1900 K) [69]. The Sutherland's law is expressed as:

$$\mu(T) = \mu_0 \frac{T}{T_0}^{3/2} \frac{T_0 + S}{T + S}, \tag{1.14}$$

where $\mu_0 = 1.716 \times 10^{-5}$ Pa.s, $S = 110.4$ K, and $T_0 = 273.15$ K. The conductivity is deduced from the Prandtl number, the heat capacity at constant pressure, and the viscosity:

$$\lambda(T) = \frac{C_p}{Pr}\mu(T). \tag{1.15}$$

Within this temperature domain, the variations of the adiabatic index of air are very small. Hence, the heat capacity, C_p, is assumed to be constant and is computed with the average of the wall temperatures. The Prandtl number varies between the simulations, depending on the studied conditions. However, for a particular simulation, the Prandtl number is supposed to be constant over the domain.

1.4.3 Low Mach number equations

The mathematical formulation of incompressible fluid flow differs from the one of compressible fluid flow since, in the first case, the density is constant and permits simplifying the Navier-Stokes equations. The theory of low Mach number flow aims to narrow the gap between those two different formulations of fluid flow. The Low Mach number assumption was proposed by Paolucci [2] in 1982. This hypothesis is suitable for the computation of convection in a fluid in the presence of large density gradients. Note that in Boussinesq's hypothesis, the compression forces are neglected, except the force associated with the computation of the hydrostatic buoyancy. This assumption is only valid for low-temperature variations ($\Delta T < 30\ K$) [70, 71] and thus not applicable to the field of solar receivers. Under the Low Mach number approximation, the Navier-Stokes equations describe the internal wave propagation, but they do not contain acoustic waves. Neglecting the effects of these last waves permits suppressing the associated numerical constraint. Thus, the numerical methods developed for incompressible flow can be used.

The Mach number permits assessing the subsonic, sonic, or supersonic nature of a flow. It is defined with the speed of sound:

$$Ma = \frac{U_\star}{c_\star}. \tag{1.16}$$

Assuming the ideal gas law, the speed of sound can be computed with the temperature, $c_\star = \sqrt{\gamma r T_\star}$. The low Mach number approximation is based on the removal of the term of order bigger or equal to Ma^2. Classically, this hypothesis is employed for Mach number below 0.3. The approach proposed by Paolucci [2] relies on two steps. In the first step, the Navier-Stokes equations are written with the dimensionless numbers that characterize the relative importance of the competing physical processes. This is detailed in section 1.4.3.1. In the second step, each dimensionless variable is approximated with a power series of the squared Mach number, and the orders higher than one are truncated, see section 1.4.3.2.

1.4.3.1 Dimensionless Navier-Stokes equations

Each dimensionless variable, X^o, is defined as a ratio between the variable, X, and a value characteristic of the flow considered, $X_\star$,

$$X^o = X/X_\star, \tag{1.17}$$

where X is successively $t, L, U, T, \rho, P, \mu, \lambda, C_v$, and C_p.

Three dimensionless numbers permit characterizing the flow. The Reynolds number traduces the ratio between the convective and viscous transfers of momentum,

$$Re = \frac{\rho_\star U_\star L_\star}{\mu_\star}. \tag{1.18}$$

The Prandtl number represents the ratio between the momentum diffusivity and the thermal diffusivity,

$$Pr = \frac{\mu_\star C_{p\star}}{\lambda_\star}. \tag{1.19}$$

In the equation written below, the Péclet number is used. It is defined as the product of the Reynolds and the Prandtl numbers, $Pe = RePr$, and traduces the relative importance of the convective and conductive heat transfers.

The Navier–Stokes equations, written with the dimensionless numbers are:

- Mass conservation equation

$$\frac{\partial \rho^o}{\partial t^o} + \frac{\partial \rho^o U_j^o}{\partial x_j^o} = 0, \tag{1.20}$$

- Momentum conservation equation

$$\frac{\partial \rho^o U_i^o}{\partial t^o} = -\frac{\partial \rho^o U_j^o U_i^o}{\partial x_j^o} - \frac{1}{\gamma Ma^2}\frac{\partial P^o}{\partial x_i^o} + \frac{1}{Re}\frac{\partial \Sigma_{ij}^o}{\partial x_j^o}, \tag{1.21}$$

- Energy conservation

$$C_v^o \frac{\partial \rho^o T^o}{\partial t^o} = -C_v^o \frac{\partial \rho^o U_j^o T^o}{\partial x_j^o} - \frac{\gamma}{Pe}\frac{\partial Q_j^o}{\partial x_j^o} - (\gamma - 1)P^o \frac{\partial U_j^o}{\partial x_j^o} + \gamma(\gamma - 1)\frac{Ma^2}{Re}\Sigma_{ij}^o \frac{\partial U_i^o}{\partial x_j^o}, \tag{1.22}$$

- Ideal gas law

$$P^o = \rho^o T^o, \tag{1.23}$$

with Σ_{ij}^o the nondimensionalized viscous stress tensor,

$$\Sigma_{ij}^o = 2\mu^o S_{ij}^o - \frac{2}{3}\mu^o S_{kk}^o \delta_{ij}, \tag{1.24}$$

and Q_j^o the nondimensionalized conductive heat flux,

$$Q_j^o = -\lambda^o \frac{\partial T^o}{\partial x_j^o}. \tag{1.25}$$

1.4.3.2 Low Mach number equations

Paolucci [2] proposes to express each variable as a power series of the squared Mach number.

$$X^o = X^{(0)} + Ma^2 X^{(1)} + \mathcal{O}(Ma^4) \tag{1.26}$$

Since the Mach number is assumed to be low, the term of order superior or equal to Ma^2 can then be neglected. Rewritting the equations (1.20)-(1.23) with the asymptotic developments results in:

- Mass conservation equation

$$\frac{\partial \rho^{(0)}}{\partial t^{(0)}} + \frac{\partial \rho^{(0)} U_j^{(0)}}{\partial x_j^o} = \mathcal{O}(Ma^2), \tag{1.27}$$

- Momentum conservation equation

$$\frac{\partial \rho^{(0)} U_i^{(0)}}{\partial t^{(0)}} = -\frac{\partial \rho^{(0)} U_j^{(0)} U_i^{(0)}}{\partial x_j^o} - \frac{1}{\gamma^{(0)} Ma^2}\frac{\partial P^{(0)}}{\partial x_i^o} - \frac{1}{\gamma^{(0)}}\frac{\partial P^{(1)}}{\partial x_i^o} + \frac{1}{Re}\frac{\partial \Sigma_{ij}^{(0)}}{\partial x_j^o} + \mathcal{O}(Ma^2), \tag{1.28}$$

- Energy conservation

$$C_v^{(0)}\frac{\partial \rho^{(0)} T^{(0)}}{\partial t^{(0)}} = -C_v^{(0)}\frac{\partial \rho^{(0)} U_j^{(0)} T^{(0)}}{\partial x_j^o} - \frac{\gamma^{(0)}}{Pe}\frac{\partial Q_j^{(0)}}{\partial x_j^o} - (\gamma^{(0)} - 1)P^{(0)}\frac{\partial U_j^{(0)}}{\partial x_j^o} + \mathcal{O}(Ma^2), \tag{1.29}$$

- Ideal gas law

$$P^{(0)} = \rho^{(0)} T^{(0)} + \mathcal{O}(Ma^2), \tag{1.30}$$

The Mach number is supposed to be low ($Ma << 1$). For that reason, the main terms in the conservation momentum equation are those of order $\mathcal{O}(Ma^{-2})$:

$$\frac{1}{\gamma^{(0)}}\frac{\partial P^{(0)}}{\partial x_i^o} = 0, \tag{1.31}$$

which leads to

$$\frac{\partial P^{(0)}}{\partial x_i^o} = 0, \tag{1.32}$$

The spatial variations of zeroth-order pressure are at least of order $\mathcal{O}(Ma^{-2})$. Put in perspective with the Paolucci assumption, it traduces the homogeneity of this pressure. The momentum conversation equation can be written with the term of order inferior to $\mathcal{O}(Ma^{-2})$.

$$\frac{\partial \rho^{(0)} U_i^{(0)}}{\partial t^{(0)}} = -\frac{\partial (\rho^{(0)} U_j^{(0)} U_i^{(0)})}{\partial x_j^o} - \frac{1}{\gamma^{(0)}}\frac{\partial P^{(1)}}{\partial x_i^o} + \frac{1}{Re}\frac{\partial \Sigma_{ij}^{(0)}}{\partial x_j^o}. \tag{1.33}$$

1.4.3.3 Dimensioned low Mach number equations

Redimensioning equations (1.20)-(1.23) results in the low Mach number equations:

- Mass conservation equation

$$\frac{\partial \rho}{\partial t} + \frac{\partial \rho U_j}{\partial x_j} = 0, \tag{1.34}$$

- Momentum conservation equation

$$\frac{\partial \rho U_i}{\partial t} = -\frac{\partial \rho U_j U_i}{\partial x_j} - \frac{\partial P}{\partial x_i} + \frac{\partial \Sigma_{ij}}{\partial x_j}, \tag{1.35}$$

- Energy conservation equation

$$\frac{\partial U_j}{\partial x_j} = -\frac{1}{\gamma P_0}\left[(\gamma - 1)\frac{\partial Q_j}{\partial x_j} + \frac{\mathrm{d}P_0}{\mathrm{d}t}\right], \tag{1.36}$$

- Ideal gas law

$$T = \frac{P_0}{\rho r}, \tag{1.37}$$

where the pressure involved in the energy equation, and denoted $P_0 = P_\star P^{(0)}$, represents the mean pressure in the computational domain and only depends on the time ($\partial P_0/\partial x_i = 0$). It is called the thermodynamical pressure and computed thanks to the ideal gas law. The mechanical pressure, P, appears in the momentum conservation equation and is spatially varying. Note that equation (1.36) is obtained from equation (1.29) by applying the ideal gas law which leads to a constant product ρT since the thermodynamical pressure is constant.

1.4.3.4 Heat source

In solar power towers, the solar radiation is concentrated in the front wall of the solar receiver. The irradiated wall converts the concentrated solar energy into heat then transfers the heat of the concentrated sunlight to the fluid by conduction. The very high temperature of the hot wall induces substantial radiative transfers. Therefore, the opposed wall, which is insulated from the ambient air, receives a large proportion of the hot wall radiation and its temperature becomes higher than the mean fluid temperature. It results in fluid heating from both sides of the solar receiver.

In this study the flow passing through the solar receiver is modeled with a bi-periodical channel flow. This allows to simulate various sections of the solar absorber. The bi-periodical conditions permit obtaining the convergence of the flow parameter statistics but imply the study of a fully developed flow. A source term is then introduced in the energy equation to compensate the contributions of the walls and allows the thermal development of the flow. Modifying the heat source permits studying of various temperature profiles, *i.e.* various axial location in the solar receiver. The energy equation described by equation (1.36) becomes:

$$\frac{\partial U_j}{\partial x_j} = -\frac{1}{\gamma P_0}\left[(\gamma - 1)\left(\frac{\partial Q_j}{\partial x_j} - H_s\right) + \frac{\mathrm{d}P_0}{\mathrm{d}t}\right], \tag{1.38}$$

where H_s is the volumic heat source.

The heat source has been validated with an analytic solution. The results are given in appendix B.

1.5 Numerical settings

The Navier-Stokes equations are coupled and highly non-linear. Thus, their resolution is very complex. Up to now, the general solution of this set of equations remains unknown. Analytical solutions have only been found for the most simple problems characterized by purely laminar flow passing through an academic geometry. The existence of weak solutions to the incompressible case was proved in Leray [72]. Furthermore, the weak solutions of the compressible Navier-Stokes equations were analyzed to characterize them [73, 74]. Numerous studies investigated the strong solution existence as well as their properties [75, 76]. Note that the Navier-Stokes existence and smoothness problem belongs to the Millennium Prize Problems [77].

In this study, turbulent flows are investigated. The turbulence appears when the source of kinetic energy which drives the fluid in motion is intense and able to overcome the viscosity effects. The turbulent flows are characterized by irregular patterns, unpredictable behavior, and the existence of numerous space and time scales [78]. Since no analytical solution has been found up to now, numerical simulations and experiments are the only way to analyze these flows. The Navier-Stokes equations describe a continuous flow but the computers can only solve discrete problems. For that reason, it is necessary to discretize both the computational domain and the equations. We use a finite difference method in a staggered grid system. The time derivatives are approximated with a third-order Runge-Kutta scheme. The software used to perform the simulations is TrioCFD [3]. The resolution algorithm and the numerical schemes are described in this section.

1.5.1 Resolved algorithm

This section gives the resolution algorithm implemented in TrioCFD to solve the low Mach number equations (1.34)-(1.37). The algorithm intents to numerically verify as many conservation properties as possible. Pressure and velocity are computed with a projection method. The reader is referred to [79, 80] for an introduction on the projection methods. Projection models rely on a two-step procedure. First, an intermediate velocity field is computed by ignoring the pressure term in the momentum conservation equation. Afterward, this ephemeral velocity is adjusted using a pressure equation to impose the constraint of the energy conservation equation on the divergence of the velocity.

The variables involved in the low Mach number equations are solved in the order given below. Note that the time derivatives are given with an explicit Euler discretization to simplify the reading of the expression. However, in the actual algorithm, they are discretized using a third-order Runge-Kutta method [5].

1. The density is computed from the mass conservation equation,

$$\rho^{n+1} = -\Delta t \left[\nabla \cdot (\rho^n \boldsymbol{U}^n)\right] + \rho^n. \tag{1.39}$$

2. The thermodynamical pressure and temperature using a fixed-point iteration, for k from 0 to 3, (note that this value is empirically determined to obtain convergence) of:

   (a) the thermodynamical pressure is computed from the integration on the whole domain of the energy conservation equation and taking into account the heat source,

$$\frac{1}{\gamma - 1}\frac{\mathrm{d}P_0}{\mathrm{d}t} = \frac{1}{V}\int_V \frac{\partial Q_j}{\partial x_j} - H_s \, \mathrm{d}V, \tag{1.40}$$

leading, after applying the divergence theorem and discretizing the equation, to:

$$P_0^{n+1,k+1} = \frac{P_0^n}{1-(\gamma-1)\dfrac{\Delta t}{P_0^{n+1,k}}\left(\dfrac{1}{V}\displaystyle\int_\omega \lambda_\omega \nabla T^{n+1,k}\, dS - H_s\right)}, \tag{1.41}$$

(b) the temperature is deduced from the ideal gas law,

$$T^{n+1,k+1} = \frac{P_0^{n+1,k+1}}{r\rho^{n+1}}, \tag{1.42}$$

3. The kinematic viscosity is determined with Sutherland's law,

$$\mu^{n+1} = \mu_0 \left(\frac{T^{n+1}}{T_0}\right)^{\frac{3}{2}} \frac{T_0 + S_1}{T^{n+1} + S_1}. \tag{1.43}$$

4. The thermal conductivity is deduced from the Prandtl number,

$$\lambda^{n+1} = \frac{\mu^{n+1} C_p}{Pr}. \tag{1.44}$$

5. The energy conservation equation is used to compute the divergence of velocity,

$$\nabla \cdot \boldsymbol{U}^{n+1} = \frac{1}{\gamma P_0^{n+1}} \left[(\gamma-1)\left(\nabla \cdot (\lambda^{n+1}\nabla T^{n+1}) - H_s\right) - \frac{P_0^{n+1} - P_0^n}{\Delta t}\right]. \tag{1.45}$$

6. The intermediate velocity is obtained thanks to the momentum conservation equation without the pressure term,

$$\boldsymbol{U}^* = \frac{\Delta t}{\rho^n}\left[\boldsymbol{U}^n \nabla \cdot (\rho^n \boldsymbol{U}^n) - \nabla \cdot (\rho^n \boldsymbol{U}^n \boldsymbol{U}^n) + \nabla \cdot \left(\mu^n (\nabla \boldsymbol{U}^n + \nabla^T \boldsymbol{U}^n)\right) - \frac{2}{3}\nabla\left(\mu^n \nabla \cdot \boldsymbol{U}^n\right)\right] + \boldsymbol{U}^n. \tag{1.46}$$

7. The mechanical pressure is deduced from the divergence of the intermediate velocity,

$$\nabla \cdot \left(\frac{1}{\rho^n}\nabla P^{n+1}\right) = \frac{\nabla \cdot \boldsymbol{U}^* - \nabla \cdot \boldsymbol{U}^{n+1}}{\Delta t}. \tag{1.47}$$

8. Lastly, the velocity is computed from the momentum conservation equation,

$$\boldsymbol{U}^{n+1} = -\frac{\Delta t}{\rho^n}\nabla P^{n+1} + \boldsymbol{U^*}. \tag{1.48}$$

This algorithm permits obtaining a stable thermodynamical pressure once the flow is established, as seen on figure 1.2. This pressure exhibits fluctuations with periods in the order of few characteristic times, $\tau_c = \delta/U_\tau$, and around an average of 1.0055×10^6 Pa. The peaks lies between $\pm 0.1\%$ of the mean thermodynamical pressure.

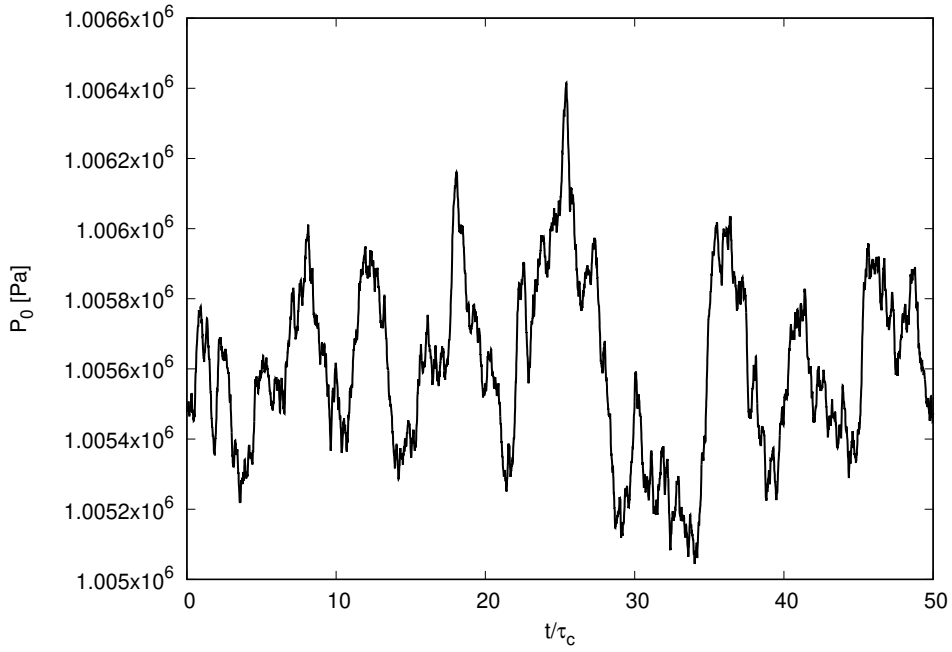

Figure 1.2 – Thermodynamical pressure as a function of time.

1.5.2 Discretization of the equations

Numerical schemes are used to discretize continuous equations. The Navier-Stokes equations are a set of partial differential equations involving time and spatial derivatives. A large number of studies highlight the importance of the numerical schemes in LES [81, 82, 83, 84, 85, 86] and in DNS [87, 88]. In the next, LES and DNS are carried out with the same numerical conditions on the same software. The solution obtained by the resolution of the discretized equations can no more be exact but it has to be as close as possible to the solution of the continuous problem. The following criteria are crucial to the performance of a numerical scheme:

- Local consistency: the discretization of a partial differential equation should tend to the exact solution as the mesh size tends to zero. Given a partial differential equation $Pu = f$ and a finite difference scheme, $P_{\Delta t,\Delta x} v = f$, the finite difference scheme is consistent with the partial differential equation if for any smooth function $\Psi(x,t)$, $||P\Psi - P_{\Delta t,\Delta x}\Psi|| \to 0$ as $\Delta t, \Delta x \to 0$

- Stability: numerical errors which are generated during the computation of the solution should not be magnified. $P_{\Delta t,\Delta x} v_i^n = 0$ for a first-order equation is stable in a stability region Λ if there is an integer J such that for any positive time T, there is a constant C_T such that

$$||v^n||_{\Delta x} \leq C_T \sum_{j=1}^{J} ||v^j||_{\Delta x} \tag{1.49}$$

for $0 \leq n\Delta t \leq T$, with $(\Delta t, \Delta x)$ belonging to the stability region. Considering $||v^n||_{\Delta x}$ the

L2-norm of a grid function v,

$$||v^n||_{\Delta x} = \sqrt{\Delta x \sum_{m=-\infty}^{\infty} |v_m|^2}. \tag{1.50}$$

- Global convergence: the numerical solution should approach the exact solution of the partial differential equation and converge to it as the mesh size tends to zero.
- Respect of physical constraints: underlying conservation laws have to be respected at the discrete level and quantities such as densities, temperatures, concentrations *etc.* have to remain non-negative and free of spurious wiggles.

The mass convection term of the mass conservation equation is discretized using the third-order QUICK scheme proposed by Leonard [6] with a FRAM filtering [89]. In the momentum conservation equation, the momentum convection is approximated with a fourth-order centered scheme and the momentum diffusion terms are discretized with a second-order centered scheme. In the energy conservation equation, the divergence of velocity and the temperature diffusion are given by a second-order centered scheme. The velocity components are at the center of the cell faces they are perpendicular to. The scalar variables are located at the center of the cells.

In the solar receiver, the accurate determination of the wall heat flux is critical. The wall heat flux is defined by:

$$\Phi_w = \lambda_w \left.\frac{\partial T}{\partial y}\right|_w. \tag{1.51}$$

During this thesis, we increase the order of accuracy of the numerical scheme used to compute the wall heat flux, which was a first-order off-centered scheme, by modifying the TrioCFD code. The spatial temperature derivative is discretized with a second-order off-centered scheme:

$$\left.\frac{\partial T}{\partial y}\right|_w = \frac{(y_2 - y_w)(y_1 - y_w)}{(y_2 - y_1)} \left(T_2 \frac{1}{(y_2 - y_w)^2} - T_1 \frac{1}{(y_1 - y_w)^2} - T_w \frac{(y_1 - y_w)^2 - (y_2 - y_w)^2}{(y_1 - y_w)^2 (y_2 - y_w)^2} \right) \tag{1.52}$$

The implementation of the discretization has been performed in C++ programming language and allows the parallel computation. The scheme has been validated in a very simple case study with an analytical solution. The results are provided in appendix A.

1.5.3 Temporal stability criteria

The time step of the simulation, denoted Δt, is computed at each iteration to respect stability criteria. The time step of the simulation is only determined by the stability requirements of the momentum conservation equation. Indeed, the energy conservation equation has no stability constraints since it acts as a constraint on the pressure in the resolution algorithm. Two stability criteria are used. The Courant-Friedrichs-Lewy (CFL) condition [90] is a necessary condition for convergence while solving certain partial differential equations numerically. It arises in the numerical analysis of explicit time integration schemes. The CFL condition can be seen as a sort of discrete "light cone" condition, meaning that the time step must be kept small enough so that information has enough time to propagate through the space discretization. In other words, the solution at the next time step must be able to include all the physical information that influences the solution from the previous time step. The CFL condition is often confused

with linear stability conditions or nonlinear stability conditions. However, it is not a sufficient condition for stability. The convection stability time step is given by

$$\frac{1}{\Delta t_{\text{conv}}} = \max_{x,y,z} \left[\frac{U_x}{\Delta x} + \frac{U_y}{\Delta y} + \frac{U_z}{\Delta z} \right]. \tag{1.53}$$

A second stability time step is associated to momentum diffusion. It is defined by:

$$\frac{1}{\Delta t_{\text{diff}}} = \max_{x,y,z} \left[2\nu \left(\frac{1}{\Delta x^2} + \frac{1}{\Delta y^2} + \frac{1}{\Delta z^2} \right) \right]. \tag{1.54}$$

The time step of the simulation computed as the half of the harmonic mean of these two values:

$$\frac{1}{\Delta t} = \frac{1}{\Delta t_{\text{conv}}} + \frac{1}{\Delta t_{\text{diff}}}. \tag{1.55}$$

Note that, in practice, the time step is only updated if it is less than the previous time step, or if the relative difference between the current and the previous time step is more than 5 %.

1.6 Modeling of the solar receiver

1.6.1 Computation domain size and discretization

The gas-pressurized solar receiver is the place of complex flows characterized by strong asymmetric heating of a highly turbulent gas flow. An academic channel geometry is used to reproduce the flow characteristics encountered in a slice of solar receiver, see Figure 1.3. The channel is 3 mm in height. The wall-normal direction is denoted (y). The streamwise (x) and spanwise (z) directions are periodic. It gives the ability to investigate different locations in the solar receiver by modifying the wall temperatures, that are spatially and temporally constant in this study. Note that in the real conditions, the wall temperatures of the channel are not homogeneous and the thermal boundary conditions are neither fixed wall temperatures nor fixed wall heat flux. Indeed, the solar radiation is concentrated on the front wall of the solar receiver in the form of a spot. The maximum concentration is reached at the center of the spot then the concentration decreases as the distance from the center increases. Furthermore, the concentrated solar radiation is mainly influenced by the position of the sun in the sky, the quality of ambient air (relative humidity and pollutant levels), and the quality of the heliostats. Thus, the concentrated radiation is temporally varying. Here, the hypothesis of homogeneous wall temperatures is reasonnable since the study is performed for a fixed location in the solar receiver (see yellow line in figure 1.3).

In part I, the thermal-large eddy simulations are studied in both isothermal and anisothermal channels. In the first case, both wall temperatures are fixed at 293 K. In the second case, the hot and cold wall temperatures are respectively fixed at $T_h = 1300\ K$ ($y = 2\delta$) and $T_c = 900\ K$ ($y = 0$). This creates a temperature gradient in the wall-normal direction. In part II, a large number of combinations of hot and cold wall temperature are investigated. Since the channel is periodic, the dissipative action of the viscous shear stress is not balanced out by a streamwise pressure gradient. A streamwise volume force is added to the channel to maintain a constant friction. This replicates the effect of a streamwise pressure gradient and results in a constant mass flow. The computation domain is a three-dimensional channel enclosed by two walls. The domain size is $L_x \times L_y \times L_z = 4\pi\delta \times 2\delta \times 4/3\pi\delta$, with $\delta = 3$ mm for all the simulations performed in this

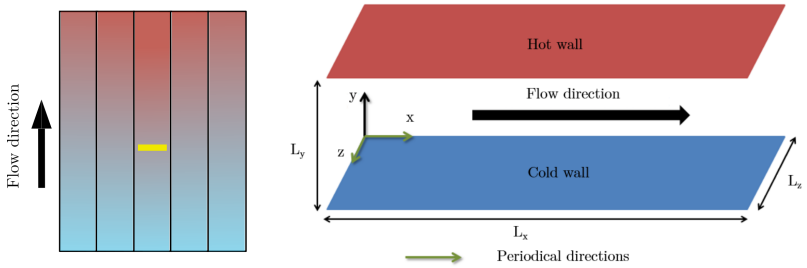

Figure 1.3 – On the left, the yellow line schematizes the slice of solar receiver that is pictured by the bi-periodical channel displayed on the right.

study. Since there are strong wall-normal gradients of temperature and velocity, a nonuniform mesh is used in the wall-normal coordinate direction (y). The solar receiver is modeled with a three-dimensional channel. The streamwise and spanwise directions are discretized with a uniform grid spacing. In the wall-normal direction, which is submitted to high velocity and temperature gradients, the mesh is nonuniform. The wall-normal grid points are given by a hyperbolic tangent law.

$$y_k = L_y \left(1 + \frac{1}{a} \tanh\left[\left(\frac{k-1}{N_y - 1} - 1\right) \tanh^{-1}(a)\right]\right), k \in [1, N_y], \tag{1.56}$$

with a the mesh dilatation parameter and N_y the number of grid points in the wall-normal direction.

1.6.2 Data processing

Turbulent flows are chaotic, meaning that independent experiments or simulations with close initial conditions lead to different results. The Reynolds decomposition is classically used and consider each instantaneous variable, f, as the sum of its mean part, $\langle f \rangle$, and its fluctuating part, f':

$$f = \langle f \rangle + f'. \tag{1.57}$$

By definition, the statistical mean of the fluctuating part is equal to zero. Reynolds averaging is often used in fluid dynamics to separate turbulent fluctuations from the mean-flow. It consists in the average of a large number of independent experiments, denoted N:

$$\langle f \rangle = \lim_{N \to \infty} \frac{1}{N} \sum_{i=1}^{N} f_i. \tag{1.58}$$

The ergodicity hypothesis, formulated by Boltzmann in 1871, allows to assimilate the Reynolds average to an average over time and the homogeneous directions. Hence, the first- and second-order statistics analyzed in the following are only dependent on the wall-normal direction (y).

The instantaneous results obtained in the simulations are unsteady and non homogeneous, see the instantaneous field of streamwise velocity obtained with DNS in Figure 1.5. These results are spatially averaged in the two homogeneous directions in order to be compared with other simulations. Once the flow is fully developed, an average over the time is performed in order to

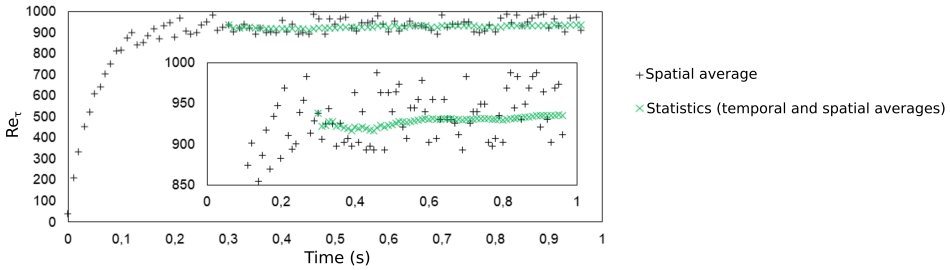

Figure 1.4 – Spatial and spatiotemporal average of the friction Reynolds number as a function of the simulated time.

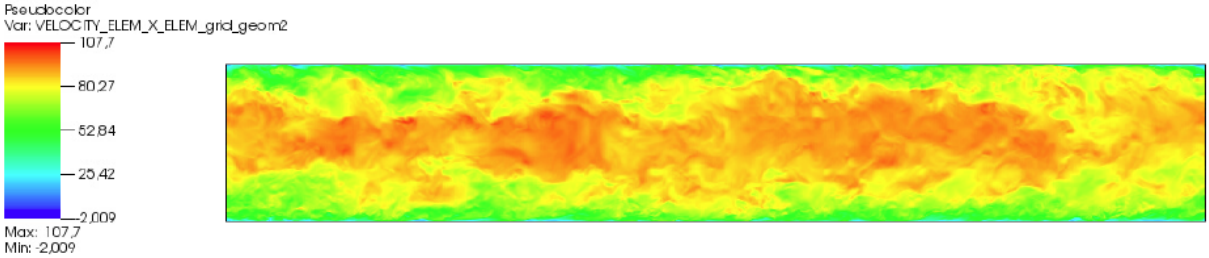

Figure 1.5 – Instantaneous field of streamwise velocity obtained with DNS.

obtain converged results. This is illustrated in Figure 1.4. When the spatially averaged friction Reynolds number is fluctuating around a stable value, the spatiotemporal average is reset and the simulation proceed until the statistics of the friction Reynolds number stabilize.

1.7 Validation

To the author knowledge, there is no reference data in the working conditions of the gas-pressurized solar receiver. For that reason, the numerical method is validated by comparing the DNS results in the isothermal case with reference data from the literature. Dupuy *et al.* [91] already validated the numerical method at friction Reynolds number of 180 and 395 thanks to the DNS of Moser *et al.* [7], Vreman and Kuerten [8], and Lee and Moser [9]. In the present study, we investigate larger mass flow in order to be closer to the solar receiver conditions and compare a DNS to the results of Hoyas and Jiménez [10]. The authors performed a DNS at a friction Reynolds number of 934 in a bi-periodical channel whose dimensions are $L_x \times L_y \times L_z = 8\pi\delta \times 2\delta \times 3\pi\delta$. The wall-normal profiles of streamwise velocity and the correlations of velocity normalized by the friction velocity are compared in Figure 1.6. The comparison shows that the present DNS fit very well the data of Hoyas and Jiménez. Note that, the present DNS marginally overestimates the peak of the streamwise velocity correlation. This is probably to the finer mesh employed by Hoyas and Jiménez.

In appendix F, the numerical setting and the mean flow variables of the three performed DNS are listed.

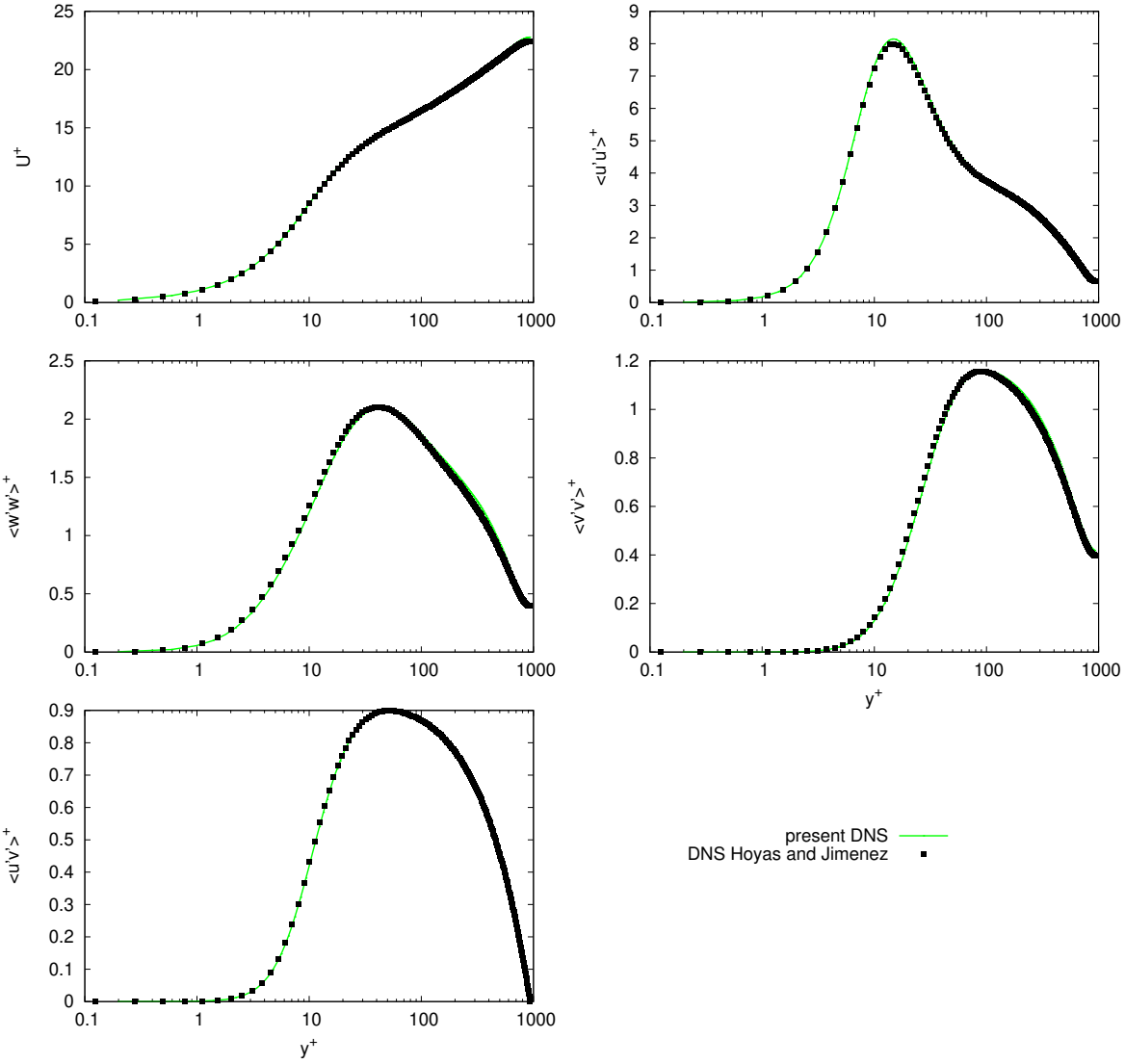

Figure 1.6 – Comparison of the present DNS results with a DNS performed by Hoyas and Jiménez [10] at a friction Reynolds number of 930.

1.8 Conclusion of chapter 1

The gas-pressurized solar receiver technology permits reaching very high temperatures and consequently to improve the power conversion efficiency of solar power towers. However, the absorber is characterized by very complex flows that involve strong asymmetric heating from both sides of a turbulent flow. The levels of temperature and wall heat flux are high. These extreme operating conditions induce a strong coupling between the dynamic and the temperature which renders the comprehension of the flow difficult. A bi-periodical channel is used to model the solar receiver

since it is well adapted to reproduce the physic encountered in these systems: turbulence and asymmetric heating of the fluid.

The Navier-Stokes equations describe flows. Up to now, there is no analytical solution of these equations for turbulent flows. For that reason, they require to be numerically solved in the studied conditions. By neglecting the effect of the acoustic waves, the Low Mach number equations mitigate the computational cost of the simulations and allow the use of numerical methods developed for incompressible flows. The equation system is closed with the ideal gas law. The strong coupling between the dynamic and the temperature occurring in the solar receiver is taken into account. The low Mach number equations are solved thanks to the code TrioCFD. A source term is introduced in the energy conservation equation. It enables the study of different fluid temperature profiles and, thus, to investigate various axial locations in the solar receiver.

The presented setup is used in the following to develop a multi-scale approach. It aims to perform DNS, LES, and wall heat flux estimation thanks to a heat transfer correlation in the working conditions of solar receivers that are characterized by a strong coupling between the intense turbulence and the asymmetric heating of the fluid. In part I, the results of DNS are utilized to analyze the flow behavior in those extreme conditions and to perform *a posteriori* tests of large eddy simulation at high Reynolds numbers in various thermal conditions. In part II, a heat transfer correlation, adapted to asymmetric heating, is developed and used to study the wall heat flux analysis.

Part I

Analysis of flow physics and *a posteriori* tests of large eddy simulations

The present part addresses the micro- and meso-scales of the multi-scale approach. The Direct Numerical Simulations (DNS) are used to investigate the flow physics and provide reference data for the *a posteriori* tests of Large Eddy Simulations (LES). A large number of LES are performed and compared with the DNS. This part is divided into two chapters. In chapter 2, generalities on LES are presented. In chapter 3, the DNS and LES are carried out in isothermal conditions. The focus is placed on turbulence. In chapter 4, the simulations are performed in the extreme operating conditions of gas-pressurized solar receivers. The temperature effects are analyzed. Chapter 5 concludes on the flow physics and the tests of LES.

Chapter 2

Generalities on large eddy simulations

Contents

2.1 Introduction of chapter 2

The Navier–Stokes equations proposed by Claude-Louis Navier and George Gabriel Stokes in the 1840s constitute a rigorous description of fluid flow. However, except for very simple problems, analytic solutions cannot be obtained, meaning that these equations could not be solved in most practical flows. Flow simulations await the emergence of computers. One of the earliest types of calculations resembling modern Computational Fluid Dynamic (CFD) were those of Richardson who attempt, in 1910, to forecast the weather during a single day by direct computation. His predictions were completely wrong but they set the basis for modern CFD. With the increasing power of computers, CFD became widely used in industry. However, many complex flow simulations remain infeasible due to excessive computational cost.

Concerning the turbulence simulations, current CFD methods are divided into three main approaches. The most detailed of these approaches is the Direct Numerical Simulation (DNS). The Navier-Stokes equations are solved on a very fine mesh to resolve all the spatial and temporal scales present in the flow. However, up to now, DNS are only performed in research laboratories due to their very high computational cost. In industry, the Reynolds Averaged Navier-Stokes

equations (RANS) are mostly used. It consists of an averaging operation applied to the Navier-Stokes equations to obtain the mean equations of fluid flows. These new equations introduce new apparent stresses known as Reynolds stresses resulting in a second-order tensor of unknowns that requires a model to close the system. In RANS simulations, the equations are time-averaged. For that reason, only steady state flows can be computed. This approach does not need substantial computational resources. Hence, it is well adapted to studies of device at the metric level performed by engineers on a single computer. The Large Eddy Simulation (LES) is the third approach. It solves the large scales of turbulence and models the small scales in order to reproduce their effects on the larger scales. Thus, LES is a compromise between DNS and RANS in terms of wealth of information and computational cost [92, 93]. Contrary to the traditional RANS simulation, it enables the computation of unsteady flows. LES is commonly used in laboratory researches but is becoming more and more present in the industry thanks to the increase of computer power. Note that, several sub-categories of CFD methods exist. The two mains are: (1) the Unsteady RANS (URANS) allow to simulate statistically unsteady flows [94, 95, 96]; (2) the Detached Eddy Simulation (DES) acts as LES with a wall model [97, 98, 99]. The model switches to a subgrid-scale formulation when the mesh is fine enough for LES calculations.

The operating conditions of gas-pressurized solar receivers are characterized by a strong coupling between the dynamic and the temperature. The flow complexity and the scale gap between the smallest turbulent structures and the size of the solar receiver are high. For that reason, the LES is particularly suitable to investigate the flow passing through the solar receiver. The development of the solar power towers requires to optimize the heat transfer from the concentrated solar radiation to the fluid. These simulations represent a very interesting compromise between the computational cost and the quality and quantity of the obtained information. They permit performing a large number of simulations in different dynamic and thermal conditions. For that reason, they constitute the essential link between the DNS and the heat transfer correlation used to perform studies of the entire system. This chapter is organized as follows. The main principles of LES are given in section 2.2. The concepts of turbulence filtering and subgrid-scale modeling are respectively detailed in section 2.3 and section 2.4. Lastly, a short review of the generalities on LES is proposed and the scope of the DNS and LES studies in given in section 2.5.

2.2 Main principles

In large eddy simulations, the larger structures of motion are resolved and the small structures are only taken into account with regard to their effect on the larger structures [100, 101, 102]. A spatiotemporal filter is used to separate the resolved scales from the modeled scales [6]. The LES involving an algebraic model assumes the universality of small scales: they are supposed to be independent of large-scale driving mechanisms [103]. They are neither affected by large turbulent structure nor by the boundary condition of the studied domain and can be considered as isotropic, self-similar, and containing very little kinetic energy [104]. According to Sagaut [101], the error generated by the discretization of the Navier-Stokes equations can be seen as the sum of three errors. The projection error, err_π is due to the fact that the solution obtained is approximated with a finite number of freedom degrees. The discretization error, err_d, traduces the approximation of the partial derivatives on a discrete domain with numerical schemes. Lastly, as the smallest scales of the exact solution are missing, the obtained solution cannot be exact, this is called the resolution error, err_r. This is summarized by

$$err = err_\pi + err_d + err_r. \tag{2.1}$$

As the projection error cannot be avoided, the best LES solution can be obtained by vanishing the sum of the discretization error and the resolution error in such a way that only the projection error remains. This can be achieved in two ways.

- The Implicit LES (ILES) aims to balance the discretization error and the resolution error in such way that
$$err_d + err_r = 0. \tag{2.2}$$
No model term is introduced in the resolved equations. Subgrid-scale modeling relies solely on the numerical truncation error. The numerical method is chosen to balance the two errors. For more details on the ILES approach, the reader is referred to [105].

- The explicit LES is the most used method and is classically denoted as LES. The objective of this approach is to cancel both discretization and resolution errors,
$$err_d = err_r = 0. \tag{2.3}$$
The discretization error is handled by the numerical method. An additional term is introduced in the Navier-Stokes equation and aims to cancel the resolution error. This term is a model and should account for the effects of the high-frequency modes on the low-frequency modes. There exist two types of models. On one side, the functional models strive to represent the kinetic energy transfers. On the other side, the structural models aim to represent the structure of the subgrid-scale tensor.

The reader interested in the error in LES is referred to the book of Sagaut [101] for further details on the theory. More practical analysis of the errors are given in [106, 107, 108, 109]. The main principles of the large eddy simulation have been introduced. The filtering and modeling parts are detailed in the two next sections.

2.3 Turbulence filtering

2.3.1 Filter properties

In LES, the smallest eddies are not resolved, they are modeled in order to take into account their effect on the large eddies. The scale separation is performed by applying a spatiotemporal filter, that is low-pass in frequency, on the instantaneous solution. The filter is associated with a convolution product. For simplicity the definition and properties are given in the homogeneous case, meaning that the filter is considered isotropic. The filtered field $\overline{\psi}$ is defined for any field ψ as
$$\overline{\psi}(x,t) = \int_{-\infty}^{\infty}\int_{-\infty}^{\infty} \psi(\xi,\tau)G(x-\xi,t-\tau,x,t)\,d\xi\,d\tau, \tag{2.4}$$
where G is the convolution kernel. $\overline{\Delta}_t$ and $\overline{\Delta}$ are respectively the characteristic filter time and filter length associated with the convolution kernel, whose expression depends on the type of filter chosen. Note that this expression is classically symbolized by:
$$\overline{\psi} = G \star \psi. \tag{2.5}$$

The unresolved part of $\psi(x,t)$ is denoted $\psi'(x,t)$ and computed as follows:
$$\psi'(x,t) = \psi(x,t) - \overline{\psi}(x,t), \tag{2.6}$$

or

$$\psi'(x,t) = \psi(x,t) - G \star \psi(x,t). \tag{2.7}$$

In most of the LES, only spatial filtering is achieved since it implicitly induces time filtering. The reader is referred to [110, 111] for more details on time filtering in LES.

The filter should respect three properties:

1. conservation of constants
$$\overline{C} = C; \tag{2.8}$$
2. linearity, always satisfied by definition of the product of convolution. For any fields ψ_1 and ψ_2,
$$\overline{\psi_1 + \psi_2} = \overline{\psi}_1 + \overline{\psi}_2; \tag{2.9}$$
3. commutation with spatial and temporal derivatives:
$$\overline{\frac{\partial \psi}{\partial x}} = \frac{\partial \overline{\psi}}{\partial x}, \tag{2.10}$$
and
$$\overline{\frac{\partial \psi}{\partial t}} = \frac{\partial \overline{\psi}}{\partial t}. \tag{2.11}$$

The commutation with temporal derivative is always respected but the commutation with spatial derivative is only respected for isotropic filters. The reader is referred to van der Bos and Geurts [112] for more details on the errors associated with the commutation errors. Note that generally, the filter is not idempotent, $\overline{\overline{\psi}} \neq \overline{\psi}$ and $\overline{\psi'} \neq 0$. The Gaussian filter, the box filter, and the sharp spectral filter (also known as sinc filter) are ordinarily used for spatial filtering in LES [113].

2.3.2 Implicit/Explicit filtering

The filtering process can be either explicit or implicit. In the first case, the convective term is filtered explicitly to lower the number of scales of the solution. It restores a consistent level of spectral content to each term in the numerical solution of the filtered Navier-Stokes equations. The approach consists of the explicit definition of a filter length and considerably mitigates the influence of the method on the grid and the numerical errors. The filter length has to be larger than the local cell size. On one hand, it enables to permanently damp the small-scale motions that are admitted by the mesh, but not accurately represented by the discrete differencing operators. On the other hand, it reduces the spectrum of resolved scales. More comprehensive information on explicit filtering can be found in [114, 115, 116, 117, 53, 118]. In the case of implicit filtering, there is no well-defined filter shape, the filter is implicitly obtained by the resolved equations, the mesh, the numerical method and the subgrid-scale model. The main drawbacks of this method are the inability to control numerical error and the fact that the direction of the computed derivative is the only direction in which the filtering is performed. Thus, a different one-dimensional filter is applied to each term in the LES equation, and the actual equation being solved cannot be rigorously derived from the Navier–Stokes equations. Nevertheless, despite these shortcomings, implicit filtering is significantly more used. It takes full advantage of the grid resolution and avoids the computation of a subfilter scale model term, which leads to a reduction of the computational cost when compared to the explicit filtering approach [119, 120, 121, 106, 122].

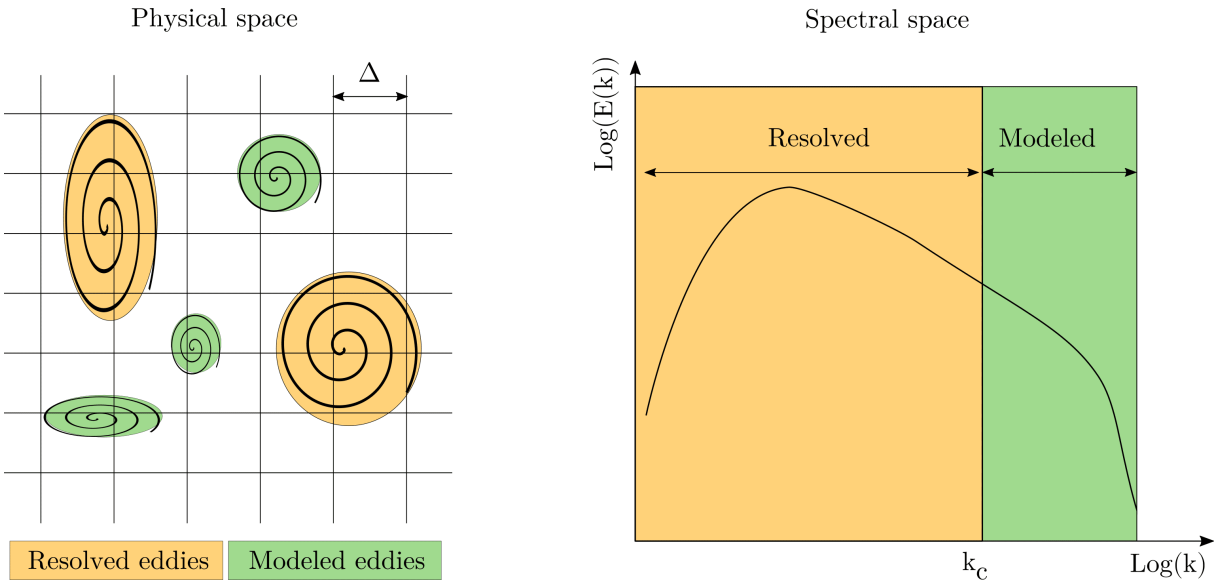

Figure 2.1 – Scale separation in the spectral and the physical spaces. The figure is inspired from [101].

2.3.3 Application to the resolved equations

In this study, the LES are performed with an implicit spatial filtering and no time filtering is considered. Hence, the filter length is derived from the discretization of the Navier-Stokes equations on the computational grid. It is given by:

$$\Delta = \sqrt[3]{\Delta_x \Delta_y \Delta_z}, \tag{2.12}$$

with Δ_x, Δ_y, and Δ_z the mesh sizes in the three spatial directions. The filtering applied to the exact solution stems from the filter associated with the mesh size and the filters induced by the numerical error and the modeling error. Figure 2.1 shows the filtering applied in LES. In physical space, the eddies smaller than 2Δ are modeled. The right graph exhibits the scale separation in the spectral space. The kinetic energy, E, is plotted as a function of the wavenumber, k, in logarithmic scale. The eddies associated with small wave numbers are resolved while those having a wave number larger than the cutoff wavenumber, $k_c = \pi/\Delta$, are modeled.

Applying a filter to the low-Mach number equations (1.34-1.37), results in:

- Mass conservation equation

$$\frac{\partial \bar{\rho}}{\partial t} + \frac{\overline{\partial \rho U_j}}{\partial x_j} = 0, \tag{2.13}$$

- Momentum conservation equation

$$\frac{\partial \overline{\rho U_i}}{\partial t} = -\frac{\overline{\partial \rho U_j U_i}}{\partial x_j} - \frac{\overline{\partial P}}{\partial x_i} + \overline{\frac{\partial}{\partial x_j}\left[\mu\left(\frac{\partial U_i}{\partial x_j} + \frac{\partial U_j}{\partial x_i}\right)\right]} - \frac{2}{3}\overline{\frac{\partial}{\partial x_i}\left(\mu \frac{\partial U_j}{\partial x_j}\right)}, \tag{2.14}$$

- Energy conservation equation

$$\frac{\overline{\partial U_j}}{\partial x_j} = -\frac{1}{\gamma P_0}\left[(\gamma - 1)\overline{\frac{\partial}{\partial x_j}\left(-\lambda \frac{\partial T}{\partial x_j}\right)} + \frac{\mathrm{d}P_0}{\mathrm{d}t}\right], \tag{2.15}$$

- Ideal gas law

$$P_0 = r\overline{\rho T}, \tag{2.16}$$

Note that since P_0 is spatially constant, $\overline{P_0} = P_0$.

In the operating conditions of gas-pressurized solar receivers, the temperature and consequently the density are strongly varying. A filtering based on the Favre average is then more suitable [123]. It consists in the extension of the incompressible decomposition to the compressible case thanks to the introduction of a density weighted averaging [124, 125, 126]. Applied on a variable X, the Favre average, denoted $\widetilde{(\cdot)}$, leads to:

$$\widetilde{X} = \frac{\overline{\rho X}}{\overline{\rho}}. \tag{2.17}$$

Assuming the commutation of the filter and the spatial derivatives, the Favre filtering of the low Mach number equations gives:

- Mass conservation equation

$$\frac{\partial \overline{\rho}}{\partial t} + \frac{\partial \overline{\rho}\widetilde{U}_j}{\partial x_j} = 0, \tag{2.18}$$

- Momentum conservation equation

$$\frac{\partial \overline{\rho}\widetilde{U}_i}{\partial t} = -\frac{\partial \overline{\rho}\widetilde{U_j U_i}}{\partial x_j} - \frac{\partial \overline{P}}{\partial x_i} + \frac{\partial}{\partial x_j}\left[\overline{\mu}\left(\frac{\partial \widetilde{U}_i}{\partial x_j} + \frac{\partial \widetilde{U}_j}{\partial x_i}\right)\right] - \frac{2}{3}\frac{\partial}{\partial x_i}\left(\overline{\mu}\frac{\partial \widetilde{U}_j}{\partial x_j}\right), \tag{2.19}$$

- Energy conservation equation

$$\frac{\partial \widetilde{U_j/\rho}}{\partial x_j} = -\frac{1}{\gamma P_0}\left[(\gamma-1)\frac{\partial}{\partial x_j}\left(-\lambda(\widetilde{T})\frac{\partial \widetilde{T}}{\partial x_j}\right) + \frac{\mathrm{d}P_0}{\mathrm{d}t}\right], \tag{2.20}$$

- Ideal gas law

$$P_0 = r\overline{\rho}\widetilde{T}, \tag{2.21}$$

Two non-resolved terms remain: $\widetilde{U_i U_j}$ and $\widetilde{U_j/\rho}$. They can be expressed as function of $\widetilde{U}$, U'', $\widetilde{1/\rho}$, and $1/\rho''$; where U'' and $1/\rho''$ correspond to the non resolved part of the filtered velocity and the filtered density. The non-resolved part of the variable X is defined as follows:

$$X'' = X - \widetilde{X} \tag{2.22}$$

The Leonard decomposition [15] gives:

$$\widetilde{U_i U_j} = \widetilde{\left(\widetilde{U}_i + U_i''\right)\left(\widetilde{U}_j + U_j''\right)} = \widetilde{\widetilde{U}_i\widetilde{U}_j} + \widetilde{\widetilde{U}_i U_j''} + \widetilde{U_i''\widetilde{U}_j} + \widetilde{U_i''U_j''}, \tag{2.23}$$

and

$$\widetilde{U_j/\rho} = \widetilde{\left(\widetilde{U}_j + U_j''\right)(1/\overline{\rho} + 1/\rho'')} = \widetilde{\widetilde{U}_j/\overline{\rho}} + \widetilde{\widetilde{U}_j/\rho''} + \widetilde{U_j''/\overline{\rho}} + \widetilde{U_j''/\rho''}. \tag{2.24}$$

Applying this decomposition to the momentum equation (2.14) leads to:

$$\frac{\partial \overline{\rho}\widetilde{U}_i}{\partial t} = -\frac{\partial \overline{\rho}\widetilde{U}_j\widetilde{U}_i}{\partial x_j} - \frac{\partial \overline{P}}{\partial x_i} + \frac{\partial}{\partial x_j}\left[\overline{\mu}\left(\frac{\partial \widetilde{U}_i}{\partial x_j} + \frac{\partial \widetilde{U}_j}{\partial x_i}\right)\right] - \frac{2}{3}\frac{\partial}{\partial x_i}\left(\overline{\mu}\frac{\partial \widetilde{U}_j}{\partial x_j}\right) - \frac{\partial \overline{\rho}G_{U_iU_j}}{\partial x_j}, \tag{2.25}$$

with

$$G_{U_iU_j} = \widetilde{\widetilde{U}_i U_j''} + \widetilde{U_i''\widetilde{U}_j} + \widetilde{U_i''U_j''} = \widetilde{C}_{ij}^{UU} + \widetilde{R}_{ij}^{UU} + \widetilde{L}_{ij}^{UU} = \widetilde{U_iU_j} - \widetilde{U}_i\widetilde{U}_j, \tag{2.26}$$

and

$$\begin{cases} C_{ij}^{UU} = \widetilde{\widetilde{U}_i U_j''} + \widetilde{U_i''\widetilde{U}_j} \\ R_{ij}^{UU} = \widetilde{U_i''U_j''} \\ L_{ij}^{UU} = \widetilde{\widetilde{U}_i\widetilde{U}_j} - \widetilde{U}_i\widetilde{U}_j \end{cases}$$

Processing similarly with the energy equation (2.15) gives:

$$\frac{\partial \widetilde{U}_j}{\partial x_j} = -\frac{1}{\gamma P_0}\left[(\gamma-1)\frac{\partial}{\partial x_j}\left(-\lambda(\widetilde{\rho})\frac{\partial \widetilde{T}}{\partial x_j}\right) + \frac{\mathrm{d}P_0}{\mathrm{d}t}\right] - \frac{\partial \bar{\rho} G_{U_j/\rho}}{\partial x_j}, \tag{2.27}$$

with

$$G_{U_j/\rho} = \widetilde{\widetilde{U}_j/\rho''} + \widetilde{U_j''/\bar{\rho}} + \widetilde{U_j''/\rho''} = \widetilde{C}_j^{U/\rho} + \widetilde{R}_j^{U/\rho} + \widetilde{L}_j^{U/\rho} = \widetilde{U_j/\rho} - \widetilde{U}_j/\bar{\rho}, \tag{2.28}$$

and

$$\begin{cases} C_j^{U/\rho} = \widetilde{\widetilde{U}_j/\rho''} + \widetilde{U_j''/\bar{\rho}} \\ R_j^{U/\rho} = \widetilde{U_j''/\rho''} \\ L_j^{U/\rho} = \widetilde{\widetilde{U}_j/\bar{\rho}} - \widetilde{U}_j/\bar{\rho} \end{cases}$$

Equations (2.25) and (2.27) are unclosed. The subgrid term accounting for the velocity-velocity correlation, $G_{U_iU_j}$, and the subgrid term accounting for the velocity-density correlation $G_{U_j/\rho}$ must be expressed in terms of features of the resolved (filtered) fields.

2.4 Subgrid-scale modeling

The LES equations describe the behavior of the large turbulent scale result of the Navier–Stokes equations filtering. The differentiation and filtering operations must commute to keep the same structure as the Navier–Stokes equations. However, in inhomogeneous turbulent flows, the minimum size of eddies that requires to be resolved depends on the regions of the flow. Hence, the filtering operation has to be carried out with a spatially dependent filter width. In general, the commutations between filtering and differentiation, as well as filtering and multiplication is not respected when the filter width is nonuniform [127, 128]. Subgrid terms are introduced in the LES equations in order to balance this non-commutation. These terms involve non-linear products and cannot be directly computed. Thus, they are modeled with the variables resolved in LES.

The Navier-Stokes equations are invariant under various transformations of the coordinate system. They ensure a fluid description independent of the reference frames and relate to scaling and conservation laws [129]. It is desirable that the basic equations of LES, and thus the subgrid-scale models, respect the same properties [130, 131]. In addition to the symmetry properties, several requirements have to be fulfilled. Focusing on the near-wall region, modeled stresses should follow the same asymptotic behavior as the actual turbulent stresses, ensuring that dissipative effects induced by the subgrid-scale model vanish quickly enough near solid boundaries. The Reynolds stress tensor being a statistical average, the associated modeled tensor should be realizable: symmetric positive semidefinite.

In the studied configuration, the two most significant subgrid terms according to Dupuy *et al.* [21] are introduced in the Low Mach number equations. They are the velocity-velocity correlation, $G_{U_iU_j} = \widetilde{U_iU_j} - \widetilde{U}_i\widetilde{U}_j$, and the velocity-density correlation, $G_{U_j\rho} = \widetilde{U_j/\rho} - \widetilde{U}_j/\overline{\rho}$.

Turbulence depends on the fluid motion itself thus the eddy-viscosity concept relies on a function of some flow characteristics. This can be achieved algebraically (zero-equation models) or by solving one or more additional transport equations, denoted n-equation turbulence model, where n is the number of transport equations. The reader is referred to ref. [132, 133] for examples of one-equation model, and to ref. [134, 135] for examples of two-equation models. In this study, the focus is placed on zero-equation models. The velocity-velocity correlation and the velocity-density correlation are respectively expressed as:

$$G_{U_iU_j} = \tau_{ij}^{mod}(\widetilde{\boldsymbol{U}}, \overline{\Delta}), \tag{2.29}$$

and

$$G_{U_j\rho} = \pi_{j}^{mod}(\widetilde{\boldsymbol{U}}, 1/\overline{\rho}, \overline{\Delta}), \tag{2.30}$$

2.4.1 Functional modeling

Functional models aim to reproduce the energetic action of the subgrid-scale eddies on the structures of the resolved scale. The forward energy cascade process is approximated thanks to a diffusion term [136]. Following the Boussinesq hypothesis, this additional diffusion can be represented by the introduction of an eddy-viscosity. For that reason, the functional models are also called eddy-viscosity models. The Boussinesq hypothesis corresponds to an alignment between Reynolds stress and mean strain tensors [137]. See Schmitt [138] for further historical remarks and a direct evaluation of its validity. In functional modeling, the backward energy transfer is neglected. The Reynolds stress tensor is given by:

$$\tau_{ij}^{\text{mod}}(\boldsymbol{U}, \overline{\boldsymbol{\Delta}}) = -2\nu_t^{\text{mod}}\left(S_{ij} - \tfrac{1}{3}S_{kk}\right), \tag{2.31}$$

where $S_{ij} = \frac{1}{2}\left(\partial_j\overline{U}_i + \partial_i\overline{U}_j\right)$ the rate of deformation tensor and ν_t^{mod} the eddy-viscosity. Since $\left(S_{ij} - \frac{1}{3}S_{kk}\right)$ as zero trace, only the deviatoric part of the Reynolds stress tensor transport momentum is then modeled:

$$\tau_{ij}^{\text{mod}}(\boldsymbol{U}, \overline{\boldsymbol{\Delta}}) = -2\nu_t^{\text{mod}}\left(S_{ij}\right), \tag{2.32}$$

The isotropic contribution can be added to the filtered pressure. It is then often neglected in the literature. Nevertheless, some authors suggest to model it [139, 130, 140].

The density-velocity subgrid term is computed with eddy-diffusivity models. They involve the turbulent Prandtl number, Pr_t:

$$\pi_j^{mod}(\widetilde{\boldsymbol{U}}, \phi, \overline{\Delta}) = -\frac{\nu_t^{mod}(\mathbf{g}, \mathbf{d}, \overline{\Delta})}{Pr_t} d_j, \tag{2.33}$$

with $\boldsymbol{d_j} = \partial\phi/\partial x_j$ the scalar gradient. $Pr_t = 0.9$ is the turbulent Prandtl number, defined as the ratio between the momentum eddy-diffusivity and the heat transfer eddy-diffusivity.

The first subgrid-scale stress model was proposed by Smagorinsky in 1963 [141]. He assumes that the subgrid-scale viscosity is proportional to the characteristic length of the cell size, Δ, and to the product $\Delta||\widetilde{S}||$, where $||\widetilde{S}|| = \sqrt{2\widetilde{S}_{ij}\widetilde{S}_{ij}}$. The Smagorinsky model is based on an invariant that does not asymptotically vanish near walls, which is problematic for simulating most of the commonly encountered flows [142]. Many authors highlight its over dissipative behavior [143,

144, 145, 146]. The Smagorinsky model has been the subject of a large number of improvement attempts [147, 148]. Other well known models are the Wall-Adapting Local Eddy-viscosity (WALE) model, proposed by Nicoud [14]; the Anisotropic-Minimum-Dissipation (AMD) model of Rozema [13], the Vreman model [149], the Sigma model [150], the VSS model [151], the QR model [152], the S3PQR model [153].

2.4.2 Structural modeling

Structural models are established with no prior knowledge of the interaction between the subgrid scales and the resolved scales. They focus on predicting the exact subgrid-scale term by a direct reconstruction. Structural models do not locally assume the same eddy-viscosity or eddy-diffusivity for all directions of the flow and are able to take into account the backward energy cascade process. Structural models are either based on series expansions or the scale-similarity hypothesis. The first structural model relying on the Taylor series was derived by Clark *et al.* [154]. The scale-similarity model was first introduced by Bardina *et al.* [16] in 1980. It assumes a correspondence between the statistical structure of the flow at different filtering levels. These two models often tend to poorly estimate the subgrid-scale energy production leading to unstable simulations. To correct this drawback, Lu and Porté-Agel propose a modulated gradient model [155].

2.4.3 Mixed modeling

Mixed models use both structural and functional models in order to take advantage of the two types of models. They are commonly constructed as a linear combination of the structural and functional models [156, 157, 114]. Recently, Lee *et al.* [158] proposed two-parameter mixed models for transitional and turbulent flows. They decomposed the subgrid-scale stress into the modified Leonard stress, modified cross stress, and modified subgrid-scale Reynolds stress terms. The modified Leonard stress term is explicitly computed using an extension of the filtered Bardina model proposed by Horiuti [159]. The modified subgrid-scale Reynolds stress is approximated by the dynamic Smagorinsky model or by a dynamic global model. Streher *et al.* [12] propose a two-layer mixed model for the LES of isothermal channel flow: the near-wall region is parametrized with the combination of the AMD [13] and the scale similarity model of Bardina [16], whereas the outer region is computed with the scale similarity model only. They obtain very good results on first- and second-order statistics. The multiplicative mixed models proposed by Dupuy *et al.* [160] and Ghaisas and Frankel [161] can also be considered of mixed models.

2.5 Conclusion of chapter 2

In this chapter, the main principles of the Large Eddy Simulation (LES) have been described. This CFD approach permits producing accurate results with a reasonable computational cost. However, due to the resolution of the Navier-Stokes equations on a discrete domain and the low-pass filtering in frequency, LES induces projection errors, discretization errors, and resolution errors. Improving LES results requires vanishing these errors. In Implicit LES (ILES) the discretization error is supposed to compensate for the resolution error. The current researches focus on the introduction of a subgrid-scale model aiming to reduce the resolution error to zero. In this case, the numerical schemes and the mesh sizes are usually chosen to mitigate the discretization error. Two types of subgrid-scale models are used. Functional models rely on the

concept of eddy-viscosity and provide a generally good estimation of the energy transfer from the resolved scales towards the subgrid scales (no backward energy cascade process). Structural models are either based on the Taylor series or the scale-similarity hypothesis.

In the next, investigation of the flow physics is carried out and *a posteriori* tests of LES are performed in turbulent channel flows. The LES are assessed with Direct Numerical Simulations (DNS) performed in the same conditions and on the same code. They represent the central link in the multi-scale approach performed in this thesis since they are used to develop a heat transfer correlation in part II. In chapter 3, the comparison is carried out in isothermal conditions. Then, in chapter 4, the LES and DNS are achieved in the operation conditions of gas-pressurized solar receivers. Two wall-normal temperature profiles, representing two different axial locations in the solar receiver are studied.

Chapter 3

A posteriori tests of large eddy simulations in isothermal conditions

Contents

3.1 Introduction of chapter 3

The solar receiver is the place of very complex flows characterized by a strong coupling between the temperature and the dynamic of the flow. As a first step, it is necessary to investigate the flow at the turbulence level encountered in solar receivers in the isothermal conditions. The performance of the Large Eddy Simulation (LES) turbulence models are thus analyzed without the additional difficulty induced par the temperature effect. The isothermal flow can then be compared to the anisothermal flow to highlight the modifications induced by the temperature gradient.

Large eddy simulation consists in the modeling of turbulence scales that are smaller than the filter size which is the local mesh size when the filter is defined by the mesh. As the mesh used in

LES does not intend to be able to capture the high-frequency modes of the turbulence, no grid convergence can be obtained when performing implicit filtering. Hence, the LES accuracy relies on a combination of the subgrid-scale model, the filtering operation, and the numerical method.

The case study of the isothermal channel flow is commonly studied in the literature. These types of flows possess a direction of inhomogeneity. For that reason, they are much more complex than the case study of homogeneous turbulence. Open channel flows, called channel flows in the next for sake of simplicity, involve physical mechanisms that can overtake the possibilities of the subgrid models. The fluid viscosity, the distance between the two walls, and the fluid velocity directly impact the fluid motion. The velocity gradient in the boundary layer, that is due to the no-slip boundary condition and develops along the streamwise direction of the two planes, is responsible for the turbulence production. The generated structures are then ejected toward the outer region of the flow. The case studies involving non-homogeneous turbulence are thus a good but difficult test case for subgrid-scale model of LES. Besides, the channel configuration permits studying the parietal flows which are commonly encountered in the industry.

The isothermal channel flow is one of the reference test case for the assessment of LES turbulence model [142, 14, 149, 13]. In LES, the turbulence production phenomena near the solid boundaries have to be well approximated. To this end, the near-wall region, corresponding to the dissipation zone, is either modeled or simulated. LES carried out with a wall model enable the simulation with a uniform grid since the flow behavior in the vicinity of the wall is modeled. This is valuable because it permits avoiding the numerical issues associated with non-uniform meshes. Moreover, the uniformity of the grid renders the simulation of flows at a very high Reynolds number affordable. Some most known wall models are given here: Deardorff [162], Schumann [163], Mason and Callen [119], Piomelli *et al.* [164], Marusic *et al.* [165]. The reader is referred to Bose and Park [166] for a review of the recent investigation of the wall-modeled LES in complex turbulent flows. Nicoud *et al.* [167] performed LES wall-modeling based on suboptimal control theory and linear stochastic estimation. An optimal control strategy was used to force the outer LES towards the desired solution by controlling the wall stress boundary conditions. They show that the dynamically relevant part of the optimal wall stresses can be predicted from the local velocity field. Chung and Pullin [168] developed an LES wall model based on subgrid-scale stretched vortices in a turbulent channel flow at a high Reynolds number. Their wall model produces satisfying results of the first-order statistics. Xu *et al.* [169] proposed a structural function that combines the wall distance and the von Karman length scale and allows to simulate turbulent flows at high Reynolds numbers, even with a coarse grid resolution. However, the results obtained with wall-modeled LES are generally middling on second-order statistics and the addition of a wall model to the classical turbulence model used further from the wall may induce new problems. These are the reasons why, in the literature, most of the LES studies of channel flow involve a non-homogeneous grid in the wall-normal direction. The grid is classically refined in order to simulate the near-wall structure. As the distance from the walls grows, the cell size increases, and the effect of the turbulence model is strengthened. Practically, to simulate the structures in the vicinity of the wall the minimum resolution of the first cell in the wall-normal direction is classically set to $\Delta_y^+ = 2$ [170, 171]. The Wall Resolved Large Eddy Simulation (WRLES), is usually denoted as LES since it corresponds to the majority of the LES performed studies.

In the literature, LES of isothermal channel flows are mostly carried out at relatively low Reynolds numbers. Dupuy *et al.* [17] studied a large number of zero-equation algebraic models at a friction Reynolds number of 180. Each model is tested on three mesh levels. Iliescu [172] assessed an approximate deconvolution LES model at friction Reynolds number of 180 and 395

and compared it with the gradient model and the Smagorinsky model. Higher friction Reynolds are reached in the following papers. Winckler and Rani [173] evaluated the performance of different subgrid kinetic energy models. A dynamic subgrid kinetic energy model, a static coefficient kinetic energy model, and a "no-model" method were compared with DNS results at two friction Reynolds numbers of 180 and 590, keeping the grid constant. Bose *et al.* [174] investigated LES with explicit filtering at friction Reynolds numbers of 180, 395, and 640. They used the dynamic Smagorinsky subfilter stress model. Kremer and Bogey [175] performed LES in turbulent channel flows using relaxation filtering as a subgrid-scale model. The studied friction Reynolds numbers are 300, 350, 600, and 960. Nevertheless, to the author's knowledge, there is no LES assessing several models at a high friction Reynolds number. The study presented in this chapter is about the *a posteriori* tests of LES in an isothermal channel flow at a friction Reynolds number of 930. The LES are performed with a turbulence model for the momentum convection subgrid term. They are assessed on the turbulence first-order and second-order statistics and are compared to the data of a Direct Numerical Simulation (DNS) carried out in the same conditions.

The outline of this chapter is the following. In section 3.2, the configuration of the study is described. In section 3.3, the investigated turbulence models are detailed. In section 3.4, the results are given and discussed. Lastly, section 3.5 concludes on the LES performed in the isothermal conditions.

3.2 Study configuration

The LES are performed in a fully developed three-dimensional turbulent channel flow. The streamwise (x) and spanwise (z) directions are periodic. The flow is enclosed by two plane walls in the wall-normal direction (y). The domain size is $4\pi\delta \times 2\delta \times 4/3\pi\delta$ with $\delta = 3$mm. The thermodynamical pressure, P_0, is 10 bars. A streamwise volume force is added to the channel to replicate the effect of a streamwise pressure gradient and maintain a constant mass flow rate. The friction Reynolds number is 930.

The numerical settings of the study presented in this chapter are those described in Section 1.5. The mesh follows a staggered grid system and is uniform in homogeneous directions. In the wall-normal coordinate direction (y), it follows the hyperbolic tangent law described in Eq. 3.1. This law permits capturing the strong velocity gradients induced by the walls:

$$y_k = L_y \left(1 + \frac{1}{a}\tanh\left[\left(\frac{k-1}{N_y-1}\right)\tanh^{-1}(a)\right]\right), \tag{3.1}$$

where a is the mesh dilatation parameter and N_y is the number of grid points in the wall-normal direction. Table 3.1 provides the mesh investigated in this study. The LES meshes are described by acronyms for the sake of simplicity. The first, second, and third characters are respectively associated with the streamwise, wall-normal, and spanwise directions. "A" accounts for the highest considered resolution in a particular direction whereas "D" represents the coarsest resolution. The wall-normal resolution is maintained constant since it is substantially less impacting the results than the resolution in other directions as long as the first point is in the linear region of the viscous sublayer [171].

Regarding the discretization of the derivatives, the time derivatives are approximated with a third-order Runge-Kutta scheme. The momentum convection term is either discretized with a fourth-order centered scheme or with a second-order centered scheme. The terms "(c4)" or "(c2)" written after the model name indicate the numerical scheme used for the discretization of

Table 3.1 – Grid spacing of the DNS and LES.

Name	Number of grid points $N_x \times N_y \times N_z$	Dimensionless cell size Δ_x^+ ; $\Delta_y^+(0)$; $\Delta_y^+(\delta)$; Δ_z^+
DNS	$1152 \times 746 \times 768$	10.1 ; 0.39 ; 5.1 ; 5.1
AAA	$192 \times 152 \times 128$	61 ; 1 ; 30 ; 30
BAB	$160 \times 152 \times 96$	73 ; 1 ; 30 ; 41
CAC	$128 \times 152 \times 72$	91 ; 1 ; 30 ; 54
DAD	$96 \times 152 \times 48$	122 ; 1 ; 30 ; 81

the momentum convection term. The mass convection term is computed with the Quadratic Upstream Interpolation for Convective Kinematics (Quick) [6], It considers a three-point upstream weighted quadratic interpolation for the cell face values and is third-order accurate in terms of Taylor series truncation error.

3.3 Turbulence models

Functional, structural, and mixed models are investigated. The studied subgrid-scale models are described in the next subsections.

3.3.1 Functional models

Functional models rely on the artificial subgrid viscosity proposed by Boussinesq [137]. They only model the energy transfer from the resolved to the subgrid-scales. Since the subgrid term is mainly diffusive it can be represented with a turbulent viscosity. The Reynolds stress tensor is computed as follows:

$$\tau_{ij}^{mod}(\widetilde{\boldsymbol{U}}, \overline{\Delta}) = -2\nu_t^{mod}(\mathbf{g}, \mathbf{d}, \overline{\Delta})S_{ij}, \tag{3.2}$$

with $S_{ij} = 0.5(g_{ij} + g_{ji})$ the rate of the deformation tensor, $\mathbf{g}$ the velocity gradient, given by $g_{ij} = \partial\widetilde{U}_i/\partial x_j$, and ν_t^{mod} the turbulent viscosity which is specific to each model.

In the next, the following functional models are considered:

- WALE model [14]:

$$\nu_t^{WALE}\left(\mathbf{g}, \mathbf{d}, \overline{\Delta}\right) = \left(C^{WALE}\overline{\Delta}\right)^2 \frac{\left(S_{ij}^d S_{ij}^d\right)^{3/2}}{\left(S_{mn}S_{mn}\right)^{5/2} + \left(S_{mn}^d S_{mn}^d\right)^{5/4}}, \tag{3.3}$$

- AMD model [13]:

$$\nu_t^{AMD}\left(\mathbf{g}, \mathbf{d}, \overline{\Delta}\right) = C^{AMD}\frac{max(0, -G_{ij}S_{ij})}{g_{mn}g_{mn}}, \tag{3.4}$$

- Sigma model [150]:

$$\nu_t^{Sigma}\left(\mathbf{g}, \mathbf{d}, \overline{\Delta}\right) = \left(C^{Sigma}\overline{\Delta}\right)^2 \frac{\sigma_3(\sigma_1 - \sigma_2)(\sigma_2 - \sigma_3)}{\sigma_1^2}, \tag{3.5}$$

where S_{ij}^d is the traceless symmetric part of the squared velocity gradient tensor, $\sigma_1 > \sigma_2 > \sigma_3$ are the three singular values of $\mathbf{g}$, and $G_{ij} = \overline{\Delta_k}^2 g_{ik} g_{jk}$ is the gradient model.

The subgrid-scale modeling needs to keep the generic properties of the filtered Navier-Stokes equations. Deville *et al.* [176] provide the expression that the stress tensor has to respect in order to preserve the invariance properties:

$$\begin{aligned} \tau_{ij} = \quad & a\ (\mathbf{S_{ij}} \cdot \gamma \otimes \gamma + \gamma \otimes \gamma \cdot \mathbf{S_{ij}}) + b\ \gamma \otimes \gamma \cdot \mathbf{S_{ij}} \cdot \gamma \otimes \gamma + c\ \mathbf{S_{ij}} \\ & + (d\ tr(\mathbf{S_{ij}}) + e\ \mathbf{S_{ij}} : \gamma \otimes \gamma)\mathbf{I} + e\ tr(\mathbf{S_{ij}} \gamma \otimes \mathbf{e}), \end{aligned} \tag{3.6}$$

with γ the unit vector used to represent the streamwise direction of the flow, $\mathbf{I}$ the identity matrix, and a, b, c, d and e coefficients.

Taking $\gamma = \mathbf{e_x}$, the streamwise direction of the flow, $a = 0.5$, $b = -1$, and $c = d = e = 0$, and considering the studied geometry, leads to the $H^{(4)}$ version of the tensorial AMD model proposed by Dupuy *et al.* [17, 145]:

$$\tau_{ij}^{H^{(4)}AMD}\left(\mathbf{U}, \overline{\Delta}\right) = H_{ij}^{(4)} \tau_{ij}^{AMD}\left(\mathbf{U}, \overline{\Delta}\right), \tag{3.7}$$

with

$$H_{ij}^{(4)} = \begin{pmatrix} 0 & 1 & 1 \\ 1 & 0 & 0 \\ 1 & 0 & 0 \end{pmatrix}. \tag{3.8}$$

The functional model constants used are the following: $C^{WALE} = 0.55$, $C^{AMD} = 0.3$, $C^{AMDs} = 0.3$, and $C^{Sigma} = 1.5$.

3.3.2 Structural modeling

Structural modeling aims to model the structure of the subgrid-scale stress tensor. The gradient model family involves formal series expansions while the scale similarity approach assumes the similarity between the resolved and the modeled turbulent scales. One structural model of each type of approach is investigated in this study:

- Gradient model [15]:

$$\tau_{ij}^{grd} = \frac{1}{12} C^{grd} \overline{\Delta_k}^2 g_{ik} g_{jk}, \tag{3.9}$$

  where the model constant is $C^{grd} = 1.0$.

- Scale similarity model [16]:

$$\tau_{ij}^{sim} = C^{sim}\left(\widehat{\widetilde{U}_j \widetilde{U}_i} - \widehat{\widetilde{U}}_j \widehat{\widetilde{U}}_i\right), \tag{3.10}$$

The test filter, denoted $\widehat{\cdot}$, is explicitly computed in LES. Two test filters are considered in the present work. The box filter is obtained with an average over three cells in the three directions. In one dimension, its expression is given by:

$$\overline{\psi}(x_i) = \frac{\psi(x_{i+1})\Delta(x_{i+1}) + \psi(x_i)\Delta(x_i) + \psi(x_{i-1})\Delta(x_{i-1})}{\Delta(x_{i+1}) + \Delta(x_i) + \Delta(x_{i-1})}, \tag{3.11}$$

where $\Delta(x_i)$ is the local cell size around the point x_i. Note that an off-centre scheme is used at the walls. The associated simulation is denoted "Sim".

The Laplacian filter involves the Taylor series expansion of the box filter using the local cell size as the filter width:

$$\overline{\psi}(x_i) = \psi(x_i) + \frac{[\Delta(x_i)]^2}{24} \frac{\partial^2 \psi}{\partial x^2}\bigg|_i, \tag{3.12}$$

where the second derivative is approximated using a second-order centered finite difference approximation. It is denoted "SiL" in the next. The scale similarity model constants are $C^{Sim} = 1.0$ and $C^{SiL} = 1.0$.

3.3.3 Mixed modeling

The multiplicative mixed model (MMG model) proposed by Dupuy *et al.* [160] is considered. It is a functional model constructed such that its magnitude is expressed by the gradient model and its orientation is aligned with the rate of deformation tensor:

$$\nu_t^{MMG}(\mathbf{g}, \mathbf{d}) = -C^{MMG} \frac{G_{kk}}{|\mathbf{S}|}, \tag{3.13}$$

where $C^{MMG} = 0.05$.

A model combining the scale similarity model of Bardina [16] and the AMD model of Rozema *et al.* [13], denoted "AMD+Sim" is tested. The subgrid-scale tensor is then computed as the sum of the subgrid-scale tensors obtained with the functional and structural models.

3.4 Results and discussion

3.4.1 Comparison of the large eddy simulations and direct numerical simulation

Direct numerical simulations and large eddy simulations provide instantaneous fields. The exposed results are averaged in time as well as in the streamwise and spanwise directions. This combination of averages is denoted by $\langle \cdot \rangle$. In the simulation involving functional models, only the deviatoric Reynolds stresses can be reconstructed and compared with DNS data without filtering process [11, 12] because they are traceless. For that reason, in this study, the isotropic part of the Reynolds stresses is systematically removed:

$$R_{ij}^{dev} = R_{ij} - \frac{1}{3} R_{kk} \delta_{ij}. \tag{3.14}$$

The modeled terms are added to the associated quantity to provide an exact comparison between LES and DNS.

$$R_{ij}^{DNS,dev} = R_{ij}^{LES,dev} + \langle \tau_{ij}^{SGS}(\mathbf{U}, \overline{\Delta}) \rangle^{dev}, \tag{3.15}$$

where $R_{ij}^{DNS} = \langle U_i U_j \rangle - \langle U_i \rangle \langle U_j \rangle$ and $R_{ij}^{LES} = \langle \widetilde{U}_i \widetilde{U}_j \rangle - \langle \widetilde{U}_i \rangle \langle \widetilde{U}_j \rangle$. Note that the coordinates x_1, x_2, x_3 and x, y, z as well as U_1, U_2, U_3 and U, V, W are used interchangeably for practical reasons. For the off-diagonal Reynolds stresses, Eq. 3.15 becomes :

$$R_{ij}^{DNS} = R_{ij}^{LES} + \langle \tau_{ij}^{SGS}(\mathbf{U}, \overline{\Delta}) \rangle, \text{ for i} \neq \text{j}. \tag{3.16}$$

The results normalized in wall units are indicated by a superscript "+": $x_i^+ = x_i U_\tau / \nu$, $U_i^+ = U_i / U_\tau$, and $\langle R_{ij} \rangle^+ = \langle R_{ij} \rangle / U_\tau^2$. The friction velocity is given by $U_\tau = \sqrt{\nu \partial \langle U \rangle / \partial y}$.

3.4.2 Data processing

The LES results are compared to DNS using the following procedure. Firstly, the DNS wall-normal profiles are interpolated on the mesh used for LES, then values are compared as expressed below :

$$\epsilon_X^{LES_j} = \frac{\sum_{i=1}^{N_y/2} log\left(\frac{y_{i+1}}{y_i}\right) \left|\left(X_i^{LES_j} - X_i^{DNS}\right) X_i^{LES_j}\right|}{\sum_{i=1}^{N_y} log\left(\frac{y_{i+1}}{y_i}\right) X_i^{DNS^2}} + \frac{\sum_{i=1}^{N_y/2} log\left(\frac{2\delta - y_{i+1}}{2\delta - y_i}\right) \left|\left(X_{Ny/2-i+1}^{LES_j} - X_{Ny/2-i+1}^{DNS}\right) X_{Ny/2-i+1}^{LES_j}\right|}{\sum_{i=1}^{N_y} log\left(\frac{2\delta - y_{i+1}}{2\delta - y_i}\right) X_i^{DNS^2}} \tag{3.17}$$

Where ϵ is the error, X is the observed value, LES_j refers to the jth tested model, y_i is the ith node in the wall-normal direction, and δ is the half-height of the channel. Since the good estimation of the near-wall turbulence is critical, a logarithmic ratio is applied aiming to give more importance to near wall values than to mid-channel values. Furthermore, the error computed in the absolute value is weighted by the local value to emphasize the importance of the peaks.

The simulation are assessed on the streamwise velocity profile and the following velocity correlations:

- $\langle u'u' \rangle$, the covariance of the longitudinal velocity,
- $\langle v'v' \rangle$, the covariance of the wall-normal velocity,
- $\langle w'w' \rangle$, the covariance of the transversal velocity,
- $\langle u'v' \rangle$, the correlation of longitudinal and wall-normal velocities.

The final error of the jth LES model on the streamwise velocity, Err_{mean}, and the final error of the jth LES model on the velocity fluctuations, Err_{rms} by adding the error obtained for each value and dividing this sum by the results of the worst model:

$$Err_{mean}^{LES,j} = \frac{\epsilon_U^{LES_j}}{max\left(\epsilon_U^{LES}\right)}, \tag{3.18}$$

$$Err_{rms}^{LES,j} = \frac{\sum_X \epsilon_X^{LES_j}}{max\left(\sum_X \epsilon_X^{LES}\right)}, \tag{3.19}$$

where X is successively $\langle u'u' \rangle^{dev}$, $\langle v'v' \rangle^{dev}$, $\langle w'w' \rangle^{dev}$, $\langle u'v' \rangle$.

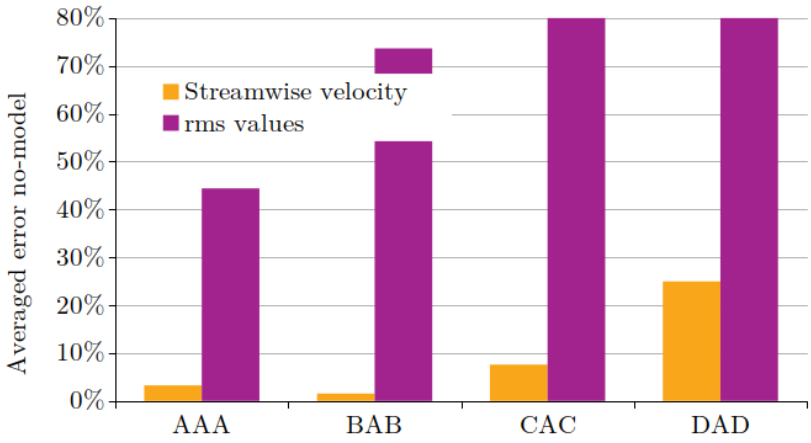

Figure 3.1 – Averaged errors obtained with four different meshes on mean quantities and rms values. Simulations without model are studied.

3.4.3 Mesh sensitivity

In LES with implicit filtering, no grid convergence can be obtained [174]. Hence, mesh sensitivity analyses are generally performed. In Figure 3.1, the four meshes presented in Table 3.1 are investigated. To facilitate the reading of the figure, the results of the "CAC" and "DAD" meshes have been truncated. They are respectively 128% and 271%. In the homogeneous directions, the finer the mesh is, the better are the results on the second-order statistics. Regarding the streamwise velocity, it appears that the best results are obtained with the "BAB" mesh. It permits to somewhat compensate the resolution and the projection error. Thus, the "BAB" grid is used in the next and the simulations performed without a subgrid-scale model are denoted ILES (for Implicit Large Eddy Simulation). The subgrid-scale models are employed in order to improve the approximation of the fluctuations of velocities.

3.4.4 Assessment of turbulence models

Firstly, a global evaluation of the LES is achieved in order to obtained an overview of the performance of each model. Then, some of the LES are selected for a detailed analysis. Two ILES are performed with either a fourth-order centered scheme or a second-order centered scheme. It permits studying the numerical scheme's effect on the results.

3.4.4.1 Global evaluation

Eleven LES are carried out and their results are presented in Figure 3.2. The physical analysis of the model performance is given in Section 3.4.4.2 in light of the detailed results. The top graph gives the normalized error on the streamwise velocity, computed following the algorithm described in Section 3.4. The results show that the "AMD (c4)" and the "AMD+Sim (c4)" simulations are significantly less accurate than the others on the streamwise velocity. The tensorial version, denoted "AMDt (c4)", permits significantly improving the results of the AMD model on this quantity. The "Grd (c4)", "SiL (c4)", "MMG (c4)", and the two ILES provide the best approximation of the streamwise velocity. The middle graph exposes the results concerning the

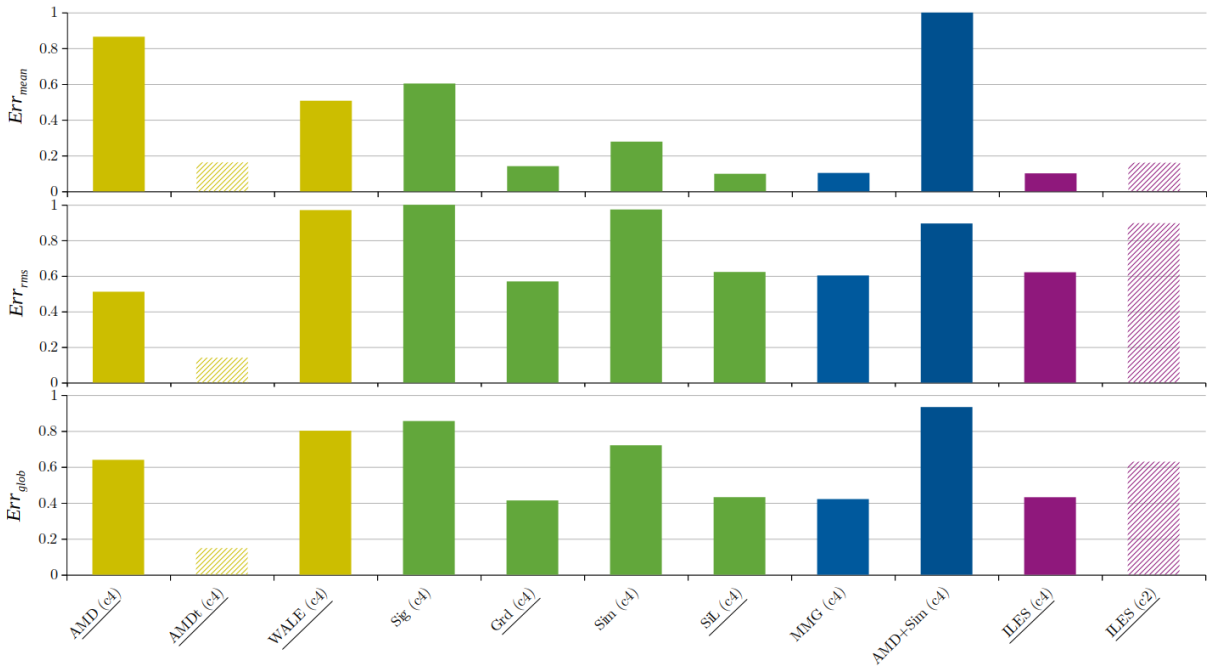

Figure 3.2 – Normalized error of the subgrid models on the mean streamwise velocity and the correlation of velocities.

velocity fluctuations. The simulations can be divided into three groups: (1) the worst consist in the AMD model, the WALE model, the Sigma model, the scale similarity model associated with the box filter, the mixed model "AMD+Sim" and the ILES carried out with the second-order centered scheme; (2) the intermediate group consists in the gradient model, the scale similarity model performed with the Laplacian filter, the MMG model, and the ILES (c4); (3) the third group is constituted of the tensorial AMD model which provides substantially better results. The ILES associated with the fourth-order scheme is significantly better than the one performed with the second-order scheme on the velocity fluctuations. The bottom graph summaries the results of the two above graph thanks to a weighted average (1 mean quantity and 4 rms quantities):

$$Err_{glob}^{LES,j} = \frac{Err_{mean}^{LES,j} + 4Err_{rms}^{LES,j}}{5}. \tag{3.20}$$

The global results highlight the better performance of the "AMDt (c4)" simulation when compared to the other models. The underlined simulations are those selected for a detailed analysis.

3.4.4.2 Detailed analysis

In this section, the 7 selected LES are more precisely analyzed. Figures 3.3 and 3.4 present the relative error of the LES on the five investigated quantities. The relative errors on the streamwise velocity and the cross-correlation are given in Figure 3.3. Except for the "AMD (c4)" simulation which provides a poor estimation of the streamwise velocity, all the simulations produce satisfying results on this quantity. The errors of the models on the cross-correlation

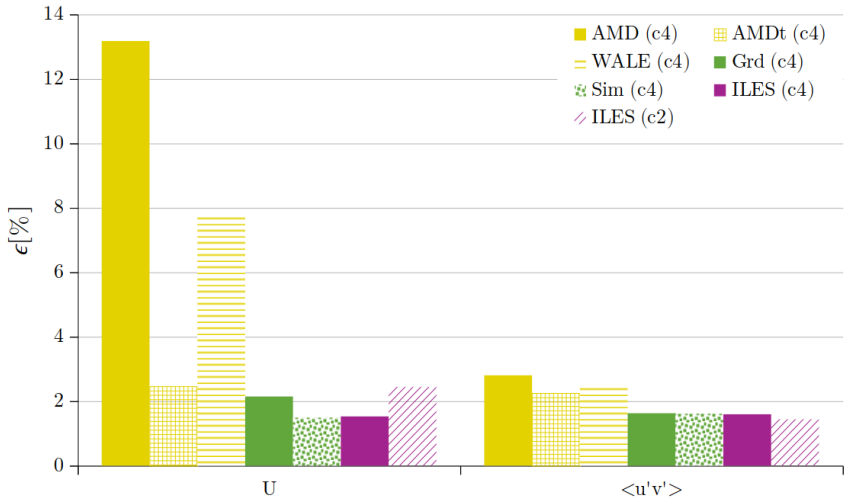

Figure 3.3 – Relative error of the subgrid models on the mean streamwise velocity and the correlation of the streamwise and the wall-normal velocity.

are low. Figure 3.4 gives the relative error on the isotropic velocity fluctuations. The wall-normal velocity is the best-approximated quantity. On the contrary, the spanwise velocity is the most difficult to predict. The results of the "WALE (c4)" and the "ILES (c2)" simulations on the correlation of spanwise velocity have been truncated to facilitate the reading of the figure. The obtained values respectively 238% and 210%. The "AMDt (c4)" simulation is significantly better than the other models and provides the streamwise and spanwise velocity fluctuations within 20%. The error on the spanwise velocity is about 30%. Regarding the structural models, they produce similar results on the streamwise velocity fluctuations. The scale similarity model is slightly better on the wall-normal velocity approximation than the gradient model but poorer on the spanwise velocity. The fourth-order centered scheme used for the discretization of the momentum convection permits mitigating the error on the velocity fluctuations when compared to the second-order scheme. Its influence is comparable with the turbulence model effect.

The normalized streamwise velocity profile is the one of a canonical boundary layer. As shown in Figure 3.5, it can be well approximated by the continuous law of Reichardt [177] given by:

$$U^+ = \frac{1}{\kappa} log(1 + \kappa y^+) + 7.8 \left[1 - exp\left(-\frac{y^+}{11} \right) - \frac{y^+}{11} exp\left(-\frac{y^+}{3} \right) \right], \tag{3.21}$$

with $\kappa = 0.4$ the von Kármán constant. Note that between $y^+ = 30$ and $y = \delta$, the non linear behavior of the profile is not reproduced. This region corresponds to the logarithmic inertial layer $30 < y^+; y^+/\delta << 1$ and the wake region described in Sagaut [101].

Figure 3.6 exhibits the wall-normal velocity profile of the five investigated quantities. The results are plotted as a function of the logarithm of the classically normalized wall distance in order to focus on the near the wall-flow motions. The dimensionless streamwise velocity profile is well predicted by all the models except the WALE and the AMD models which tend to overestimate it.

The $\langle u'u' \rangle^{dev}$, $\langle v'v' \rangle^{dev}$, and $\langle w'w' \rangle^{dev}$ terms show peaks around $y^+ = 12$. They are due to the successive bursts of the low-velocity pockets near the end of the inner region ($y/\delta = 0.2$) inducing

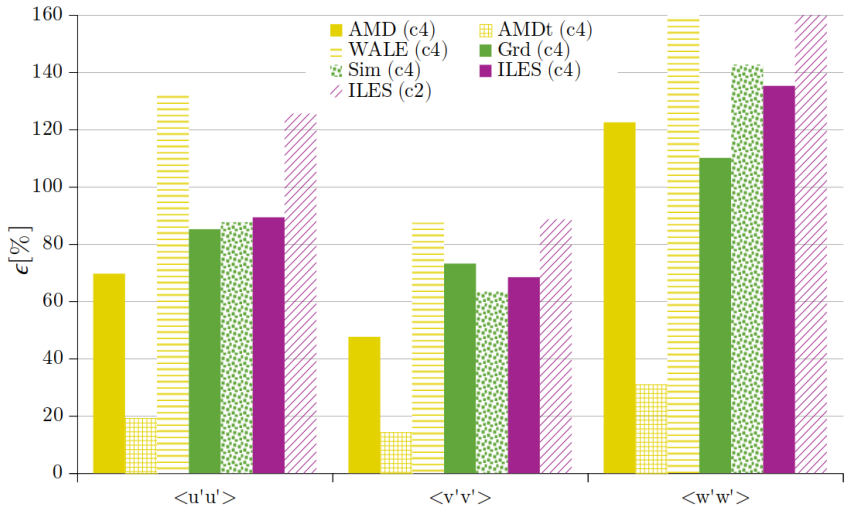

Figure 3.4 – Relative error of the subgrid models on the isotropic fluctuations of velocities.

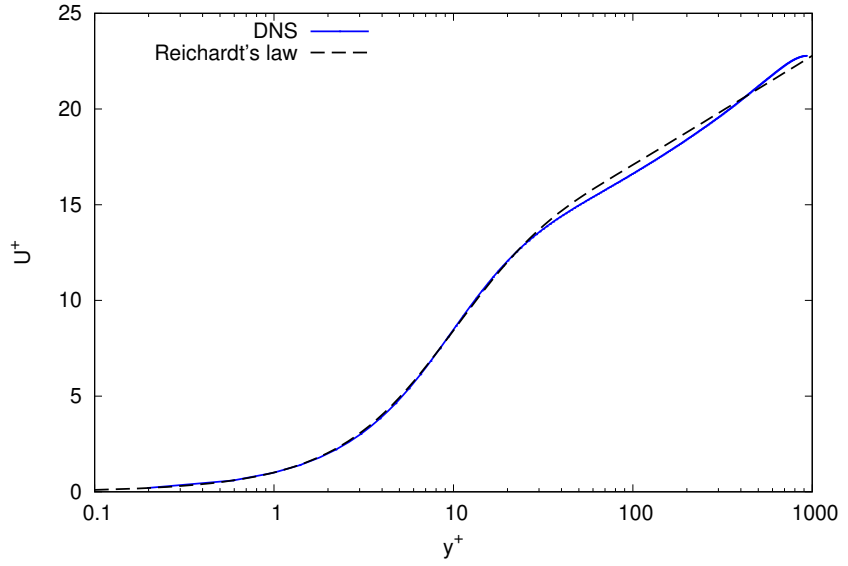

Figure 3.5 – Streamwise velocity profile obtained with the DNS and the Reichardt's law.

fast fluid motions towards the wall that sweeps the near-wall zone in the streamwise and spanwise directions. These intermittent phenomena induce strong fluctuations of the velocity and produce most of the turbulent energy. The fluctuations of velocities show a reduction of the decrease of the velocity fluctuations in the region $70 < y^+ < 200$, which corresponds to the meso layer of the logarithmic region. This is observed by several authors studying the high Reynolds effects [18, 19, 20]. Particularly, the $\langle w'w' \rangle^{dev}$ quantity reach a plateau in this zone. The peaks of the velocity correlations are present at the right location for all LES but the magnitude of the peaks is overestimated. Nevertheless, the tensorial version of the AMD model permits significantly improving these results. The overestimation of the peaks by the WALE and the AMD models

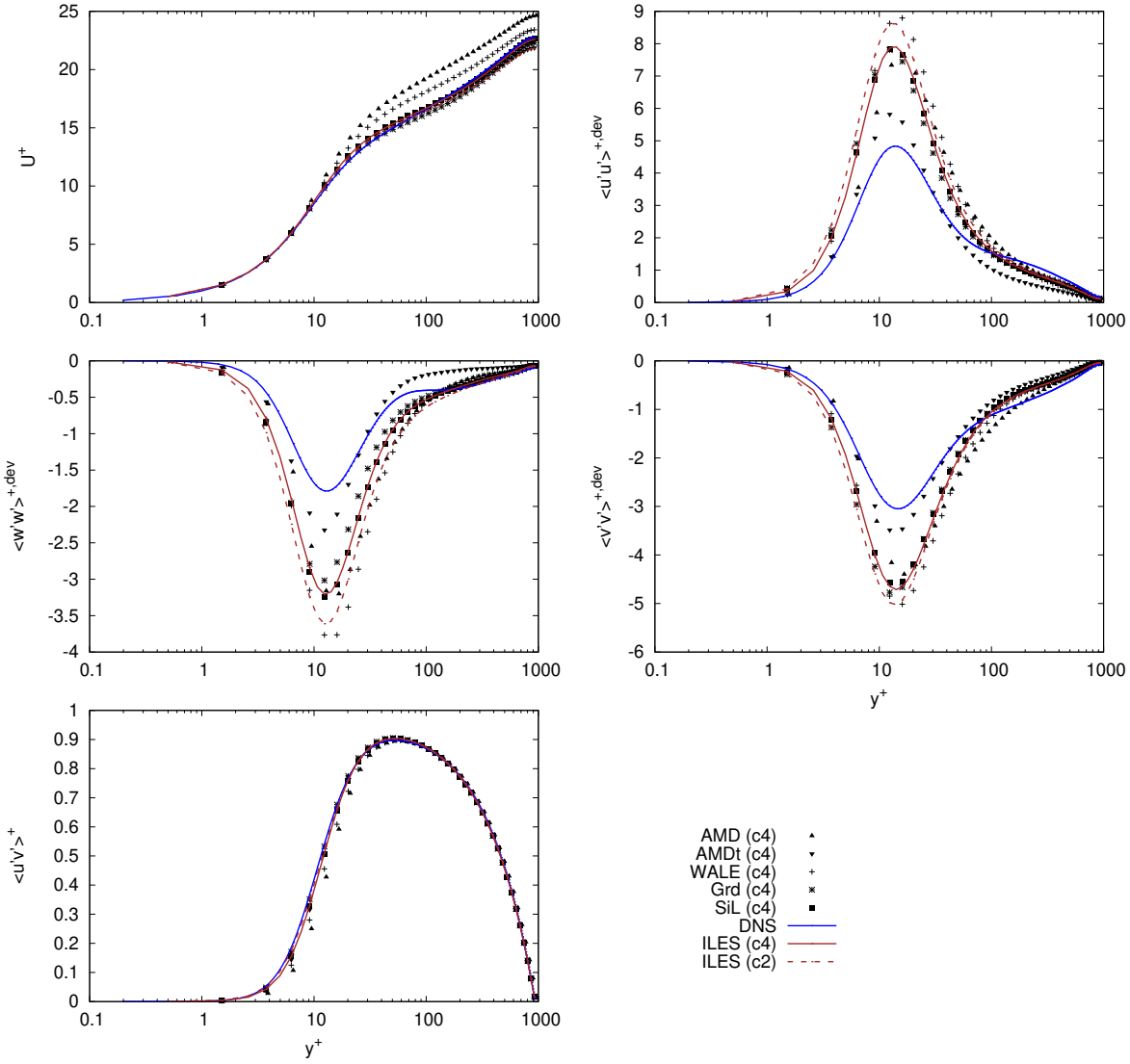

Figure 3.6 – Comparison of the LES wall-normal profiles with the DNS.

should partly be due to its overestimation of the streamwise velocity. Indeed, increasing the mean fluid velocity induces strong velocity gradients near the walls which are responsible for the increase of the velocity fluctuations. The structural models seem to be not enough dissipative. The numerical scheme has an effect on these values. Increasing the order of accuracy of the scheme leads to mitigate the overestimation of the peaks thanks to the enhancement of the mesh convergence induced by the reduction of the associated error. The decrease of the streamwise velocity fluctuations and spanwise velocity fluctuations is overestimated by the tensorial AMD model while the other LES tend to underestimate it. The $\langle u'v' \rangle$ is well predicted by all the simulations. The implication of this term in the balance of the momentum conservation constrains

it to follow a particular profile, leading to similar results between LES and DNS.

3.5 Conclusion of chapter 3

In this chapter, *a posteriori* tests of large eddy simulations have been conducted in a highly turbulent isothermal channel flow. The incompressible Navier-Stokes equations have been solved. LES performed with functional, structural, and mixed turbulence models have been compared to the results of a direct numerical simulation carried out in the same conditions. Two numerical schemes used for the discretization of the momentum convection term have been investigated.

The DNS carried out in the isothermal conditions shows characteristics of high Reynolds number flows. The large turbulent scales give rise to a reduction of the decrease of the velocity fluctuations in the region $70 < y^+ < 200$. The fluctuations of the spanwise velocity deviatoric part exhibit a plateau in this zone.

The global assessment of the models gives an overview of the model performance. Then, seven of the LES are selected for a detailed analysis. The choice of the numerical scheme has a significant influence on the diagonal terms of the Reynolds stress tensor. Increasing the order of accuracy permits improving the estimation of the profiles. The results show substantial differences in the efficiency of the turbulence models. The models are in good agreement with the DNS results on the streamwise velocity and the correlation of the streamwise and the wall-normal velocity. The deviatoric parts of the covariances of the three velocity components are much more difficult to predict. All the LES overestimate the magnitude of the velocity fluctuation peaks. The simulation conducted with the tensorial version of the AMD model is significantly better than the others since it mitigates the overestimation of the profile.

The assessment of LES turbulence models in the isothermal conditions is a prerequisite before the study of the coupling between the temperature and the dynamic of the flow. In the next, anisothermal flows representative of the working conditions of solar receivers are studied. Chapter 4 aims to test the turbulence models of large eddy simulations in complex flows characterized by strong temperature gradients in addition to the intense turbulence already investigated in the present chapter.

Chapter 4

A posteriori tests of large eddy simulations in anisothermal conditions

Contents

4.1 Introduction of chapter 4

The optimization of the solar receiver requires to deepen the understanding of the strong coupling between the dynamic and the temperature. The *a posteriori* tests of turbulence models in those complex conditions permit assessing the performance of the Large Eddy Simulations (LES) while considering all the sources of error.

Most flows encountered in applied systems are complex and involve turbulence as well as temperature gradients. Particularly, in a large number of energy conversion systems, the flows are strongly anisothermal. In many cases, LES can be achieved with reasonable simplifications of the studied problem. The computational cost remains relatively high but thanks to the increase in computer power some industries have already started to use LES and it is expected that this CFD approach becomes even more popular in the near future. For that reason, LES of anisothermal flows are commonly encountered in the literature.

The combustion phenomena well illustrate the point discussed in the above paragraph. Its complexity requires simulations that provide a large amount of information. Some recent examples of LES studies associated with combustion phenomena are given below. Cheng *et al.* [178] perform thermo-acoustic LES of self-excited spray combustion instability in an aero-engine combustor to study the mechanisms of combustion instability. The results provide new prospects into more complex mechanisms and influencing factors of the combustion instability. Ong *et al.* [179] investigate the underlying mechanism that governs the ignition phenomena of spray flames. The effect of the nozzle diameters and the ambient temperature are analyzed. Adamo *et al.* [180] carry out LES of lean combustion in a transparent combustion chamber engine. Srivastava and Jaberi [181] perform out LES of complex multi-component diesel fuels in high temperature and pressure turbulent flows. The LES studies are also well adapted to strongly anisothermal flows occurring in the nuclear field. Jogee *et al.* [182] investigate the LES of anisothermal flow over a circular cylinder. They highlight the effect of temperature on flow dynamics. Lu *et al.* [183, 184] analyze the temperature fluctuation in a mixing tee and its effect on the thermal fatigue of component in nuclear power plants.

The numerical method and the models used for the LES of turbulent flows play a major role in the accuracy of the results. The anisothermal conditions require solving the energy equation in addition to the classically resolved mass and momentum conservation equations. Besides, in the

operating conditions of the gas-pressurized solar receivers, the coupling between the dynamic of the flow and the temperature is strong and complicates the LES. This chapter aims to investigate the performances of the LES in the working conditions of the solar receivers and the flow behavior thanks to the reference data provided by the Direct Numerical Simulations (DNS). In section 4.2, the LES are compared to the DNS in the operating conditions of an infinitely long solar receiver. In section 4.3, the LES are assessed in conditions that could be encountered in existing solar receivers. In section 4.4, the flow behavior and the LES results are compared with regard to the two configurations. Section 4.5 concludes on the LES performed in anisothermal conditions.

4.2 Paper 1: Investigation of Thermal Large-Eddy Simulation approaches in a highly turbulent channel flow submitted to strong asymmetric heating

This section reproduces the paper of M. David, A. Toutant, and F. Bataille untitled Investigation of Thermal Large-Eddy Simulation approaches in a highly turbulent channel flow submitted to strong asymmetric heating and published in *Physics of Fluids*.

Abstract

This study deals with Thermal Large-Eddy Simulation (T-LES) of anisothermal turbulent channel flow in the working conditions of solar receivers used in concentrated solar power towers. The flow is characterized by high-temperature levels and strong heat fluxes. The hot and cold friction Reynolds numbers of the simulations are respectively 630 and 970. The Navier-Stokes equations are solved under the low Mach number approximation and the thermal dilatation is taken into account. The momentum convection and the density-velocity correlation subgrid terms are modeled. Functional, structural, and mixed subgrid-scale models are investigated. A tensorial version of the classical Anisotropic Minimum-Dissipation (AMD) model is studied and produces good results. A Quick scheme and a second-order centered scheme are tested for the discretization of the mass convection term. Firstly, a global assessment of 22 large-eddy simulations is proposed then 6 are selected for a careful analysis including profiles of mean quantities and fluctuation values as well as a comparison of instantaneous fields. Probability density functions of wall heat fluxes are plotted. The results point out that thermal large-eddy simulations performed with the Quick scheme tend to underestimate the wall heat flux whereas the second-order centered scheme significantly improves its estimation. Thermal large-eddy simulations tend to overestimate the peaks of velocity correlations. When regarding the dimensionless profiles of fluctuations, the tensorial AMD model provides better results than the other assessed models. For the heat flux estimation, the best agreement is found with the AMD model combined with the second-order centered scheme.

4.2.1 Introduction

This study falls within the research on the solar receivers of concentrated solar power towers. The solar receiver is crossed by an asymmetrically heated and highly turbulent airflow. Turbulent flows submitted to asymmetric heating are a challenging field of research. They are ubiquitous in many application fields such as heat exchangers, nuclear reactors, electronic devices, and solar receivers. Turbulence is described by the equations of Navier-Stokes. The complexity of these equations renders the Direct Numerical Simulations (DNS) of turbulence inapplicable to most

of systems because of the required computational cost. Thermal large-eddy simulation (T-LES) is a family of methods aiming to obtain a low-cost three-dimensional unsteady simulation of an anisothermal turbulent flow. Large scales are explicitly resolved, while small scales, more computationally expensive to resolve, are accounted for by their modeled effect on larger scales. The separation between resolved and modeled scales is generally performed using a low-pass filter. Subgrid models are necessary to close the governing equations. In this paper, we assess various turbulence models of T-LES in an asymmetrically heated turbulent channel flow under the low Mach number approximation. Fully developed channel flow is a popular test case for subgrid models of LES [185, 186, 187, 145, 17, 160, 188, 189, 190, 191, 53, 13, 103, 192, 131, 150]. This geometry appears as a good test case for turbulence model because of its near-wall behavior presenting small coherent scales in the viscous sublayer. The working conditions studied are close to the ones encountered in existing solar receivers. They are characterized by highly turbulent airflow, asymmetrical heating, high-temperature levels, and strong heat fluxes.

In 1996, Wang and Pletcher [193] were the first authors to perform LES of channel flows with high-heat transfer rates at low-Mach and low-Reynolds numbers. They use the incompressible dynamic subgrid-scale (SGS) model of Germano *et al.* [142] extended to compressible case by Moin *et al.* [194]. Two wall temperature ratios were tested: 1.02 and 3.0. They show that the temperature-velocity correlations are very dependent on the heat transfer rate. The velocity fluctuations are enhanced with heating. However, the temperature fluctuations are bigger at the cold wall when scaled by the local mean quantities. Nicoud [4] tests three finite-difference schemes to solve the Navier-Stokes equations under the low-Mach number approximation. The friction Reynolds number is 180. The assessed algorithms are algorithms with low numerical dissipation. They exhibit fourth-order spatial and second-order temporal accuracy. A variable coefficient Poisson equation is used to solve the pressure equation. The author carries out simulations with temperature ratios of 1.01, 2, 4, 6, 8, and 10. The three tested algorithms are stable for the three first temperature ratios. Daileys *et al.* [190] perform LES at constant wall heat flux using a compressible solver at a bulk Reynolds number of 11000. The mass flow rate is imposed. The wall-to-bulk temperature ratios are 1.05 and 1.48 for the heated case and 0.56 for the cooled case. As Wang and Pletcher [193], the authors use the incompressible dynamic SGS model of Germano *et al.* [142] extended to compressible case by Moin *et al.* [194]. They point out that heating and cooling influence the mean velocity and temperature profiles. The bigger the wall-to-bulk temperature ratio is, the smaller the average turbulent kinetic is. The friction velocity is 26 percent higher in the high heating case and 27 percent lower in the high cooling case as compared to the low heating results. Moreover, the peaks of resolved turbulent stress are slightly larger for the high cooling case compared to the low heating results. Lessani and Papalexandris [195] focus their attention on channel flows at high wall temperature ratios. They do not consider compressibility effects meaning that the density variations are only influenced by temperature variations. The Navier-Stokes equations are solved under the low-Mach number approximation. In their working condition, the friction Reynolds number is 180. As Daileys *et al.* [190] and Wang and Pletcher [193], they notice that the mean velocity profile on the cold side deviates from the isothermal logarithmic law of the wall. However, the hot side is near the incompressible isothermal law of the wall. The turbulent kinetic energy in the near-wall region is higher on the cold side than on the hot side meaning that heating tends to laminarize the flow. The temperature fluctuations are more intense near the cold wall. The biggest peak of temperature fluctuations is observed on the hot side but far from the wall. Bellec *et al.* [196] investigate the thermal boundary layer spatial developments in a turbulent channel flow submitted to asymmetric heating using LES. Wall temperatures are 590 K and

380 K. The friction Reynolds number is 395. The Wall-Adapting Local Eddy-viscosity (WALE) model proposed by Nicoud and Ducros [14] is used. They highlight that the coupling between temperature and velocity fields modifies both the mean and the fluctuations profiles. The fluid heating tends to reduce the peak of classically scaled fluctuations of the three components of velocity compared to an isothermal case. Serra *et al.* [188] study an asymmetrically heated turbulent channel flow with imposed wall temperatures. The temperature ratios are 1.01, 1.07, and 2. Simulations are performed for two friction Reynolds numbers: 180 and 395. Navier-Stokes equations are solved under the low-Mach number approximation. As in the study of Bellec *et al.* [196], the WALE model of Nicoud and Ducros [14] is used. The authors investigate the impact of thermal gradients. For low-temperature ratios (1.01 and 1.07), the variations of the viscosity and the conductivity can be fixed at constant values. The authors mention that the constant subgrid-scale Prandtl number and the dynamic calculation of the subgrid-scale Prandtl number produce similar results. As in Refs. [190, 193, 195], the temperature ratio modify the mean profiles, the fluctuations and the correlations. Yahya *et al.* [197] investigate turbulent forced convective flow in an anisothermal channel at low-Mach thanks to the WALE subgrid model [14]. Results for four friction Reynolds numbers are presented: 150, 180, 245, and 460. The wall temperature ratio varies between 1.01 and 5. They point out that turbulence is enhanced at the cold side. The turbulent kinetic energy is lower at the hot wall than at the cold wall. They also notice that the turbulent structures are very short and densely populated in the vicinity of the cold wall. Near the hot wall, turbulence produces large elongated vortices and long streaky structures. For high-temperature ratio and low friction Reynolds number, they observe relaminarization of the fluid at the hot side. Serra *et al.* [198] propose a summary of works on non-isothermal turbulent flows with asymmetric wall temperatures.

A posteriori tests are widely studied in the literature. They are considered to be the ultimate tests of model performance since they consider all the simulation factors (combining effects of numerical discretization, time integration, and averaging) [199]. For that reason, we carry out *a posteriori* tests of the subgrid models to assess their efficiency. Few *a posteriori* tests dealing with isotropic turbulence are described below. Kosović *et al.* [200] perform LES of decaying isotropic turbulence on a periodic cubic domain. They study two phenomenological subgrid-scale models using *a posteriori* tests of compressible turbulent flow. Hickel *et al.* [201] proposed an *a posteriori* analysis of the spectral numerical dissipation in simulations of freely decaying homogeneous isotropic turbulence. Vashishtha *et al.* [202] used renormalized viscosity to perform LES of decaying homogeneous and isotropic turbulence in a cubical domain. They compare LES and DNS results and show that the LES is able to capture the evolution of total energy and total dissipation rate as well as the energy spectrum and flux. Isothermal wall-bounded turbulent flows are also widely encountered in the literature. Dupuy *et al.* [17] perform *a posteriori* tests of subgrid-scale models in an isothermal turbulent channel. They assess five functional eddy-viscosity models (Wall-Adapting Local Eddy-viscosity, Sigma, Anisotropic Minimum-Dissipation, Kobayashi, and anisotropic Smagorinsky) and two structural models (gradient and scale-similarity). The gradient model is found to be not sufficiently impactful to significantly alter the flow. It must be filtered and amplified. The turbulence anisotropy is poorly represented by functional models. They also test dynamic versions of models but they do not notably improve the prediction of models. The Anisotropic Minimum-Dissipation (AMD) tensorial eddy-viscosity model provides good results on the wall shear stress and the turbulence anisotropy. Horiuti [203] investigates the Bardina model [16] in turbulent isothermal channel flow. Thanks to *a posteriori* tests, he shows that this model has a strong negative correlation with the Leonard term for the SGS cross-stress term. The Bardina model plays a role as a backscattering of subgrid-scale energy in the buffer layer,

which considerably improves the accuracy of LES. Stolz *et al.* [204] employs both *a priori* and *a posteriori* analysis to test an approximate deconvolution model for the large-eddy simulation of incompressible flows. Some studies also involve this type of test to evaluate particular LES methods and to quantify the LES sensitivity to simulation parameters. For instance, Vreman *et al.* [84] compare LES of the temporal mixing layer with *a posteriori* tests using the dynamic mixed model in combination with five different numerical schemes. They point out that the numerical method has a strong influence on the results. Rezaeiravesh *et al.* [171] also mention the major role of numerical error. Indeed, in the working conditions studied by the authors, the errors induced by the WALE subgrid-scale model are dominated by the numerical error. Geurts and van der Bos [205] investigate explicit filtering. They show that the numerical high-pass effects are dependent on the subfilter resolution, defined as the ratio of filter width and grid spacing. The more the filter width is close to the grid spacing, the more the numerically effects are salient. For a ratio between 1 and 2, the induced numerically effects are comparable to, or even larger than the turbulent stresses. Kremer *et al.* [175] assess the resolution requirement and Reynolds number effects of turbulent channel flow using relaxation filtering. *A posteriori* tests indicate that LES using relaxation filtering approach is efficient to simulate fully turbulent wall-bounded flows provided that grid resolution is sufficient and that largest scales are not overly affected by numerical dissipation. Another example is the work of Keating *et al.* [206] which combines *a priori* and *a posteriori* tests to compare three inflow conditions of turbulent wall-bounded flow. The authors investigate a synthetic turbulence generation method, a recycling method, and a forcing method including a control loop. This last method is found to be effective by generating turbulence with the correct Reynolds stresses and correlations within less than ten channel half heights.

It seems that very few studies are assessing LES subgrid-scale models with *a posteriori* tests of anisothermal channel flow. Dupuy *et al.* [145] perform T-LES in strongly anisothermal turbulent channel flows. The ratio of wall temperatures is 2. They solve the Navier-Stokes equations under the low-Mach number approximation in two formulations: the velocity formulation and the Favre formulation. Both the momentum convection subgrid term and the density-velocity correlation subgrid term are modeled. They study functional eddy-viscosity or eddy-diffusivity models, structural models, tensorial models, and dynamic versions of these models at friction Reynolds number of 180 and 395. The best results are obtained with the Favre formulation. Among the tested models, the AMD and the scale-similarity approaches are the most satisfying. To the author's knowledge, there is no *a posteriori* test of LES subgrid models in a highly turbulent channel flow submitted to asymmetric heating. This paper aims to fulfill this gap in the literature by assessing T-LES models in the discussed working conditions.

The outline of this paper is as follows: in Sec.4.2.2, the resolved equations are expressed. The investigated subgrid-scale models are described in Sec.4.2.3. The channel flow configuration and the numerical method are presented in Sec.4.2.4. The results of the models are summarized and discussed in Sec.4.2.5. Then, six T-LES approaches are selected for an accurate study.

4.2.2 Filtered low-Mach number equations

In this section, we present the formalism of the resolved equations. Following the recommendations of Dupuy *et al.* [145] we use the Favre formulation to filter the equations. It involves Favre-filtered variables, based on the density-weighted Favre filter ($\widetilde{\cdot}$). The variables are defined for any field ψ as $\widetilde{\psi} = \overline{\rho\psi}/\overline{\rho}$, where ($\bar{\cdot}$) is the unweighted classical filter. The two most significant subgrid terms mentioned by Dupuy *et al.* [160] are considered: a subgrid term related to the non-

linearity of momentum convection and another modeling the correlation of density and velocity. The low-Mach number Navier-Stokes equations admit large variations in gas density while remain acoustically incompressible [2]. This approximation, well adapted to the studied conditions, introduces two pressures: the mechanical pressure and the thermodynamical pressure which is homogeneous. The low Mach number hypothesis permits to reduce the computational time to reach convergence by increasing the fractionnal time step when compared to as the resolution of the compressible Navier-Stokes equations. The Stokes' hypothesis is assumed. See Papalexandris for further details on the applicability of the Stokes' hypothesis to low Mach number flows [207]. The solved equations are presented below.

- Mass conservation equation

$$\frac{\partial \overline{\rho}}{\partial t} + \frac{\partial \overline{\rho}\widetilde{U}_j}{\partial x_j} = 0, \tag{4.1}$$

- Momentum conservation equation

$$\frac{\partial \overline{\rho}\widetilde{U}_i}{\partial t} = -\frac{(\partial \overline{\rho}\widetilde{U}_j\widetilde{U}_i + \rho G_{U_jU_i})}{\partial x_j} - \frac{\partial P}{\partial x_i} + \frac{\partial \Sigma_{ij}(\widetilde{\boldsymbol{U}}, \widetilde{T})}{\partial x_j}, \tag{4.2}$$

- Energy conservation equation

$$\frac{\partial}{\partial x_j}(\widetilde{U}_j + \overline{\rho} G_{U_j/\rho}) = -\frac{1}{\gamma P_0}\left[(\gamma - 1)\frac{\partial Q_j(\widetilde{T})}{\partial x_j} + \frac{\mathrm{d}P_0}{\mathrm{d}t}\right], \tag{4.3}$$

- Ideal gas law

$$\widetilde{T} = \frac{P_0}{\overline{\rho} r} \tag{4.4}$$

where ρ is the density, T is the temperature, γ is the heat capacity ratio, $r = 330$ J.kg^{-1}.K^{-1} is the ideal gas specific constant, t is the time, P is the mechanical pressure, P_0 the thermodynamical pressure, U_i is the ith component of velocity, $\mathrm{d}/\mathrm{d}t$ is the time derivative (total derivative since P_0 is homogeneous), and x_i is the Cartesian coordinate in the ith direction. The subgrid term relative to momentum convection is $G_{U_jU_i} = \widetilde{U_jU_i} - \widetilde{U}_j\widetilde{U}_i$ and the subgrid term relative to the density-velocity correlation is expressed as $G_{U_j/\rho} = \widetilde{U_j/\rho} - \widetilde{U}_j/\overline{\rho}$. The Einstein summation convention is used. The functions $\Sigma_{ij}(\widetilde{\boldsymbol{U}}, \widetilde{T})$ and $Q_j(\widetilde{T})$ are used to compute the shear-stress tensor and conductive heat flux associated with a given velocity and temperature. The particular form of the energy conservation equation, involving the velocity divergence, is obtained (1) by applying the ideal gas law to the energy equation written in terms of transport of temperature; (2) by using the fact that the thermodynamical pressure is homogeneous. This formulation is also used by Nicoud [4] and Dupuy *et al.* [145]. The thermodynamical pressure is computed by integrating Eq. 4.3 over the volume of the computational domain:

$$\frac{\mathrm{d}P_0}{\mathrm{d}t} = -\frac{\gamma - 1}{V}\int Q_j(\widetilde{T})\mathrm{d}S_j \tag{4.5}$$

where V is the volume of the computational domain and S_j are the boundaries of the computational domain.

Newtonian fluid and Fourier's law are assumed, leading to the following expressions:

$$\Sigma_{ij}(\widetilde{\boldsymbol{U}},\widetilde{T}) = \mu(\widetilde{T})(\frac{\partial \widetilde{U}_i}{\partial x_j} + \frac{\partial \widetilde{U}_j}{\partial x_i}) - \frac{2}{3}\mu(\widetilde{T})\frac{\partial \widetilde{U}_k}{\partial x_k}\delta_{ij}, \tag{4.6}$$

$$Q_j(\widetilde{T}) = -\lambda(\widetilde{T})\frac{\partial \widetilde{T}}{\partial x_j}, \tag{4.7}$$

with $\mu(\widetilde{T})$ as the dynamic viscosity, $\lambda(\widetilde{T})$ as the thermal conductivity, and δ_{ij} as the Kronecker symbol.

The fluid used is air. The viscosity is computed using the Sutherland's law [69].

$$\mu(\widetilde{T}) = \mu_0 \frac{\widetilde{T}}{T_0}^{3/2} \frac{T_0 + S}{\widetilde{T} + S}, \tag{4.8}$$

where $\mu_0 = 1.716 \times 10^{-5}\ Pa.s$, $S = 110.4$ K, and $T_0 = 273.15$ K. The Prandtl number is supposed to be constant, Pr= 0.87 and the heat capacity at constant pressure $C_p = 1155$ J.kg^{-1}.K^{-1}. The conductivity is deduced from the Prandtl number, the heat capacity at constant pressure, and the viscosity.

$$\lambda(\widetilde{T}) = \frac{C_p}{Pr}\mu(\widetilde{T}). \tag{4.9}$$

4.2.3 Subgrid-scale models

The following formalism is introduced to express the models for momentum convection subgrid term and density-velocity correlation subgrid term.

$$G_{U_jU_i} \approx \tau_{ij}^{mod}(\widetilde{\boldsymbol{U}}, \overline{\Delta}) \tag{4.10}$$

$$G_{U_j/\rho} \approx \pi_j^{mod}(\widetilde{\mathbf{U}}, 1/\overline{\rho}, \overline{\Delta}) \tag{4.11}$$

The subgrid-scale tensors, τ_{ij} and π_{ij}, are computed thanks to variables resolved in T-LES. The function used to compute the subgrid-scale tensor depends on the model used. In this study, zero algebraic models without wall function or wall model are investigated. Functional, structural, and mixed models are assessed. They are listed in the following subsections. In the following of this article, the filter length scale is computed using $\overline{\Delta} = \left(\overline{\Delta}_x\overline{\Delta}_y\overline{\Delta}_z\right)^{1/3}$. The filter length scale and the mesh size are equal.

4.2.3.1 Functional models

Functional modeling consists in reproducing the action of the subgrid terms by introducing a term that have a similar effect. This term does not have necessarily the same structure as the subgrid tensor. In functional modeling, the action of the subgrid scales on the resolved scales is mainly an energetic action. This approach does not consider the backward energy cascade and is often over-dissipative. The subgrid-scale tensor relative to momentum convection is computed by analogy with molecular diffusion:

$$\tau_{ij}^{mod}(\widetilde{\boldsymbol{U}}, \overline{\Delta}) = -2\nu_t^{mod}(\mathbf{g}, \mathbf{d}, \overline{\Delta})S_{ij}, \tag{4.12}$$

where $S_{ij} = 0.5(g_{ij} + g_{ji})$ is the rate of the deformation tensor, $\mathbf{g}$ is the velocity gradient: $g_{ij} = \partial\widetilde{U}_i/\partial x_j$, and ν_t^{mod} is the turbulent viscosity whose expression depends on the model used.

The eddy-diffusivity models are used for the density-velocity subgrid term. They involves the subgrid-scale Prandtl number, Pr_t:

$$\pi_j^{mod}(\widetilde{\boldsymbol{U}}, \phi, \overline{\Delta}) = -\frac{\nu_t^{mod}(\mathbf{g}, \mathbf{d}, \overline{\Delta})}{Pr_t} d_j \tag{4.13}$$

with $\boldsymbol{d_j} = \partial\phi/\partial x_j$ the scalar gradient. Pr_t is the turbulent Prandtl number and is equal to 0.9.

The following eddy-viscosity models are studied in this paper.

- WALE model [14]

$$\nu_t^{WALE}\left(\mathbf{g}, \mathbf{d}, \overline{\Delta}\right) = \left(C^{WALE}\overline{\Delta}\right)^2 \frac{\left(S_{ij}^d S_{ij}^d\right)^{3/2}}{\left(S_{mn}S_{mn}\right)^{5/2} + \left(S_{mn}^d S_{mn}^d\right)^{5/4}} \tag{4.14}$$

- AMD [13]

$$\nu_t^{AMD}\left(\mathbf{g}, \mathbf{d}, \overline{\Delta}\right) = C^{AMD} \frac{max(0, -G_{ij}S_{ij})}{g_{mn}g_{mn}} \tag{4.15}$$

- Scalar AMD model [22]

$$\nu_t^{AMD}\left(\mathbf{g}, \mathbf{d}, \overline{\Delta}\right) = C^{AMDs} \frac{max(0, -D_j d_j)}{d_m d_m} \tag{4.16}$$

- Sigma [150]

$$\nu_t^{Sigma}\left(\mathbf{g}, \mathbf{d}, \overline{\Delta}\right) = \left(C^{Sigma}\overline{\Delta}\right)^2 \frac{\sigma_3(\sigma_1 - \sigma_2)(\sigma_2 - \sigma_3)}{\sigma_1^2} \tag{4.17}$$

With S_{ij}^d the traceless symmetric part of the squared velocity gradient tensor, $\sigma_1 > \sigma_2 > \sigma_3$ the three singular values of $\mathbf{g}$, $G_{ij} = \overline{\Delta_k}^2 g_{ik}g_{jk}$ the gradient model, and $D_j = \overline{\Delta_k}^2 g_{jk}d_k$ the gradient model for the density-velocity correlation subgrid term. Unless otherwise is stated, the functional model constants used are $C^{WALE} = 0.55$, $C^{AMD} = 0.3$, $C^{AMDs} = 0.3$, and $C^{Sigma} = 1.5$.

Tensorial eddy-viscosity models are interesting to take into account the anisotropy of the flow by weighting each component of the subgrid-scale model. One of the bases of modeling is to conserve the generic properties of the filtered Navier-Stokes equations. The theory proposed by Deville *et al.* [176] provides the expression that the stress tensor needs to follow in order to respects the invariance properties:

$$\begin{aligned} \tau_{ij} = \quad & a\ (\mathbf{S_{ij}} \cdot \gamma \otimes \gamma + \gamma \otimes \gamma \cdot \mathbf{S_{ij}}) + b\ \gamma \otimes \gamma \cdot \mathbf{S_{ij}} \cdot \gamma \otimes \gamma + c\ \mathbf{S_{ij}} \\ & + (d\ tr(\mathbf{S_{ij}}) + e\ \mathbf{S_{ij}} : \gamma \otimes \gamma)\mathbf{I} + e\ tr(\mathbf{S_{ij}}\gamma \otimes \mathbf{e}) \end{aligned} \tag{4.18}$$

Where γ the unit vector used to represent the streamwise direction of the flow, $\mathbf{I}$ is the identity matrix, and a, b, c, d and e are coefficients.

In this paper, we test the tensorial model obtained by taking $\gamma = \mathbf{e_x}$, the streamwise direction of the flow, $a = 0.5$, $b = -1$, and $c = d = e = 0$. Considering the studied configuration of a bi-periodic plane channel flow, this tensorial model is equivalent to the $H^{(4)}$ version of the AMD model proposed by Dupuy *et al.* [17, 145]:

$$\tau_{ij}^{H^{(4)}AMD}\left(\mathbf{U}, \overline{\Delta}\right) = H_{ij}^{(4)} \tau_{ij}^{AMD}\left(\mathbf{U}, \overline{\Delta}\right) \tag{4.19}$$

With

$$H_{ij}^{(4)} = \begin{pmatrix} 0 & 1 & 1 \\ 1 & 0 & 0 \\ 1 & 0 & 0 \end{pmatrix} \tag{4.20}$$

In the following, the simulation noted "AMDt+AMDs" involves the tensorial AMD model for the computation of momentum convection subgrid term and the scalar AMD model for the density-velocity correlation subgrid term.

4.2.3.2 Structural models

Structural modeling aims at approximating the subgrid tensor, τ, by constructing it from an evaluation of the filtered velocity or a formal series expansion. They are established with no prior knowledge of the nature of the interaction between the subgrid scales and the resolved scales. Drawbacks of structural models are generally a poor prediction of the dissipation and their inclination to be unstable. Two structural models are investigated.

- Scale similarity model [16]

$$\tau_{ij}^{sim} = C^{sim}\left(\widehat{\widetilde{U}_j\widetilde{U}_i} - \widehat{\widetilde{U}}_j\widehat{\widetilde{U}}_i\right) \tag{4.21}$$

$$\pi_{j}^{sim} = C^{sim}\left(\widehat{\widetilde{U}_j\widetilde{\phi}} - \widehat{\widetilde{U}}_j\widehat{\widetilde{\phi}}\right) \tag{4.22}$$

The scale similarity hypothesis consists in assuming that the statistical structure of the tensor of the subgrid scales is similar to that of the smallest resolved scales. Sagaut [208] explains that this model generally produces good results. However, it is slightly dissipative and tends to underestimate the energy cascade. Box and Laplacian filters are tested for the scale similarity model, associated simulations are respectively noted as "Sim" and "SiL" in Section 4.2.5. The box filter is computed as an average over three cells in the three directions. The Laplacian filter involves the Taylor series expansion of the box filter using the local cell size as the filter width.

- Gradient model [15]

$$\tau_{ij}^{grd} = \frac{1}{12}C^{grd}\overline{\Delta_k}^2 g_{ik}g_{jk} \tag{4.23}$$

$$\pi_{j}^{grd} = \frac{1}{12}C^{grd}\overline{\Delta_k}^2 g_{ik}d_{k} \tag{4.24}$$

Unless otherwise is stated, the structural model constants used are $C^{Sim} = 1.0$ and $C^{grd} = 1.0$.

4.2.3.3 Mixed models

Mixed modeling aims at combining the advantages of functional and structural models. On the one hand, the functional approaches generally correctly take into account the level of the energy transfers between the resolved and the subgrid scales. On the other hand, the structural models generally produce a good approximation of the structure of the subgrid tensor and are able to capture anisotropic effects and disequilibrium [209, 210, 103]. We study two mixed models: the multiplicative mixed model (MMG model) proposed by Dupuy *et al.* [160] and a model coupling the tensorial version of the AMD model and the scale similarity model. The multiplicative mixed

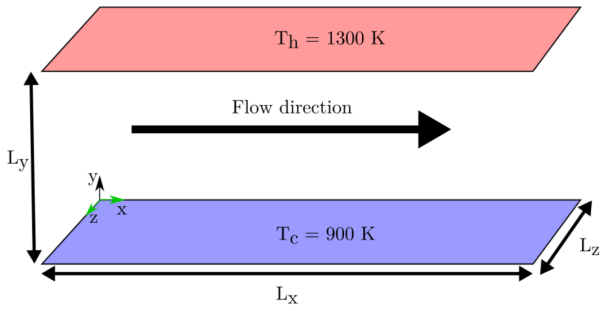

Figure 4.1 – Geometry of the channel flow. The periodic directions are in green.

model based on the gradient model (MMG model) is a functional model constructed such that its magnitude is determined by the gradient model and its orientation is aligned with the rate of deformation tensor or the scalar gradient depending on the subgrid term.

$$\nu_t^{MMG}(\mathbf{g},\mathbf{d}) = -C^{MMG}\frac{G_{kk}}{|\mathbf{S}|} \tag{4.25}$$

where $C^{MMG} = 0.05$. The second mixed model is the scale similarity associated with the tensorial version of the AMD model for the momentum convection and associated with the scalar AMD for the density-velocity correlation, (sim + AMDt - sim + AMDs).

4.2.4 Study configuration

4.2.4.1 Channel flow configuration

The study configuration is close to the working conditions of the gas-pressurized solar receivers of concentrated solar power towers. The solar receiver is assumed to be an infinitely long and wide channel. One wall of the channel absorbs concentrated solar light whereas the other is insulated. To reproduce these conditions, thermal large-eddy simulations are performed in a fully developed three-dimensional turbulent channel flow asymmetrically heated. The channel is displayed in Fig. 4.1. It is periodic in the streamwise (x), and spanwise (z) directions and enclosed by two plane walls in the wall-normal direction (y). The domain size is $4\pi\delta \times 2\delta \times 4/3\pi\delta$ with $\delta = 3$mm. The temperatures of the plates are fixed to 1300 K for the hot wall ($y = 2\delta$) and 900 K for the other wall, designed as cold wall ($y = 0$). The wall temperature ratio is then 1.44. Note that, in gas-pressurized solar receivers the inertia of the walls is important meaning that air is passing through a channel at almost temporally constant wall temperatures. However, neither the temperature nor the heat flux are spatially constant over the walls of the solar receiver. Avellaneda *et al.* [211] show that there are not significant differences between the two types of thermal boundaries conditions for turbulent low Mach channel flow under asymmetric high temperature gradient. The thermodynamical pressure, P_0, is 10 bars. The hot and cold friction Reynolds numbers are respectively 630 and 970, leading to a mean friction Reynolds number of 800.

4.2.4.2 Numerical settings

Simulations are carried out using a finite difference method in a staggered grid system. Mesh is uniform in the homogeneous directions (x and z) and follows a hyperbolic tangent law in the

Table 4.1 – DNS and T-LES mesh characteristics. The dimensionless mesh size is given for the cold wall, which corresponds to the highest friction Reynolds number.

Name	Number of grid points $N_x \times N_y \times N_z$	Dimensionless mesh size Δ_x^+ ; $\Delta_y^+(0)$; $\Delta_y^+(\delta)$; Δ_z^+
DNS	$1152 \times 746 \times 768$	10.7 ; 0.41 ; 5.3 ; 5.3
AAA	$192 \times 152 \times 128$	64 ; 1.0 ; 32 ; 32
BAB	$160 \times 152 \times 96$	77 ; 1.0 ; 32 ; 43
CAC	$128 \times 152 \times 72$	96 ; 1.0 ; 32 ; 57
DAD	$96 \times 152 \times 48$	128 ; 1.0 ; 32 ; 85

wall-normal coordinate direction (y). Time derivatives are calculated with a third-order Runge-Kutta scheme. Momentum convection is approached using a fourth-order centered scheme. Velocity divergence, which is the temperature convection, and temperature diffusion are discretized with centered second-order schemes. For mass convection, a Quick and a centered second-order schemes are compared. This last scheme has been used by Streher *et al.* [12] in a LES study dealing with isothermal channel flow and produces very good results. High-resolution spatial discretization methods such as the compact finite difference schemes proposed by Lele [212] are not tested in this study. Indeed, despite their accuracy, they are difficult to implement in complex geometries. Their use would complicate the simulations of more complex geometries of solar receivers. TrioCFD software [3] is used to perform the simulations. This code has been developed by the French Alternative Energies and Atomic Energy Commission and has been used in many simulations of fluid flows [213, 211, 17, 145, 214, 27].

$$y_k = L_y \left(1 + \frac{1}{a}\tanh\left[\left(\frac{k-1}{N_y - 1}\right)\tanh^{-1}(a)\right]\right) \tag{4.26}$$

where a is the mesh dilatation parameter and N_y is the number of grid points in the wall-normal direction. The meshes used for DNS and T-LES are given in Table 4.1. For the LES meshes, the first, second, and third characters respectively correspond with the x, y, and z directions. Character "A" stands for the highest resolution tested in a particular direction whereas "E" accounts for the coarsest resolution. The resolution in the wall-normal direction is not studied since it is substantially less impacting the results than the resolution in other directions, as explained by Rezaeiravesh and Liefvendahl [171].

4.2.5 Results and discussion

The results of the simulations are spatially-averaged in the homogeneous directions and are time-averaged. This combination of averages is denoted by $\langle\cdot\rangle$. The T-LES results are assessed with a DNS performed in the same conditions. We investigate mean quantities and covariances. In this work, T-LES models that are traceless, functional models, and partially traceless, mixed models, are studied. For these models, only the deviatoric Reynolds stresses can be reconstructed and compared with DNS data without filtering process [11]. It is the reason why, for the diagonal Reynolds stresses, we compare the DNS deviatoric Reynolds stress tensor, $R_{ij}^{DNS,dev}$, to the LES deviatoric Reynolds stress tensor, $R_{ij}^{LES,dev}$, plus the averaged deviatoric subgrid-scale stress tensor, $\langle\tau_{ij}^{SGS}\rangle^{dev}$:

$$R_{ij}^{DNS,dev} = R_{ij}^{LES,dev} + \langle\tau_{ij}^{SGS}(\mathbf{U}, \overline{\Delta})\rangle^{dev}, for\ i = j \tag{4.27}$$

where $R_{ij}^{DNS} = \langle U_i U_j \rangle - \langle U_i \rangle \langle U_j \rangle$ and $R_{ij}^{LES} = \langle \widetilde{U}_i \widetilde{U}_i \rangle - \langle \widetilde{U}_i \rangle \langle \widetilde{U}_j \rangle$. Note that the coordinates x_1, x_2, x_3 and x, y, z as well as U_1, U_2, U_3 and U, V, W are used interchangeably for practical reasons. As for the off-diagonal Reynolds stresses, the full Reynolds stress tensor is investigated since there is no reconstruction issue.

$$R_{ij}^{DNS} = R_{ij}^{LES} + \langle \tau_{ij}^{SGS}(\mathbf{U}, \overline{\Delta}) \rangle, \tag{4.28}$$

Concerning the velocity-temperature correlations, the same procedure is applied.

$$R_{i\theta}^{DNS} = R_{i\theta}^{LES} + \langle \pi_{i}^{SGS}(\mathbf{U}, T, \overline{\Delta}) \rangle \tag{4.29}$$

With $R_{i\theta}^{DNS} = \langle U_i \theta \rangle - \langle U_i \rangle \langle \theta \rangle$ and $R_{ij}^{LES} = \langle \widetilde{U}_i \widetilde{\theta} \rangle - \langle \widetilde{U}_i \rangle \langle \widetilde{\theta} \rangle$. Here $\pi_i^{SGS}(\mathbf{U}, T, \overline{\Delta})$ is linked to $\pi_i^{SGS}(\mathbf{U}, 1/\overline{\rho}, \overline{\Delta})$ by the ratio r/P_0 thanks to ideal gas law.

A "+" superscript following a variable indicates that this variable is normalized with the classical scaling: $x_i^+ = x_i U_\tau / \nu$, $U_i^+ = U_i / U_\tau$, $\langle R_{ij} \rangle^+ = \langle R_{ij} \rangle / U_\tau^2$, and $\langle U_i' \theta' \rangle^+ = \langle U_i' \theta' \rangle / (U_\tau \theta_\tau)$. The friction velocity and the friction temperature are respectively defined as $U_\tau = \sqrt{\nu \partial U / \partial x_2}$, and $\theta_\tau = \phi_w / (\rho C_p U_\tau)$, where ϕ_w is the conductive heat flux at the wall.

In subsection 4.2.5.3, results of 22 T-LES involving the models presented in 4.2.3 are summarized and discussed. Six selected T-LES are detailed in subsection 4.2.5.4.

4.2.5.1 Data processing

This section presents results of T-LES models in order to evaluate their efficiency. T-LES results are compared to DNS using the following procedure. Firstly, we interpolate the DNS wall-normal profiles on the mesh used for T-LES, then values are compared as expressed below :

$$\epsilon_X^{LES_j} = \frac{\sum_{i=1}^{N_y/2} log\left(\frac{y_{i+1}}{y_i}\right) \left| \left(X_i^{LES_j} - X_i^{DNS}\right) X_i^{LES_j} \right|}{\sum_{i=1}^{N_y} log\left(\frac{y_{i+1}}{y_i}\right) X_i^{DNS^2}} + \frac{\sum_{i=1}^{N_y/2} log\left(\frac{2\delta - y_{i+1}}{2\delta - y_i}\right) \left| \left(X_{Ny/2-i+1}^{LES_j} - X_{Ny/2-i+1}^{DNS}\right) X_{Ny/2-i+1}^{LES_j} \right|}{\sum_{i=1}^{N_y} log\left(\frac{2\delta - y_{i+1}}{2\delta - y_i}\right) X_i^{DNS^2}} \tag{4.30}$$

Where ϵ is the error, X is the observed value, LES_j refers to the jth tested model, y_i is the ith node in the wall-normal direction, and δ is the half height of the channel. Note that the logarithmic ratio aims to give more importance to near wall values than to mid-channel values. Moreover, the error calculated in the absolute value is weighted by the local value to accentuate the importance of peak values.

T-LES models are assessed on 11 physical quantities divided into two groups:

- Mean
  - ⋆ U, the longitudinal velocity profile,
  - ⋆ V, the wall-normal velocity profile,
  - ⋆ T, the temperature profile,

  - ⋆ ϕ, the normal conductive heat flux at the wall.

- Correlations
  - ⋆ $\langle u'u' \rangle^{dev}$, the covariance of the longitudinal velocity,
  - ⋆ $\langle v'v' \rangle^{dev}$, the covariance of the wall-normal velocity,
  - ⋆ $\langle w'w' \rangle^{dev}$, the covariance of the transversal velocity,
  - ⋆ $\langle \theta'\theta' \rangle$, the covariance of temperature,
  - ⋆ $\langle u'v' \rangle$, the correlation of longitudinal and wall-normal velocities,
  - ⋆ $\langle u'\theta' \rangle$, the correlation of longitudinal velocity and temperature,
  - ⋆ $\langle v'\theta' \rangle$, the correlation of wall-normal velocity and temperature.

Then, we compute the final error of the jth T-LES model on mean quantities, Err_{mean}, and the final error of the jth T-LES model on covariance, Err_{rms} by adding the error obtained for each value and dividing this sum by the results of the worst model:

$$Err_{mean}^{LES,j} = \frac{\sum\limits_{X} \epsilon_X^{LES_j}}{max\left(\sum\limits_{X} \epsilon_X^{LES}\right)} \tag{4.31}$$

where X is successively U, V, T and ϕ.

$$Err_{rms}^{LES,j} = \frac{\sum\limits_{X} \epsilon_X^{LES_j}}{max\left(\sum\limits_{X} \epsilon_X^{LES}\right)} \tag{4.32}$$

where X is successively the square root of $\langle u'u' \rangle^{dev}$, $\langle v'v' \rangle^{dev}$, $\langle w'w' \rangle^{dev}$, $\langle \theta'\theta' \rangle$, $\langle u'v' \rangle$, $\langle u'\theta' \rangle$, and $\langle v'\theta' \rangle$.

4.2.5.2 Preparatory study

Mesh sensitivity analysis A mesh sensitivity analysis is carried out in the studied conditions. The four LES meshes exposed in Tab. 4.1 are tested. The averaged errors on mean quantities and rms values are presented. The results of each LES mesh are compared with the results obtained with the DNS mesh presented in Tab. 4.1. Fig. 4.2 displays the errors committed by LES performed (1) without model ("no-model") involving the second-order centered scheme to discretize the mass convection term; (2) with the tensorial model ("AMDt + AMDs") associated with the Quick scheme. The results are sensitive to mesh refinement as classically observed (see for instance Kremer and Bogey [175] and Dupuy *et al.* [145]). The top-graph shows that the error on mean quantities is non-monotonic for the no-model simulations. The best results are obtained with the "BAB" and "CAC" meshes for which the induced numerical dissipation is improving the results. Regarding rms values, the error is decreasing with the mesh refinement. The error committed with "CAC" and "DAD" meshes are truncated on the graph. For the "CAC" mesh, the averaged error on mean quantities is 67%; for the "DAD" mesh, it is 131%. Regarding the "AMDt + AMDs" model (bottom-graph), the errors are decreasing with a monotonic tendency. These results indicate that introducing a model permits to decrease the mesh sensitivity of the

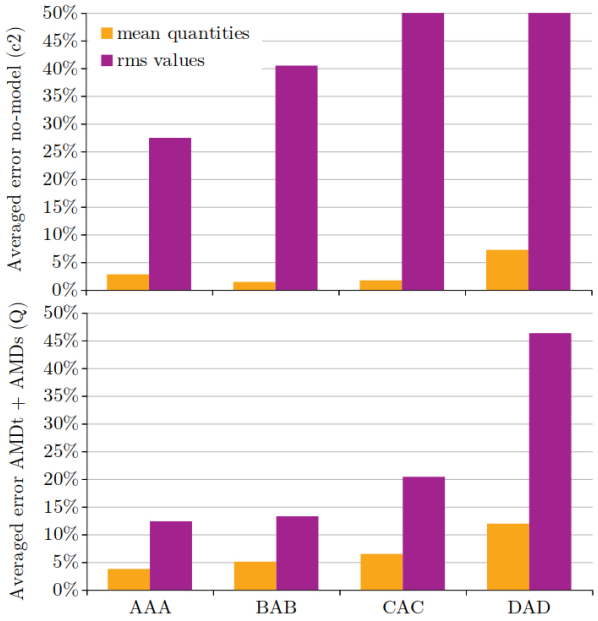

Figure 4.2 – Averaged errors obtained with four different meshes on mean quantities and rms values. Simulations without model and with the tensorial functional model are studied.

error, which is profitable. The improvement of the results on rms values almost reach a plateau for the meshes "AAA" and "BAB". For this reason and its accuracy on mean quantities with the no-model (c2) simulation, the "BAB" mesh is selected in the following. It seems to be a good compromise between the result accuracy and the computational time. The no-model simulations performed with the "BAB" mesh are called ILES thereafter.

Evaluation of Implicit Large-Eddy Simulation In implicit Large-Eddy Simulations (ILES) the truncation error of the discretization scheme is employed to model the effects of unresolved scales instead of an explicit computation of the SGS stress tensor, see Refs. [201, 192, 215] for more detail on ILES. Two ILES are tested and compared with the results of the simulations involving turbulence models in the following. The ILES solution combining the selected mesh and numerical scheme (mass convection and momentum convection are respectively approached with a Quick scheme and a fourth-order centered scheme) is compared to a no-model simulation. This no-model simulation aims to reproduce the one performed by Streher *et al.* [12] in an isothermal turbulent channel flow at a friction Reynolds number of 950, see Fig. 4.3. Note that, this simulation is performed with the same numerical setup as the one of Streher *et al.*, except the time derivatives which are computed with a third order Runge-Kutta scheme instead of a second-order Adams–Bashforth time integration scheme. Moreover, the dimensionless cell sizes are close but not identical. However, the streamwise velocity profile obtained by the no-model simulation is similar to the one obtained by Streher *et al.* [12]. For that reason, this no-model simulation is named "no-model Streher *et al.*" in Fig. 4.3. The ILES are assessed with the DNS performed by Hoyas and Jiménez [10]. The resolution of the DNS of Hoyas and Jiménez is $\Delta x^+ = 11$, $\Delta y(0)^+ = 0.28$, $\Delta y(\delta)^+ = 7.6$, and $\Delta z^+ = 5.7$. The results show that the proposed ILES, performed with the BAB mesh, gives a very accurate estimation of the streamwise velocity

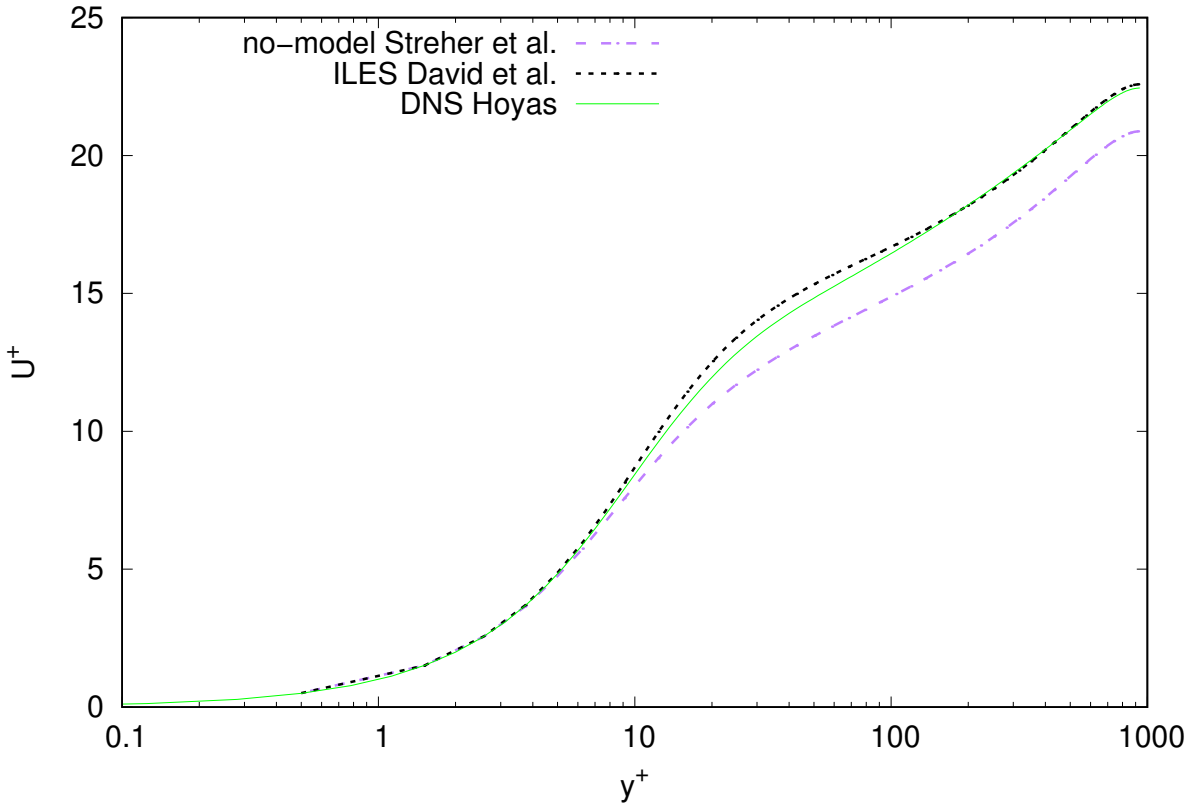

Figure 4.3 – Comparison of the streamwise velocity profile obtained with the no-model simulation of Streher *et al.* and the proposed ILES (noted as ILES David *et al.*).

profile and is better than the "no-model Streher *et al.*" simulation. The mesh used by Streher *et al.* is, yet, 1.5 times finer in the streamwise direction and 2 times finer in the spanwise direction than the mesh selected for the ILES. The wall normal resolution of the mesh proposed by Streher *et al.* is $\Delta y^+(0) = 1.5$ and $\Delta y^+(\delta) = 28$. It demonstrates that the numerical dissipation induced by the selected mesh is profitable. It explains the accuracy of the ILES on the prediction of mean quantities observed in the following.

4.2.5.3 General results and assessment of LES models

The LES models are tested on the mean quantities and the correlations presented above. Implicit LES are also assessed. As it is difficult to differentiate the numerical error from the model error with *a posteriori* tests, this study aims to propose solutions combining a mesh, a turbulence model, and a numerical scheme. Fig. 4.4 presents the normalized difference between DNS and various T-LES approaches. The top-graph stands for the T-LES error on mean quantities. The results indicate that the second-order centered scheme significantly improves the efficiency of functional models when regarding the error on mean quantities. The results of the scale similarity model are slightly deteriorated. Concerning mixed models, they are more efficient with the second-order centered scheme. The best results are obtained with the WALE model combined with the second-order centered scheme. Note that, with the used numerical setting, the performance of the implicit LES is satisfying when regarding mean quantities. The middle

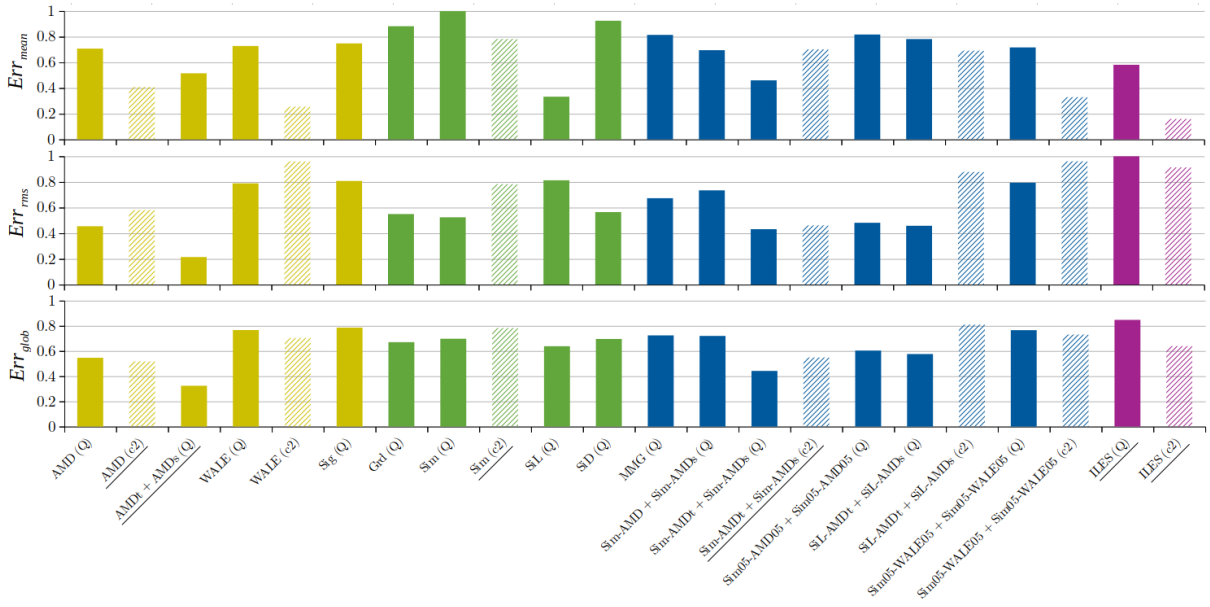

Figure 4.4 – Normalized error of various T-LES approaches. From top to bottom, the error concerns mean quantities, correlations, and global error. Yellow, green, and blue colors respectively stand for functional, structural, and mixed models. Purple color accounts for ILES. Full bars represent the simulations performed with the Quick scheme for the discretization of the mass convection whereas hatched bars are for T-LES using the second-order centered scheme. The six selected T-LES are underlined.

graph accounts for the T-LES error on correlations. The second-order centered scheme tends to deteriorate the LES correlation prediction of all the models. The best estimation of these values is obtained with the combination of tensorial AMD for the momentum convection subgrid term and scalar AMD for the density-velocity subgrid term. The ILES poorly estimate the correlations. The bottom-graph is the weighted average of the two first histograms and proposes a global error for each T-LES approach. The weight associated with mean quantities is four since there are four mean quantities and the weight related to correlations is seven. Globally, the best results are obtained with the "AMDt + AMDs", followed by the "AMD (c2)" model. Note that the simulation combining the tensorial AMD and scalar AMD models does not converge when performed with the second-order centered scheme.

We select the "AMD (c2)", "AMDt + AMDs (Q)", "Sim (c2)", and "Sim-AMDt + Sim-AMDs (c2)" models as well as the "ILES (Q)" and the "ILES (c2)" simulations for a more careful analysis.

Fig. 4.4 highlights the significant effects of the numerical scheme used for the discretization of the mass convection term on the results. Table 4.2 shows the results obtained with ILES for both schemes on each value. The mass convection has only low influence on the longitudinal velocity and on the covariances of velocities. However, the choice of the numerical scheme has substantial consequences on the wall-normal velocity. The second-order centered scheme, few dissipative, provides a much better estimation of the wall-normal velocity than the Quick scheme. These good results on the wall-normal velocity affect directly the thermal values by modifying the behavior of turbulent structures. Effects are salient on the conductive heat fluxes at walls, the velocity-temperature correlations, and the fluctuations of temperature. Considering the numerical setup

Table 4.2 – Comparison of the numerical scheme effect on the error committed by ILES on each variable.

	ϵ_U	ϵ_V	ϵ_T	ϵ_ϕ	$\epsilon_{\langle u'u'\rangle^{dev}}$	$\epsilon_{\langle v'v'\rangle^{dev}}$	$\epsilon_{\langle w'w'\rangle^{dev}}$	$\epsilon_{\langle u'v'\rangle}$	$\epsilon_{\langle u'\theta'\rangle}$	$\epsilon_{\langle v'\theta'\rangle}$	$\epsilon_{\langle \theta'\theta'\rangle}$
ILES (Q)	3.2	16.6	0.7	18.7	54.8	40.8	85.4	3.6	19.3	16.7	23.9
ILES (c2)	3.1	1.9	0.5	0.3	51.6	38.5	80.6	4.6	28.4	2.0	77.8

and the working conditions of this study, the second-order centered scheme is much better than the Quick scheme for the heat fluxes and the velocity-temperature correlations. Nonetheless, the Quick scheme is preferable for the prediction of temperature fluctuations.

4.2.5.4 Detailed results of selected models

Results obtained with the selected simulations are detailed here. They are divided into two parts. Firstly, mean quantities are presented then covariances and rms values are studied.

Mean quantities Fig. 4.5 gives the relative error of the six selected models on the mean quantities. The longitudinal velocity profile is predicted within 4% of error excepted for the AMD model associated with the second-order centered scheme. However, the estimation of the "AMD (c2)" approach on wall-normal velocity is the best. The mixed model is not able to produce a satisfying prediction of the wall-normal velocity profile. It seems that the particular behavior of the scale-similarity model on the hot side is responsible for the poor results of the mixed model on this side. All the models provide a very good estimation of the temperature profile. Lastly, the DNS heat flux is correctly predicted ($\epsilon < 6\%$) for all models excepted "AMDt + AMDs (Q)". The error committed on the flux is likely due to the Quick scheme used to compute the mass convection. Indeed, similar errors on heat flux are observed for all models when associated with the second-order centered scheme.

The profiles of dimensionless longitudinal velocity, wall-normal velocity, and temperature are plotted as functions of the wall-normal direction (Fig. 4.6). The top-left graph shows that, excepted the "AMD (c2)" T-LES which tends to overestimate the velocity, the models give a good approximation along with the entire profile of longitudinal velocity. Deviations between T-LES and DNS appear after $y^+ = 15$ and remain almost constant across the logarithmic law. The top-right graph describes the wall-normal velocity profile. This value skyrockets in the buffer layer (from $y^+ = 2$ to $y^+ = 30$) and reaches a constant velocity zone in the logarithmic layer. The "AMDt + AMDs (Q)" approach tends to underestimate the magnitude of the DNS profile. As seen in Fig. 4.5, the "AMD (c2)" T-LES is better than the other models. Note that, the "ILES (c2)" provides very satisfying results on this profile. Lastly, the temperature profile is analyzed on the bottom-left graph. As for the longitudinal velocity profile, the differences between T-LES and DNS emerge at $y^+ = 15$. However, on the cold side, the scale-similarity and the mixed models are close to the DNS profile. On the hot side, the AMD model and the tensorial AMD model are the best.

Covariances and rms values Covariance and rms values can be seen as second-order statistics since they deal with turbulence structures. They are more complex to predict but gives useful information on the flow. The errors committed on covariances and rms values are exposed in Fig. 4.7. As expected, the accuracy of the models on covariances and rms values is poorer

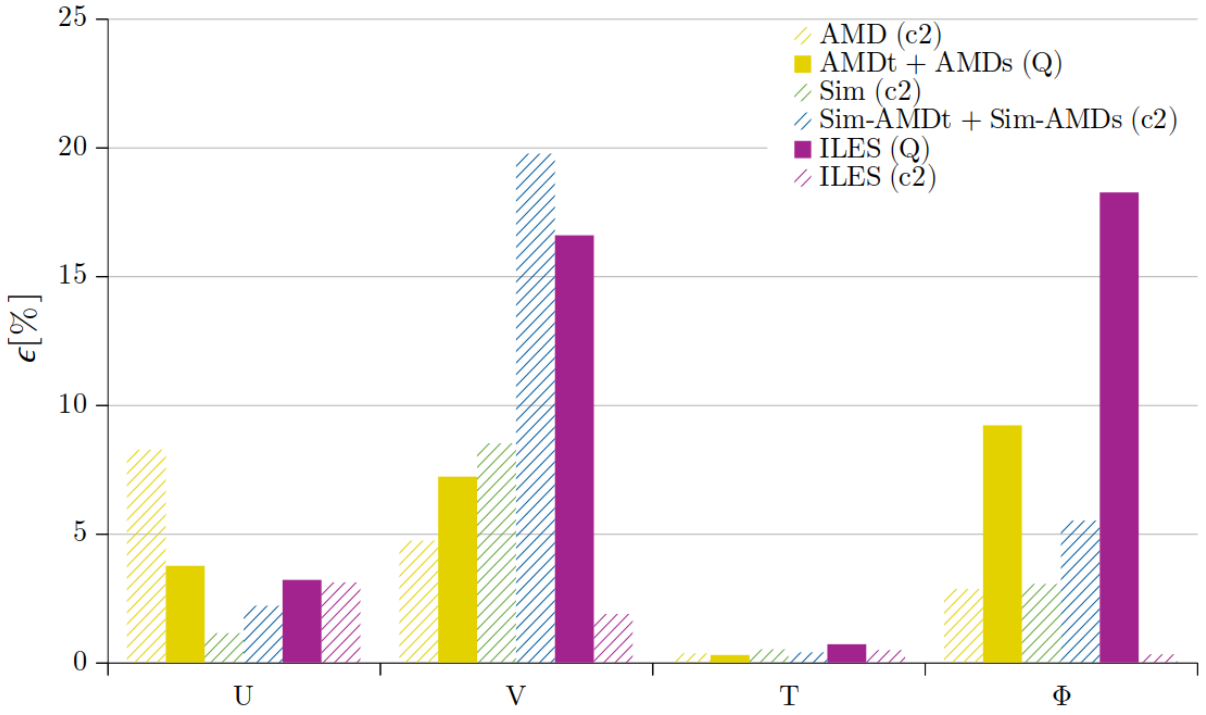

Figure 4.5 – Relative error on mean quantities for selected T-LES approaches. Yellow, green, and blue colors respectively stand for functional, structural, and mixed models. Full bars represent the simulations performed with the Quick scheme for the discretization of the mass convection whereas hatched bars are for T-LES using the second-order centered scheme.

than the results on mean quantities. The same model ranking is observed for the three velocity fluctuations. The biggest errors are committed on the covariance of transversal velocity. The "AMDt + AMDs (Q)" approach is the best among those studied. The results on the correlation $\langle u'v' \rangle$ are very satisfying for all the models. Once again, the "AMDt + AMDs (Q)" approach produces the best results. It is probably thanks to its tensorial formulation which allows it to reproduce the strong wall-normal anisotropy of channel flow. The temperature fluctuations are more correctly estimated with the mixed model. The correlation between longitudinal velocity and temperature is a substantial challenge for T-LES. With 20% of error, the "AMDt + AMDs (Q)" T-LES produces the closest results to DNS. The correlation of wall-normal velocity and temperature is globally well predicted with an error inferior to 10%. The results of the scale-similarity and the mixed model on the fluctuations of heat flux show a very good agreement with DNS. Those of the "AMDt + AMDs (Q)" approach have 20% of error. The "ILES (c2)" gives a poor approximation of this quantity. The deviatoric part of the diagonal terms of the Reynolds stress tensor and the cross velocity correlation are plotted along the wall-normal direction in Fig. 4.8. From top-left to bottom-right, the $\langle u'u' \rangle^{dev}$, $\langle v'v' \rangle^{dev}$, $\langle w'w' \rangle^{dev}$, and $\langle u'v' \rangle$ are observed. Regarding the flow behavior, we notice that the peaks of the correlations are bigger on the cold side than on the hot side, despite a higher friction velocity value contributing to the denominator of the dimensionless numbers. This can be due to the reduced local friction Reynolds number on the hot side, also seen in Boutrouche *et al.* [216], Bellec *et al.* [196], and Yahya *et al.* [197]. The three diagonal components of the Reynolds shear stress tensor show a peak around $y^+ = 15$ indicating that the dynamics of the near-wall turbulence is controlled by turbulence structures

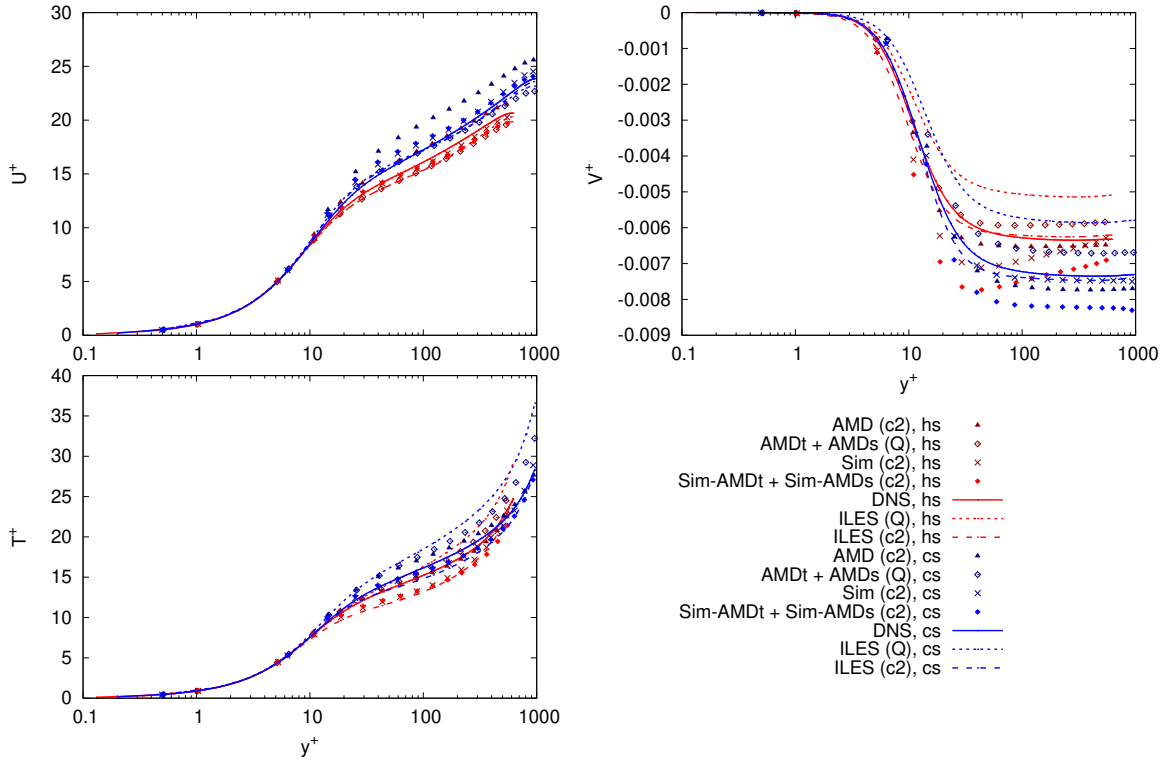

Figure 4.6 – Profiles of dimensionless longitudinal velocity, wall-normal velocity and temperature along the wall-normal direction of the channel.

present is this region. On the hot side, the peak is slightly shifted toward the wall. The T-LES models tend to overestimate the $\langle u'u' \rangle^{dev}$, $\langle v'v' \rangle^{dev}$, and $\langle w'w' \rangle^{dev}$ peaks at both sides of the channel. This tendency is also observed by Dupuy *et al.* [145]. The tensorial model produces very good estimation of the velocity covariances on the hot side. The scale similarity model gives the worst approximation, probably because its poorly dissipative behavior induces an overestimation of turbulence levels. Indeed, the scale-similarity model does not take into account the smallest unresolved scales where the most dissipation of turbulent subgrid-scale energy takes place. This lack of dissipation should be responsible for the exaggerated fluctuations of velocities predicted by the scale-similarity model. The cross-correlation $\langle u'v' \rangle$ is well captured by all T-LES.

Fig. 4.9 depicts the correlation of longitudinal velocity and temperature, the correlation of wall-normal velocity and temperature, and the covariance of temperature. The $\langle u'\theta' \rangle$ correlation exhibits peaks around $y^+ = 15$. Once again, the cold side presents a bigger peak than the hot side. These high values of $\langle u'\theta' \rangle$ are due to the streaks encountered in the buffer layer. Apart from the tensorial model, all T-LES overestimate the peaks. This overestimation is moderate on the hot side but substantial on the cold side. Concerning the "AMDt + AMDs (Q)" model, it underestimates the peaks. The tensorial formulation must be responsible for these encouraging results of the turbulent streamwise heat flux. The better results of the models on the hot side are probably due to a finer dimensionless cell size which improves the prediction of near-wall behaviors. The propagated errors from the viscous sublayer to the buffer layer are then lower on the hot side. The $\langle v'\theta' \rangle$ correlation is displayed. The profile is characterized by a strong

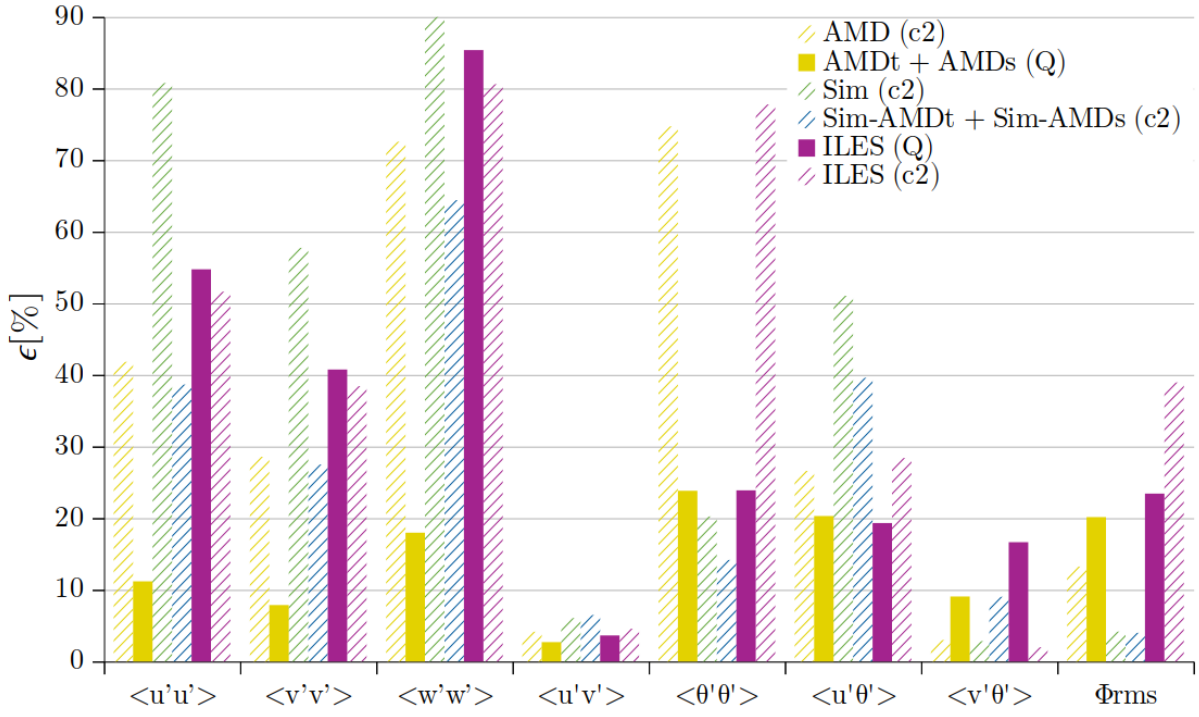

Figure 4.7 – Relative error on covariances for selected T-LES approaches. Yellow, green, and blue colors respectively stand for functional, structural, and mixed models. Full bars represent the simulations performed with the Quick scheme for the discretization of the mass convection whereas hatched bars are for T-LES using the second-order centered scheme.

increase of the correlation in absolute value in the range $y^+ \in [4; 20]$, as observed for the wall-normal velocity profile. T-LES estimations are good. The $\langle v'\theta' \rangle$ DNS profile is particularly well approximated on the hot side. It is probably due to the finer relative mesh size when compared to as the cold side. On the cold side, the "AMD (c2)" and "AMDt + AMDs (Q)" approaches give the best results. We observe that the fluctuations of temperature are constituted of three peaks. The biggest fluctuations are reached in the centerline because of packets of hot and cold fluid that come from the walls and collect near the centerline, as observed by Johansson and Wikström [217]. The two secondary peaks are located at $y^+ = 15$. Regarding the LES models, the best approximation of the dimensionless covariance of temperature is obtained with the "AMDt + AMDs (Q)" model. Indeed, this approach provides a very accurate estimation of the dimensionless covariance temperature profile. The scalar AMD, specifically devised to model the density-velocity correlation and consistent with the exact subfilter stress tensor on anisotropic grids, is probably responsible for these good results.

Instantaneous fields Instantaneous fields are helpful to analyze fluid behavior. It is also a good means to assess the effects of LES subgrid-scale models and numerical schemes.

Firstly, the probability density of normalized heat flux are presented in Fig. 4.10. The dimensionless conductive wall heat flux is computed using Eq. 4.33.

$$\phi^* = \frac{\phi - \phi_{mean}}{\phi_{plot,max} - \phi_{mean}} \tag{4.33}$$

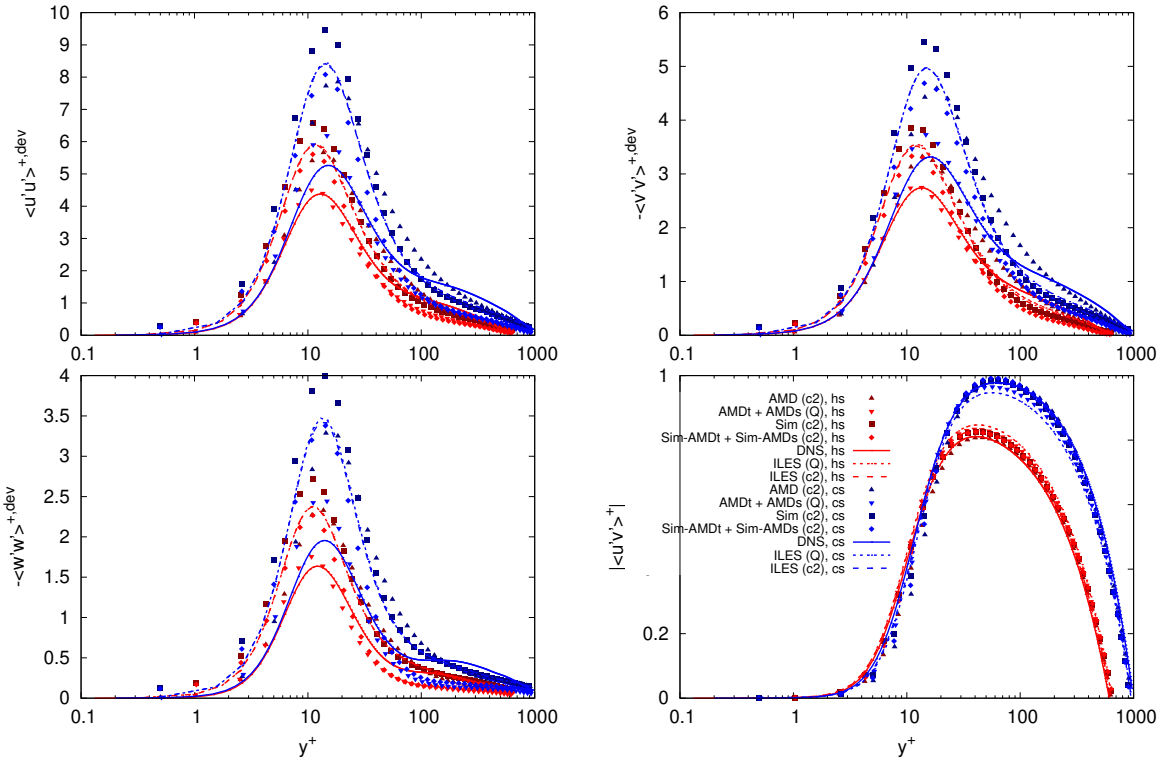

Figure 4.8 – Profiles of dimensionless covariances of longitudinal velocity, wall-normal velocity, transversal velocity as well as longitudinal and wall-normal velocities along the wall-normal direction of the channel. Note that the absolute value of the $\langle u'v' \rangle^+$ is plotted.

Where $\phi_{plot,max} = 260\ kW/m^2$ is the biggest considered value of heat flux for plots of instantaneous wall heat flux in Fig. 4.11. For each density probability of each model, six instantaneous fields of wall heat flux have been averaged in order to obtain smooth curves. Since the density probability observed at hot and cold walls are similar, data of both hot and cold side have been used. For all simulations, the maximum probability is reached for a normalized heat flux slightly lower than the mean heat flux. The peak location of the "AMD (c2)" and "ILES (c2)" simulation is similar to that of DNS. For the other simulations, the maximum is reached for values closer to the mean heat flux. The magnitude of T-LES heat flux density probability is bigger than the results of DNS and the peak is thinner than that of DNS. It traduces the underestimation of the heat flux fluctuations. The "AMD (c2)" simulation provides good results in spite of its slight overestimation of the maximum.

The instantaneous fields of hot and cold wall heat fluxes are displayed in Fig. 4.11. From top to bottom, the simulations "DNS", "ILES (c2)", "ILES (Q)", "AMD (c2)", and "AMDt + AMDs (Q)" are presented. "Sim (c2)" and "Sim-AMDt+Sim-AMDs (c2)" are not displayed because they are respectively similar to "AMDt + AMDs (Q)" and "ILES (Q)". The pseudocolor maps of DNS are covered by small red stains representing high heat fluxes. Those high values are due to high-frequency turbulent structures which increase the wall-normal convection and bring fluid masses at low temperatures close to the wall. The fluid behavior induces better heat transfer in those regions. The DNS maximum wall heat flux ($637\ kW/m^2$) is more than six

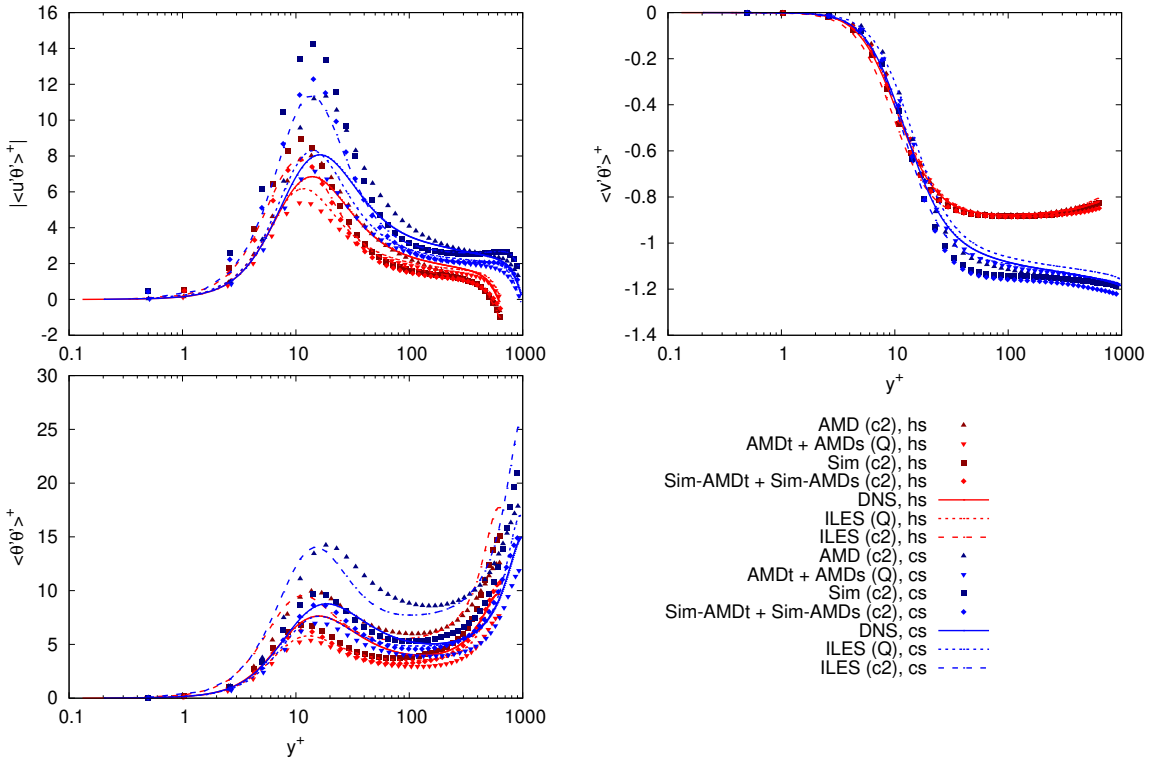

Figure 4.9 – Profiles of dimensionless correlations of longitudinal velocity and temperature, wall-normal velocity and temperature as well as the covariance of temperature along the wall-normal direction of the channel. Note that the absolute value of the $\langle u'\theta' \rangle^+$ is plotted.

times bigger than the mean heat flux (97 kW/m^2). Blue zones, traducing very low heat transfer, appear to be linked to long structures oriented toward the streamwise direction. These stains may reveal the presence of streaks above the viscous sublayer of the involved regions. The T-LES patterns of heat fluxes show the same behaviors: small regions of high flux and long zones of low flux oriented toward the streamwise direction. Simulations performed with the Quick scheme tend to underestimate the mean heat flux and the fluctuations. Simulations performed with the second-order centered scheme produce results similar to DNS. However, when the Quick scheme is used, high values of heat flux are truncated. The "AMDt + AMDs" model counterbalance somewhat this behavior but its effect is not enough impactful.

4.2.6 Conclusion

In this paper, LES turbulence models and implicit T-LES are compared to DNS results. A Quick and a second-order centered schemes are tested for the discretization of the mass convection term. Firstly, 22 T-LES approaches are assessed on mean quantities and correlations. Six of them are selected for a more accurate analysis. A comparison of these T-LES is performed for each mean quantity and each correlation by integrating the error committed by simulations. We also evaluate the conductive heat flux fluctuations at walls. Moreover, the mean quantities and correlations are plotted as functions of wall-normal distance. Lastly, instantaneous fields of selected T-LES approaches are investigated.

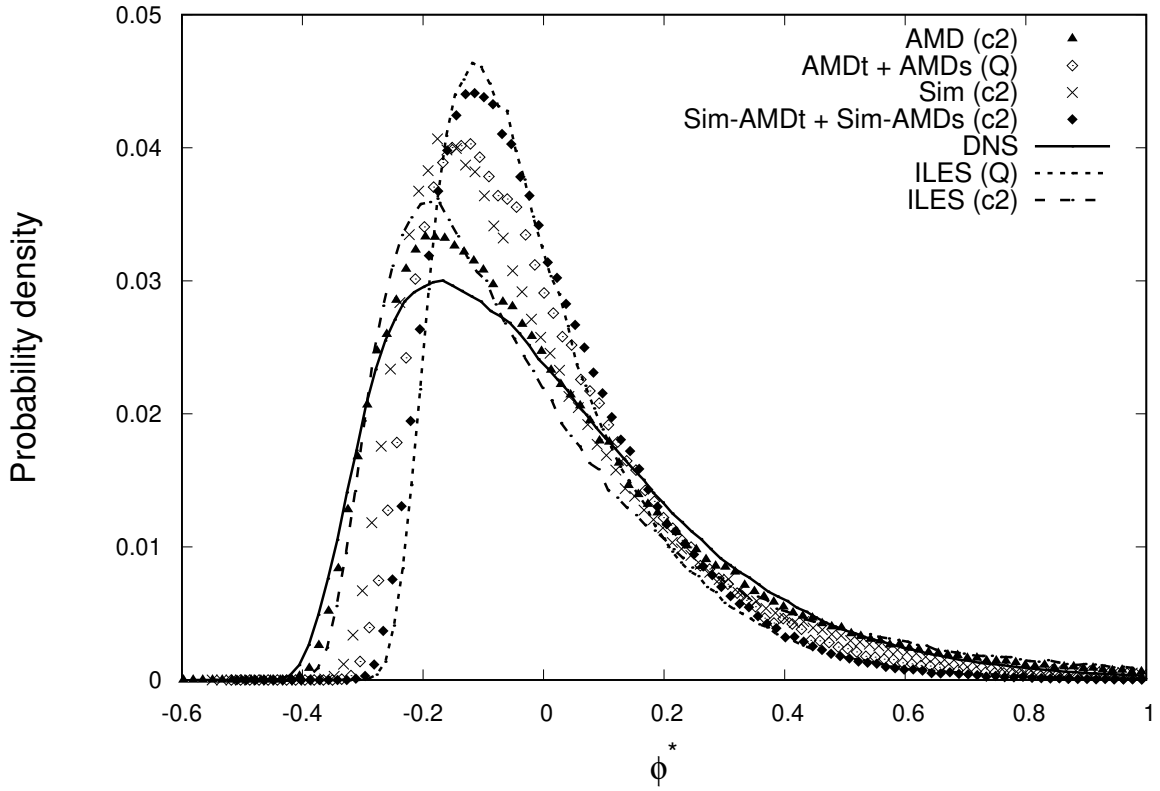

Figure 4.10 – Probability density of normalized heat flux.

The results indicate that, considering the numerical setup used, the ILES involving the second-order centered scheme contests the best T-LES models studied in this paper on mean quantities. However, the investigation of covariance, rms heat flux, and instantaneous fields highlights the limits of the ILES performed in this study.

As expected, the comparison of the Quick scheme and the second-order centered scheme for the discretization of the mass convection term points out that the streamwise velocity and the Reynolds shear stresses are not significantly influenced by the choice of the numerical scheme. Nevertheless, the numerical scheme effect is substantial on the wall-normal velocity, the conductive wall heat-flux, and the correlations involving the temperature. The T-LES performed with the Quick scheme tends to underestimate the conductive wall heat flux. The second-order centered scheme permits to significantly improve the results on this quantity. This scheme improves the results on the wall-normal velocity as well as the correlation of wall-normal velocity and temperature but it does not impact the wall-normal velocity variances and covariances with streamwise velocity and deteriorates the temperature correlation. This partial improvement suggests that the second order-centered scheme modifies the turbulent structures obtained with DNS simulation. Considering the mean heat flux and the density probability, the best agreement is found with the AMD model combined to the centered scheme.

The T-LES combining the tensorial AMD model to compute the momentum convection and the scalar AMD for the density-velocity correlation, and involving the Quick scheme provides a satisfying estimation of mean quantities and very good results on the classical "+" scaling of

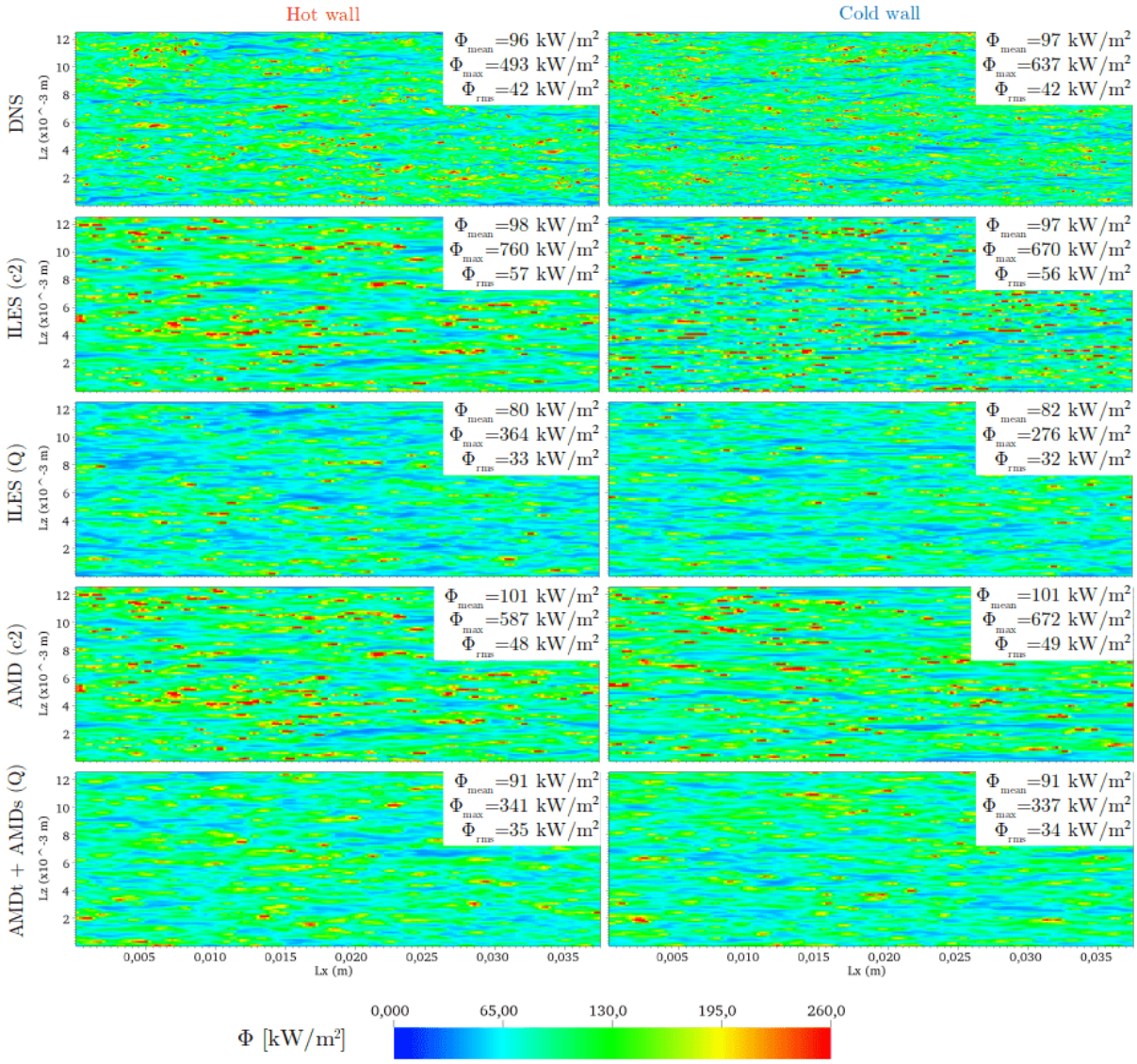

Figure 4.11 – Instantaneous fields of hot and cold wall heat fluxes. Pictures on the left (respectively right) side correspond to the hot (respectively cold) wall.

correlations. The superiority of this T-LES approach is particularly salient on the covariances of velocities. This result indicates that the tensorial AMD model is able to take into account the anisotropy of the flow.

The studied mixed models provide encouraging results. However, the results obtained show that those models require further investigation in order to benefit of the advantages of the functional and structural methods.

Acknowledgments

The authors gratefully acknowledge the CEA for the development of the TRUST platform. This work was granted access to the HPC resources of CINES under the allocation 2019-A0062A05099 and 2020-A0082A05099 made by GENCI. The authors also acknowledge the Occitania region for

their funding of the thesis grant.

Data Availability Statements

The data that support the findings of this study are available from the corresponding author upon reasonable request.

References

[2] S. Paolucci. "Filtering of Sound from the Navier-Stokes Equations." In: *NASA STI/Recon Technical Report N* 83 (1982).

[3] C. Calvin, O. Cueto, and P. Emonot. "An object-oriented approach to the design of fluid mechanics software". In: *ESAIM: Mathematical Modelling and Numerical Analysis - Modélisation Mathématique et Analyse Numérique* 36.5 (2002), pp. 907–921.

[4] F. Nicoud. "Conservative High-Order Finite-Difference Schemes for Low-Mach Number Flows". In: *Journal of Computational Physics* 158.1 (2000), pp. 71–97.

[10] S. Hoyas and J. Jiménez. "Reynolds Number Effects on the Reynolds-Stress Budgets in Turbulent Channels". In: *Physics of Fluids* 20.10 (2008), p. 101511.

[11] G. S. Winckelmans, H. Jeanmart, and D. Carati. "On the Comparison of Turbulence Intensities from Large-Eddy Simulation with Those from Experiment or Direct Numerical Simulation". In: *Physics of Fluids* 14.5 (2002), pp. 1809–1811.

[12] L. B. Streher et al. "Mixed Modeling for Large-Eddy Simulation: The Single-Layer and Two-Layer Minimum-Dissipation-Bardina Models". In: *AIP Advances* 11.1 (2021), p. 015002.

[13] W. Rozema et al. "Minimum-Dissipation Models for Large-Eddy Simulation". In: *Physics of Fluids* 27.8 (2015), p. 085107.

[14] F. Nicoud and F. Ducros. "Subgrid-Scale Stress Modelling Based on the Square of the Velocity Gradient Tensor". In: *Flow, Turbulence and Combustion* 62.3 (1999), pp. 183–200.

[15] A. Leonard. "Energy Cascade in Large-Eddy Simulations of Turbulent Fluid Flows". In: *Advances in Geophysics*. Ed. by F. N. Frenkiel and R. E. Munn. Vol. 18. Turbulent Diffusion in Environmental Pollution. Elsevier, 1975, pp. 237–248.

[16] J. Bardina, J. Ferziger, and W. Reynolds. "Improved Subgrid-Scale Models for Large-Eddy Simulation". In: *13th Fluid and PlasmaDynamics Conference*. Fluid Dynamics and Co-Located Conferences. American Institute of Aeronautics and Astronautics, 1980.

[17] D. Dupuy, A. Toutant, and F. Bataille. "A Posteriori Tests of Subgrid-Scale Models in an Isothermal Turbulent Channel Flow". In: *Physics of Fluids* 31.4 (2019), p. 045105.

[22] M. Abkar, H. J. Bae, and P. Moin. "Minimum-Dissipation Scalar Transport Model for Large-Eddy Simulation of Turbulent Flows". In: *Physical Review Fluids* 1.4 (2016), p. 041701.

[27] M. David, A. Toutant, and F. Bataille. "Numerical Development of Heat Transfer Correlation in Asymmetrically Heated Turbulent Channel Flow". In: *International Journal of Heat and Mass Transfer* 164 (2021), p. 120599.

[53] S. Singh, D. You, and S. T. Bose. "Large-Eddy Simulation of Turbulent Channel Flow Using Explicit Filtering and Dynamic Mixed Models". In: *Physics of Fluids* 24.8 (2012), p. 085105.

[69] W. Sutherland. "The Viscosity of Gases and Molecular Force". In: *The London, Edinburgh, and Dublin Philosophical Magazine and Journal of Science* 36.223 (1893), pp. 507–531.

[84] B. Vreman, B. Geurts, and H. Kuerten. "Comparison of Numerical Schemes in Large-Eddy Simulation of the Temporal Mixing Layer". In: *International journal for numerical methods in fluids* 22.4 (1996), pp. 297–312.

[103] U. Piomelli, G. N. Coleman, and J. Kim. "On the Effects of Nonequilibrium on the Subgrid-Scale Stresses". In: *Physics of Fluids* 9.9 (1997), pp. 2740–2748.

[131] M. H. Silvis, R. A. Remmerswaal, and R. Verstappen. "Physical Consistency of Subgrid-Scale Models for Large-Eddy Simulation of Incompressible Turbulent Flows". In: *Physics of Fluids* 29.1 (2017), p. 015105.

[142] M. Germano et al. "A Dynamic Subgrid-scale Eddy Viscosity Model". In: *Physics of Fluids A: Fluid Dynamics* 3.7 (1991), pp. 1760–1765.

[145] D. Dupuy, A. Toutant, and F. Bataille. "A Posteriori Tests of Subgrid-Scale Models in Strongly Anisothermal Turbulent Flows". In: *Physics of Fluids* 31.6 (2019), p. 065113.

[150] F. Nicoud et al. "Using Singular Values to Build a Subgrid-Scale Model for Large Eddy Simulations". In: *Physics of Fluids* 23.8 (2011), p. 085106.

[160] D. Dupuy, A. Toutant, and F. Bataille. "A Priori Tests of Subgrid-Scale Models in an Anisothermal Turbulent Channel Flow at Low Mach Number". In: *International Journal of Thermal Sciences* 145 (2019), p. 105999.

[171] S. Rezaeiravesh and M. Liefvendahl. "Effect of Grid Resolution on Large Eddy Simulation of Wall-Bounded Turbulence". In: *Physics of Fluids* 30 (2018).

[175] F. Kremer and C. Bogey. "Large-Eddy Simulation of Turbulent Channel Flow Using Relaxation Filtering: Resolution Requirement and Reynolds Number Effects". In: *Computers and Fluids* 116 (2015), pp. 17–28.

[176] M. O. Deville and T. B. Gatski. *Mathematical Modeling for Complex Fluids and Flows*. Berlin, Heidelberg: Springer Berlin Heidelberg, 2012. ISBN: 978-3-642-25294-5 978-3-642-25295-2.

[185] J. .-.-B. Chapelier and G. Lodato. "A Spectral-Element Dynamic Model for the Large-Eddy Simulation of Turbulent Flows". In: *Journal of Computational Physics* 321 (2016), pp. 279–302.

[186] M. Terracol, P. Sagaut, and C. Basdevant. "A Time Self-Adaptive Multilevel Algorithm for Large-Eddy Simulation". In: *J. Comput. Phys.* 184.2 (2003), pp. 339–365.

[187] Y. M. Lee et al. "Assessment of Two-Parameter Mixed Models for Large Eddy Simulations of Transitional and Turbulent Flows". In: *Journal of Mechanical Science and Technology* 34.2 (2020), pp. 727–743.

[188] S. Serra, A. Toutant, and F. Bataille. "Thermal Large Eddy Simulation in a Very Simplified Geometry of a Solar Receiver". In: *Heat Transfer Engineering* 33.6 (2012), pp. 505–524.

[189] C. Brun et al. "Large Eddy Simulation of Compressible Channel Flow". In: *Theoretical and Computational Fluid Dynamics* 22.3 (2008), pp. 189–212.

[190] L. D. Dailey, N. Meng, and R. H. Pletcher. "Large Eddy Simulation of Constant Heat Flux Turbulent Channel Flow With Property Variations: Quasi-Developed Model and Mean Flow Results". In: *Journal of Heat Transfer* 125.1 (2003), pp. 27–38.

[191] E. Lenormand, P. Sagaut, and L. T. Phuoc. "Large eddy simulation of subsonic and supersonic channel flow at moderate Reynolds number". In: *International Journal for Numerical Methods in Fluids* 32.4 (2000), pp. 369–406.

[192] S. Hickel and N. A. Adams. "On Implicit Subgrid-Scale Modeling in Wall-Bounded Flows". In: *Physics of Fluids* 19.10 (2007), p. 105106.

[193] W.-P. Wang and R. H. Pletcher. "On the Large Eddy Simulation of a Turbulent Channel Flow with Significant Heat Transfer". In: *Physics of Fluids* 8.12 (1996), pp. 3354–3366.

[194] P. Moin et al. "A Dynamic Subgrid-scale Model for Compressible Turbulence and Scalar Transport". In: *Physics of Fluids A: Fluid Dynamics* 3.11 (1991), pp. 2746–2757.

[195] B. Lessani and M. V. Papalexandris. "Numerical Study of Turbulent Channel Flow with Strong Temperature Gradients". In: *International Journal of Numerical Methods for Heat & Fluid Flow* 18.3/4 (2008). Ed. by A. J. Nowak and R. A. Białecki, pp. 545–556.

[196] M. Bellec, A. Toutant, and G. Olalde. "Large Eddy Simulations of Thermal Boundary Layer Developments in a Turbulent Channel Flow under Asymmetrical Heating". In: *Computers & Fluids*. A Special Issue in Honor of Cecil "Chuck" E. Leith 151 (2017), pp. 159–176.

[197] S. M. Yahya, S. F. Anwer, and S. Sanghi. "Turbulent Forced Convective Flow in an Anisothermal Channel". In: *International Journal of Thermal Sciences* 88 (2015), pp. 84–95.

[198] S. Serra et al. "Asymmetric Reverse Transition Phenomenon in Internal Turbulent Channel Flows Due to Temperature Gradients". In: *International Journal of Thermal Sciences* 159 (2021), p. 106463.

[199] C. Meneveau and J. Katz. "Scale-Invariance and Turbulence Models for Large-Eddy Simulation". In: *Annual Review of Fluid Mechanics* 32.1 (2000), pp. 1–32.

[200] B. Kosović, D. I. Pullin, and R. Samtaney. "Subgrid-Scale Modeling for Large-Eddy Simulations of Compressible Turbulence". In: *Physics of Fluids* 14.4 (2002), pp. 1511–1522.

[201] S. Hickel, N. A. Adams, and J. A. Domaradzki. "An Adaptive Local Deconvolution Method for Implicit LES". In: *J. Comput. Phys.* 213.1 (2006), pp. 413–436.

[202] S. Vashishtha et al. "Large Eddy Simulation of Hydrodynamic Turbulence Using Renormalized Viscosity". In: *Physics of Fluids* 31.6 (2019), p. 065102.

[203] K. Horiuti. "The Role of the Bardina Model in Large Eddy Simulation of Turbulent Channel Flow". In: *Physics of Fluids A: Fluid Dynamics* 1.2 (1989), pp. 426–428.

[204] S. Stolz, N. A. Adams, and L. Kleiser. "An Approximate Deconvolution Model for Large-Eddy Simulation with Application to Incompressible Wall-Bounded Flows". In: *Physics of Fluids* 13.4 (2001), pp. 997–1015.

[205] B. J. Geurts and F. van der Bos. "Numerically Induced High-Pass Dynamics in Large-Eddy Simulation". In: *Physics of Fluids* 17.12 (2005), p. 125103.

[206] A. Keating et al. "A Priori and a Posteriori Tests of Inflow Conditions for Large-Eddy Simulation". In: *Physics of Fluids* 16.12 (2004), pp. 4696–4712.

[207] M. V. Papalexandris. "On the Applicability of Stokes' Hypothesis to Low-Mach-Number Flows". In: *Continuum Mechanics and Thermodynamics* 32.4 (2020), pp. 1245–1249.

[208] P. Sagaut. *Large Eddy Simulation for Incompressible Flows*. 3ème. Springer, 1998.

[209] R. Akhavan et al. "Subgrid-Scale Interactions in a Numerically Simulated Planar Turbulent Jet and Implications for Modelling". In: *Journal of Fluid Mechanics* 408 (2000), pp. 83–120.

[210] C. Meneveau and J. Katz. "Conditional Subgrid Force and Dissipation in Locally Isotropic and Rapidly Strained Turbulence". In: *Physics of Fluids* 11.8 (1999), pp. 2317–2329.

[211] J. M. Avellaneda, F. Bataille, and A. Toutant. "DNS of Turbulent Low Mach Channel Flow under Asymmetric High Temperature Gradient: Effect of Thermal Boundary Condition on Turbulence Statistics". In: *International Journal of Heat and Fluid Flow* 77 (2019), pp. 40–47.

[212] S. K. Lele. "Compact Finite Difference Schemes with Spectral-like Resolution". In: *Journal of Computational Physics* 103.1 (1992), pp. 16–42.

[213] A. Toutant. "Numerical Simulations of Unsteady Viscous Incompressible Flows Using General Pressure Equation". In: *Journal of Computational Physics* 374 (2018), pp. 822–842.

[214] F. Aulery et al. "Spectral Analysis of Turbulence in Anisothermal Channel Flows". In: *Computers & Fluids*. A Special Issue in Honor of Cecil "Chuck" E. Leith 151 (2017), pp. 115–131.

[215] J. A. Domaradzki and N. A. Adams. "Direct Modelling of Subgrid Scales of Turbulence in Large Eddy Simulations". In: *Journal of Turbulence* 3 (2002), N24.

[216] V. Boutrouche et al. "Influence of the Turbulence Model for Channel Flows with Strong Transverse Temperature Gradients". In: *International Journal of Heat and Fluid Flow* 70 (2018), pp. 79–103.

[217] A. V. Johansson and P. M. Wikström. "DNS and Modelling of Passive Scalar Transport in Turbulent Channel Flow with a Focus on Scalar Dissipation Rate Modelling". In: *Flow, Turbulence and Combustion* 63.1 (2000), p. 223.

4.3 Paper 2: Thermal Large-Eddy Simulations of a turbulent channel flow asymmetrically heated from both walls

The conditions studied in section 4.2 correspond to those of an infinitely long solar receiver that permits reaching a thermal establishing of the temperature profile. It results from this configuration that the mean fluid temperature is almost equal to the average of the wall temperatures. However, in practice, the mean fluid temperature never exceeds the cold wall temperature. In section 4.3, the studied conditions are representative of those obtained in a real gas-pressurized solar receiver. The mean fluid temperature is chosen to be slightly below the cold wall temperature, corresponding to an axial location near the outlet of the absorber. These new conditions induce asymmetric wall temperature gradients and modify the flow behavior. The LES subgrid-scale

models are investigated in these very complex conditions. The following section aims to analyze the flow behavior and to assess the reliability of the models in these new working conditions.

This section reproduces the paper of M. David, A. Toutant, and F. Bataille untitled thermal Large-Eddy Simulations of a turbulent channel flow asymmetrically heated from both walls submitted to strong asymmetric heating and published in *Physics of Fluids*.

Abstract

Thermal Large-Eddy Simulations (T-LES) and a Direct Numerical Simulation (DNS) are carried out in a bi-periodical channel with hot and cold wall temperatures of respectively 900 K and 1300 K. The mean fluid temperature is lowered below the cold wall temperature thanks to a heat source, resulting in a both walls heating of the fluid. The hot and cold wall friction Reynolds numbers are respectively 640 and 1000. These conditions are representative of the working conditions of gas-pressurized solar receiver of solar power tower. The Low Mach number Navier-Stokes equations are solved. The coupling between the dynamic and the temperature effects is considered. In the T-LES, both the momentum convection and the density-velocity correlation subgrid terms are modeled. Functional models, structural models, and mixed models are considered. A tensorial version of the Anisotropic Minimum-Dissipation (AMD) model is also investigated. The Quick and the second-order centered schemes are tested for the discretization of the mass convection term. Firstly, an overview of the results of 17 T-LES on first- and second-order statistics is proposed. It permits selecting 6 of these simulations for a detailed analysis consisting in the investigation of profiles of mean quantities and turbulent correlations. A particular attention is given to the wall heat fluxes because it is a critical point for the design and the optimization of solar receivers. Overall, the first-order statistics are better predicted than the second-order's. The tensorial AMD model takes advantage of the classical AMD model properties and better reproduces the anisotropy of the flow thanks to its formulation. The tensorial AMD model produces the most reliable and efficient results among the considered models.

4.3.1 Introduction

This paper addresses the low Mach-number Thermal Large-Eddy Simulation (T-LES) of strongly anisothermal turbulent channel flows heated from both sides. The studied conditions are commonly encountered in many industrial processes such as heat exchangers, nuclear reactors [218, 219], thermal solar systems [220, 188, 56]. Particularly, in the field of concentrated solar power, the solar receiver is a key component. It aims to convert solar radiation into heat of the transfer fluid. Solar receivers are characterized by an intense turbulence and a strong asymmetric heating of the fluid. The academic channel geometry is well adapted to reproduce these characteristics and has been selected. Several studies are conducted to optimize it [221, 222]. To this end, it is necessary to (1) deepen our understanding of the kind of flow and (2) provide reliable means to test proposed optimizations. With the increase of computing capacity, simulations have emerged to play a major role in the research of wall-bounded turbulence. In 1987, Kim *et al.* [223] were among the first authors to provide reliable turbulence statistics in fully developed channel flows. A large number of studies dealing with isothermal turbulent flows at mean Reynolds numbers inferior or equal to 395 have been carried out since then [17, 224, 225]. Direct numerical simulations of highly turbulent channel flow are more recent [7, 226, 227, 10, 9]. Simulation of anisothermal turbulent channel flows are even newer. Kawamura [228] performed DNS of turbulent heat transfer in channel flow with respect to Reynolds and Prandtl number effects. The temperature was,

however, a passive scalar. Few studies take into account the coupling between turbulence and temperature. For instance, Dupuy *et al.* [160, 145] and Aulery *et al.* [214] investigated channel flows at friction Reynolds numbers of 180 and 395. Recently, David *et al.* [229] performed a DNS of an anisothermal channel flow at a friction Reynolds of 970. In these studies, the fluid temperature was close to the average of the wall temperatures, meaning that the fluid was heated by one wall and cooled by the other. In most industrial applications, the fluid is heated on both sides. For these reasons, in this study we carry out a DNS at a friction Reynolds of 1000 with a mean fluid temperature lower than the wall temperature. This simulation is representative of the working conditions encountered in gas-pressurized solar receivers of solar power towers and in many systems involving heat exchangers.

Currently, the computational cost of the DNS renders the simulation of turbulent flow associated with complex geometries unfeasible. The LES is a family of methods aiming to obtain a low-cost three-dimensional unsteady simulation of a turbulent flow. The reader is referred to Ref. [230] for a quick overview of its history and a review of its current state. In LES, large scales are explicitly resolved, while small scales, more computationally expensive to resolve, are accounted for by their modeled influences on larger turbulent structures. Generally, the scale separation is performed with implicit filtering meaning that, the grid is the LES low-pass filter. Subgrid-scale models must be used to close the governing equations of the filtered fields. They should follow physical and numerical constraints relying on the idea that subgrid-scale models have to be consistent with important mathematical and physical properties of the Navier-Stokes equations and the turbulent stresses. The subgrid model should conserve the basic properties of the Navier-Stokes equations, induce the same type of effect as the modeled term, and allow the flow driving mechanisms. It should also vanish if there is no subgrid-scale. Among the numerical constraints, the subgrid-scale model should not alter the stability of the simulation [208]. Silvis *et al.* [131] detail the symmetry requirements, the desired near-wall scaling behavior of the subgrid-scale stresses, the realizability constraints, and requirements on the production of subgrid-scale kinetic energy. They show that certain model constraints are not compatible with each other.

On a classical LES grid, the balance between convective transport and diffusive dissipation, which is the driving force of turbulence, is deteriorated. The success of a turbulence model depends on its ability to capture and compensate this imbalance. Zero-equation models assume that the small scales are universal and can be computed with the resolved flow variables. The LES models are usually divided into two groups. (1) Functional models consist in reproducing the action of the small scales by introducing a subgrid viscosity that has a similar effect on the bigger turbulent scales. Functional approaches are specifically designed to reproduce the same effect as the exact term on the resolved physics. However, they often are over-dissipating since they do not model the backward of the energy cascade. Some of the most used functional models are given below. The Smagorinsky model [141] is probably the most known of the functional models since it is the first developed eddy-viscosity model. It is very simple to implement but significantly over-dissipative. Nonetheless, a large number of newer models rely on the Smagorinsky model basis. The Wall-Adapting Local Eddy-viscosity (WALE) model [231] is dedicated to complex geometries. It involves the square of the velocity gradient tensor to model the strain and the rotation rate of the smallest resolved turbulent fluctuations. The WALE model has been deeply analyzed by Kim *et al.* [232] in the canonical transitional boundary layer, producing good results. Nicoud *et al.* [150] propose the σ-model which is derived from the analysis of the singular values of the resolved velocity gradient tensor. It can be used in flows with non-homogeneous directions in space or time. The σ-model appears to be particularly efficient for wall-bounded flows. The

Anisotropic Minimum-Dissipation model (AMD) [13] takes advantage of the desirable practical and theoretical properties of the QR model [152] and is applicable on anisotropic grids. This model gives the minimum eddy dissipation required to dissipate the energy of sub-filter scales. It appropriately switches off in laminar and transitional flows and is consistent with the exact subfilter stress tensor on both isotropic and anisotropic grids. The AMD model gives good agreement with DNS in turbulent channel flows [17, 145, 229].

The Kobayashi model [233] relies on coherent structures for rotating homogeneous turbulence and turbulent channel flow. It gives similar results as the Smagorinsky results in the common LES test case but does not require to average or clip the model parameter, use an explicit wall-damping function, or modify the fixed parameter. Vreman [149] proposes a model that is characterized by a relatively small dissipation in transitional and near-wall regions that, as the Kobayashi model, does not involve averaging, or clipping procedures, explicit filtering, and is invariant by rotation for isotropic filter widths. Trias *et al.* [153] propose a general framework for eddy-viscosity models based on a 5D phase space of invariants. They build three invariants of the second-order tensor GG^T, where G is the gradient tensor, and use them to derive the S3PQR model. A model based on the second-order volumetric strain-stretching (VSS) tensor is proposed by Ryu and Iaccarino [151]. It is tested in freely decaying isotropic turbulence, incompressible turbulent channel flow, and compressible turbulent channel flows. Studying LES of incompressible flows, Silvis *et al.* [131] express a model based on the vortex stretching magnitude which respects all the properties listed in its paper except the nonzero subgrid dissipation for non-laminar flow types and the sufficient subgrid dissipation for scale separation. The structure-function model [234] relies on a kinetic energy spectrum local in space, calculated thanks to a local second-order velocity structure-function, to compute the spectral eddy-viscosity. This model is a generalization of the spectral eddy-viscosity to highly intermittent situations in physical space. Tensorial subgrid viscosities are formulated to deal with anisotropic turbulence. The spectral model proposed by Aupoix [235] includes all the coupling mechanisms between large and small scales. Pressure and transfer effects are defined as integrals over the subgrid scales. However, it induces high computational costs. Horuiti [156] extends the Smagorinsky model to the anisotropic case. The third-order terms in an anisotropic representation model of the Reynolds stresses are used to determine the eddy-viscosity velocity scale. Dupuy *et al.* [17] propose various tensorial viscosity computed with the AMD model. The $H^{(4)}$ version tested in Refs. [160, 17, 145, 229] produces encouraging results. (2) Structural models aim at approximating the subgrid tensor by constructing it from an evaluation of the filtered velocity or a formal series expansion [208]. The advantage of starting from the exact unclosed expression of the term to model is that the resulting closure often shares a similar structure with the exact term. They do not suppose that the small structures always drain energy from the large scales, and they can predict the exact subgrid-scale terms more accurately than eddy-viscosity models. Hence, they could enhance the capture of anisotropic effects and the prediction of energy transfer and disequilibrium. Drawbacks of structural models are generally a poor prediction of the dissipation and their inclination to be unstable [208]. The reader is referred to the review of structural models proposed by Lu and Rutland [236].

Mixed modeling relies on the linear combination of the functional and structural approaches. It aims to take advantage of the generally good estimation of the energy transfer between the resolved and the subgrid scales of the functional models and to benefit from the accurate prediction of the subgrid tensor obtained with structural models. Mixed models show encouraging results in various tests Refs. [157, 156, 237, 238, 239, 114]. Streher *et al.* [12] propose a two-layer mixed model for the LES of isothermal channel flow: the near-wall region is parameterized with

the combination of the AMD and the scale similarity model [16], whereas the outer region is computed with the scale similarity model only. The obtained results are in very good agreement with the DNS of Moser *et al.* [7] and Hoyas and Jiménez [10].

In anisothermal flows, the temperature variations impact the turbulence and *vice-versa* which renders the simulation of such flows more complicated [193, 190, 195, 240, 197]. The asymmetric heating of the flow induces specific turbulent structures on both sides of the channel. The high heat fluxes are linked to high-frequency turbulent scales and strong wall-normal velocities. In those conditions, the density-velocity correlation term is not negligible anymore and requires to be modeled in addition to the velocity-velocity correlation term classically modeled [160]. The modeling of the subgrid-scale heat flux in LES for turbulent thermal flows has often been based on the hypothesis of Eidson [241] which assumes that the energy transfer from the resolved scales to the subgrid scales is proportional to the gradient of resolved temperature. The subgrid-scale thermal diffusivity is traditionally represented based on the Reynolds analogy and the concept of turbulent Prandtl number. Rasam *et al.* [242] propose an explicit algebraic subgrid scalar flux model based on the modeled transport equation of the subgrid-scale scalar flux. It is strongly dependent on the accuracy of the subgrid-scale stress prediction. The obtained turbulent scalar flux is not necessarily aligned with the resolved scalar gradient. Furthermore, the inherent dependence on the resolved rotation-rate tensor renders the model suitable for LES of rotating flow applications. Wang *et al.* [243, 244, 245] develop a series of models which includes the resolved strain-rate tensor, the rotation rate tensor, and the temperature gradient. Contrary to the classical dynamic eddy thermal diffusivity subgrid-scale heat flux model, the three new models proposed in this study admit more degrees of freedom and consequently provide a more realistic geometrical and physical representation of the subgrid-scale heat flux vector. Peng and Davidson [246] propose a model that accounts for the subgrid-scale heat flux in terms of the large-scale strain rate and the temperature gradient in all directions, which is equivalent to using a tensor diffusivity. The proposed model formulates the subgrid-scale heat flux. Hence, it allows the large-scale thermal gradient in other directions to modify the subgrid-scale heat flux in the direction with no statistical temperature gradient. The minimum-dissipation scalar transport model is an extension of the AMD model proposed by Rozema [13]. This model is successfully tested in a thermally stratified atmospheric boundary layer flows by Abkar and Moin [22]. Particularly, it accurately estimates the expected surface-layer similarity profiles and power spectra for both velocity and scalar concentration. Ries *et al.* [247] suggest a wall-adapted anisotropic heat flux model. It is designed for complex turbulent thermal flow. The model accounts for variable fluid properties and anisotropic effects in the unresolved temperature scales; does not require *ad-hoc* treatments or dynamic procedure to obtain the correct near-wall behavior; its formulation is consistent with the second law of thermodynamics.

This study follows up on a previous paper focused on anisothermal turbulent channel flow heated from one side and cooled from the other [229]. The results are extended regarding the new working conditions inducing a stronger wall heat flux on the hot side and an opposed direction of the heat transfer at the cold wall. The objective of this work is twofold: provide reference data of a turbulent channel flow strongly and asymmetrically heated from both sides and assess a large number of LES models in those conditions thanks to *a posteriori* tests.

The organization of this paper is as follows: Sec. 4.3.2 describes the resolved equations. The investigated subgrid-scale models are detailed in Sec. 4.3.3. The channel flow configuration and the numerical method are presented in Sec. 4.3.4. In Sec. 4.3.5, the results of the present DNS are compared with those of the DNS performed at similar friction Reynolds numbers but different thermal conditions by David *et al.* [229]. Then, the Thermal Large-Eddy Simulations (T-LES)

are investigated: the global efficacy of the T-LES are presented and six of them are subjected to detailed analysis . A final section concludes.

4.3.2 Filtered low-Mach number equations

We consider the large-eddy simulation of the low Mach number equations in the Favre formulation as described in the work of David *et al.* [229]. The Favre formulation involves Favre-filtered variables, based on the density-weighted Favre filter ($\widetilde{\cdot}$). For any field ψ, the variables are expressed as $\widetilde{\psi} = \overline{\rho\psi}/\overline{\rho}$, where ($\overline{\cdot}$) is the unweighted classical filter. The two most significant subgrid terms highlighted by Dupuy *et al.* [160] are modeled: a subgrid term related to the velocity-velocity correlation and another modeling the density-velocity correlation. The Navier-Stokes are solved under the low-Mach number approximation, which admits large variations in gas density while remains acoustically incompressible [2]. This hypothesis, well adapted to the studied conditions, introduces two pressures: the mechanical pressure, which is the relative pressure and is variable in space, and the thermodynamical pressure, which is the reference static pressure and is homogeneous. In the used algorithm the mechanical pressure is computed from the constraint equation of the velocity divergence. The low-Mach number is assumed to be valid for Mach numbers below 0.3. In the studied configuration, the Mach number is 0.12. The resolution of the Navier-Stokes equations under the low-Mach number approximation permits to lower the computational cost of simulations by increasing the fractional time step when compared to the resolution of the compressible Navier-Stokes equations. In the simulations, the computation of the diffusion is explicit. The time step is computed at each iteration to respect the stability criterion. In the studied configuration, the diffusion time step is smaller than the convection time step. The LES and DNS diffusion time steps are close because the size of the first cell is similar in both simulations. Indeed, in the achieved LES the viscous sublayer is resolved. All the turbulence time scales are expected to be captured: the simulated time is about 0.1 s and the diffusion time step is about $3 \cdot 10^{-8}$ s, resulting in a ratio between the two quantities of $3 \cdot 10^{6}$. In this study, the Stokes' hypothesis is assumed. The reader is referred to Ref. [207] for precise explanations on the applicability of the Stokes' hypothesis to low Mach number flows. A source term is introduced in the energy equation to allow the study of different axial locations in a solar receiver by modifying the fluid temperature. The bigger the source term is, the lower the fluid temperature is, traducing a location closer to the inlet of a solar receiver. This source term is homogeneous all over the computational domain and constant in time. It has been set to 55 MW/m^3 to obtain a mean fluid temperature below but near the cold wall temperature which is representative of close to the outlet fluid temperature in gas-pressurized solar receivers. The low-Mach number Navier-Stokes equations are given below.

- Mass conservation equation:

$$\frac{\partial \overline{\rho}}{\partial t} + \frac{\partial \overline{\rho}\widetilde{U}_j}{\partial x_j} = 0, \tag{4.34}$$

- Momentum conservation equation:

$$\frac{\partial \overline{\rho}\widetilde{U}_i}{\partial t} = -\frac{(\partial \overline{\rho}\widetilde{U}_j\widetilde{U}_i + \overline{\rho}G_{U_jU_i})}{\partial x_j} - \frac{\partial \overline{P}}{\partial x_i} + \frac{\partial \Sigma_{ij}(\widetilde{\boldsymbol{U}}, \widetilde{T})}{\partial x_j}, \tag{4.35}$$

- Energy conservation equation:

$$\frac{\partial(\widetilde{U}_j + \overline{\rho}G_{Uj/\rho})}{\partial x_j} = -\frac{1}{\gamma P_0}\left[(\gamma - 1)\left(\frac{\partial Q_j(\widetilde{T})}{\partial x_j} - H_s\right) + \frac{\mathrm{d}P_0}{\mathrm{d}t}\right], \tag{4.36}$$

- Ideal gas law:

$$\widetilde{T} = \frac{P_0}{\overline{\rho} r}, \tag{4.37}$$

where ρ is the density, T is the temperature, $\gamma = 1.33$ is the heat capacity ratio of air at 1100 K, r is the ideal gas specific constant, t is the time, P is the mechanical pressure, P_0 the thermodynamical pressure, U_i is the ith component of velocity, $\mathrm{d}/\mathrm{d}t$ is the time derivative (total derivative since P_0 is homogeneous), and x_i is the Cartesian coordinate in the ith direction. $H_s = 55$ MW/m^3 is the source term. The volume of the studied channel is 2.8×10^{-6} m^3. The source term is chosen to represent a fluid temperature in the range of the experimental working conditions of a solar receiver. The obtained mean fluid temperature is below the cold wall temperature leading to fluid heated from both sides. The subgrid term relative to momentum convection is $G_{U_jU_i} = \widetilde{U_jU_i} - \widetilde{U}_j\widetilde{U}_i$ and the subgrid term relative to the density-velocity correlation is expressed as $G_{U_j/\rho} = \widetilde{U_j/\rho} - \widetilde{U}_j/\overline{\rho}$. This last term is beneficial for the prediction of temperature-related statistics [145]. The Einstein summation convention is used. The shear-stress tensor and conductive heat flux associated with a given velocity and temperature are computed with the functions $\Sigma_{ij}(\widetilde{\boldsymbol{U}}, \widetilde{T})$ and $Q_j(\widetilde{T})$. The particular form of the energy conservation equation, involving the velocity divergence, is obtained as follows. The ideal gas law is applied to the energy equation written in terms of transport of temperature. Then, the homogeneity property of the thermodynamical pressure is used. This formulation of the energy conservation equation is also used in Refs. [4, 145, 229]. The coupling between the thermodynamic pressure, the density, and the temperature are considered thanks to the ideal gas law. The thermodynamical pressure is obtained by integrating Eq. 4.36 over the volume of the computational domain:

$$\frac{\mathrm{d}P_0}{\mathrm{d}t} = -(\gamma - 1)\left(\frac{1}{V}\int Q_j(\widetilde{T})\mathrm{d}S_j - H_s\right) \tag{4.38}$$

where V is the volume of the computational domain and S_j are the boundaries of the computational domain.

Newtonian fluid and Fourier's law are assumed, leading to the following expressions:

$$\Sigma_{ij}(\widetilde{\boldsymbol{U}}, \widetilde{T}) = \mu(\widetilde{T})\left(\frac{\partial \widetilde{U}_i}{\partial x_j} + \frac{\partial \widetilde{U}_j}{\partial x_i}\right) - \frac{2}{3}\mu(\widetilde{T})\frac{\partial \widetilde{U}_k}{\partial x_k}\delta_{ij}, \tag{4.39}$$

$$Q_j(\widetilde{T}) = -\lambda(\widetilde{T})\frac{\partial \widetilde{T}}{\partial x_j}, \tag{4.40}$$

with $\mu(\widetilde{T})$ the dynamic viscosity, $\lambda(\widetilde{T})$ the thermal conductivity, and δ_{ij} the Kronecker symbol.

The fluid used is air. The viscosity is computed using the Sutherland's law [69]:

$$\mu(\widetilde{T}) = \mu_0 \frac{\widetilde{T}}{T_0}^{3/2} \frac{T_0 + S}{\widetilde{T} + S}, \tag{4.41}$$

where $\mu_0 = 1.716 \times 10^{-5}\ Pa \cdot s$, $S = 110.4$ K, and $T_0 = 273.15$ K. The Prandtl number is supposed to be constant, Pr$= 0.87$ and the heat capacity at constant pressure $C_p = 1155\ \mathrm{J \cdot kg^{-1} \cdot K^{-1}}$. The conductivity is deduced from the Prandtl number, the heat capacity at constant pressure, and the viscosity:

$$\lambda(\widetilde{T}) = \frac{C_p}{\mathrm{Pr}}\mu(\widetilde{T}). \tag{4.42}$$

4.3.3 Subgrid-scale modeling

In this section, each type of modeling is presented and the construction of the models is given. The models for the velocity-velocity correlation subgrid term and density-velocity correlation subgrid term are expressed as follows:

$$G_{U_jU_i} \approx \tau_{ij}^{mod}(\widetilde{\boldsymbol{U}}, \overline{\Delta}), \tag{4.43}$$

$$G_{U_j/\rho} \approx \pi_{j}^{mod}(\widetilde{\mathbf{U}}, 1/\overline{\rho}, \overline{\Delta}). \tag{4.44}$$

The subgrid-scale tensors, τ_{ij} and π_j, are computed thanks to variables resolved in T-LES. Each model has its proper expression of the subgrid-scale tensors. The considered models are detailed below. This includes functional models and structural models. Note that in the following of this article, the filter length scale is computed using the mesh size in the three directions $\overline{\Delta} = \left(\overline{\Delta}_x\overline{\Delta}_y\overline{\Delta}_z\right)^{1/3}$. Since no explicit filter is used, the filter length scale and the mesh size are combined.

4.3.3.1 Functional modeling

Functional models introduce an artificial subgrid viscosity which accounts for the effect of the non-resolved small turbulence scales. The subgrid-stress tensor relative to the velocity-velocity correlation is expressed as follows:

$$\tau_{ij}^{mod}(\widetilde{\boldsymbol{U}}, \overline{\Delta}) = -2\nu_t^{mod}(\mathbf{g}, \mathbf{d}, \overline{\Delta})S_{ij}, \tag{4.45}$$

where $S_{ij} = 0.5(g_{ij} + g_{ji})$ is the rate of the deformation tensor, $\mathbf{g}$ is the velocity gradient, expressed as $g_{ij} = \partial\widetilde{U}_i/\partial x_j$, and ν_t^{mod} is the turbulent viscosity and is specific to each model. The density-velocity subgrid term is computed with eddy-diffusivity models. They involve the turbulent Prandtl number, $\mathrm{Pr_t}$:

$$\pi_j^{mod}(\widetilde{\boldsymbol{U}}, \phi, \overline{\Delta}) = -\frac{\nu_t^{mod}(\mathbf{g}, \mathbf{d}, \overline{\Delta})}{\mathrm{Pr_t}} d_j, \tag{4.46}$$

with $\boldsymbol{d_j} = \partial\phi/\partial x_j$ the scalar gradient. $\mathrm{Pr_t} = 0.9$ is the turbulent Prandtl number, defined as the ratio between the momentum eddy-diffusivity and the heat transfer eddy-diffusivity.

The following functional models are investigated in this study.

- WALE model [231]:

$$\nu_t^{WALE}\left(\mathbf{g}, \mathbf{d}, \overline{\Delta}\right) = \left(C^{WALE}\overline{\Delta}\right)^2 \frac{\left(S_{ij}^d S_{ij}^d\right)^{3/2}}{\left(S_{mn}S_{mn}\right)^{5/2} + \left(S_{mn}^d S_{mn}^d\right)^{5/4}}, \tag{4.47}$$

- AMD model [13]:

$$\nu_t^{AMD}\left(\mathbf{g}, \mathbf{d}, \overline{\Delta}\right) = C^{AMD}\frac{max(0, -G_{ij}S_{ij})}{g_{mn}g_{mn}}, \tag{4.48}$$

- Scalar AMD model [22]:

$$\nu_t^{AMD}\left(\mathbf{g}, \mathbf{d}, \overline{\Delta}\right) = C^{AMDs}\frac{max(0, -D_j d_j)}{d_m d_m}, \tag{4.49}$$

- Sigma model [150]:

$$\nu_t^{Sigma}\left(\mathbf{g},\mathbf{d},\overline{\Delta}\right)=\left(C^{Sigma}\overline{\Delta}\right)^2\frac{\sigma_3(\sigma_1-\sigma_2)(\sigma_2-\sigma_3)}{\sigma_1^2}, \tag{4.50}$$

with S_{ij}^d the traceless symmetric part of the squared velocity gradient tensor, $\sigma_1>\sigma_2>\sigma_3$ the three singular values of $\mathbf{g}$, $G_{ij}=\overline{\Delta_k}^2 g_{ik}g_{jk}$ the gradient model, and $D_j=\overline{\Delta_k}^2 g_{jk}d_k$ the gradient model for the density-velocity correlation subgrid term. Unless otherwise is stated, the functional model constants used are $C^{WALE}=0.55$, $C^{AMD}=0.3$, $C^{AMDs}=0.3$, and $C^{Sigma}=1.5$.

The modeling of the subgrid scale requires to preserve the generic properties of the filtered Navier-Stokes equations. Deville *et al.* [176] gives the expression that the stress tensor should follow to conserve the invariance properties:

$$\begin{aligned}\tau_{ij}= \quad & a\ (\mathbf{S_{ij}}\cdot\gamma\otimes\gamma+\gamma\otimes\gamma\cdot\mathbf{S_{ij}})+b\ \gamma\otimes\gamma\cdot\mathbf{S_{ij}}\cdot\gamma\otimes\gamma+c\ \mathbf{S_{ij}}\\ & +(d\ tr(\mathbf{S_{ij}})+e\ \mathbf{S_{ij}}:\gamma\otimes\gamma)\mathbf{I}+e\ tr(\mathbf{S_{ij}}\gamma\otimes\mathbf{e}),\end{aligned} \tag{4.51}$$

with γ the unit vector used to represent the axes of a Cartesian coordinate system, $\mathbf{I}$ the identity matrix, and a, b, c, d and e coefficients.

The tensorial model obtained by taking $\gamma=\mathbf{e_x}$, the streamwise direction of the flow, $a=0.5$, $b=-1$, and $c=d=e=0$. Considering the studied geometry, this tensorial model is equivalent to the $H^{(4)}$ version of the AMD model proposed by Dupuy *et al.* [17, 145]:

$$\tau_{ij}^{H^{(4)}AMD}\left(\mathbf{U},\overline{\Delta}\right)=H_{ij}^{(4)}\tau_{ij}^{AMD}\left(\mathbf{U},\overline{\Delta}\right), \tag{4.52}$$

with

$$H_{ij}^{(4)}=\begin{pmatrix}0&1&1\\1&0&0\\1&0&0\end{pmatrix}. \tag{4.53}$$

In this paper, the tensorial AMD model is associated with the scalar AMD model. The simulation denoted "AMDt+AMDs" is a T-LES combining the tensorial AMD model for the computation of velocity-velocity correlation subgrid term and the scalar AMD model for the density-velocity correlation subgrid term.

4.3.3.2 Structural modeling

Two structural models are considered in this study:

- Scale similarity model [16]:

$$\tau_{ij}^{sim}=C^{sim}\left(\widehat{\widetilde{U}_j\widetilde{U}_i}-\widehat{\widetilde{U}}_j\widehat{\widetilde{U}}_i\right), \tag{4.54}$$

$$\pi_j^{sim}=C^{sim}\left(\widehat{\widetilde{U}_j\widetilde{\phi}}-\widehat{\widetilde{U}}_j\widehat{\widetilde{\phi}}\right). \tag{4.55}$$

The scale similarity hypothesis assumes that the statistical structure of the tensor of the subgrid scales is similar to that of the smallest resolved scales. The test filter, $\widehat{\cdot}$, is explicitly computed in LES. Two test filters are considered. The simulation denoted "Sim" uses a box filter computed

as an average over three cells in the three directions. In one dimension, its expression is given by:

$$\overline{\psi}(x_i) = \frac{\psi(x_{i+1})\Delta(x_{i+1}) + \psi(x_i)\Delta(x_i) + \psi(x_{i-1})\Delta(x_{i-1})}{\Delta(x_{i+1}) + \Delta(x_i) + \Delta(x_{i-1})}, \tag{4.56}$$

where $\Delta(x_i)$ is the local cell size around the point x_i. The simulation denoted "SiL" is carried out with a Laplacian filter which involves the Taylor series expansion of the box filter using the local cell size as the filter width:

$$\overline{\psi}(x_i) = \psi(x_i) + \frac{[\Delta(x_i)]^2}{24}\frac{\partial^2\psi}{\partial x^2}\bigg|_i. \tag{4.57}$$

The second derivative is approximated using a second-order centered finite difference approximation.

- Gradient model [15]:

$$\tau_{ij}^{grd} = \frac{1}{12}C^{grd}\overline{\Delta_k}^2 g_{ik}g_{jk}, \tag{4.58}$$

$$\pi_j^{grd} = \frac{1}{12}C^{grd}\overline{\Delta_k}^2 g_{ik}d_k. \tag{4.59}$$

Unless otherwise is stated, the structural model constants used are $C^{Sim} = 1.0$, , $C^{SiL} = 1.0$, and $C^{grd} = 1.0$.

4.3.3.3 Mixed modeling

Three mixed models are considered: (1) the multiplicative mixed model (MMG model) proposed by Dupuy *et al.* [160]; (2) a model coupling the tensorial version of the AMD model and the scale similarity model for the velocity-velocity correlation and the scale similarity associated with the scalar AMD model for the density-velocity correlation (sim + AMDt - sim + AMDs); (3) a combination of the scale similarity model with the WALE model (sim + WALE - sim + WALE). The multiplicative mixed model based on the gradient model (MMG model) is a functional model constructed such that its magnitude is expressed by the gradient model and its orientation is aligned with the rate of deformation tensor or the scalar gradient depending on the subgrid term:

$$\nu_t^{MMG}(\mathbf{g}, \mathbf{d}) = -C^{MMG}\frac{G_{kk}}{|\mathbf{S}|}, \tag{4.60}$$

where $C^{MMG} = 0.05$. The two other studied mixed models rely on a linear combination of the subgrid-scale stress tensors obtained with functional and structural models:

$$\tau^{mix} = A\tau^{func} + B\tau^{struc}, \tag{4.61}$$

where A and B are constants. τ^{func} and τ^{struc} respectively denote the subgrid-scale stress tensor modeled with functional and structural model.

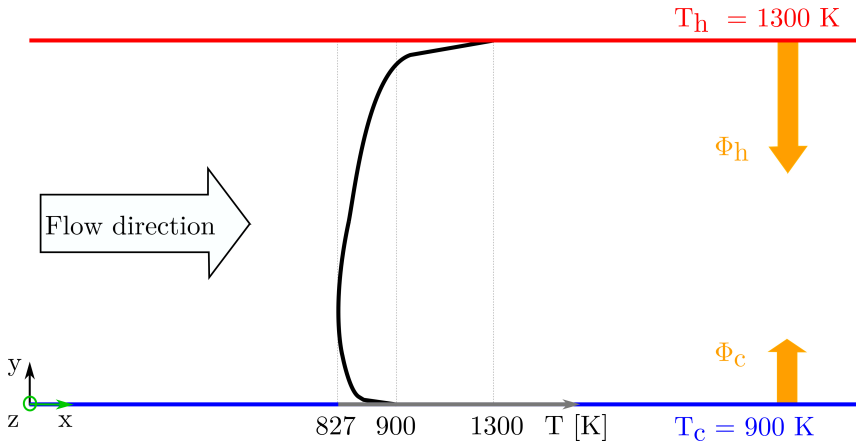

Figure 4.12 – Geometry of the channel flow. The periodic directions are in green.

4.3.4 Study configuration

4.3.4.1 Channel flow configuration

The study configuration is similar to the working conditions of gas-pressurized solar receivers of concentrated solar power towers. Solar receivers are supposed to be plane channels. One wall of the channel absorbs concentrated solar light whereas the other is insulated. To reproduce these conditions, thermal large-eddy simulations are performed in a fully developed three-dimensional turbulent channel flow asymmetrically heated. Fig. 4.12 describes the channel flow configuration. The streamwise (x) and spanwise (z) directions are periodic. The flow is bounded by two plane walls in the wall-normal direction (y). The domain size is $4\pi\delta \times 2\delta \times 4/3\pi\delta$ with $\delta = 3$mm. The temperatures of the plates are fixed to 1300 K for the hot wall ($y = 2\delta$) and 900 K for the wall representing the insulated wall and designed as "cold wall" ($y = 0$). The ratio of the wall temperatures is 1.44. Notice that, as the inertia of solar receiver walls is important, the fluid is passing through a channel at almost temporally constant wall temperatures, which justifies the choice of the thermal boundary conditions. Nevertheless, in practice, the wall temperatures are not homogeneous in the streamwise and spanwise directions. A schematic representation of the fluid temperature is given in Fig. 4.12. The mean fluid temperature is below the cold wall temperature, inducing heat transfers (ϕ_h and ϕ_c) oriented toward the fluid. The thermodynamical pressure, P_0, is 10 bars. A streamwise volume force is added to the channel to replicate the effect of a streamwise pressure gradient and maintain a constant mass flow rate. The hot and cold friction Reynolds numbers are respectively 640 and 1000. The mean friction Reynolds number is then 820.

4.3.4.2 Numerical settings

The numerical settings presented in this paper are similar to the ones described in David *et al.* [229]. The channel flow is simulated in a staggered grid system. Mesh is uniform in the homogeneous directions. In the wall-normal coordinate direction (y), it follows the hyperbolic tangent law described in Eq. 4.62 to capture the strong velocity and temperature gradients

Table 4.3 – Grid spacing of the DNS and T-LES meshes. The dimensionless cell sizes are computed at the cold wall (highest friction Reynolds number).

Name	Number of grid points $N_x \times N_y \times N_z$	Dimensionless cell size Δ_x^+ ; $\Delta_y^+(0)$; $\Delta_y^+(\delta)$; Δ_z^+
DNS	$1152 \times 746 \times 768$	10.9 ; 0.42 ; 5.4 ; 5.4
AAA	$192 \times 152 \times 128$	65 ; 1.1 ; 32 ; 33
BAB	$160 \times 152 \times 96$	78 ; 1.1 ; 32 ; 43
CAC	$128 \times 152 \times 72$	98 ; 1.1 ; 32 ; 58
DAD	$96 \times 152 \times 48$	130 ; 1.1 ; 32 ; 87

induced by walls.

$$y_k = L_y \left(1 + \frac{1}{a}\tanh\left[\left(\frac{k-1}{N_y - 1}\right)\tanh^{-1}(a)\right]\right) \tag{4.62}$$

where a is the mesh dilatation parameter and N_y is the number of grid points in the wall-normal direction. The grids employed for DNS and T-LES are listed in Tab. 4.3. The T-LES meshes are characterized by acronyms for simplicity. The first, second, and third characters are respectively associated with the streamwise, wall-normal, and spanwise directions. "A" accounts for the highest resolution considered in a particular direction whereas "D" represents the coarsest resolution. The wall-normal resolution is not investigated because it is substantially less impacting the results than the resolution in other directions as long as the first point is in the linear region of the viscous sublayer [171]. A third-order Runge-Kutta scheme computes the time derivatives. Momentum convection term is discretized with a fourth-order centered scheme. The velocity divergence (representing the temperature convection in the chosen formalism), and temperature diffusion are approximated with second-order centered schemes. A Quadratic Upstream Interpolation for Convective Kinematics (Quick) [6] scheme is used for the discretization of the mass convection term. It considers a three-point upstream weighted quadratic interpolation for the cell face values. Since the scheme is based on a quadratic function it is third-order accurate in terms of Taylor series truncation error. The second-order centered scheme, employed by Streher *et al.* [12], is also considered. The simulations are performed with TrioCFD software [3]. This code has been developed by the French Alternative Energies and Atomic Energy Commission. It is used in many simulations of fluid flows [214, 213, 17, 145, 211, 27].

4.3.5 Results and discussion

DNS and T-LES produce instantaneous fields. The presented results are then time-averaged and spatially-averaged in the streamwise and spanwise directions. This combination of averages is denoted by $\langle\cdot\rangle$. We address first-order and second-order statistics. Functional and mixed models are respectively traceless and partially traceless meaning that only the deviatoric Reynolds stresses can be reconstructed and compared with DNS data without filtering process [11, 12]:

$$R_{ij}^{dev} = R_{ij} - \frac{1}{3}R_{kk}\delta_{ij}, \tag{4.63}$$

To facilitate the comparison between LES and DNS, the modeled terms are systematically added to the associated quantity.

$$R_{ij}^{DNS,dev} = R_{ij}^{LES,dev} + \langle \tau_{ij}^{SGS}(\mathbf{U}, \overline{\Delta}) \rangle^{dev}, \tag{4.64}$$

where $R_{ij}^{DNS} = \langle U_i U_j \rangle - \langle U_i \rangle \langle U_j \rangle$ and $R_{ij}^{LES} = \langle \widetilde{U}_i \widetilde{U}_j \rangle - \langle \widetilde{U}_i \rangle \langle \widetilde{U}_j \rangle$. Note that the coordinates x_1, x_2, x_3 and x, y, z as well as U_1, U_2, U_3 and U, V, W are used interchangeably for practical reasons. For the off-diagonal Reynolds stresses, Eq. 4.64 becomes :

$$R_{ij}^{DNS} = R_{ij}^{LES} + \langle \tau_{ij}^{SGS}(\mathbf{U}, \overline{\Delta}) \rangle, \text{ for i} \neq \text{j}. \tag{4.65}$$

The same procedure is applied to the correlations of velocity and temperature:

$$R_{i\theta}^{DNS} = R_{i\theta}^{LES} + \langle \pi_{i}^{SGS}(\mathbf{U}, T, \overline{\Delta}) \rangle, \tag{4.66}$$

with $R_{i\theta}^{DNS} = \langle U_i \theta \rangle - \langle U_i \rangle \langle \theta \rangle$ and $R_{ij}^{LES} = \langle \widetilde{U}_i \widetilde{\theta} \rangle - \langle \widetilde{U}_i \rangle \langle \widetilde{\theta} \rangle$. Here $\pi_i^{SGS}(\mathbf{U}, \widetilde{T}, \overline{\Delta})$ is linked to $\pi_i^{SGS}(\mathbf{U}, 1/\overline{\rho}, \overline{\Delta})$ by the ratio r/P_0 thanks to ideal gas law.

Several normalization are used in the following of the study. The results normalized in wall units are indicated by a superscript "+": $x_i^+ = x_i U_{\tau,\,w}/\nu_w$, $U_i^+ = U_i/U_{\tau,\,w}$, $T^+ = (T_w - T)/T_{\tau,\,w}$, $\langle R_{ij} \rangle^+ = \langle R_{ij} \rangle / U_{\tau,\,w}^2$, and $\langle U_i' \theta' \rangle^+ = \langle U_i' \theta' \rangle / (U_{\tau,\,w} T_{\tau,\,w})$. The friction velocity and the friction temperature are respectively expressed as $U_{\tau,\,w} = \sqrt{\nu_w \partial U/\partial x_2}$, and $T_{\tau,\,w} = \phi_w / (\rho_w C_p U_{\tau,\,w})$, with ϕ_w the conductive heat flux at the wall.

A "$(^o)$" scaling is performed as follow: $y^o = y Re_\tau^{mean}/\delta$, $U_i^o = U_i/U_\tau^{mean}$, $\langle R_{ij} \rangle^o = \langle R_{ij} \rangle / (U_\tau^{mean})^2$, $T^o = (T_w - T)/T_\tau^{mean}$, and $\langle R_{\theta\theta} \rangle^o = \langle R_{\theta\theta} \rangle / (T_\tau^{mean})^2$. ^{mean} denote the averaging of the values obtained at both walls.

The semi-local scaling, denoted "$(^*)$", involves the mean local fluid properties instead of the fluid properties at the wall [248]. The normalized quantities are: $y^* = y U_{\tau,\,w}^*/\overline{\nu}(y)$, $U_i^* = U_i/U_{\tau,\,w}^*$, $\langle R_{ij} \rangle^* = \langle R_{ij} \rangle / \left(U_{\tau,\,w}^*\right)^2$, $T^* = T/T_{\tau,\,w}^*$, $\langle R_{i\theta} \rangle^* = \langle R_{i\theta} \rangle / \left(U_{\tau,\,w}^* T_{\tau,\,w}^*\right)$, $\langle R_{\theta\theta} \rangle^* = \langle R_{\theta\theta} \rangle / \left(T_{\tau,\,w}^*\right)^2$, with, $U_{\tau,\,w}^* = \sqrt{\mu_w/\overline{\rho}(y) \partial U/\partial y}$ and $T_{\tau,\,w}^* = \phi_w / \left(\overline{\rho}(y) C_p U_{\tau,\,w}^*\right)$

In the figures representing wall-normal profiles and involving the wall-unit or semi-local scaling, the hot and cold sides are not separated by the center plan of the channel but by the plan corresponding to zero wall-normal velocity of the DNS results. It is located at a normalized distance of $y/(2\delta) = 0.21$ from the cold wall. Hence, the cold side designs the range $0 < y/(2\delta) < 0.21$ and the region characterized by $0.21 < y/(2\delta) < 1$ is denoted hot side in the following. The hot, respectively cold, side is designed by "hs", respectively "cs" in the key of figures.

4.3.5.1 Validation of the numerical method

To the authors knowledge, there is no reference data in the studied conditions. For that reason, a DNS has been carried out in isothermal conditions and compared with the DNS of Hoyas and Jiménez [10] at a friction Reynolds number of 930. The mesh refinement is very close to the one selected for the anisothermal study: $\Delta_x^+ = 10.1$, $\Delta_y^+(0) = 0.39$, $\Delta_y^+(\delta) = 5.1$, and $\Delta_z^+ = 5.1$. The results are given in Figure 4.13. They show that both the first- and second-order statistics are in very good agreement. Furthermore, Dupuy *et al.* [21] achieved successful comparisons of the code and numerical method used with the DNS of Lee and Moser [9] at friction Reynolds numbers of 180 and 395. Toutant and Bataille [249] performed mesh convergence analysis in anisothermal conditions. Hence, these works permit validating the achieved DNS.

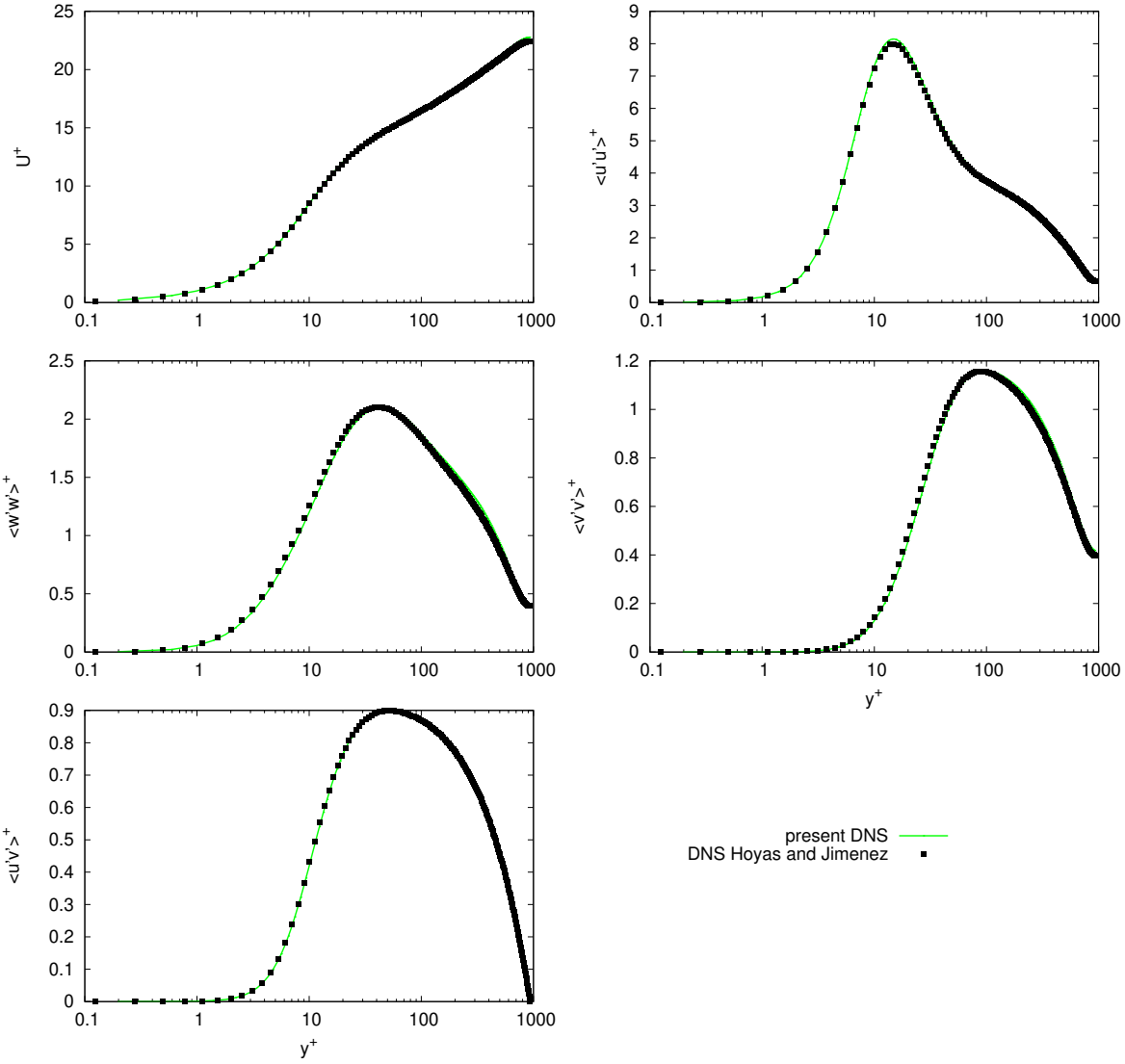

Figure 4.13 – Profiles of dimensionless longitudinal velocity and velocity correlations along the wall-normal direction of the channel at a friction Reynolds number of 930.

4.3.5.2 Effects of the wall heat transfer intensity

In this section, the focus is placed on the physic of the flow. Direct Numerical simulations provide very detailed results and are then suitable to investigate the effect of the high wall heat transfer on the flow. The impact of the temperature distribution obtained in the present conditions and the study of David *et al.* [229] are compared on first- and second-order statistics. In the work of David *et al.* the simulations are performed without source term in the energy equation. Hence, the fluid temperature is close to the average of the wall temperatures, meaning that the fluid is heated by one wall and cooled by the other. Thereafter, the DNS performed by David *et al.* will be denoted "DNS without source term" for simplicity. In the present study, the fluid

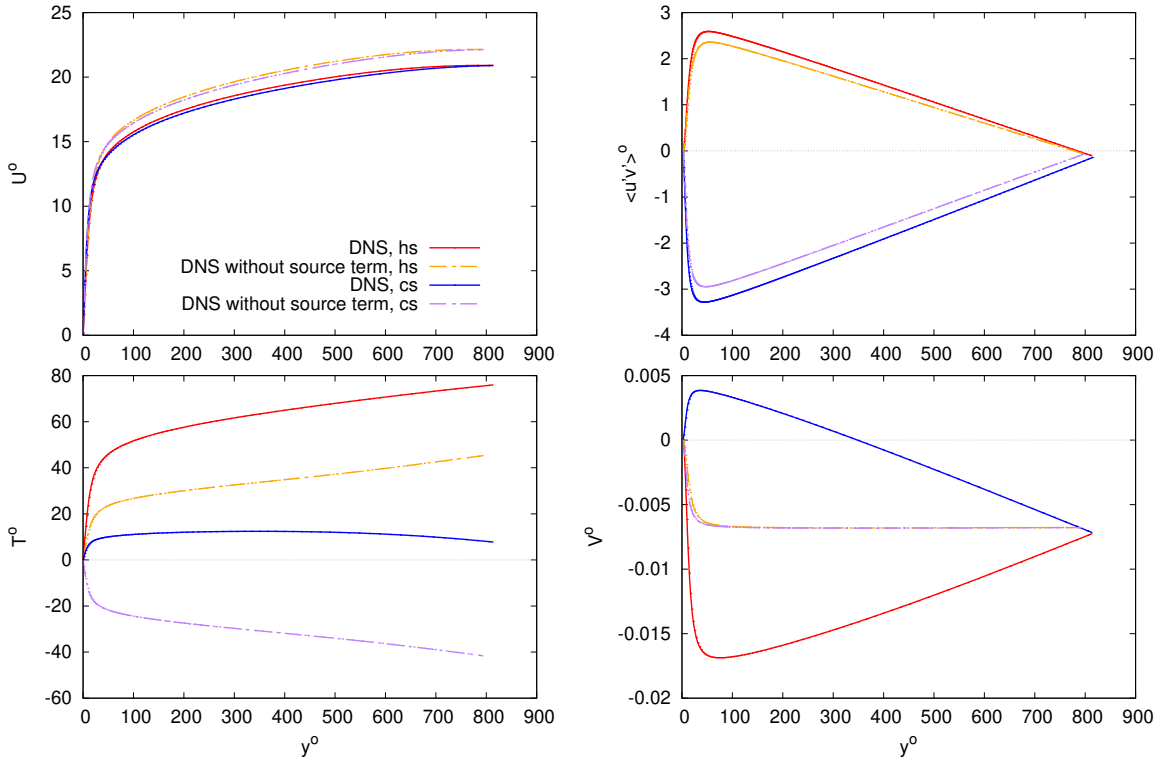

Figure 4.14 – Profiles of dimensionless longitudinal velocity, correlation of longitudinal and wall-normal velocities, wall-normal velocity, and temperature along the wall-normal direction of the channel.

temperature is lowered below the cold wall temperature thanks to the addition of a source term in the energy equation, see Sec. 4.3.2.

The results on U, $\langle u'v' \rangle$, T, and V are presented in Fig. 4.14. They are normalized with the $(^o)$ scaling that is described in Section 4.3.5. The streamwise velocity and the cross-correlation term are involved in the balance of the momentum equation 4.35. As for the temperature and the wall-normal velocity, they are involved in the balance of the energy equation 4.36. The results show that the location of the maximum streamwise velocity and the vanishing of the $\langle u'v' \rangle$ correlation coincide and is slightly shifted toward the hot side of the channel. On the contrary, the behavior of the temperature and wall-normal velocity profiles traduce an equilibrium located on the cold side. Indeed, near $y^o = 350$, there is an inflection in the cold temperature profile, and the wall-normal velocity vanishes. The results show that lowering the fluid temperature induces a reduction of the normalized streamwise velocity in the logarithmic region and the outer layer when compared to the DNS without source term. This is explained by the higher density of the fluid in the present DNS. The streamwise velocity is higher on the cold side than on the hot side in the vicinity of the walls. Then it becomes higher on the hot side, after $y^o = 30$. The present DNS exhibits bigger peaks of the cross-correlation than the DNS without source term. This is due to the magnitude and orientation of the wall-normal velocity. The profiles of wall-normal velocity are significantly different. The magnitude of the wall-normal velocity is four times higher on the hot side than on the cold one. This is explained by the intensity of the wall heat fluxes.

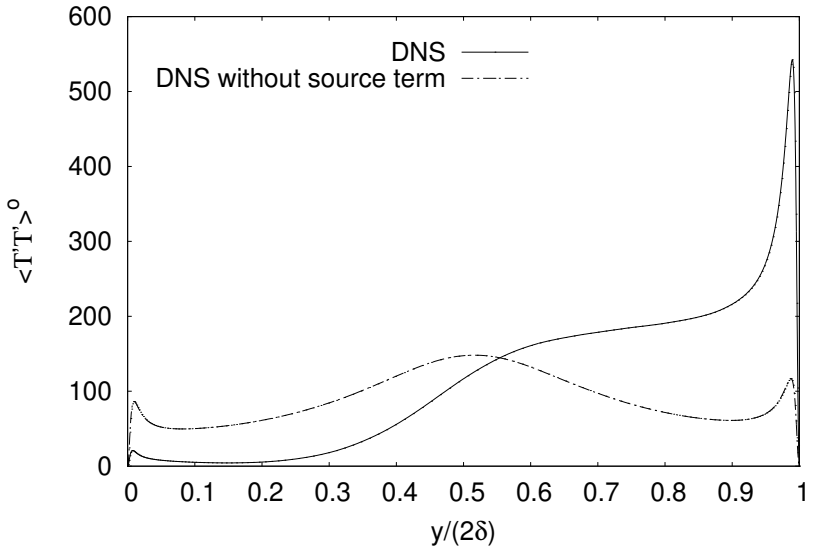

Figure 4.15 – Profiles of normalized temperature covariance along the wall-normal direction of the channel.

The profiles of normalized temperature covariance along the wall-normal direction of the channel are given in Fig. 4.15. The results show that the fluctuations of temperature are highly asymmetric in the present DNS. The magnitude of the hot side peak is more than 25 times bigger than the cold peak. The central peak observed in the DNS without source term, due to the combination of the temperature gradient and the large turbulence structure in the center of the channel, is not observed in the present simulation. This is explained by the profile of fluid temperature which admit a minimum, *i.e.* a zero gradient temperature, around $y/(2\delta) = 0.21$. The minimum temperature fluctuations are observed between $y/(2\delta) = 0.08$ and $y/(2\delta) = 0.21$ because of the combination of low-temperature gradient and the weak temperature transport due to the vicinity of the wall.

The components of the Reynolds stress tensor are also compared with the DNS without source term performed by David *et al.* The semi-local scaling permits the mitigation of the asymmetry between both sides [250]. The cold side is located between the cold wall and the region where the wall-normal velocity vanishes ($y/(2\delta) = 0.21$). The rest of the channel is denoted hot side. For that reason, the hot profiles are longer than the cold profiles. In Fig. 4.16, the DNS results show peaks of the velocity correlations around $y^* = 15$ for the diagonal terms, corresponding to the production of low- and high-speed streaks [251]. They are due to the succeeding bursts of the low-velocity pockets near the end of the inner region which induce fast fluid motions towards the wall. These motions sweep the near-wall zone in the streamwise and spanwise directions. The fluctuations of velocities show a plateau of the spanwise velocity fluctuations in the region $70 < y^* < 200$ corresponding to the meso layer of the logarithmic region. The biggest fluctuations are those of the streamwise velocity, followed by the fluctuations of the wall-normal velocity and the fluctuations of the spanwise velocity. The peaks of these correlations are very slightly shifted toward the center of the channel when compared to the DNS without source term. Their magnitude is, also, somewhat lower. On the hot side, this is probably due to the higher magnitude of the wall-normal velocity that tends to pull the streaks away from the wall.

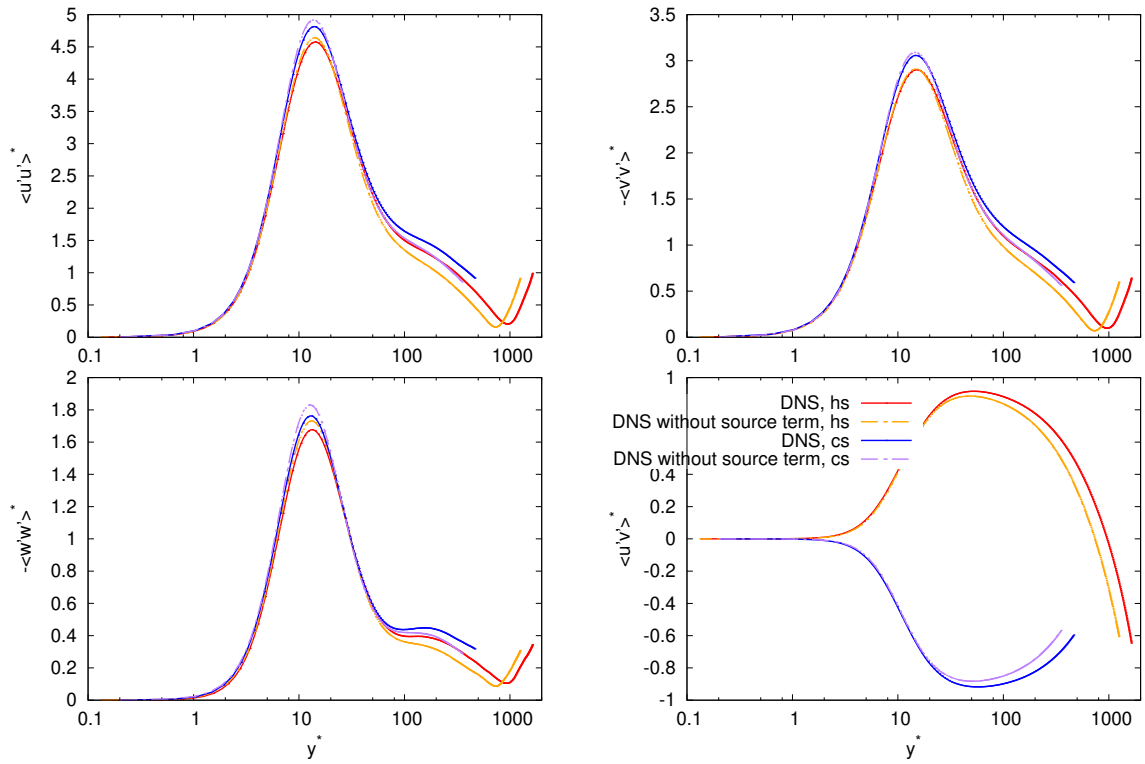

Figure 4.16 – Profiles of the velocity correlations in the wall-normal direction. The statistics are normalized with a semi-local scaling.

They are further from the hot wall and thus submitted to less shear stress which mitigates the peak of the correlation. On the cold side, the wall-normal velocity is opposed when compared to the DNS without source term, meaning that the streaks are moved towards the logarithmic region instead of being oriented closer to the wall. After, $y^* = 50$, on both sides the fluctuations of velocities are bigger in the present DNS than in the DNS of David *et al.* This agrees with the behavior of the streaks, that are moved further from the walls, discussed above. There is an inflection of the hot profiles of $\langle u'u' \rangle^*$, $\langle v'v' \rangle^*$, $\langle w'w' \rangle^*$ in the results of both DNS. In the present DNS, the inflection point is farther from the hot wall than in the DNS without source term. This is, once again, explained by the influence of the wall-normal velocity which ejects the streaks toward the outer layer. The same reason explains the difference obtained in the cross-correlation profiles. The comparison of the results provided by classical ($^+$) scaling (Fig. 4.23), show that the cold side peaks are bigger than the peaks of the hot side, as usually observed in the literature (see Refs. [197, 196, 216]). The correlation of streamwise and wall-normal velocities exhibits peaks around $y^+ = 30$ for the hot side and $y^+ = 50$ for the cold side, which are the signature of bursting events [251]. They consist of ejections and sweeps, respectively corresponding to an outflow of low-speed fluid from the wall and inflow of high-speed fluid toward the wall [78].

The correlations involving the temperature are exposed in Fig. 4.17. Similarly to the velocity-velocity correlations, the DNS show peaks of $\langle u'\theta' \rangle^*$ and $\langle \theta'\theta' \rangle^*$ around $y^* = 15$. The $\langle u'\theta' \rangle^*$ cold peak is mitigated when compared to the DNS without source term. A secondary peak is observed on the hot side near $y^* = 1300$. It corresponds with the shift of the maximum velocity toward

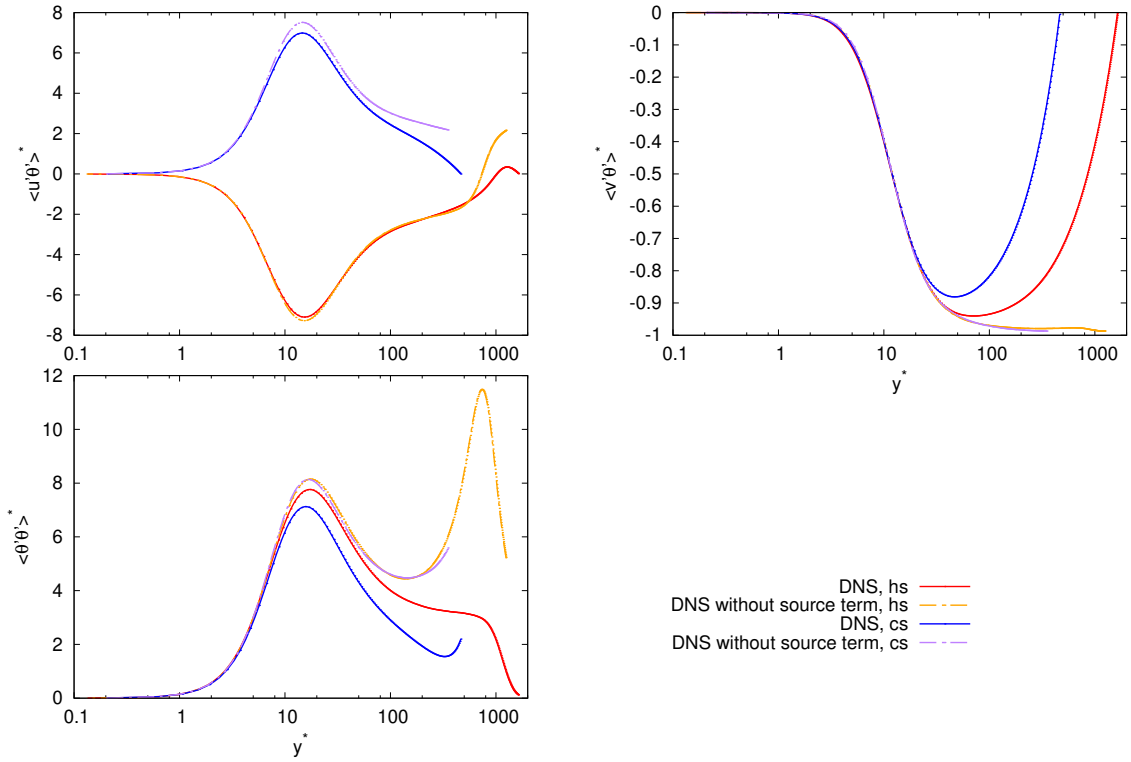

Figure 4.17 – Profiles of the velocity-temperature correlations and temperature covariance along the wall-normal direction of the channel. The statistics are normalized with a semi-local scaling.

the hot side. This is not observed in the DNS without source term. The strong asymmetry of wall heat flux is responsible for this behavior. The correlation of wall-normal velocity and temperature traduces the same flow behaviors as those explained in the discussion concerning the V^o profile. This correlation vanishes exactly in the same location as the wall-normal velocity. The $\langle\theta'\theta'\rangle^*$ correlation exhibits higher peaks at the hot side than at the cold side. This is not observed in the DNS without source term of David *et al.*, in which the peak of the cold side is significantly bigger, and traduces the strong temperature gradient caused by high wall heat flux. There is an inflection of the cold side profile around $y^* = 300$. Hence, the minimum of the fluctuations is obtained closer to the cold wall than the vanishing of the wall-normal velocity. The principal peak of the correlation of the temperature observed in the DNS of David *et al.* is not reproduced in the present conditions.

The detailed results of the wall heat flux are critical since the coupling between dynamic and temperature is substantial in the studied conditions. To simplify the reading of the T-LES assessment, the DNS results on wall heat fluxes are given in the figures presented in Sec. 4.3.5.3. Fig. 4.25 exposes the probability density of normalized heat flux. On both sides, the maximum probability is reached for heat flux slightly lower than the mean heat flux.The maximum density probability is 0.04 on the cold wall whereas it is only 0.03 on the hot wall. Fig. 4.26 gives the instantaneous fields of both wall heat fluxes. Small red stains depict high heat fluxes while blue zones represent low heat fluxes. The DNS results show very high-frequency turbulent structures that enhance the wall-normal convection. The fluid structures at relatively low temperatures

are driven in the vicinity of the wall. At the hot wall, the maximum wall heat flux reaches 1250 kW/m^2, *i.e.* about 4.8 times the mean hot wall heat flux. On the cold side, the ratio between the maximum cold heat flux and the mean cold heat flux is 6.1. The results obtained by David *et al.* [229], without source term, show a ratio of 6.6 with a mean wall heat flux of 97 kW/m^2. Very low heat transfer zones appear to be associated with long structures oriented toward the streamwise direction. These blue shapes are probably due to the presence of streaks above the viscous sublayer of the involved regions. The DNS results show that the ratio between the maximum wall heat flux and the mean wall heat flux is bigger at the cold wall, see Tab. 4.6. The ratios between the RMS of wall heat flux and the mean wall heat flux are identical and equal to 0.43 at both walls. The same ratio is obtained in the DNS of David *et al.* [229] without source term. Thus, it seems that measuring the mean wall heat flux is sufficient to determine the RMS of heat flux at this wall.

Summarizing the results on first- and second-order statistics, the conditions studied in the present paper are significantly different from the conditions investigated in David *et al.* [229]. Indeed, the wall heat fluxes are different in magnitude and direction when compared to the DNS without source term. In the present DNS, the hot wall heat flux is significantly higher than the cold wall. These differences increase the asymmetry of the flow. The both sides heating conditions then induce new flow behaviors.

In the next section, Thermal-Large Eddy simulations are carried out and compared to DNS results in these complex but usually encountered conditions.

4.3.5.3 Performances of the Thermal-Large Eddy Simulations

Processing of the T-LES results The data processing is identical to the one proposed in Ref. [229]. The DNS wall-normal profiles are interpolated on the T-LES grid to compute the T-LES error, which is computed as follows:

$$\epsilon_X^{LES_j} = \frac{\sum_{i=1}^{N_y/2} log\left(\frac{y_{i+1}}{y_i}\right) \left|\left(X_i^{LES_j} - X_i^{DNS}\right) X_i^{LES_j}\right|}{\sum_{i=1}^{N_y} log\left(\frac{y_{i+1}}{y_i}\right) X_i^{DNS^2}} + \frac{\sum_{i=1}^{N_y/2} log\left(\frac{2\delta - y_{i+1}}{2\delta - y_i}\right) \left|\left(X_{Ny/2-i+1}^{LES_j} - X_{Ny/2-i+1}^{DNS}\right) X_{Ny/2-i+1}^{LES_j}\right|}{\sum_{i=1}^{N_y} log\left(\frac{2\delta - y_{i+1}}{2\delta - y_i}\right) X_i^{DNS^2}}, \tag{4.67}$$

where ϵ is the error, X is the observed value, LES_j refers to the jth tested model, y_i is the ith node in the wall-normal direction, and δ is the half-height of the channel. To increase the importance of near-wall phenomena, the logarithmic function is applied to the ratio between two successive points. Furthermore, the differences between LES and DNS are weighted by the local value of the quantity to accentuate the importance of the peak values.

T-LES models are assessed on 11 physical quantities divided into two groups:

- Mean quantities (first-order statistics)
  - ⋆ U, the longitudinal velocity profile,

- ⋆ V, the wall-normal velocity profile,
- ⋆ T, the temperature profile,
- ⋆ ϕ, the normal conductive heat flux at the wall.

- Correlations (second-order statistics)
  - ⋆ $\langle u'u' \rangle^{dev}$, the covariance of the longitudinal velocity,
  - ⋆ $\langle v'v' \rangle^{dev}$, the covariance of the wall-normal velocity,
  - ⋆ $\langle w'w' \rangle^{dev}$, the covariance of the transversal velocity,
  - ⋆ $\langle u'v' \rangle$, the correlation of longitudinal and wall-normal velocities,
  - ⋆ $\langle u'\theta' \rangle$, the correlation of longitudinal velocity and temperature,
  - ⋆ $\langle v'\theta' \rangle$, the correlation of wall-normal velocity and temperature,
  - ⋆ $\langle \theta'\theta' \rangle$, the covariance of temperature.

The final error of the jth T-LES model on the first-order statistics (mean quantities) is denoted Err_{mean}. The final error of the jth T-LES model on the second-order statistics (correlations) is denoted Err_{rms}. They are computed by adding the error obtained for each value and dividing this sum by the results of the worst model, *i.e.* the model that have the highest value resulting from the sum of the error on each quantity:

$$Err_{mean}^{LES,j} = \frac{\sum\limits_{X} \epsilon_X^{LES_j}}{max\left(\sum\limits_{X} \epsilon_X^{LES}\right)}, \tag{4.68}$$

where X is successively U, V, T and ϕ;

$$Err_{rms}^{LES,j} = \frac{\sum\limits_{X} \epsilon_X^{LES_j}}{max\left(\sum\limits_{X} \epsilon_X^{LES}\right)}, \tag{4.69}$$

where X is successively the square root of $\langle u'u' \rangle^{dev}$, $\langle v'v' \rangle^{dev}$, $\langle w'w' \rangle^{dev}$, $\langle u'v' \rangle$, $\langle u'\theta' \rangle$, $\langle v'\theta' \rangle$, and $\langle \theta'\theta' \rangle$.

Grid sensitivity analysis A grid sensitivity study is performed with the four LES meshes described in Tab. 4.3. The averaged errors on mean quantities and RMS values are presented in Fig. 4.18 for two T-LES. The top graph presents the error of a simulation carried out without a model ("no-model"). In this T-LES, the mass convection term is discretized with the second-order centered scheme. Note that the error committed with the DAD grid on RMS values is truncated in the graph to facilitate the reading. This error reaches 160 %. Refining the cell sizes in the x and z directions permits mitigating the error on RMS values. As for the results concerning mean quantities, the minimum errors are obtained for the "CAC" and "BAB" meshes. It signifies that the induced numerical dissipation is compensating some of the non-resolved scale effects. The results of the tensorial model ("AMDt + AMDs"), associated with the Quick scheme, are plotted on the bottom graph. Introducing a model permit to lower the error on the RMS value for all the studied grids. The results on mean quantities are slightly deteriorated when compared to the

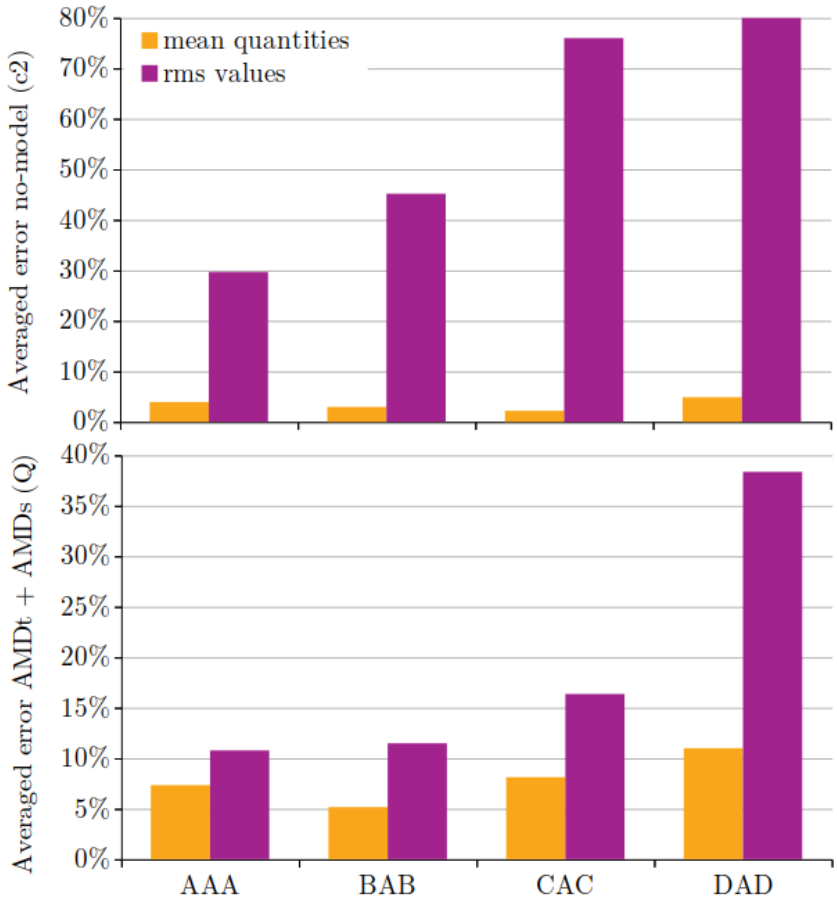

Figure 4.18 – Averaged errors obtained with four different meshes on mean quantities and RMS values. Simulations without model and with the tensorial AMD model are investigated.

no-model simulations. For instance, the error committed by the no-model simulation associated with the "BAB" mesh is 3 % while the "AMDt + AMDs" simulation has 5 % of error. The "DAD" mesh produces significantly poorer results than the other grids. Regarding the error on RMS values, the "BAB" and "AAA" meshes give similar results. However, the "BAB" grid is better for the estimation of mean quantities. Overall, the "BAB" mesh seems to be the best comprise and is selected for the following of the sudy. The results are sensitive to mesh refinement as classically observed, see Ref. [252, 145]. In the following, the no-model simulations carried out with the "BAB" grid are denoted ILES (for Implicit Large-Eddy Simulations).

General results and assessment of LES models In this section, 17 T-LES are assessed on first- and second-order statistics. The justification of the model efficacy is given with the detailed results presented in Section 4.3.5.3. *A posteriori* tests allow to assess the model taking into account all the simulation factors but they do not permit to differentiate the numerical error from the model error. Moreover, scale separation is difficult to establish because the low-pass filtering arises from a complex combination of implicit filtering by the mesh and the numerical schemes. Hence, four T-LES are successively performed with the Quick scheme, denoted (Q), and the second-order centered scheme, denoted (c2) thereafter. Tab.4.4 gives the relative errors

Table 4.4 – Relative errors obtained with the T-LES on the friction velocities and the mass flow. The values are given in percentage.

Simulation	$U_{\tau,\ h}$[m/s]	$U_{\tau,\ c}$[m/s]	$\dot{m}$ [kg/s]
DNS	4.17	3.64	$1.98 \times 10^{-}2$
Simulation	$\epsilon_{U_{\tau,\ h}}$	$\epsilon_{U_{\tau,\ c}}$	$\epsilon_{\dot{m}}$
AMD (Q)	-1.06	-2.51	5.25
AMD (c2)	2.77	-2.62	8.15
AMDt+AMDs (Q)	-2.41	-2.22	-6.78
WALE (Q)	-3.32	-3.49	-1.65
WALE (c2)	2.47	-2.74	3.27
Sig (Q)	-3.05	-3.26	0.01
Grd (Q)	-4.34	-3.32	-7.76
Sim (Q)	-0.94	-1.40	-0.71
Sim (c2)	3.06	-2.89	0.13
SiL (Q)	-3.45	-2.86	-5.66
MMG (Q)	-4.45	-3.50	-6.11
Sim-AMDt (Q)	-0.13	-1.77	-1.65
SiL-AMDt (Q)	-1.58	-2.12	-5.64
Sim05-WALE05 (Q)	19.31	12.83	-13.22
Sim05-WALE05 (c2)	14.12	13.72	-15.14
ILES (Q)	-4.81	-3.83	-7.16
ILES (c2)	1.77	-2.15	-1.49

of the T-LES on the mass flow and the friction velocity at both walls. The reference values are listed in the first line. The simulations are performed with a fixed friction at the wall. For that reason, the friction velocity of the T-LES are very close to the wall. The mass flow is predicted within 8 % of error except for the mixed models involving the scale similarity and the WALE models which produce poor results. Note that they also significantly overestimate the friction velocities. Fig. 4.19 exposes the normalized errors between DNS and T-LES. Errors on mean quantities are given on the top-graph. Overall, functional models produce good results. The "Sim (c2)", "sim-AMDt+sim-AMDs (Q)", "siL-AMDt+siL-AMDs (Q)" and "ILES (c2)" simulations are also efficient. The mixed models combining the scale similarity model and the WALE model give the worst results. Regarding the second-order statistics (middle-graph), the second-order centered scheme tends to deteriorate the results except for the "Sim-WALE+Sim-WALE" simulation. The "AMDt-AMDs (Q)", denoted tensorial AMD model for simplicity, and the "SiL-AMDt+SiL-AMDs (Q)" are significantly better than the other simulations. Once again, the mixed model "Sim-WALE+Sim-WALE" is the worst. The global results, presented in the bottom-graph show the superiority of the "AMDt-AMDs (Q)" and the "SiL-AMDt+SiL-AMDs (Q)" simulations. In the following, the "AMD (Q)", the "AMDt-AMDs (Q)", the "SiL (Q)" and the "SiL-AMDt+SiL-AMDs (Q)" simulations, as well as the two ILES, are selected for a detailed analysis. Note that the "SiL (Q)" is chosen despite its poor results because it is used in the mixed model "SiL-AMDt+SiL-AMDs".

In LES, the error induced by the numerical schemes are often significant [120, 108]. Thus, two numerical schemes used for the discretization of the mass convection are investigated with the

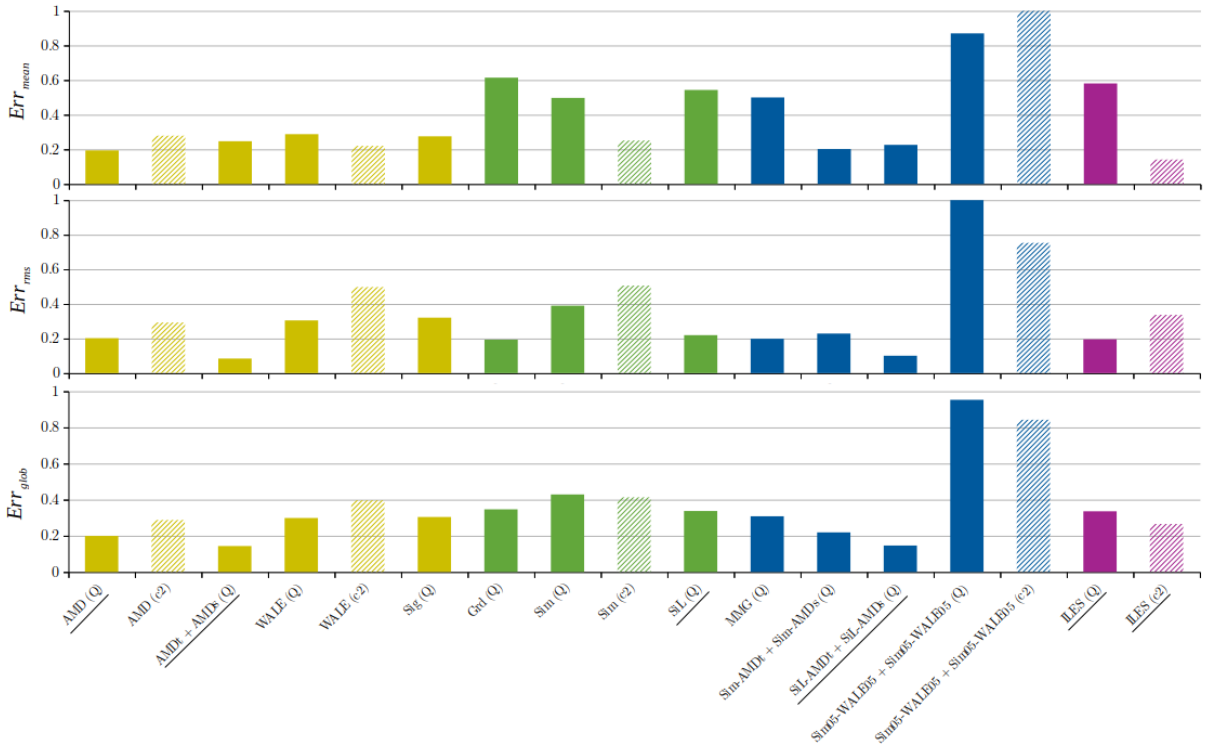

Figure 4.19 – Normalized error of various T-LES approaches. From top to bottom, the error concerns mean quantities, correlations, and global error. Yellow, green, and blue colors respectively stand for functional, structural, and mixed models. Purple color accounts for ILES. Full bars represent the simulations performed with the Quick scheme for the discretization of the mass convection whereas hatched bars are for T-LES using the second-order centered scheme. The six selected T-LES are underlined.

ILES simulations. The results on each quantity are gathered in Tab. 4.5. The mass convection scheme has a significant influence on all the studied quantities, except the temperature and the correlation of streamwise and wall-normal velocities. This is a major difference with the results obtained with a mean fluid temperature superior to the cold wall temperature. Indeed, David *et al.* [229] notice that the longitudinal velocity and the covariances of velocities were only quite sensitive to the numerical scheme chosen for the discretization of the mass convection term. The coupling between temperature and velocity is likely to be stronger in the present configuration. The second-order centered scheme improves the results when compared to the Quick scheme for the first-order statistics and the correlation of wall-normal velocity and temperature, as observed in Ref. [229]. The resolution error, due to the non-linearities, and the truncation error, caused by the numerical scheme, may balance each other. However, the second-order scheme substantially deteriorates the results on the diagonal terms of the Reynolds stress tensor. The higher-order term of the Quick scheme, by reducing the truncation error, is probably responsible for the better results obtained on these second-order statistics.

This section permits to assess a large number of T-LES. General results show that the best results are obtained with simulations involving functional models. Two functional models, a structural model, and a mixed model are selected for a detailed analysis.

Table 4.5 – Comparison of the numerical scheme effect on the error committed by ILES on each variable. The values are given in percentage.

	ϵ_{U}	ϵ_{V}	ϵ_{T}	ϵ_{ϕ_c}	ϵ_{ϕ_c}	$\epsilon_{\langle \mathrm{u'u'} \rangle^{\mathrm{dev}}}$	$\epsilon_{\langle \mathrm{v'v'} \rangle^{\mathrm{dev}}}$	$\epsilon_{\langle \mathrm{w'w'} \rangle^{\mathrm{dev}}}$	$\epsilon_{\langle \mathrm{u'v'} \rangle}$	$\epsilon_{\langle \mathrm{u'}\theta' \rangle}$	$\epsilon_{\langle \mathrm{v'}\theta' \rangle}$	$\epsilon_{\langle \theta'\theta' \rangle}$
ILES (Q)	7.1	8.5	1.6	35.1	8.6	39.1	29.5	60.2	6.6	17.3	10.0	20.7
ILES (c2)	1.9	3.8	1.2	6.4	1.5	77.4	60.0	116.1	8.0	23.9	1.7	29.0

Detailed results of selected models In this section, the results of the selected simulations are detailed. The wall-normal profiles of first- and second-order statistics are investigated. The cold side designs the range $0 < y/(2\delta) < 0.21$, corresponding to $0 < y^+ < 420$, and the region characterized by $0.21 < y/(2\delta) < 1$, corresponding to $0 < y^+ < 1010$, is denoted hot side.

First order-statistics For each simulation, the relative error, computed thanks to Eq. 4.67, is determined for four mean quantities. The results displayed in Fig. 4.20 show that, except the cold wall heat flux, all the quantities are estimated within 8% of error. The temperature profile is accurately predicted. Apart from the "ILES (c2)", all the simulations give similar results on the streamwise velocity profile. The wall-normal velocity and wall heat fluxes errors are linked. Indeed, in the vicinity of the walls, the wall heat flux is similar to the temperature gradient, which is the driver of the wall-normal velocity. Hence, a poor approximation of the wall heat flux induces errors on the wall-normal velocity profile. The "SiL (Q)" and "ILES (Q)" simulations produce poor results on these quantities. On the contrary, the other simulations provide a quite good approximation of the wall-normal velocity and the hot wall heat flux. They also give a better estimation of the cold wall heat flux than "SiL (Q)" and "ILES (Q)" simulations, even if the error on this quantity is higher than of the other. The cold wall heat flux is more sensitive to bulk temperature variations than the hot wall heat flux: even though the fluid temperature profile of T-LES is estimated within 1.6%, the error on the cold wall heat flux is relatively high.

In Fig. 4.21, the streamwise velocity, wall-normal velocity, and temperature profiles are plotted as functions of the wall-normal direction. Regarding the normalized streamwise velocity profile, except the "AMD (Q)", the T-LES provide a quite accurate estimation on the cold side. Note that the slope of the normalized velocity is not exactly reproduced in the log layer. On the hot side, the T-LES tend to underestimate the profile. The "AMD (Q)" is the only T-LES that overestimates the mass flow and underestimate the friction velocity, see Tab. 4.4. As a result, it significantly overestimates the normalized streamwise velocity despite a quite satisfying approximation of the non-normalized streamwise velocity (see Fig. 4.20). The top-right graph describes the normalized wall-normal velocity profile. The hot side is very well approximated by the T-LES. The cold wall-normal velocity profiles are also in very good agreement with the DNS, except for the structural model and the "ILES (Q)" simulation, which overestimate this quantity. The normalized temperature profiles are plotted on the bottom graph. The "ILES (c2)" provides the best cold temperature profile among the considered T-LES. However, this simulation is not efficient in the estimation of the hot side temperature profile. Even though they tend to overestimate the profiles, the tensorial AMD model and the mixed model produce the most reliable results.

Second-order statistics The second-order statistics are usually analyzed in LES [193, 204, 53, 253]. They facilitates the understanding of the flow behavior. Turbulence statistics are more complex to approximate for LES models than mean quantities. The correlations and covariances

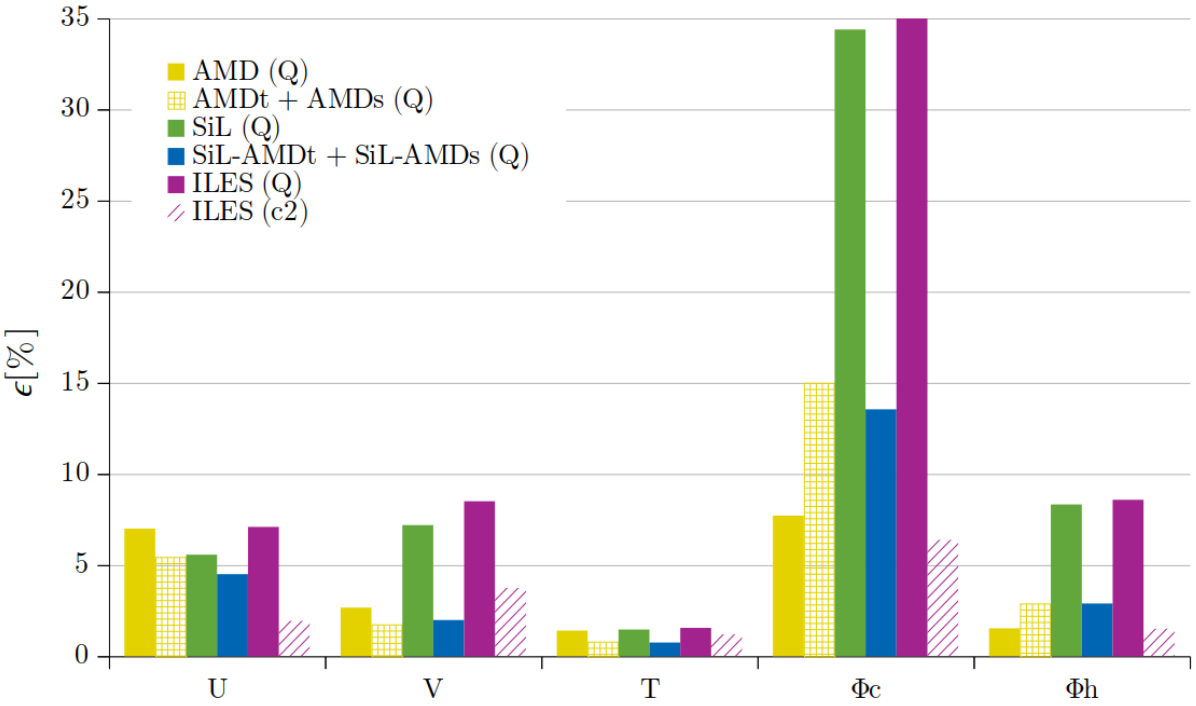

Figure 4.20 – Relative error on mean quantities for selected T-LES approaches. Yellow, green, and blue colors respectively stand for functional, structural, and mixed models. Full bars represent the simulations performed with the Quick scheme for the discretization of the mass convection whereas hatched bars are for T-LES using the second-order centered scheme.

described in Sec. 4.3.5.3 are investigated for the six selected T-LES in Fig. 4.22. Apart from the tensorial AMD model and the mixed model, the diagonal terms of the Reynolds stress tensor are poorly approximated by T-LES. The results of the "ILES (c2)" simulation are very far from those of the DNS. The ranking of the T-LES is conserved between these three quantities. The spanwise velocity correlation is the most complex quantity to estimate. Globally, the $\langle u'v' \rangle$ and $\langle v'\theta' \rangle$ are well predicted by all T-LES. The correlation of the streamwise velocity and the temperature is particularly well estimated by the "AMD (Q)" simulation, which is consistent with the exact sub-filter tensor on anisotropic grids [13]. Indeed, while other models show an error of around 18%, the "AMD (Q)" has only 5% of error. Similar results are observed on the temperature-temperature correlation. The "AMD (Q)", "AMDt + AMDs (Q)", and "SiL-AMDt + SiL-AMDs (Q)" simulations produce a very good estimation of the fluctuations of cold wall heat flux. At the hot wall, the models have about 15% of error. Notice that the best results on the wall heat flux were observed on the hot side but the best estimations on the fluctuations of wall heat flux concern the cold wall. This will be discussed in Sec. 4.3.5.3. The "ILES (c2)" produces the worst results of all the considered simulations.

Fig. 4.23 exposes the velocity-velocity correlation terms. As explained in Sec. 4.3.5, the deviatoric part of the diagonal terms of the Reynolds stress tensor is analyzed. The T-LES produce similar results on the correlations $\langle u'u' \rangle^{dev}$, $\langle v'v' \rangle^{dev}$, and $\langle w'w' \rangle^{dev}$. Hence, they are discussed together. The tensorial AMD model and the mixed model produce very good estimations of the hot side of the diagonal terms. On the cold side, the results of the tensorial AMD model and the mixed model are less remarkable but they are still the best among the considered simulations.

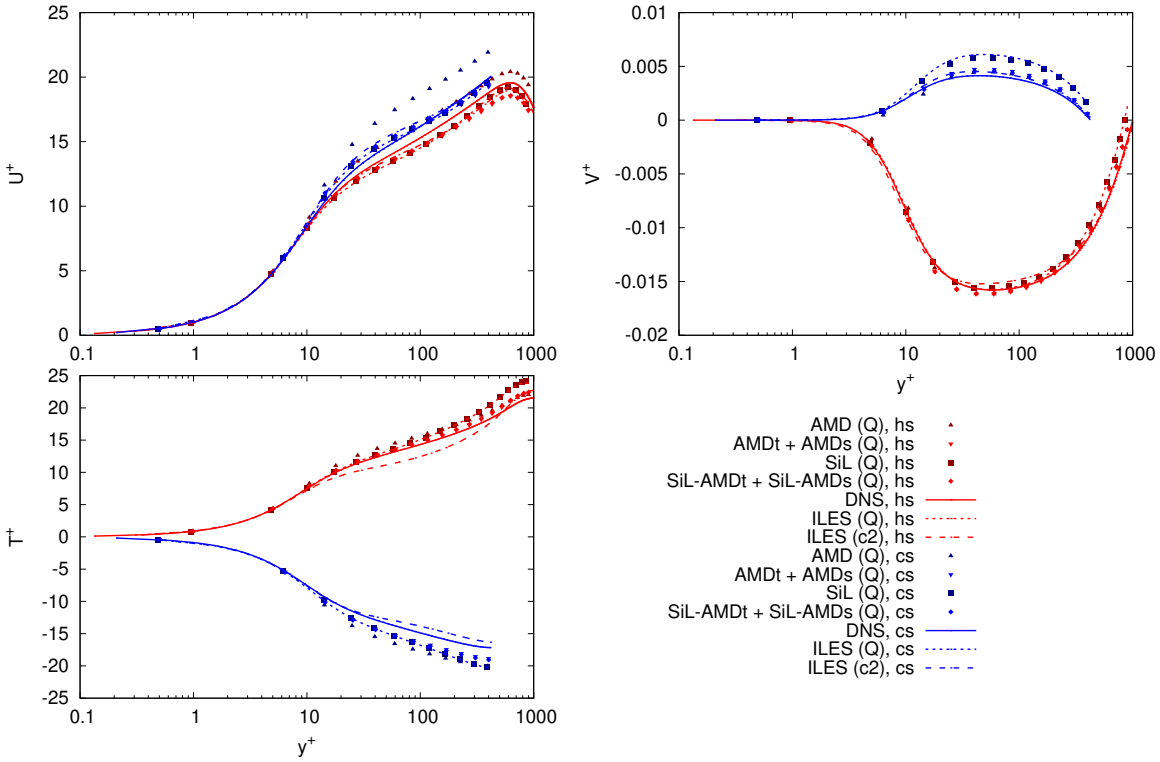

Figure 4.21 – Profiles of dimensionless longitudinal velocity, wall-normal velocity and temperature along the wall-normal direction of the channel.

These good results can be explained by the formulation of the tensorial AMD model which is able to take into account the anisotropy of the flow [145, 229]. The other simulations substantially overestimate the peaks of $\langle u'u' \rangle^{dev}$, $\langle v'v' \rangle^{dev}$, and $\langle w'w' \rangle^{dev}$ on both sides. The poorly dissipative behavior scale of the similarity model induces an overestimation of turbulence statistics. The ILES, which rely on numerical dissipation, seem to suffer from the same lack of dissipation. The normalized correlations of velocities show that the scheme used for the discretization of the mass convection term affects the results, even though it is moderate. The Quick scheme, which is third-order accurate, permits reducing the overestimation of the peaks. The T-LES give a very satisfying agreement with the DNS profile of the cross-correlation on the cold side. On the hot side, T-LES results show a moderate overestimation. The "AMD (Q)" model predicts a peak shifted toward the center of the channel. The tensorial AMD model allows adjusting this bias.

The correlations involving the temperature are exposed in Fig. 4.24. The top-left graph exhibits the $\langle u'\theta' \rangle$ correlation. The hot side profile is remarkably estimated by the "AMD (Q)" model, overestimated by the simulation involving the second-order centered scheme, and underestimated by the other simulations. The mixed model has the same principal peak magnitude as the DNS. Except the ILES (c2), all the simulations reproduce the secondary peak around $y_h^+ = 750$. The correlation of wall-normal velocity and temperature is quite well predicted by all the simulations. Nevertheless, the T-LES performed with functional models overestimate the magnitude of the cold peak. The "ILES (Q)" and "SiL (Q)" simulations underestimate the fluctuations in the outer layer. The temperature covariance is displayed in the bottom graph.

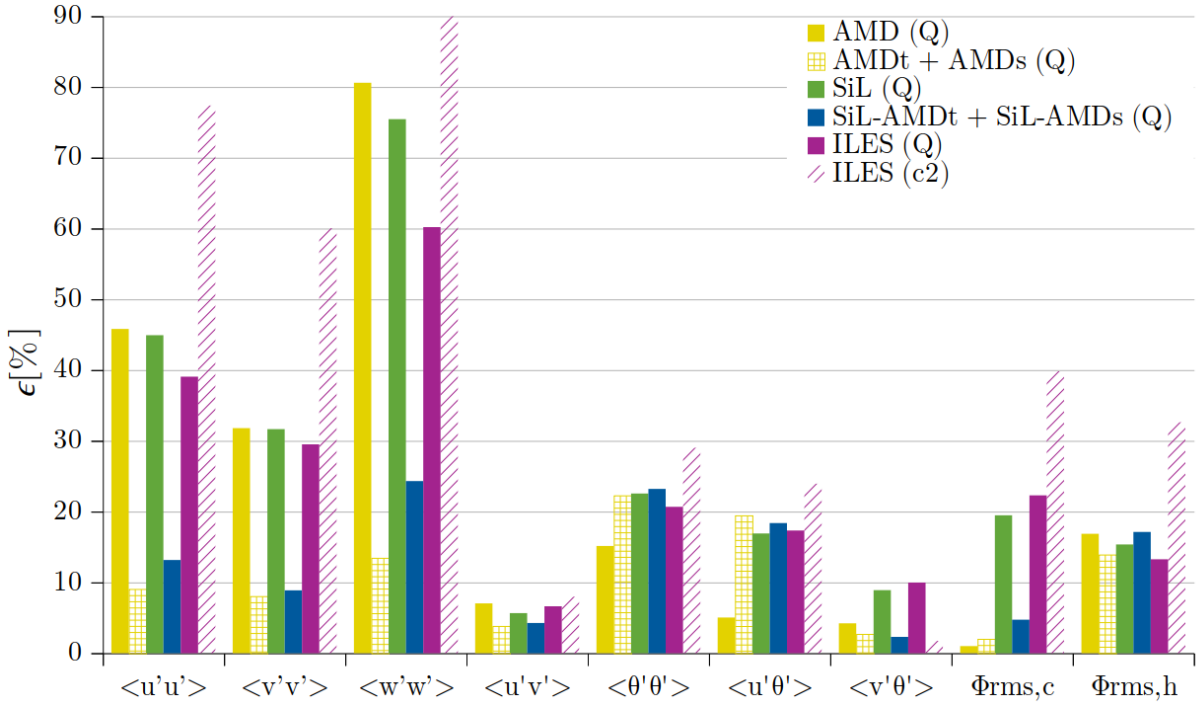

Figure 4.22 – Relative error on covariances for selected T-LES approaches. Yellow, green, and blue colors respectively stand for functional, structural, and mixed models. Full bars represent the simulations performed with the Quick scheme for the discretization of the mass convection whereas hatched bars are for T-LES using the second-order centered scheme.

The "AMD (Q)" simulation produces the best results and is particularly efficient for the prediction of the cold side peak. The other simulations carried out with the Quick scheme tend to underestimate the normalized temperature covariance on both sides. This is probably due to the upwind-like construction of the Quick scheme, used for the discretization of the mass convection term, which tends to induce numerical dissipation and, thus, reduces the covariance of temperature. Particularly, the peaks of the fluctuations in the logarithmic layer are poorly reproduced. The location of the cold side profile inflection is shifted toward the center of the channel when compared to the DNS results. On the contrary, the "ILES (c2)" simulation substantially overestimates the temperature variations. Note that the choice of the numerical scheme for the discretization of the mass convection term is substantially more impacting the normalized quantities involving the temperature than the normalized correlations of velocities.

Focus on the wall heat fluxes The wall heat fluxes estimation is a critical quantity for the design of solar receivers. For that reason, a particular attention is paid on this value.

Fig. 4.25 exposes the probability density of normalized heat flux. The dimensionless conductive wall heat flux is obtained with the following equation:

$$\phi_w^* = \frac{\phi_w - \phi_{w,mean}}{\phi_{plot,w,max} - \phi_{w,mean}} \tag{4.70}$$

where $\phi_{plot,w,max} = 3.9\phi^{DNS}_{w,\ rms} + \phi^{DNS}_{w,\ mean}$ is the biggest considered value of heat flux for plots of instantaneous wall heat flux in Fig. 4.26, *i.e.* 172 kW/m^2 at the cold wall and 700 kW/m^2 at

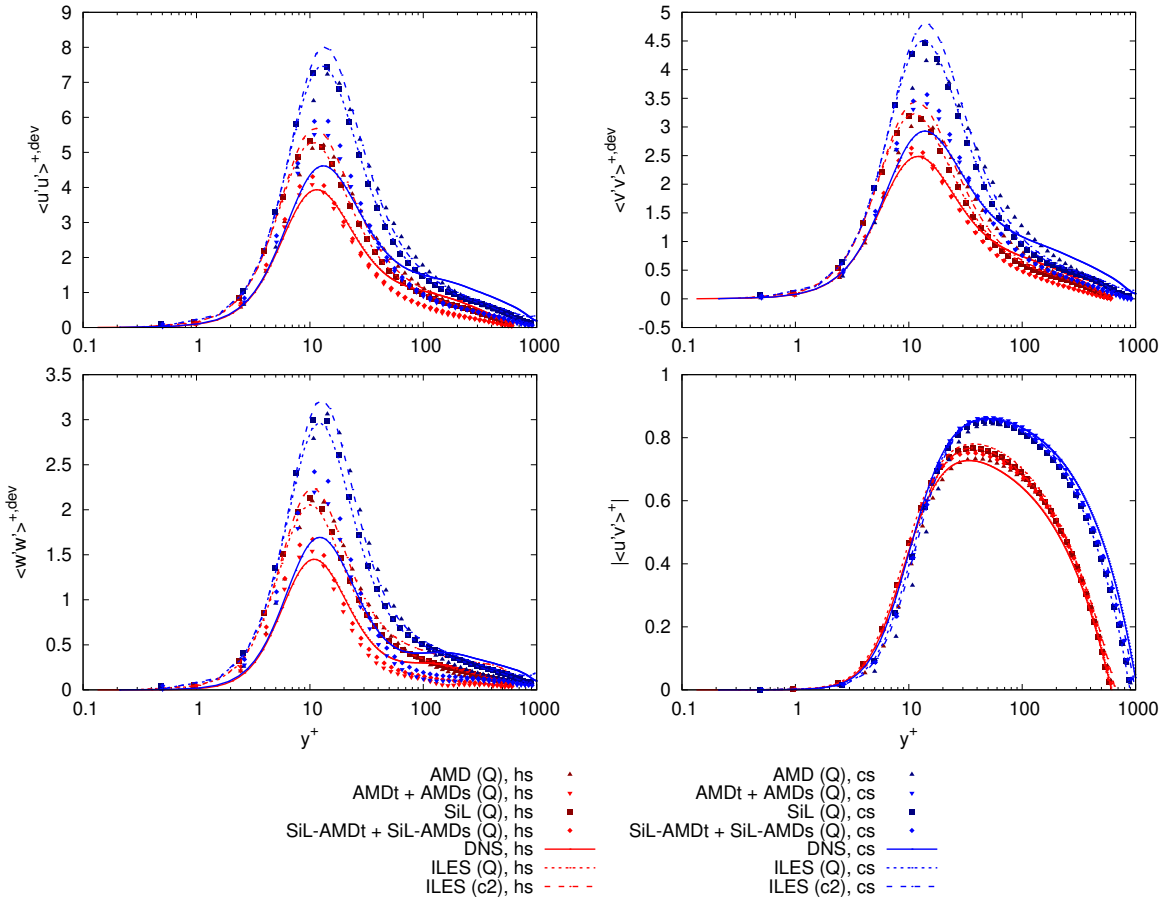

Figure 4.23 – Profiles of dimensionless covariances of longitudinal velocity, wall-normal velocity, transversal velocity as well as longitudinal and wall-normal velocities along the wall-normal direction of the channel. Note that the absolute value of the $\langle u'v' \rangle^+$ is plotted.

the hot wall. Three instantaneous fields of wall heat flux have been averaged. The probability density of the cold wall heat flux is relatively well approximated by the "AMDt+AMDs (Q)" simulation and the mixed model despite a slight overestimation of the peak. The results of the two ILES and the "SiL (Q)" simulation show that the peak is shifted toward small values of ϕ_w^* when compared to DNS. At the hot wall, the ILES (c2) is the only simulation that predicts the good location of the peak of the probability density. All the T-LES overestimate the magnitude of the peak. The predicted distribution traduces an underestimation of the fluctuation of wall heat fluxes, confirmed by Fig. 4.26. Note that the "ILES (c2)" predicts a quite high probability of very strong heat flux. The strong coupling between fluid and temperature induces very high-frequency structures that are not reproduced by all T-LES.

Fig. 4.26 represents the instantaneous fields of both wall heat fluxes. Comparing fields of T-LES with DNS permits qualitatively assessing the models on their direct representation of the flow. The results of the "SiL-AMDt+SiL-AMDs (Q)" simulation are similar to those of the "AMDt + AMDs (Q)". For that reason, they are not displayed. The left (respectively right) graphs, corresponding to the hot (respectively cold) wall heat fluxes, are plotted in the range $0 - 700$ kW/m^2 (respectively $0 - 172$ kW/m^2). Small red stains depict high heat fluxes

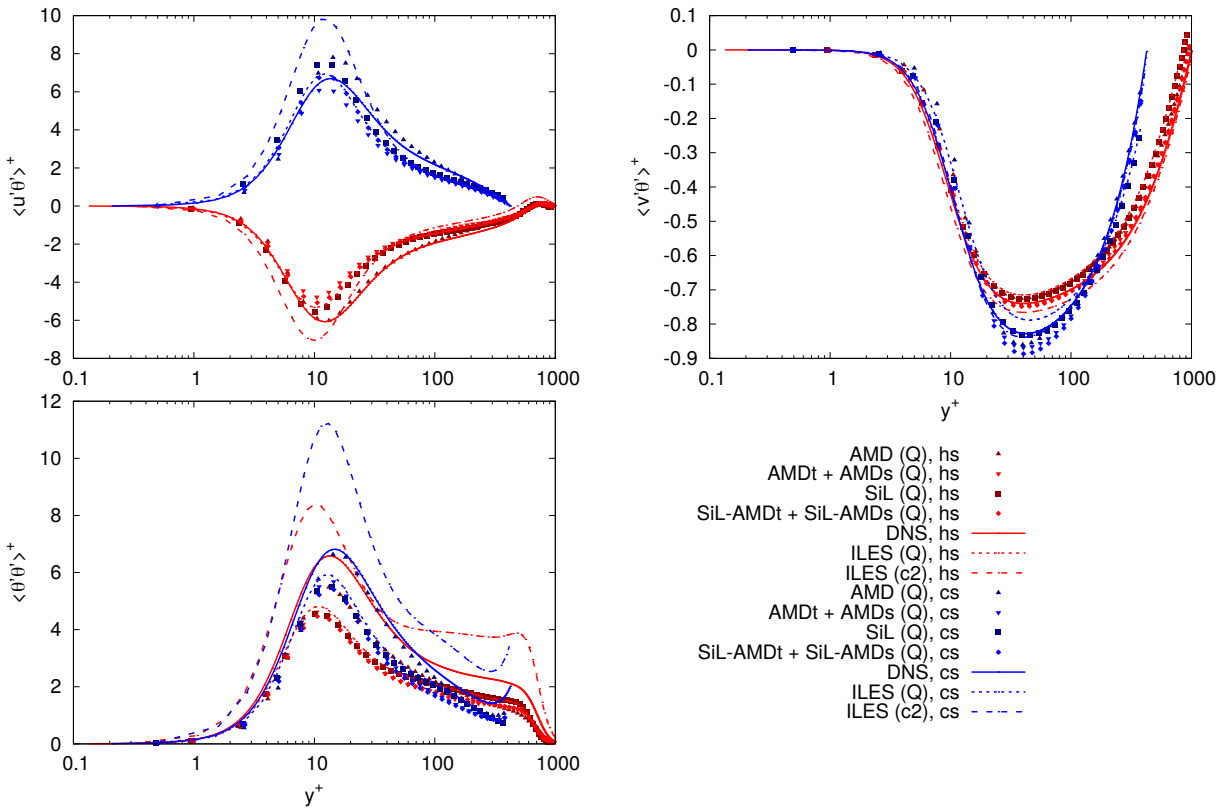

Figure 4.24 – Profiles of dimensionless correlations of longitudinal velocity and temperature, wall-normal velocity and temperature as well as the covariance of temperature along the wall-normal direction of the channel.

while blue zones represent low heat fluxes. Even though the mesh resolution of the T-LES is not fine enough to identify flow structures, the observed patterns of wall heat fluxes exhibit results similar to those of the DNS. The "ILES (c2)" gives a good approximation of the wall heat fluxes but the fluctuations and the maximum wall heat flux are overestimated. The T-LES slightly underestimate the mean wall hot heat flux and overestimate the cold one. The simulation involving the second order centered scheme gives an good estimation of the mean wall heat flux but overestimate the fluctuations and the maximum wall heat flux. Overall, the "AMD (Q)" and "AMDt+AMDs (Q)" simulations gives the best agreement of the patterns of wall heat fluxes.

Wall heat flux ratios are exposed in Tab. 4.6. The T-LES ratios of ϕ_w^{max}/ϕ_w are similar between both walls. The gap observed in DNS between the hot wall and the cold wall is not reproduced. Except the "ILES (c2)" simulation which overestimate the magnitude of the ratio between the RMS of wall heat flux and the mean wall heat flux, all T-LES tend to underestimate the magnitude of this ratio between the RMS of wall heat flux and the mean wall heat flux. This is explained by the over-dissipative behavior of the Quick scheme.

4.3.6 Conclusion

In this study, simulations are performed in the working conditions of gas-pressurized solar receivers. The flow is highly turbulent and asymmetrically heated. A source term have been introduced in the energy equation to lower the temperature profile and generate a both side heating

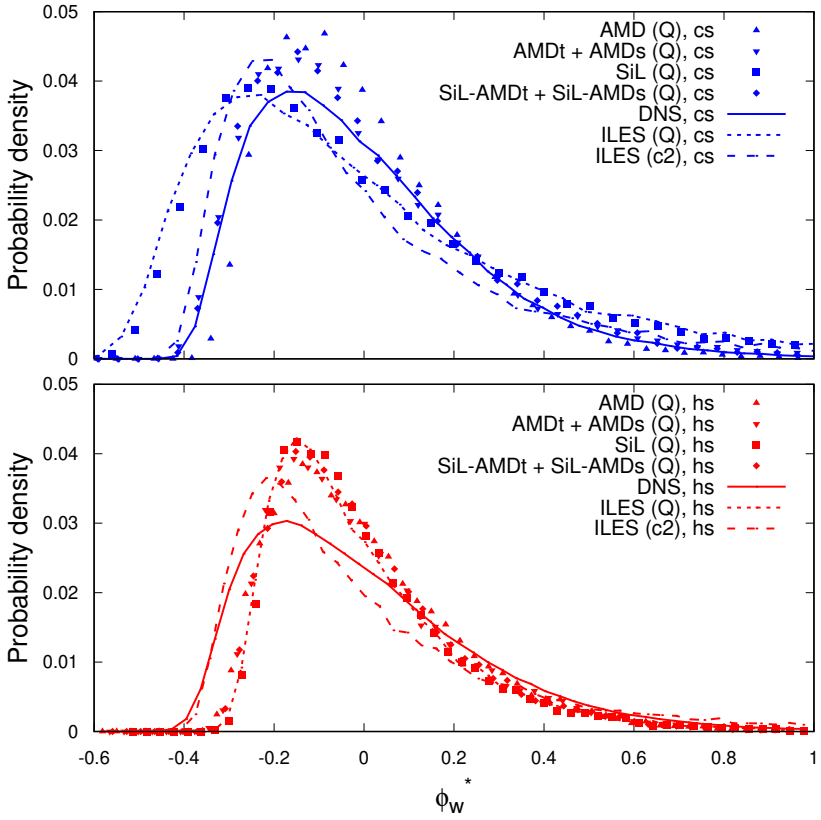

Figure 4.25 – Probability density of normalized heat flux.

of the fluid. A direct numerical simulation has been performed in order to compare the influence of the temperature distribution with a DNS carried out by David *et al.* [229] with different thermal conditions and flow behaviors. Indeed, in the present configuration, the asymmetrical temperature gradients induce different wall heat fluxes: the hot wall heat flux is significantly increased and the cold wall heat flux is opposed to the one obtained by David *et al.* in [229]. Furthermore, several Thermal-Large-Eddy-Simulations have been carried out and compared to the present direct numerical simulation. The considered T-LES involved functional, structural,

Table 4.6 – Wall heat flux ratios

Simulation	ϕ_h^{max}/ϕ_h	ϕ_c^{max}/ϕ_c	ϕ_h^{RMS}/ϕ_h	ϕ_c^{RMS}/ϕ_c
DNS	4.76	6.14	0.43	-0.43
AMD (Q)	3.46	3.63	0.35	-0.33
AMDt+AMDs (Q)	3.91	3.54	0.38	-0.36
SiL (Q)	3.72	3.62	0.39	-0.38
SiL-AMDt (Q)	3.82	3.59	0.37	-0.36
ILES (Q)	4.80	3.63	0.40	-0.38
ILES (c2)	6.95	6.21	0.58	-0.56

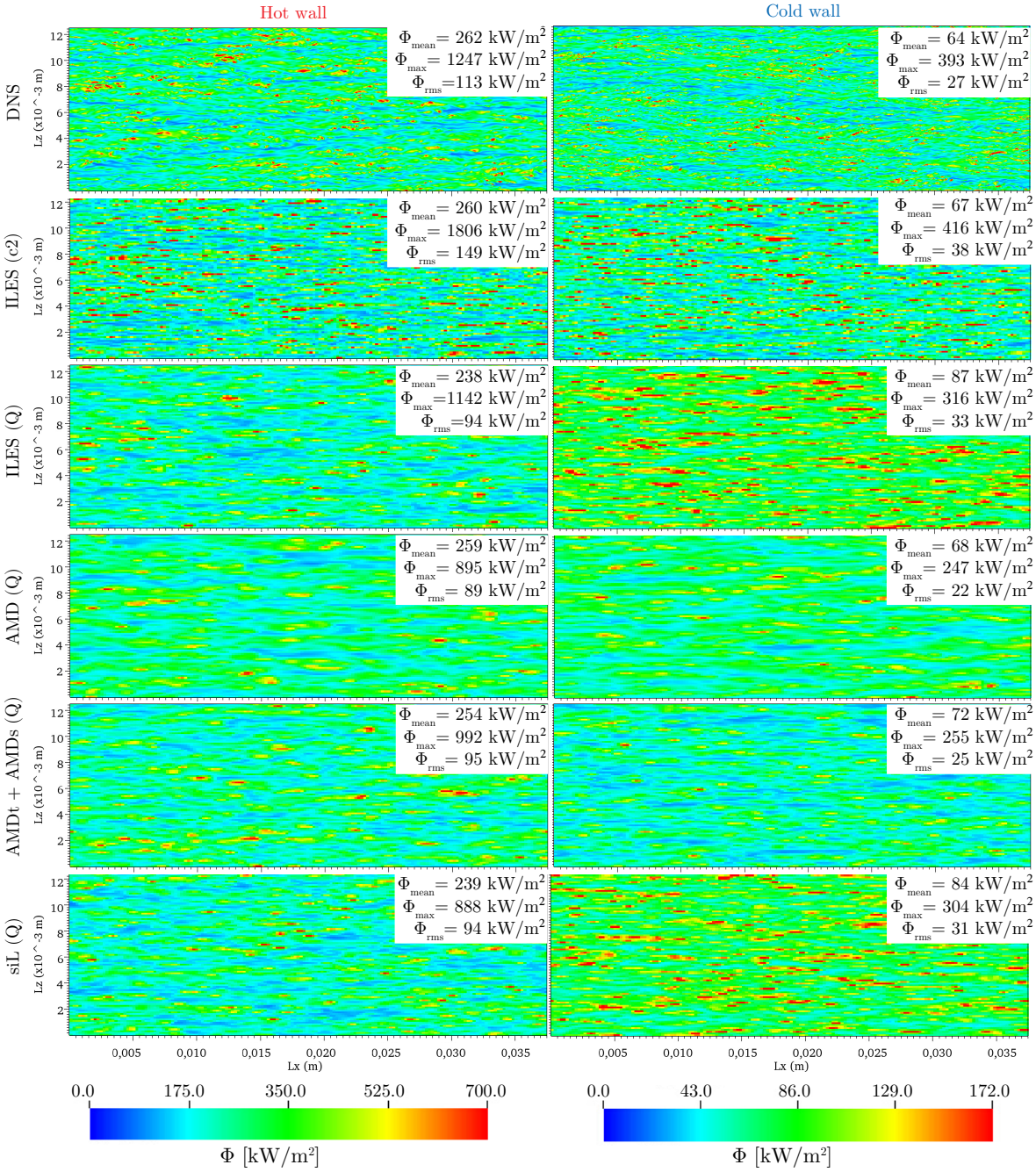

Figure 4.26 – Instantaneous fields of hot and cold wall heat fluxes. Pictures on the left (respectively right) side correspond to the hot (respectively cold) wall.

and mixed models as well as implicit LES. A Quick scheme and a second-order centered scheme have been tested for the discretization of the mass convection term. A general assessment of 17 T-LES on first- and second-order statistics has been performed. It has led to the selection of six T-LES for a precise analysis which consisted in the detailed evaluation of four mean quantities and eight correlations. The relative error was given for each quantity and each T-LES . Furthermore, the wall-normal profiles of these quantities have been plotted and discussed. Lastly, the instantaneous fields of wall heat fluxes have been studied.

The DNS results show a very strong coupling between the dynamic of the flow and the temperature. The heating of the fluid induces wall-normal velocity. Since the fluid is asymmetrically heated by both walls, these velocities are oriented toward the center of the channel and have different magnitudes. Furthermore, the area of zero wall-normal velocity is shifted toward the geometric cold side of the channel. The minimum temperature is reached at the same distance from the walls. The quantities involved in the balance of the momentum equation show inflection or vanishing on the hot side of the channel but relatively close to the geometric center. On the contrary, the quantities involved in the balance of the energy equation exhibit these particular behaviors on the cold side, at mid-length between the cold wall and the geometric center of the channel. The intense hot wall heat flux is responsible for the high magnitude of the hot side peak of the covariance of temperature. Indeed, this peak is bigger than the cold one despite a lower local turbulence. At the hot wall, the maximum wall heat fluxes encountered are more than six-time bigger than the mean wall heat flux. The fluctuations of the heat fluxes are significant, a ratio between the mean wall heat flux and the RMS of heat flux of 0.43 is observed on both sides and seems independent of the working conditions.

Regarding the T-LES results, the ILES performed with the second-order centered scheme produce a satisfying estimation of the wall heat flux but it clearly shows a lack of dissipation. This is particularly evident when analyzing the diagonal terms of the Reynolds stress tensor, the covariance of temperature, and the instantaneous field of wall heat flux. The Quick scheme seems to reduce these issues. The simulation carried out with scale similarity model has similar drawbacks that the ILES associated with the second-order scheme even though they are less salient. Once again, we suppose that it is due to a lack of dissipation. The results also show that the hot wall heat flux is better approximated by the LES models than the cold wall heat flux. This can be attributed to the smaller temperature difference between the cold wall and the bulk temperature than between the hot wall and the bulk temperature. It is interesting to note that LES models perform better when the temperature gradient is high. The first-order statistics are, globally, better approximated than the second-order statistics for all the T-LES. Nevertheless, the correlation of the streamwise and wall-normal velocities, as well as the correlation of wall-normal velocity and temperature, are well predicted. The diagonal terms of the Reynolds stress tensor are significantly overestimated by all T-LES, except the tensorial AMD model and the mixed model which combine the scale similarity model and the tensorial AMD model. The good agreement of these models is probably due to the formulation of the tensorial AMD model which permits reproducing the anisotropy of the flow. Focusing on the instantaneous fields of wall heat flux, the functional models lead to the most reliable simulations among those considered. Summarizing all the results, the tensorial version of the AMD model is the most efficient of the considered models for the study of a channel flow asymmetrically heated from both sides. The present paper permits confirming the good results of the tensorial AMD model obtained by David *et al.* in Ref. [229].

Acknowledgments

This work was granted access to the HPC resources of CINES under the allocation 2020-A0082A05099 made by GENCI. The authors acknowledge PRACE for awarding them access to Joliot-Curie at GENCI@CEA, France (PRACE Project : 2020225398). The authors gratefully acknowledge the CEA for the development of the TRUST platform. The authors gratefully acknowledge the Occitania region for their funding of the thesis grant.

Data Availability Statements

The data that support the findings of this study are available from the corresponding author upon reasonable request.

References

[2] S. Paolucci. "Filtering of Sound from the Navier-Stokes Equations." In: *NASA STI/Recon Technical Report N* 83 (1982).

[3] C. Calvin, O. Cueto, and P. Emonot. "An object-oriented approach to the design of fluid mechanics software". In: *ESAIM: Mathematical Modelling and Numerical Analysis - Modélisation Mathématique et Analyse Numérique* 36.5 (2002), pp. 907–921.

[4] F. Nicoud. "Conservative High-Order Finite-Difference Schemes for Low-Mach Number Flows". In: *Journal of Computational Physics* 158.1 (2000), pp. 71–97.

[6] B. P. Leonard. "A Stable and Accurate Convective Modelling Procedure Based on Quadratic Upstream Interpolation". In: *Computer Methods in Applied Mechanics and Engineering* 19.1 (1979), pp. 59–98.

[7] R. D. Moser, J. Kim, and N. N. Mansour. "Direct numerical simulation of turbulent channel flow up to Reτ=590". In: *Physics of Fluids* 11.4 (1999), pp. 943–945.

[9] M. Lee and R. D. Moser. "Direct Numerical Simulation of Turbulent Channel Flow up To". In: *Journal of Fluid Mechanics* 774 (2015), pp. 395–415.

[10] S. Hoyas and J. Jiménez. "Reynolds Number Effects on the Reynolds-Stress Budgets in Turbulent Channels". In: *Physics of Fluids* 20.10 (2008), p. 101511.

[11] G. S. Winckelmans, H. Jeanmart, and D. Carati. "On the Comparison of Turbulence Intensities from Large-Eddy Simulation with Those from Experiment or Direct Numerical Simulation". In: *Physics of Fluids* 14.5 (2002), pp. 1809–1811.

[12] L. B. Streher et al. "Mixed Modeling for Large-Eddy Simulation: The Single-Layer and Two-Layer Minimum-Dissipation-Bardina Models". In: *AIP Advances* 11.1 (2021), p. 015002.

[13] W. Rozema et al. "Minimum-Dissipation Models for Large-Eddy Simulation". In: *Physics of Fluids* 27.8 (2015), p. 085107.

[15] A. Leonard. "Energy Cascade in Large-Eddy Simulations of Turbulent Fluid Flows". In: *Advances in Geophysics*. Ed. by F. N. Frenkiel and R. E. Munn. Vol. 18. Turbulent Diffusion in Environmental Pollution. Elsevier, 1975, pp. 237–248.

[16] J. Bardina, J. Ferziger, and W. Reynolds. "Improved Subgrid-Scale Models for Large-Eddy Simulation". In: *13th Fluid and PlasmaDynamics Conference*. Fluid Dynamics and Co-Located Conferences. American Institute of Aeronautics and Astronautics, 1980.

[17] D. Dupuy, A. Toutant, and F. Bataille. "A Posteriori Tests of Subgrid-Scale Models in an Isothermal Turbulent Channel Flow". In: *Physics of Fluids* 31.4 (2019), p. 045105.

[21] D. Dupuy, A. Toutant, and F. Bataille. "Study of the Large-Eddy Simulation Subgrid Terms of a Low Mach Number Anisothermal Channel Flow". In: *International Journal of Thermal Sciences* 135 (2019), pp. 221–234.

[22] M. Abkar, H. J. Bae, and P. Moin. "Minimum-Dissipation Scalar Transport Model for Large-Eddy Simulation of Turbulent Flows". In: *Physical Review Fluids* 1.4 (2016), p. 041701.

[27] M. David, A. Toutant, and F. Bataille. "Numerical Development of Heat Transfer Correlation in Asymmetrically Heated Turbulent Channel Flow". In: *International Journal of Heat and Mass Transfer* 164 (2021), p. 120599.

[53] S. Singh, D. You, and S. T. Bose. "Large-Eddy Simulation of Turbulent Channel Flow Using Explicit Filtering and Dynamic Mixed Models". In: *Physics of Fluids* 24.8 (2012), p. 085105.

[56] X. Daguenet-Frick et al. "Numerical Investigation of a Ceramic High-Temperature Pressurized-Air Solar Receiver". In: *Solar Energy* 90 (2013), pp. 164–178.

[69] W. Sutherland. "The Viscosity of Gases and Molecular Force". In: *The London, Edinburgh, and Dublin Philosophical Magazine and Journal of Science* 36.223 (1893), pp. 507–531.

[78] C. Bailly and G. Comte-Bellot. *Turbulence*. Experimental Fluid Mechanics. Springer International Publishing, 2015. ISBN: 978-3-319-16159-4.

[108] B. J. Geurts. "Analysis of Errors Occurring in Large Eddy Simulation". In: *Philosophical Transactions of the Royal Society A: Mathematical, Physical and Engineering Sciences* 367.1899 (2009), pp. 2873–2883.

[114] G. S. Winckelmans et al. "Explicit-Filtering Large-Eddy Simulation Using the Tensor-Diffusivity Model Supplemented by a Dynamic Smagorinsky Term". In: *Physics of Fluids* 13.5 (2001), pp. 1385–1403.

[120] S. Ghosal. "An Analysis of Numerical Errors in Large-Eddy Simulations of Turbulence". In: *Journal of Computational Physics* 125.1 (1996), pp. 187–206.

[131] M. H. Silvis, R. A. Remmerswaal, and R. Verstappen. "Physical Consistency of Subgrid-Scale Models for Large-Eddy Simulation of Incompressible Turbulent Flows". In: *Physics of Fluids* 29.1 (2017), p. 015105.

[141] J. Smagorinsky. "General Circulation Experiments with the Primitive Equations". In: *Monthly Weather Review* 91.3 (1963), pp. 99–164.

[145] D. Dupuy, A. Toutant, and F. Bataille. "A Posteriori Tests of Subgrid-Scale Models in Strongly Anisothermal Turbulent Flows". In: *Physics of Fluids* 31.6 (2019), p. 065113.

[149] A. W. Vreman. "An Eddy-Viscosity Subgrid-Scale Model for Turbulent Shear Flow: Algebraic Theory and Applications". In: *Physics of Fluids* 16.10 (2004), pp. 3670–3681.

[150] F. Nicoud et al. "Using Singular Values to Build a Subgrid-Scale Model for Large Eddy Simulations". In: *Physics of Fluids* 23.8 (2011), p. 085106.

[151] S. Ryu and G. Iaccarino. "A Subgrid-Scale Eddy-Viscosity Model Based on the Volumetric Strain-Stretching". In: *Physics of Fluids* 26.6 (2014), p. 065107.

[152] R. Verstappen. "An Eddy-Viscosity Model Based on the Invariants of the Rate-of-Strain Tensor". In: *Direct and Large-Eddy Simulation VIII*. Ed. by H. Kuerten et al. ERCOFTAC Series. Dordrecht: Springer Netherlands, 2011, pp. 83–88. ISBN: 978-94-007-2482-2.

[153] F. X. Trias et al. "Building Proper Invariants for Eddy-Viscosity Subgrid-Scale Models". In: *Physics of Fluids* 27.6 (2015), p. 065103.

[156] K. Horiuti. "A New Dynamic Two-Parameter Mixed Model for Large-Eddy Simulation". In: *Physics of Fluids* 9.11 (1997), pp. 3443–3464.

[157] B. Vreman, B. Geurts, and H. Kuerten. "On the Formulation of the Dynamic Mixed Subgrid-scale Model". In: *Physics of Fluids* 6.12 (1994), pp. 4057–4059.

[160] D. Dupuy, A. Toutant, and F. Bataille. "A Priori Tests of Subgrid-Scale Models in an Anisothermal Turbulent Channel Flow at Low Mach Number". In: *International Journal of Thermal Sciences* 145 (2019), p. 105999.

[171] S. Rezaeiravesh and M. Liefvendahl. "Effect of Grid Resolution on Large Eddy Simulation of Wall-Bounded Turbulence". In: *Physics of Fluids* 30 (2018).

[176] M. O. Deville and T. B. Gatski. *Mathematical Modeling for Complex Fluids and Flows*. Berlin, Heidelberg: Springer Berlin Heidelberg, 2012. ISBN: 978-3-642-25294-5 978-3-642-25295-2.

[188] S. Serra, A. Toutant, and F. Bataille. "Thermal Large Eddy Simulation in a Very Simplified Geometry of a Solar Receiver". In: *Heat Transfer Engineering* 33.6 (2012), pp. 505–524.

[190] L. D. Dailey, N. Meng, and R. H. Pletcher. "Large Eddy Simulation of Constant Heat Flux Turbulent Channel Flow With Property Variations: Quasi-Developed Model and Mean Flow Results". In: *Journal of Heat Transfer* 125.1 (2003), pp. 27–38.

[193] W.-P. Wang and R. H. Pletcher. "On the Large Eddy Simulation of a Turbulent Channel Flow with Significant Heat Transfer". In: *Physics of Fluids* 8.12 (1996), pp. 3354–3366.

[195] B. Lessani and M. V. Papalexandris. "Numerical Study of Turbulent Channel Flow with Strong Temperature Gradients". In: *International Journal of Numerical Methods for Heat & Fluid Flow* 18.3/4 (2008). Ed. by A. J. Nowak and R. A. Białecki, pp. 545–556.

[196] M. Bellec, A. Toutant, and G. Olalde. "Large Eddy Simulations of Thermal Boundary Layer Developments in a Turbulent Channel Flow under Asymmetrical Heating". In: *Computers & Fluids*. A Special Issue in Honor of Cecil "Chuck" E. Leith 151 (2017), pp. 159–176.

[197] S. M. Yahya, S. F. Anwer, and S. Sanghi. "Turbulent Forced Convective Flow in an Anisothermal Channel". In: *International Journal of Thermal Sciences* 88 (2015), pp. 84–95.

[204] S. Stolz, N. A. Adams, and L. Kleiser. "An Approximate Deconvolution Model for Large-Eddy Simulation with Application to Incompressible Wall-Bounded Flows". In: *Physics of Fluids* 13.4 (2001), pp. 997–1015.

[207] M. V. Papalexandris. "On the Applicability of Stokes' Hypothesis to Low-Mach-Number Flows". In: *Continuum Mechanics and Thermodynamics* 32.4 (2020), pp. 1245–1249.

[208] P. Sagaut. *Large Eddy Simulation for Incompressible Flows*. 3ème. Springer, 1998.

[211] J. M. Avellaneda, F. Bataille, and A. Toutant. "DNS of Turbulent Low Mach Channel Flow under Asymmetric High Temperature Gradient: Effect of Thermal Boundary Condition on Turbulence Statistics". In: *International Journal of Heat and Fluid Flow* 77 (2019), pp. 40–47.

[213] A. Toutant. "Numerical Simulations of Unsteady Viscous Incompressible Flows Using General Pressure Equation". In: *Journal of Computational Physics* 374 (2018), pp. 822–842.

[214] F. Aulery et al. "Spectral Analysis of Turbulence in Anisothermal Channel Flows". In: *Computers & Fluids*. A Special Issue in Honor of Cecil "Chuck" E. Leith 151 (2017), pp. 115–131.

[216] V. Boutrouche et al. "Influence of the Turbulence Model for Channel Flows with Strong Transverse Temperature Gradients". In: *International Journal of Heat and Fluid Flow* 70 (2018), pp. 79–103.

[218] N. Silin et al. "Hydrodynamic Transition Delay in Rectangular Channels under High Heat Flux". In: *Annals of Nuclear Energy* 37.4 (2010), pp. 615–620.

[219] Z. Wang et al. "Numerical Study on Laminar-Turbulent Transition Flow in Rectangular Channels of a Nuclear Reactor". In: *Frontiers in Energy Research* 8 (2020).

[220] M. M. Sorour and Z. A. Mottaleb. "Performances of Channel-Type Flat-Plate Solar Energy Air-Heaters". In: *Applied Energy* 18.1 (1984), pp. 1–13.

[221] X. Daguenet-Frick et al. "Experimental Analysis of the Turbulent Flow Behavior of a Textured Surface Proposed for Asymmetric Heat Exchangers". In: *Flow, Turbulence and Combustion* 89.1 (2012), pp. 149–169.

[222] A. Colleoni et al. "Optimization of Winglet Vortex Generators Combined with Riblets for Wall/Fluid Heat Exchange Enhancement". In: *Applied Thermal Engineering* 50.1 (2013), pp. 1092–1100.

[223] J. Kim, P. Moin, and R. Moser. "Turbulence Statistics in Fully Developed Channel Flow at Low Reynolds Number". In: *Journal of Fluid Mechanics* 177 (1987), pp. 133–166.

[224] O. Cabrit and F. Nicoud. "DNS of a Periodic Channel Flow with Isothermal Ablative Wall". In: *Direct and Large-Eddy Simulation VII*. Ed. by V. Armenio, B. Geurts, and J. Fröhlich. ERCOFTAC Series. Springer Netherlands, 2010, pp. 33–39. ISBN: 978-90-481-3652-0.

[225] Y. Morinishi, S. Tamano, and K. Nakabayashi. "Direct Numerical Simulation of Compressible Turbulent Channel Flow between Adiabatic and Isothermal Walls". In: *Journal of Fluid Mechanics* 502 (2004), pp. 273–308.

[226] J. C. D. Álamo et al. "Scaling of the Energy Spectra of Turbulent Channels". In: *Journal of Fluid Mechanics* 500 (2004), pp. 135–144.

[227] S. Hoyas and J. Jiménez. "Scaling of the Velocity Fluctuations in Turbulent Channels up to Reτ=2003". In: *Physics of Fluids* 18.1 (2006), p. 011702.

[228] H. Kawamura, H. Abe, and Y. Matsuo. "DNS of Turbulent Heat Transfer in Channel Flow with Respect to Reynolds and Prandtl Number Effects". In: *International Journal of Heat and Fluid Flow* 20.3 (1999), pp. 196–207.

[229] M. David, A. Toutant, and F. Bataille. "Investigation of Thermal Large-Eddy Simulation Approaches in a Highly Turbulent Channel Flow Submitted to Strong Asymmetric Heating". In: *Physics of Fluids* 33.4 (2021), p. 045104.

[230] Y. Zhiyin. "Large-Eddy Simulation: Past, Present and the Future". In: *Chinese Journal of Aeronautics* 28.1 (2015), pp. 11–24.

[231] F. Nicoud and F. Ducros. "Subgrid-Scale Stress Modelling Based on the Square of the Velocity Gradient Tensor". In: *Flow, Turbulence and Combustion* 62.3 (1999), pp. 183–200.

[232] M. Kim et al. "Assessment of the Wall-Adapting Local Eddy-Viscosity Model in Transitional Boundary Layer". In: *Computer Methods in Applied Mechanics and Engineering* 371 (2020), p. 113287.

[233] H. Kobayashi. "The Subgrid-Scale Models Based on Coherent Structures for Rotating Homogeneous Turbulence and Turbulent Channel Flow". In: *Physics of Fluids* 17.4 (2005), p. 045104.

[234] O. Métais and M. Lesieur. "Spectral Large-Eddy Simulation of Isotropic and Stably Stratified Turbulence". In: *Journal of Fluid Mechanics* 239 (1992), pp. 157–194.

[235] B. Aupoix. "Subgrid Scale Models for Homogeneous Anisotropic Turbulence". In: *Direct and Large Eddy Simulation of Turbulence: Proceedings of the EUROMECH Colloquium No. 199, München, FRG, September 30 to October 2, 1985*. Ed. by U. Schumann and R. Friedrich. Notes on Numerical Fluid Mechanics. Wiesbaden: Vieweg+Teubner Verlag, 1986, pp. 37–66. ISBN: 978-3-663-00197-3.

[236] H. Lu and C. J. Rutland. "Structural Subgrid-Scale Modeling for Large-Eddy Simulation: A Review". In: *Acta Mechanica Sinica* 32.4 (2016), pp. 567–578.

[237] R. Anderson and C. Meneveau. "Effects of the Similarity Model in Finite-Difference LES of Isotropic Turbulence Using a Lagrangian Dynamic Mixed Model". In: *Flow, Turbulence and Combustion* 62.3 (1999), pp. 201–225.

[238] R. Akhavan et al. "Subgrid-Scale Interactions in a Numerically Simulated Planar Turbulent Jet and Implications for Modelling". In: *Journal of Fluid Mechanics* 408 (2000), pp. 83–120.

[239] C. Meneveau and J. Katz. "Scale-Invariance and Turbulence Models for Large-Eddy Simulation". In: *Annual Review of Fluid Mechanics* 32.1 (2000), pp. 1–32.

[240] S. Serra et al. "High-Temperature Gradient Effect on a Turbulent Channel Flow Using Thermal Large-Eddy Simulation in Physical and Spectral Spaces". In: *Journal of Turbulence* 13 (2012), N49.

[241] T. M. Eidson. "Numerical Simulation of the Turbulent Rayleigh–Bénard Problem Using Subgrid Modelling". In: *Journal of Fluid Mechanics* 158 (1985), pp. 245–268.

[242] A. Rasam, G. Brethouwer, and A. V. Johansson. "An Explicit Algebraic Model for the Subgrid-Scale Passive Scalar Flux". In: *Journal of Fluid Mechanics* 721 (2013), pp. 541–577.

[243] B.-C. Wang et al. "A General Dynamic Linear Tensor-Diffusivity Subgrid-Scale Heat Flux Model for Large-Eddy Simulation of Turbulent Thermal Flows". In: *Numerical Heat Transfer, Part B: Fundamentals* 51.3 (2007), pp. 205–227.

[244] B.-C. Wang et al. "A Complete and Irreducible Dynamic SGS Heat-Flux Modelling Based on the Strain Rate Tensor for Large-Eddy Simulation of Thermal Convection". In: *International Journal of Heat and Fluid Flow*. Revised and Extended Papers from the 5th Conference in Turbulence, Heat and Mass Transfer 28.6 (2007), pp. 1227–1243.

[245] B.-C. Wang et al. "New Dynamic Subgrid-Scale Heat Flux Models for Large-Eddy Simulation of Thermal Convection Based on the General Gradient Diffusion Hypothesis". In: *Journal of Fluid Mechanics* 604 (2008), pp. 125–163.

[246] S.-H. Peng and L. Davidson. "On a Subgrid-Scale Heat Flux Model for Large Eddy Simulation of Turbulent Thermal Flow". In: *International Journal of Heat and Mass Transfer* 45.7 (2002), pp. 1393–1405.

[247] F. Ries et al. "A Wall-Adapted Anisotropic Heat Flux Model for Large Eddy Simulations of Complex Turbulent Thermal Flows". In: *Flow, Turbulence and Combustion* 106.2 (2021), pp. 733–752.

[248] A. Patel et al. "Semi-Local Scaling and Turbulence Modulation in Variable Property Turbulent Channel Flows". In: *Physics of Fluids* 27.9 (2015), p. 095101.

[249] A. Toutant and F. Bataille. "Turbulence Statistics in a Fully Developed Channel Flow Submitted to a High Temperature Gradient". In: *International Journal of Thermal Sciences* 74 (2013), pp. 104–118.

[250] A. Patel, B. J. Boersma, and R. Pecnik. "Scalar Statistics in Variable Property Turbulent Channel Flows". In: *Physical Review Fluids* 2.8 (2017), p. 084604.

[251] M. Lesieur. *Turbulence in Fluids*. Third. Fluid Mechanics and Its Applications. Springer Netherlands, 1997. ISBN: 978-94-010-9018-6.

[252] F. Kremer and C. Bogey. "Large-Eddy Simulation of Turbulent Channel Flow Using Relaxation Filtering: Resolution Requirement and Reynolds Number Effects". In: *Computers & Fluids* 116 (2015), pp. 17–28.

[253] L. Wang et al. "Large Eddy Simulation of Turbulent Heat Transfer in a Non-Isothermal Channel: Effects of Temperature-Dependent Viscosity and Thermal Conductivity". In: *International Journal of Thermal Sciences* 146 (2019), p. 106094.

4.4 Comparison of the thermal-large eddy simulation results in both heating conditions

In this section, the effects of the two different types of heating studied in sections 8.2.4.2 and 8.2.4.2 are compared. In both cases, the mean friction Reynolds number is around 810 and the wall temperatures are fixed to 900 K for the cold wall and 1300 K for the hot wall. The first heating condition involves a fluid temperature quasi-equal to the average of the wall temperature and corresponds to a temperature profile obtained in an infinitely long solar receiver. The second heating condition is characterized by a mean fluid temperature below the cold wall temperature and represents a temperature profile that could be encountered in a real solar receiver. These two configurations induce opposite directions of the velocity in the wall-normal direction near the cold wall. For practical reasons, the associated simulations are respectively denoted as low fluid temperature (LT) and high fluid temperature (HT). They respectively correspond to heat sources of $H_s = 55$ MW/m^3 and $H_s = 0$. In the first case, the heat source removes heat from the flow which leads to the lowering of the fluid temperature. The Reynolds numbers, based on the hydraulic diameter and the bulk velocity, are 82 000 for the LT simulations and 60 000 for the HT simulations. The wall-normal profiles of the T-LES obtained in the different heating conditions are compared.

4.4.1 First-order statistics

First-order statistics give the global behavior of the flow. Figure 4.27 exposes the wall-normal profiles of streamwise, wall-normal, and temperature. The results show that the streamwise velocity is mitigated in the simulation with low fluid temperature. The wall-normal velocity profile is substantially affected by the temperature distribution. Indeed, while it is negative and with the same magnitude in the case without source term, the wall-normal velocity is asymmetric in the low-temperature case. On the hot side, the magnitude is almost three times higher in the simulation with the heat source. On the cold side, the wall-normal velocity is opposed between the two studied heating conditions. In the [LT] configuration, two peaks are observed around $y^+ = 50$. The wall-normal velocity cancels out in the cold side around $y^+ = 500$. The dimensionless temperature profiles exhibit similar profiles until $y^+ = 10$ for the hot side and $y^+ = 6$ for the cold side. In the [LT] case, the temperature reach a minimum around $y^+ = 500$ which coincides with the null wall-normal velocity. Regarding the LES results, the tendency of each profile is respected. The AMD model tends to overestimate the streamwise velocity profile while the other LES are relatively accurate. The wall-normal velocity is better predicted by the LES with functional models. The LES results seems to be improved when the temperature gradient is high. The temperature profiles are better approximated by the tensorial AMD model. Overall, the quality of the estimation provided by each model depend on the heating conditions but the performance of the models between each other is poorly influenced by the thermal configuration.

4.4.2 Second-order statistics

Second-order statistics permit investigating the flow in detail. The velocity correlations give information on the turbulent scales. They are exposed in Figure 4.28. The correlations of streamwise, spanwise, and wall-normal velocities are quite similar: they follow a bell shape and reach a maximum of magnitude around $y^+ = 13$. The DNS carried out with a source term,

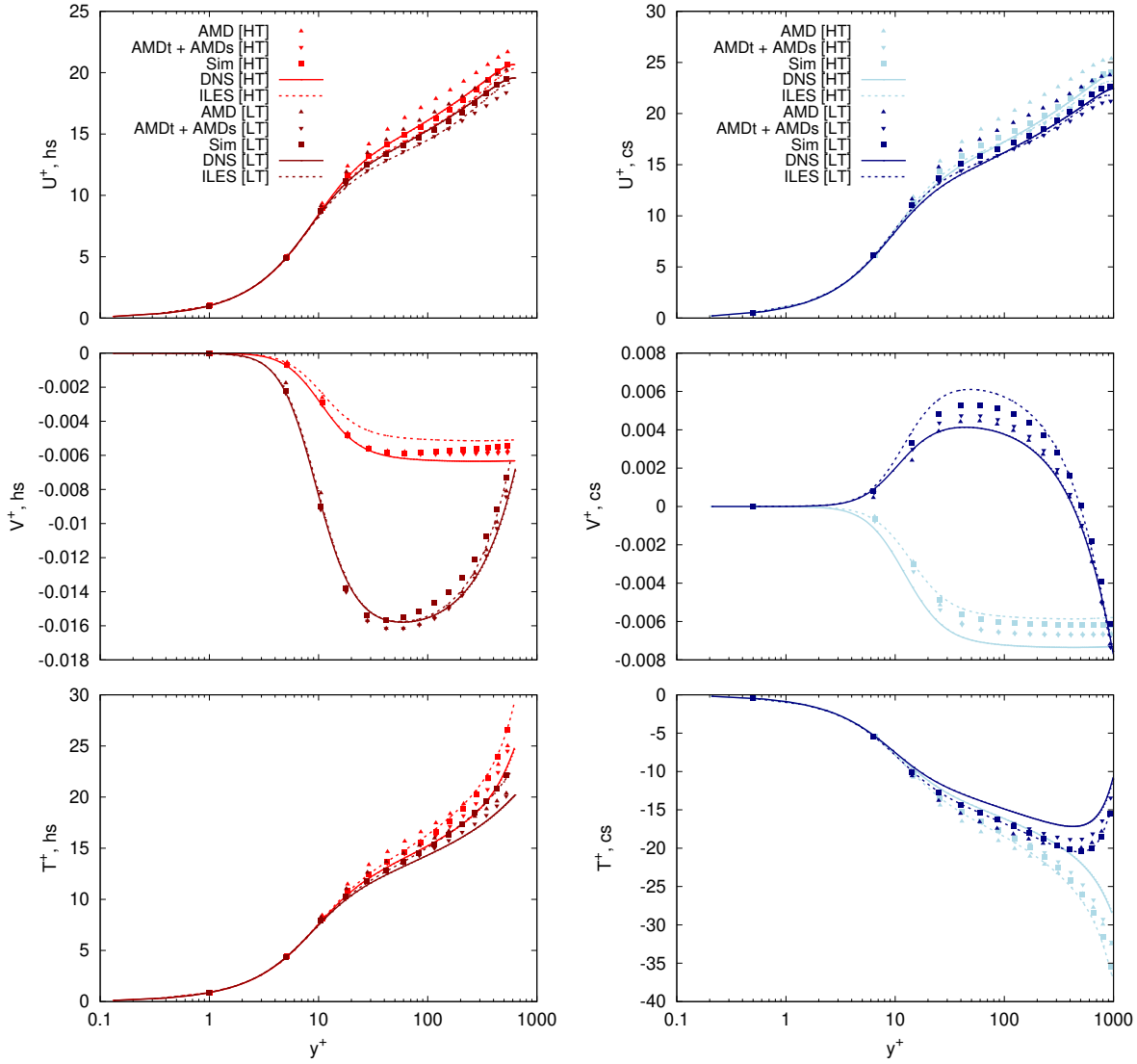

Figure 4.27 – Wall-normal profiles of mean quantities. The hot, respectively cold, profiles are plotted on the left, respectively right.

"DNS [LT]" exhibits lower velocity fluctuations than the simulation "DNS [HT]" and the peak is reached slightly closer to the walls. The extrema of the $\langle u'v' \rangle^+$ correlation are also mitigated when compared to the DNS without source term. The LES tend to overestimate the streamwise, spanwise, and wall-normal velocity correlations. The scale-similarity model seems to be not enough dissipative which explains its significant overestimation of the peaks. The tensorial AMD model produces the best results on these values. The tensorial formulation permits improving the results of the AMD model and is able to capture the anisotropy of the flow. The cross-velocity correlation is well approximated by all the LES models.

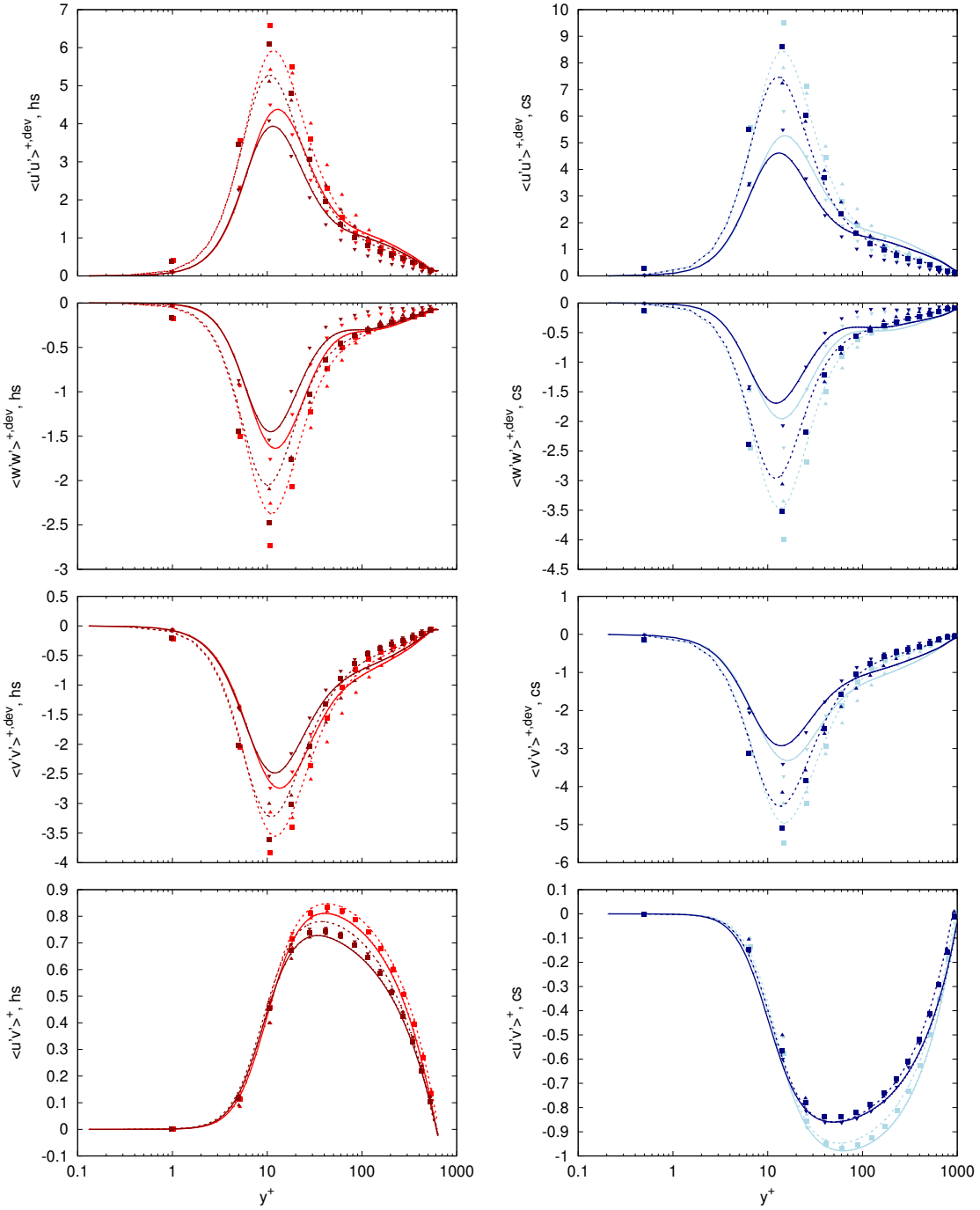

Figure 4.28 – Wall-normal profiles of velocity correlations. The hot, respectively cold, profiles are plotted on the left, respectively right.

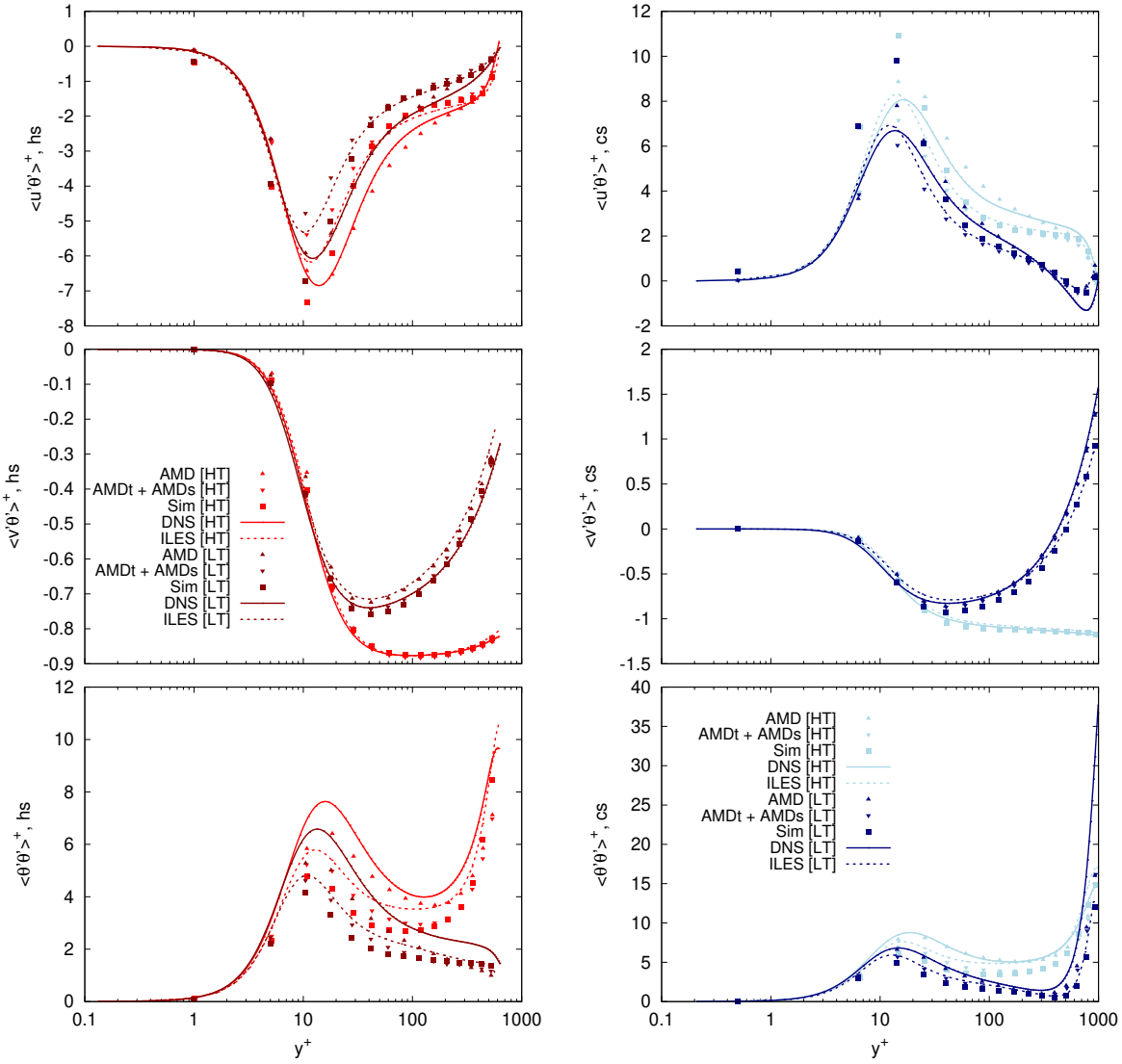

Figure 4.29 – Wall-normal profiles of correlations involving temperature. The hot, respectively cold, profiles are plotted on the left, respectively right.

The correlations involving the temperature are given in Figure 4.29. The DNS results show that the magnitude of the correlation of streamwise velocity and temperature is mitigated in the case of the DNS with the source term. The peaks are slightly shifted toward the walls. On the cold side, a secondary peak is observed close to the center of the channel. It is due to the temperature distribution. The correlation of wall-normal velocity and temperature is significantly influenced by the heat source. In the simulation with a lower bulk temperature than the cold wall temperature, the profile becomes positive on the cold side after $y^+ = 450$. On the hot side, it reaches a minimum at $y^+ = 50$. The temperature fluctuations are given on the bottom graph.

They exhibit a peak around $y^+ = 13$, as for the velocity correlations. Once again, in the "DNS [LT]", the peak is reached slightly closer to the wall. In the simulation "DNS [HT]" a third peak is observed in the center of the channel while in the simulation with a heat source, it does not exist due to the highly asymmetric temperature fluctuations, see section 4.3.5.2. The minimum is obtained for $y^+ = 300$. The AMD model and the tensorial AMD model produce satisfying results on the correlation of streamwise velocity and temperature. All the models produce quite good estimations of the correlation of wall-normal and temperature, the tensorial AMD model provides the most accurate estimation on both sides. The temperature fluctuations are poorly approximated by the LES. The AMD model is the closest to the DNS results.

The comparison of the LES performance on the second-order statistics shows that, as for the first-order statistics, the quality of the approximation provided by each model is weakly dependent on the heating conditions.

4.5 Conclusion of chapter 4

In this chapter, anisothermal Large Eddy Simulations (LES) have been performed in anisothermal channel flows. Two wall-normal distributions of temperature profiles have been studied corresponding to mean fluid temperatures of 1094 K for the case without heat source and 883 K in the other case. The wall-normal velocity profile and wall heat fluxes are directly affected by these modifications. The quantities appearing in the balance of the momentum equation exhibit particular behavior (inflection or vanishing) on the hot side of the channel relatively close to the geometric center. On the contrary, the quantities involved in the balance of the energy equation show inflection or vanishing on the cold side, at mid-length between the cold wall and the geometric center of the channel. A RMS of wall heat flux to mean heat flux ratio of 0.43 is observed on both walls of the two studied anisothermal conditions.

The LES wall-normal profiles of first- and second-order statistics have been compared to those of Direct Numerical Simulations (DNS) performed in the same conditions. Two numerical schemes have been tested for the discretization of the mass and momentum convection terms. The results show that, with the chosen LES mesh refinement, the truncation error induced by the scheme used for the approximation of the momentum convection term has a similar impact on the velocity fluctuations than the turbulence model. Similarly, the truncation error induced by the numerical scheme used to approximate the mass convection term is at least as important as the turbulence model influence on the wall-normal velocities and the wall heat fluxes.

The performances of the LES turbulence models are only slightly influenced by the type of heating on the streamwise velocity and the velocity fluctuations. The first-order statistics are better predicted than the second-order statistics. Globally, the tensorial version of the AMD model produces the best results in the three studied conditions. Its formulation allows reproducing the strong anisotropy of the flow, leading to an improvement of the results and particularly the velocity fluctuations. The T-LES tend to under-estimate the wall heat flux but the LES instantaneous fields of wall heat fluxes exhibit structures similar to those of the DNS.

The achievement of a DNS in the proper working conditions of solar receivers provides rich information on the flow. These data could be used for the design and the optimization of future solar receivers. In this thesis, they have been used to assess LES. These *a posteriori* tests of LES subgrid scale models in those particular conditions represent a first in the literature and show that there is room for improvement to fit the wall-normal profiles of DNS but the best LES models well represent most of the observed phenomena. They permit making the connection

between the reference data and applied studies. In part II, LES have been used to develop a heat transfer correlation.

Chapter 5

Conclusion of part I

This part addresses the micro- and meso-scales levels of the multi-scale approach carried out in this thesis. The Direct Numerical Simulations (DNS) provide reference data that permit analyzing the flow physics and assessing the LES subgrid-scale models. The Large Eddy Simulations (LES), which are significantly less costly, can be used to test more complex geometries or to perform parametric studies.

The simulations have been carried out in highly turbulent channel flows at a cold friction Reynolds number of about 950. The two walls of the channel create an inhomogeneity in the wall-normal direction which drives the physic of the flow. Studies have been achieved under both isothermal and anisothermal conditions. The DNS performed in the isothermal conditions exhibits features of high Reynolds number flows. The very large scale structures induce a reduction of the decrease of the velocity fluctuations in the region $70 < y^+ < 200$. This is particularly pronounced for the deviatoric part of the fluctuations of the spanwise velocity. For the anisothermal configuration, two fluid temperature profiles have been investigated. The modification of the fluid temperature induces major changes in the flow behavior. Particularly, the wall-normal velocity at the cold wall changes direction and the wall-normal velocity of the hot side is increased. The wall heat fluxes and the temperature fluctuations are significantly influenced. These modifications affect the second-order statistics.

The LES wall-normal profiles of first- and second-order statistics have been assessed thanks to those of DNS carried out in the same conditions. The study of the numerical schemes employed for the discretization of the mass and momentum convection terms show that the error committed by changing the scheme used is comparable with the effect of the subgrid-scale model on the quantities directly influenced by the discretized term. The performance of the LES turbulence models are globally satisfying. Their efficiency is influenced by the studied conditions. Indeed, the results are better when the temperature gradient is higher. The performance of the models between each others are weakly influenced by the studied configuration. No major difference between the DNS and LES results is observed. Globally, the tensorial version of the AMD model produces the best results in the three studied conditions. Its formulation allows reproducing the strong anisotropy of the flow, leading to an improvement of the results and particularly the velocity fluctuations. The LES tend to under-estimate the wall heat flux but their instantaneous fields of wall heat fluxes exhibit structures similar to those of the DNS.

Flow behaviors have been analyzed thanks to the comparison of DNS performed in various conditions and LES turbulence models have been assessed in those conditions. The DNS produce

useful information that permit testing the subgrid-scale models and could be used to propose optimizations of the solar receiver. The *a posteriori* tests of LES highlight the strengths and weaknesses of the subgrid-scale models in those particular conditions. In the proposed multi-scale approach, LES is the link between the upstream method represented DNS and the more applied tools that permit performing studies at the component scale. Part II addresses the development and the use of a heat transfer correlation.

Part II

Heat transfer correlation for asymmetrically heated channel flows

The present part addresses the macro-scale of the multi-scale approach. Chapter 6 provides general information on convective heat transfers. In chapter 7, a heat transfer correlation dedicated to solar receivers is developed thanks to the LES. In chapter 8, the correlation is used to investigate the wall heat flux sensitivity to the flow parameters. Chapter 9 concludes on the results obtained with the proposed heat transfer correlation.

Chapter 6

Introduction to convective heat transfers

The energy transport combining the effects of heat conduction and the movement of fluid is referred to as convective heat transfer. This type of transport is ubiquitous in many engineering systems. To study those exchanges, the fluid motions have to be investigated simultaneously with the heat transport process. The description of the fluid motions theoretically requires analyze of the behavior of all the particles that constitute the fluid. Hence, the laws of mechanics and thermodynamics should be applied to each particle to accurately detail the energy transfer processes. However, this approach is often impracticable and is not necessary for most of the engineering problems [254].

Convective transfers can be divided into natural convection (or free convection), forced convection, and mixed convection. In natural convection, the fluid motion is induced by its variations of density which can be due to either temperature or concentration gradients. Natural convection is widely encountered in natural phenomena such as the thermohaline circulation occurring in the oceans and in engineering systems such as solar water heaters or passive household ventilation [255]. The Rayleigh number, defined as the product of the Grashof and the Prandtl numbers, is often used to quantify free convection, it can be seen as the product of the ratio of buoyancy and viscosity forces and the ratio of momentum and thermal diffusivities [256]. In forced convection the flow motions are generated by an external source such as fans or pump. It allows to transport significant amounts of heat energy very efficiently and is then very common in engineering devices such as heat exchangers. The relevant dimensionless numbers associated with forced convection are the Reynolds number and the Prandtl number [257]. Fundamentally, forced convection is always superimposed on natural convection. The dominant type of convection can be determined by the Richardson number which expresses the ratio between the Grashof and the squared Reynolds number. In the case where they are similar, the regime is called mixed convection. In the studied concentrated solar power systems, despite the high temperature gradients encountered, the flow is driven by the forced convection. Indeed, the Richardson number is about 10^{-5}.

To facilitate the implantation of the concentrated solar power tower in the global energy mix, applied computation tools have to be developed. Heat transfer correlations are simple expressions that instantaneously provide an approximation of the wall-to-fluid heat exchange. Most correlations dealing with forced convection found in the literature produce results within

20% error in their validity domain. These levels of accuracy permit using the heat transfer correlations to perform feasibility studies, pre-sizing, and wall heat flux sensitivity analyzes of systems among other possibilities.

This part relies on the *a posteriori* tests of highly turbulent channel flows asymmetrically heated, taking account the coupling between the temperature and the dynamic of the flows, that have been performed in part I. Those tests themselves draw on the achievement of the DNS. In the present part, the LES are used for the purpose of providing simple a tool that permit investigating the wall heat fluxes in gas-pressurized solar receivers. Indeed, the heat transfer correlations of the literature are not applicable in the operating conditions of the solar receiver. Particularly, the asymmetric heating of the fluid is not considered in the existing correlations. The developed heat transfer correlation represents the last link of the multi-scale approach achieved in this thesis. In chapter 7, a heat transfer correlation applicable in the operating conditions of gas-pressurized solar receivers is developed and compared to heat transfer correlations of the literature. In chapter 8, the proposed correlation is used to investigate the wall heat flux sensitivity to the misestimation of the flow parameters.

Chapter 7

Numerical development of heat transfer correlation in asymmetrically heated turbulent channel flows

Contents

7.1 Introduction of chapter 7

Heat transfer correlations permit facilitating the pre-sizing of systems and thus increasing the development of these technologies. They are determined thanks to theoretical method, experimental data, or numerical simulations. Analytical solutions are limited to very simple laminar flows, that is why they cannot be used in most engineering fields. Experiments are classically

carried out to obtain data used to develop correlations. However, they suffer from their very high cost and the uncertainty of measurements. With the increase of computer power, numerical simulations became good mean to obtain data for the purpose of developing a correlation. Particularly, in relatively simple geometry, accurate results can be obtained at a reasonable cost.

Heat transfer correlations are developed for a particular geometry and applicable domain. In the literature, there exist heat transfer correlations applicable in forced convection and dedicated to external flows such as flows over horizontal plates (see for instance the recent correlations proposed by Lienhard for laminar, transitional and turbulent flows [258]) or flows over cylinders [259]. Heat transfer correlations for internal flows are mostly developed for pipes [260, 25]. Other geometries are also investigated but to a lesser extent.

In this chapter, a heat transfer correlation for asymmetrically heated turbulent channel flow is developed thanks to Large Eddy Simulations (LES). This heat transfer correlation represents the last link of the multi-scale approach proposed in this thesis since it permits performing studies at the component scale. The studied conditions are inspired by the operating range of gas-pressurized solar receivers, which are a Reynolds number of approximately 10^5, hot and cold wall temperatures around respectively 1300 K and 900 K, and a thermodynamical pressure of about 10 bars.

7.2 Paper 3: Numerical development of heat transfer correlation in asymmetrically heated turbulent channel flow

This section reproduces the paper of M. David, A. Toutant, and F. Bataille untitled Numerical development of heat transfer correlation in asymmetrically heated turbulent channel flow and published in *International Journal of Heat and Mass Transfer*.

Abstract

This study deals with forced convective heat transfer. It is divided into two parts. Firstly, a review of heat transfer involving forced convection in tubes and channels is proposed. In the case of channel geometry, studies dealing with symmetrically and asymmetrically heated flows as well as one side heated flows are reported. Then, a new correlation for symmetrically and asymmetrically heated channels associated with a turbulent flow is developed using Large Eddy Simulations. The Proposed Correlation, also referred to as PC, involves a specific term to handle asymmetric conditions. The domain covered by simulations is the following: heat fluxes vary between 4 and 580 kW/m^2, Prandtl number ranges from 0.76 to 3.18 and bulk Reynolds number from 10 600 to 177 000. Three correlations of the literature are compared to the one proposed in this paper. The conventional expressions tend to overestimate the Nusselt number at the hot side of asymmetrically heated channel independently of the temperature ratio. They, also, underestimate the heat transfer at the cold side, especially when the bulk temperature is close to the cold wall temperature. The proposed correlation provides great results in both heating conditions. The global accuracy associated with each correlation is quantified.

7.2.1 Introduction

Forced convective heat transfers through rectangular ducts are commonly studied in engineering field to design systems such as heat exchangers [261, 262, 263, 264, 265, 266] , nuclear reactors [267, 268], nuclear waste repositories [269], electronic devices [270] and solar receivers [271, 61, 59,

60, 56] among others. Heat transfer correlations are widely used to estimate the heat flux between fluid and surface. These expressions mostly depend on the geometry, the working fluid and the operating conditions. Laminar flow characteristics can be calculated with analytic solutions considering few assumptions. However, for turbulent flows, experimental data or numerical simulations are required to estimate heat transfer.

Large Eddy Simulation (LES) is a numerical approach in which Navier-Stokes equations are solved in every cell of a discretized three-dimensional domain. It allows to precisely estimate time dependent flow characteristics with a reasonable calculation cost, compared to Direct Numerical Simulations (DNS), by resolving larger scales of motion and modeling small scale effects on the larger scales [141, 162, 272, 273, 15]. LES is, then, very suitable to produce heat transfer results in various conditions.

Results produced need to be averaged in space and time to provide an estimation of the heat fluxes. The calculation time and the procedure required to convert raw data into usable results are still obstacles for most of engineering companies. For that reasons, LES is commonly used by researchers in order to provide more adapted tools to engineering domain such as heat transfer correlations.

Asymmetrically heated channels are of particular interest in many of the engineering fields discussed above; especially in the concentrated solar power plant for which only the irradiated wall of the receiver is subjected to a very strong solar flux which leads to asymmetric heating of the fluid [221, 274, 188]. To the authors' knowledge, there are very few studies dealing with turbulent flows in asymmetrically heated channels, despite its frequent use, and no correlation has been developed in these difficult to study but widely encountered conditions. The present investigation has been undertaken to fulfill this gap in the literature.

A review of existing studies dealing with forced convection heat transfer for tube and channel geometries is presented in section 1. In section 2, the method and the characteristics of performed numerical simulations are explained. Then, in section 3, a correlation for asymmetrically heated channels under turbulent flow conditions is proposed and compared with selected correlations from the literature. In section 4, conclusions are drawn.

7.2.2 Forced convection heat transfer in the literature

Studies relative to heat transfer in tubes are presented in subsection 7.2.2.1. Subsection 7.2.2.2 deals with heat transfer in channels.

7.2.2.1 Heat transfer in tubes

In 1933, Colburn proposed a first general method for the correlation of forced convection heat transfer and pressure drop [24]. He links the Nusselt number to the Reynolds and Prandtl numbers. Film properties are involved and the correlation is applicable for a Reynolds number upper than 10000 and a Prandtl number ranging from 0.6 to 160. However, Colburn expresses doubts on the validity of his correlation for $Pr_b > 100$. Since this pioneer paper on heat and mass transfer, a plethora of articles has been published to estimate heat transfer in various conditions. Sieder and Tate [260] base their work on Colburn's study. They propose to simplify the correlation of the latter using mainstream properties instead of film values and use a ratio of dynamic viscosity to permit estimating heating as well as cooling conditions. The applicable domain is similar to the one proposed by Colburn. Whitaker [275] investigates forced convection heat transfer correlation for flows in pipes as well as flows past flat plate, single-cylinder, single-sphere and flow in packed beds and tubes bundles. He proposes a heat transfer correlation for

each condition. The tested Prandtl numbers depend on the geometry but it covers at least the range $0.71 < Pr_b < 380$ (excepted for the flow in packed beds where only a Prandtl number equal to 0.7 is assessed). In 1976, Gnielinski [26] modified the correlation of Petukhov [276] and proposed a new equation for heat transfer in turbulent pipe flows. Dittus and Boetler [25] investigate heat transfer in automobile radiators of the tubular type. They propose to adapt the exponent of the Prandtl number to the heat transfer direction. Barnes and Jackson [277] study air, carbon dioxide and helium flows in circular tubes with large surface/gas temperature ratio. Experiments are performed under approximately uniform wall heat flux, low subsonic turbulent flow and fully developed profiles of velocity and temperature. Their work aims at measuring the effect of temperature ratio on Nusselt number for various fluids. Tests are performed in the range $4000 < Re_b < 60000$. An increase of the surface/gas temperature ratio leads to a reduction of the Nusselt number for a given Reynolds number. They propose a new correlation for each fluid. The expression developed for air was numerically tested by Dailey *et al.* [190] with a constant wall heating rate. It gives satisfying results for low and high fluid heating in turbulent channel flows. Gnielinski [278] moves forward heat transfer in tube flows and pointed out that there is no efficient correlation in this region due to the gap in the Nusselt number at $Re_b = 2300$. To fulfill this shortage in the literature, he realizes a linear interpolation of the Nusselt number between $Re_b = 2300$ and $Re_b = 4000$ using existing correlations. Experimental investigation of circular pipe flow is performed by Bertsche *et al.* [279] in the range $500 < Re_b < 23000$ and $7 < Pr_b < 41$. The correlations of Gnielinski [280, 278] and Petukhov [276] are assessed. A good agreement is found. Recently, Taler [281] provides simple correlations to estimate heat transfer in turbulent tube flow for three various Prandtl number ranges: $0.1 < Pr_b < 1$, $1 < Pr_b < 3$ and $3 < Pr_b < 1000$. The exponent of the Prandtl number and the multiplicative constant decrease when the Prandtl number grows. The exponent of the Reynolds number evolves in the opposite way. The presented correlations are summarized in Table 7.1. Note that tube sections are the most well documented in terms of correlations. These correlations are sometimes used for rectangular geometries.

A graphical view of the applicable domain, in terms of Reynolds and Prandtl numbers, of each tube correlations is presented in Fig. 7.1. The existing correlations cover large ranges of Prandtl and Reynolds numbers.

7.2.2.2 Heat transfer in rectangular ducts

In this subsection, symmetrically heated channel studies are reported in 7.2.2.2. Asymmetrically and one sided heated channel works are presented in 7.2.2.2.

Symmetric heating Dennis *et al.* [282] were among the first authors studying forced heat convection in rectangular ducts. They consider laminar flows and supplement the researches of Clark and Kays [283] with heat transfer analyses in the thermal entry region. In 1970, Battista and Perkins [23] investigated heat transfer and skin friction coefficients in air flow through vertical square ducts with significant heating. According to [284], the correlation can be extended to bulk Reynolds numbers of at least 4000. The same expression is valid for equilateral triangular ducts [285]. Heat transfer appears to be 10 % below the results obtained by Perkins and Worsoe-Schmidt [286] with circular tubes. Sudo *et al.* [287] assess Dittus-Boelter correlation with experimental data in turbulent channel flows symmetrically heated and heated from one side. It appears that the estimation of heat transfer proposed by Dittus-Boettler [25] gives prediction within an error of ± 20 % for symmetrically heated channels. For the one side heated conditions,

Author (date)	Expression	Domain
Gnielinski (2013)	$Nu = \left(1 - \frac{Re_b - 2300}{4000-2300}\right) Nu_{lam,2300} + \frac{Re_b - 2300}{4000-2300} Nu_{turb,4000}$	$2300 < Re_b < 4000$
Whitaker (1972)	$Nu = 0.015 Re_b^{0.83} Pr_b^{0.42} \left(\frac{\mu_b}{\mu_w}\right)^{0.14}$	$0.48 < Pr_b < 592$ $2300 < Re_b < 100000$ $0.44 < (\mu_b/\mu_w) < 2.5$
Gnielinski *et al.*[1] (1976)	$Nu = \frac{(f/2)(Re_b - 1000) Pr_b}{1+12.7\sqrt{f/2}(Pr_b^{2/3}-1)} \left[1 + \left(\frac{D_h}{L_x}\right)^{2/3}\right] K$	$3000 < Re_b < 1000000$ $0.5 < Pr_b < 200$
Taler and Taler (2017)	$Nu = 0.02155 Re_b^{0.8018} Pr_b^{0.7095}$	$3000 < Re_b < 1000000$ $0.1 < Pr_b < 1$
Taler and Taler (2017)	$Nu = 0.01253 Re_b^{0.8413} Pr_b^{0.6179}$	$3000 < Re_b < 1000000$ $1 < Pr_b < 3$
Taler and Taler (2017)	$Nu = 0.00881 Re_b^{0.8991} Pr_b^{0.3911}$	$3000 < Re_b < 1000000$ $3 < Pr_b < 1000$
Barnes et Jackson[2] (2006)	$Nu = 0.023 Re_b^{0.8} Pr_b^{0.4} \left(\frac{T_w}{T_b}\right)^{n_{Ba}}$	$4000 < Re_b < 60000$ $Pr_b = 0.7$
Colburn[3] (1933)	$Nu = 0.023 Re_f^{0.8} Pr_f^{1/3}$	$Re_b > 10000$ $0.6 < Pr_b < 160$
Dittus-Boetler (1930)	$Nu = 0.023 Re_b^{0.8} Pr_b^{n_{DB}}$	$Re_b > 10000$ $0.7 < Pr_b < 120$
Sieder and Tate (1936)	$Nu = 0.027 Re_b^{0.8} Pr_b^{0.33} \left(\frac{\mu_b}{\mu_w}\right)^{0.14}$	$10000 < Re_b < 110000$ $0.7 < Pr_b < 16700$

Table 7.1 – Heat transfer correlations for tube flows. [1] $K = (Pr_b/Pr_w)^{0.11}$ for liquid and $K = (T_w/T_b)^{n_{Gn}}$ for gas. In the case of air flow, $n_{Gn} = 0.45$. [2] In the case of air flow $n_{Ba} = -0.4$. $n_{DB} = 0.4$ for fluid heating and $n_{DB} = 0.3$ for cooling. [3] The fluid properties are evaluated at the film temperature.

at high Reynolds number, some predicted Nusselt numbers scatter outside the ±20 % error lines. Experimental studies in a narrow rectangular channel have been carried out by Ma *et al.* [268] with deionized water. They point out that the non-heated friction factor and the average Nusselt number are well predicted with traditional relations. Ma *et al.* [268] notice that, for channel flows, the transition regime appears at a slightly larger Reynolds number than for tube flows. They propose another correlation valid for $4000 < Re_b < 13000$ and $3.9 < Pr_b < 4$. Liang *et al.* [288] perform experiments in vertical and horizontal narrow rectangular channels with deionized water for bulk Reynolds numbers between about 300 and 6200. The Nusselt number seems independent of the channel orientation, meaning that the force of gravity has little effect in these conditions. The heat transfer coefficient increases quickly with the mass flow and slowly with the heat flux. Wang *et al.* [289] study the laminar to turbulent transition region in rectangular channel. Their experiments are in the range $1000 < Re_b < 20000$ and $2.1 < Pr_b < 3.5$. The lower and upper critical Reynolds numbers of the laminar to turbulent transition increase with the decrease in Prandtl number. Another experimental investigation of forced convection heat transfer in narrow rectangular channels has been performed by Jo *et al.* [290] with demineralized water. Upward and downward flows are compared. The authors highlight that the flow orientation has no significant effect on heat transfer. Correlations for laminar and turbulent flows in the entrance region and in the fully developed region are proposed. The error relative to the turbulent flow in the fully developed region is ±18.5 %. Ghione *et al.* [291] carried out rectangular channel flow experiments with water under strong heat fluxes and high mass flows. Two channel heights are evaluated. They find that the correlation of Dittus-Boetler underestimates the heat transfer for high Reynolds numbers, which is in agreement with [292]. The authors also notice that reducing

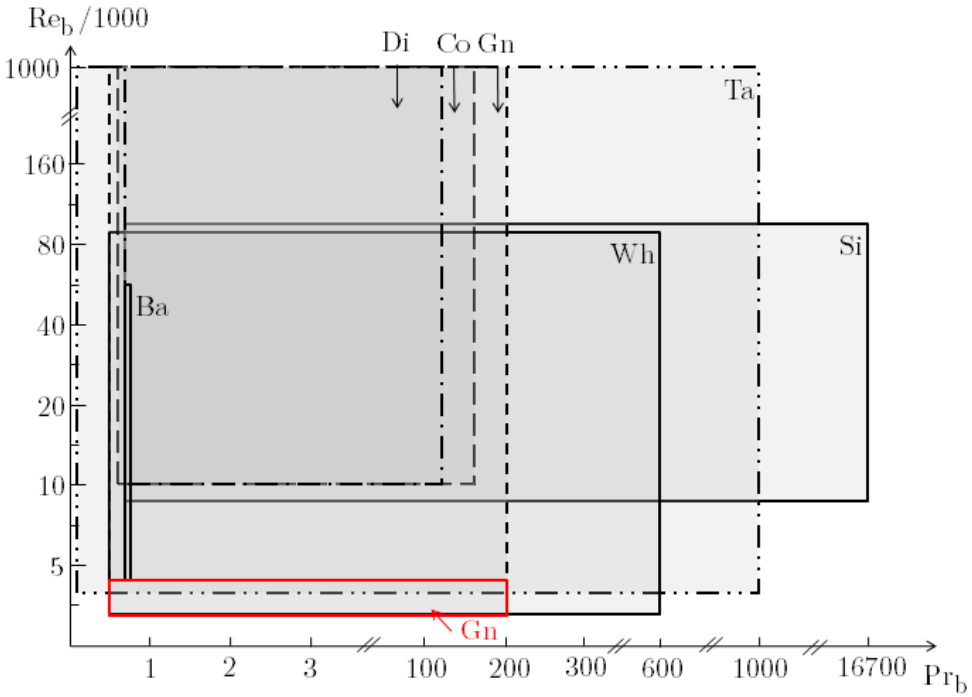

Figure 7.1 – Applicable range of heat transfer correlations for tubes. The two letters at the top right corner of the domains refer to the first author of the correlations reported in Table 7.1. Red contours signify that the correlation is applicable in the entrance region.

the channel height leads to heat transfer enhancement. Moreover, they propose correlations for fully developed boiling flow. Mortean and Mantelli [263] adapt the correlation of Stephan and Preußer [293] developed for tube flows to channel flows: the first term (4.364 in [293]) is replaced by 3.63 which is the Nusselt number adopted by the literature for fully developed flow in square channels. Mortean *et al.* [264] provide an expression for the transition region $1800 < Re_b < 4000$ which combines laminar and turbulent Nusselt number correlations in the manner of Gnielinski [278]. The mean difference between this equation and the experimental data is 13.9 %. With the same data, the heat transfer expression proposed by Gnielinski for tubes has a mean difference of 19.8 %. In a recent experimental study, Sun *et al.* [294] perform non uniform and uniform heating of a rectangular channel flow. The results indicate that the average Nusselt number is affected by the form of the transverse heating. They test 15 heat transfer equations and develop a new one for laminar to beginning of turbulence region of water flows. The correlation is applicable for $3000 < Re_b < 10000$ and $3.5 < D_h < 4.5$. The aspect ratio width to depth of the channel is between 20 and 30.

Heat transfers are also studied thanks to numerical simulations. In 1994, Wang *et al.* [295] investigated heat transfer in a 180 degrees turning duct with several turn configurations. Their numerical study uses an extended version of the $k-\epsilon$ turbulence model and agrees favorably with experimental data for Nusselt estimation. Qin and Pletcher [296] performed LES of turbulent mixed convection heat transfer in a variable-property thermally developing rotating square. A fairly satisfactory agreement between prediction and experimental results is obtained. Dailey *et al.* [190] carried out LES of a channel flow under constant heat flux boundary conditions. They

Author (date)	Expression	Domain
Mortean *et al.* (2019)	$Nu = 3.63 + 0.086 \frac{(1/L^*)^{1.33}}{1+0.1Pr_b(Re_b D_h/L_x)^{0.83}}$	$400 < Re_b < 2400$ $0.7 < Pr < 7$ $L* > 0.03$
Jo *et al.* (2013)	$Nu = 0.911 Re_b^{0.1418} Pr_b^{0.082} Gz^{0.296}$	$Re_b < 3000$ $2.64 < Pr_b < 6.46$
Wang *et al.* (2012)	$Nu = 0.04 \left(Re^{2/3} - 160\right) Pr_b^{1.5} \left[1 + (\frac{D_h}{L_x})^{2/3}\right] \left(\frac{\mu_b}{\mu_w}\right)^{0.11}$	$2500 < Re_b < 7500$ $2.2 < Pr < 3.5$
Battista and Perkins[1] (1970)	$Nu = 0.021 Re_b^{0.8} Pr_b^{0.4} \left(\frac{T_w}{T_b}\right)^{-0.7} \left[1 + \left(\frac{x_p}{D_h}\right)^{-0.7} \left(\frac{T_w}{T_b}\right)^{0.7}\right]$	$4000 < Re_b < 49000$ $Pr_b = 0.7$ $Tw/Tb < 2.13$ $22 < x_p/D_h < 155$
Jo *et al.* (2014)	$Nu = 0.0097 Re_b^{0.7705} Pr_b^{0.143} Gz^{0.217}$	$5000 < Re_b < 54000$ $2.64 < Pr_b < 6.46$

Table 7.2 – Heat transfer correlations for channel flow in the entrance region. [1] The temperatures are expressed in degrees Fahrenheit and the correlation is for square ducts.

study strong heating and cooling leading to high wall-to-bulk temperature ratios ($T_w/T_b = 1.5$ in the heated case and $T_w/T_b = 0.56$ in the cooling case). Fluid properties are temperature dependent. High heating and cooling as well as low heating conditions are investigated and compared to empirical correlations. The high cooling and low heating cases are in good agreement with most of the heat transfer correlations. However, for high heating conditions, the Nusselt number obtained by correlations is lower than the one predicted by LES. The effects of channel aspect ratio on thermally developing flow and heat transfer are studied by Lee and Garimella [270]. Boundary conditions are circumferentially constant wall temperature and axially constant wall heat flux. The authors propose generalized Nusselt correlations for microchannel heat sinks and compare them with other conventional correlations and experimental data. The results indicate that the more the channel is flattened, the bigger the Nusselt number is. Sato *et al.* [297] investigate the effect of the Prandtl number on heat transfer enhancement in a dimpled-channel flow. Their work covers the range $1000 < Re_b < 10600$. Simulations are conducted for Prandtl numbers of 0.2, 0.7 and 3. They define a thermal performance parameter (also seen in [271]), which is the ratio between the Nusselt number to the pressure drop compared to the same ratio for a flat channel flow at the same bulk Reynolds number, and plot it against various mass flows. The results suggest that the best heat transfer enhancement thanks to the dimples is reached for high Prandtl number at a bulk Reynolds number of 2000 which is in the end of the laminar region. Thermal entrance length in microchannel flows is analyzed, for different aspect ratios of channels, by Su *et al.* [298] thanks to simulations. The Reynolds number is lower than 2000. The results of this study show that the longest thermal entrance length is reached for a channel three times wider than deep. Furthermore, the Nusselt number is found to increase with the aspect ratio which is in agreement with [270, 291, 292].

A summary of the most used correlations, depending on the entrance length, for rectangular channels is proposed in Table 7.2. Correlations for fully developed conditions are reported in Table 7.3.

A graphical view of the applicable domain, in terms of Reynolds and Prandtl numbers, of each channel correlations is presented in Table 7.2. The Prandtl number range between 1.2 and 5.9 is very well covered by the existing correlations for laminar to highly turbulent region. However, there is a lack of correlations for Prandtl number inferior to one, especially at high

Author (date)	Expression	Domain
Liang *et al.* (2012)	$Nu = 3.975 Re_b^{0.109} Pr_b^{1/3}$	$Re_b < 2300$ Deionized water
Jo *et al.* (2013)	$Nu = 2.0129 Gz^{0.3756}$	$Re_b < 3000$ $2.64 < Pr_b < 6.46$
Mortean *et al.* (2012)	$Nu_{transi} = \left[\left(Nu_{lam}^6 + Nu_{turb}^6\right)\right]^{1/6}$	$1800 < Re_b < 4000$ Water
Liang *et al.* (2012)	$Nu = 0.00666 Re_b^{0.933} Pr_b^{0.4}$	$2300 < Re_b < 7000$ Deionized water
Sun *et al.* (2020)	$Nu = 0.212\left(Re_b^{0.6} - 83.4\right) Pr_b^{0.4}\left(1 - \frac{D_h}{L_x}\right)^{2/3}$	$3000 < Re_b < 10000$ Deionized water
Ma *et al.* (2011)	$Nu = 0.00354 Re_b Pr_b^{0.4}$	$4000 < Re_b < 13000$ $3.9 < Pr_b < 4.1$
Battista and Perkins[1] (1970)	$Nu = 0.021 Re_b^{0.8} Pr_b^{0.4}\left(\frac{T_w}{T_b}\right)^{-0.7}$	$4000 < Re_b < 49000$ $Pr_b = 0.7$ $Tw/Tb < 2.13$
Jo *et al.* (2014)	$Nu = 0.0058 Re_b^{0.9383} Pr_b^{0.4}$	$5000 < Re_b < 54000$ $2.64 < Pr_b < 6.46$
Ghione *et al.* (2016)	$Nu = 0.0044 Re_b^{0.960} Pr_b^{0.568}\left(\frac{\mu_b}{\mu_w}\right)^{0.14}$	$10000 < Re_b < 269000$ $1.2 < Pr_b < 5.94$ $2\delta = 2.161mm$
Ghione *et al.* (2016)	$Nu = 0.00184 Re_b^{1.056} Pr_b^{0.618}\left(\frac{\mu_b}{\mu_w}\right)^{0.14}$	$10000 < Re_b < 177000$ $1.18 < Pr_b < 5.70$ $2\delta = 1.509mm$

Table 7.3 – Heat transfer correlations for channel flow in the fully developed region. [1] The temperature are expressed in degrees Fahrenheit and the correlation is for square ducts.

Reynolds number.

Asymmetric and one sided heated channel studies involving forced convection Asymmetrically heated channel flow is commonly studied with natural convection [299, 300, 301]. These conditions are mainly investigated for building applications [302, 303, 304]. However, few publications handle asymmetric heating associated with forced convection and even less dealing with turbulent flows. Osborne and Incropera [305] investigate laminar flow in the thermal entrance region through a horizontal asymmetrically heated plate channel . In this experimental study mixing natural and forced convection, various small heat fluxes are fixed (inferior to 6 kW/m^2). Vertical temperature distributions are plotted, flow visualization is achieved and heat transfer analysis is carried out. In their study, the top plate conditions are poorly influenced by buoyancy. When the flow is symmetrically heated, the heat transfer is significantly enhanced by buoyancy at the bottom wall. Mixed convection of air in a horizontal channel heated from one side has been investigated by Gau *et al.* [306]. The authors show that the increase of the buoyancy parameter leads to an elevation of the Nusselt number normalized by $Re_b^{0.4}$. Heat transfer in the studied configuration is much greater than in the case involving vertical channel flow. Hwang *et al.* [307] study forced convection in an asymmetrically heated packed channel filled with glass spheres. Following their experimental runs, they provide a correlation to estimate heat transfer thanks to the Reynolds number and diameter of the solid particles. The authors state that, at similar Reynolds number, forced convective heat transfer of Freon-113 in a packed channel is about three times higher than in an empty channel. Conventional Nusselt number at the cold wall of an asymmetrically heated channel becomes infinite and then negative

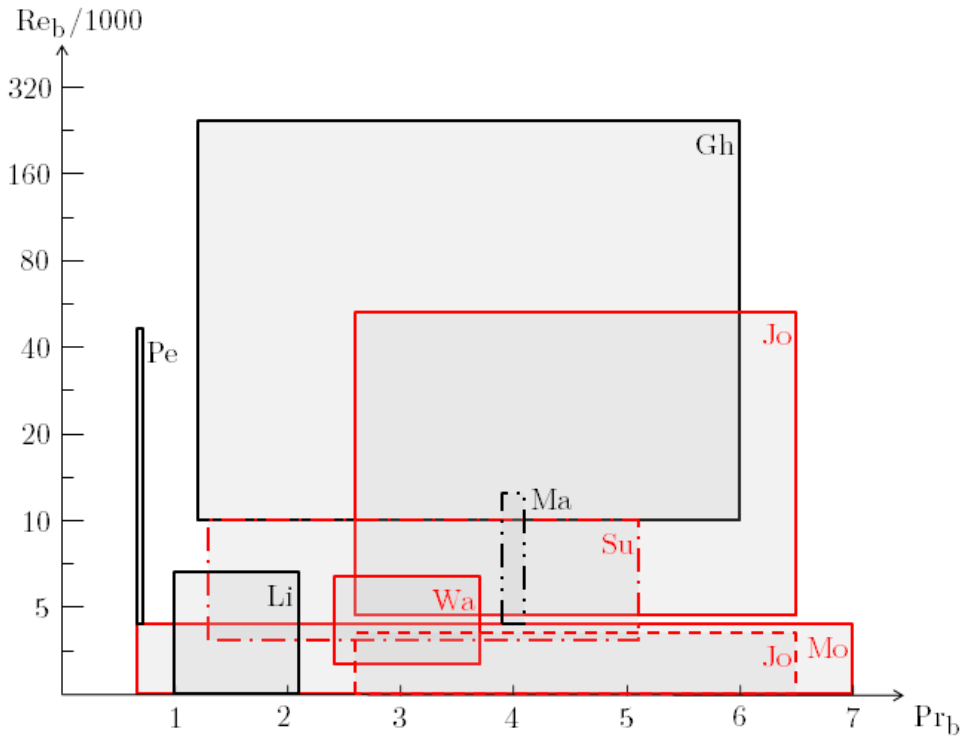

Figure 7.2 – Applicable range of heat transfer correlations for rectangular channels. The two letters at the top right corner of the domains refer to the first author of the correlations reported in tables 7.2 and 7.3. Red contours signify that the correlation is applicable in the entrance region.

when the bulk temperature tends toward and overtakes the cold wall temperature. To avoid this singularity, Nield [308] defines a mean Nusselt number as:

$$Nu_m = \frac{D_h q_m}{\lambda_w (T_m - T_b)} \tag{7.1}$$

with q_m the mean heat flux and T_m the mean wall temperature. An analytic study leads to Nusselt expressions for slug flow, Poiseuille flow and Couette flow. Nield [308] studies laminar flows and shows that, as long as the velocity profile is symmetric with respect to the midline of the channel, the Nusselt number is independent of the asymmetry. He demonstrates the validity of his method for the isoflux and isotemperature cases. Moreover, Nield [308] explains how to get wall information (temperatures or heat flux depending on boundary conditions) from his average Nusselt number. Nevertheless, it seems difficult to operate with turbulent conditions. Mitrovic *et al.* [309] study the asymmetric Graetz problem, which is defined as steady-state forced convection heat transfer, with plane laminar flow confined by two parallel plates that are kept at constant but different temperatures. Their numerical simulation of the problem agrees excellently with the analytic solution. It shows that the singularity of the Nusselt number occurs at different axial positions and depends on the thermal asymmetry and fluid inlet conditions. The authors pointed out that there is no correlation in the literature that accounts for possible jumps of the Nusselt number relative to the cold wall. Another asymmetric study of channel flow has been achieved by

Repata and Satyamurti [310]. Their numerical work assumes laminar and incompressible, steady flow of a Newtonian fluid with constant thermophysical properties. They show that the heat flux varies monotonically with the axial distance even though the conventional Nusselt number is discontinuous. The modified Nusselt number proposed by Nield [308] is continuous. The authors affirm that this modified Nusselt number is applicable for the case of equal wall temperatures and coincides with the classical definition. In the laminar case, the fully developed condition is reached when the temperature varies linearly from the temperature at one wall to the temperature at the other wall. Kuznetov and Nield [311], investigate forced convection in a channel partly occupied by a bidisperse porous medium under asymmetric heating. Thanks to an analytic study, they show that a singularity of the modified Nusselt number proposed by Nield in [308] appears under certain heating conditions. When plotting against an asymmetrical heating parameter, this singularity relies on the bidisperse porous medium thickness. Asymmetric heating of air in a square microchannel has been investigated by van Male *et al.* [312]. Nusselt correlations are developed for laminar and plug flows. For laminar flow, the Reynolds number is between 200 and 500. An analytic description of heat and mass transfer is provided for plug flow. In [292], Ma *et al.* perform experimental tests on heat transfer enhancement with longitudinal vortices in a narrow rectangular channel heated from one side. The used fluid is water. The results indicate that in the laminar region, longitudinal vortices enhance the heat transfer of about 100 % for an increase of flow resistance of only 11 %. In the case of turbulent flow, the flow resistance modification is higher than the heat transfer (an increase of 100 % for a 87 % enhancement of heat transfer).

Torii and Yang [313] carry out numerical simulations of thermal fluid-flow transport phenomena in a channel under asymmetric heat flux. They use the $k-\epsilon$ turbulence model and two equations heat transfer model. The authors compare theoretical solutions for turbulent and laminar heat transfer proposed by Kays and Crawford [283] to assess the laminarization process. Their results show that if a channel is heated from exclusively one wall the fluid flow cannot be laminarized contrary to the case of tube flow. Few correlations for tube flows laminarization are compared to flow laminarization in channel heated from both sides.

No correlation of asymmetrically heated turbulent channels flows is proposed in the literature, however, physical effects of the coupling between temperature and velocity have been numerically investigated in [314, 214, 211, 315] for similar working conditions. These studies show that the coupling between temperature and dynamic should be considered to properly describe the flow in case of asymmetric heating conditions. It is illustrated by the poor efficiency of the conventional correlations when handling asymmetric heating (see subsection 7.2.4.3). The specificity of heat transfer in asymmetrically heated channel flows requires a new correlation to be properly estimated. It is the purpose of this paper.

7.2.3 Numerical simulations

7.2.3.1 Physical and numerical settings

Physical setting Large Eddy Simulations (LES) are performed to investigate convective heat transfer of fully developed turbulent channel flow. Navier-Stokes equations are solved under the low Mach number approximation proposed by Paolucci [2]. This assumption permits considering the coupling effect between temperature and dynamic, as advised by the literature [314, 214, 211, 315] while neglecting acoustic effects, which are very small in the current conditions. The flow is driven by forced convection. Indeed, the Richardson number is about 10^{-3} for the simulations at lowest Reynolds numbers, meaning that the buoyancy effects are negligible compared to the

kinetic effects. Newtonian fluid and Fourier's law are assessed. Equations are expressed using a Favre filtered variable built with density weighted Favre filter ($\widetilde{\cdot}$) defined for any field ψ as $\widetilde{\psi} = \widetilde{\rho\psi}/\overline{\rho}$. The AMD model [13] is applied to estimate the momentum convection subgrid term $\left(\widetilde{U_j U_i} - \widetilde{U_j}\widetilde{U_i}\right)$, where U_i and U_j are respectively the i-th and j-th component of velocity, and density-velocity correlation subgrid term $\left(\widetilde{U_j/\rho} - \widetilde{U_j}/\overline{\rho}\right)$. This model has shown a good agreement with Direct Numerical Simulations (DNS) in asymmetrically heated channel associated with turbulent flows [160, 21]. The fluid is air. Sutherland's law [69] is applied to calculate the viscosity. In each simulation, the Prandtl number is constant. The heat capacity at constant pressure is also fixed.

Geometry and mesh The channel is periodic in the streamwise (x) and spanwise (z) directions and enclosed by two plane walls in the wall-normal direction (y). The temperatures of the plates are fixed. Note that Avellaneda *et al.* [211] studied the influence of thermal boundary conditions (fixed wall temperatures versus imposed heat flux) for channel flow under asymmetric high temperature gradient and show that there are no significant differences on the main turbulence statistics. Figure 7.3 presents the geometry in case of asymmetrical heating. The coolest wall is referred to as "cold wall" and hottest is referred to as "hot wall". The domain size is $L_x \times L_y \times L_z = 4\pi\delta \times 2\delta \times 4/3\pi\delta$ with $\delta = 0.003$ m. LES are carried out using a finite difference

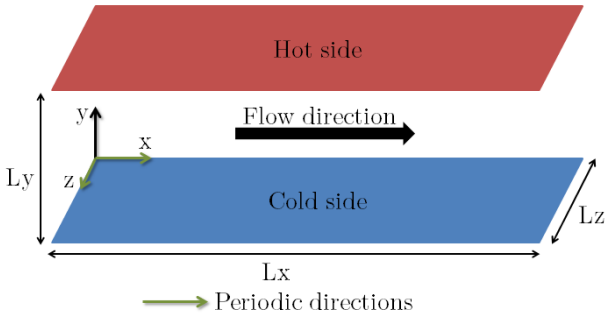

Figure 7.3 – Geometry of the channel flow.

method in a staggered grid system. Mesh is uniform in the homogeneous directions and follows a hyperbolic tangent law in the wall-normal coordinate direction. For practical reasons, the same mesh is used for all calculations and is composed of 2.3 millions of cells distributed as follow : $N_x \times N_y \times N_z = 160 \times 152 \times 96$. The dimensionless cell size varies with the conditions of simulation. Meshes characteristics are presented in Table 7.4. The coarsest LES has a dimensionless size of the first cell of 1.39 in the wall normal direction which is in the viscous sublayer. A streamwise volume force is added in the momentum equation to balance wall friction. Similarly, a source term is included in the energy equation to permit testing various profiles of temperature inducing different heat fluxes.

7.2.3.2 Computation of Nusselt numbers using Large Eddy Simulation

Comparisons with Direct Numerical Simulations (DNS), performed for different heating conditions and various mass flows, indicate that LES systematically underestimate heat flux and

Meshes characteristics	Δ_x^+	$\Delta_y^+(0)$	$\Delta_y^+(\delta)$	Δ_z^+
Coarsest mesh	103.5	1.39	42.5	57.5
Finest mesh	10.7	0.14	4.4	5.9
Average mesh	48.9	0.64	20.1	27.1
Std	25.4	0.37	10.4	14.1

Table 7.4 – Meshes characteristics at cold wall (highest friction velocity). Std means standard deviation.

Nusselt number. However, this error is predictable because it is proportional to the dimensionless cell sizes and can be corrected by introducing a multiplication factor. For that reason, in this paper, all results of LES are corrected to reproduce the heat fluxes that would have been obtained with DNS. For each wall, the Nusselt number is calculated using the temporally and spatially averaged heat flux of the wall, q_w. Its expression is given by equation 7.2.

$$Nu_w = \frac{q_w D_h}{\lambda_w (T_w - T_b)} \tag{7.2}$$

Where D_h is the hydraulic diameter, λ_w the thermal conductivity, T_w and T_b respectively the wall and bulk temperatures.

The calculation of the Nusselt number with this methodology is validated against experiments achieved by Jo *et al.* [290]. Nine comparisons are performed for three Reynolds numbers and two Prandtl numbers (see Table 7.5). The results show satisfying agreement. Indeed, the relative error, $r_i = \left(Nu^{LES} - Nu^{Jo}\right)/Nu^{Jo}$, obtained is inferior to 8.3 % for each tested configuration, which is smaller than the error range of experimental measures. The validation with experimental data of Jo *et al.* are performed until a bulk Reynolds number of 35620 corresponding to a fully turbulent flow.

Characteristics	Re_b	Pr_b	$T_w - T_b$	r_i
L-L-M	11816	2.64	24.6	2.4 %
L-L-H	12029	2.64	48.4	1.9 %
M-H-L	23376	3.18	9.4	-5.9 %
M-L-L	23377	2.64	9.5	-1.9 %
M-H-M	23529	3.18	18.1	-1.9 %
M-L-H	23685	2.64	27.0	-1.7 %
H-L-L	35082	2.64	10.0	-8.3 %
H-L-M	35276	2.64	17.4	-5.5 %
H-L-H	35620	2.64	30.2	-3.6 %

Table 7.5 – Comparison of the Nusselt number obtained by the experiments of Jo *et al.* and the performed simulations. In the first column, X-X-X refers to Reynolds number, Prandtl number and temperature difference: “L" means low, “M" medium, and “H" high. r_i is the relative error and is calculated as follow: $r_i = \left(Nu^{LES} - Nu^{Jo}\right)/Nu^{Jo}$

As for as asymmetric heating conditions, LES have been compared to DNS results for three bulk Reynolds numbers (23000, 60000 and 82000) at a Prandtl number of 0.8. Two velocity profiles have been investigated. Results show a good agreement with 3% of error on velocity and temperature profiles.

7.2.4 Correlation for asymmetrically heated channel associated with turbulent flows

7.2.4.1 Development of the proposed correlation

To the authors' knowledge, no expression is available in the literature to estimate heat transfer in an asymmetrically heated channel associated with turbulent flows. The Proposed Correlation, referred to as "PC" in figures and tables, is developed thanks to 70 LES divided into 30 simulations with symmetric heating and 40 simulations with asymmetric heating. The Battista and Perkins [23] form of the correlation was assumed and a new term, involving the wall temperature, T_w, bulk temperature, T_b and mean wall temperature, $T_m = (T_c + T_h)/2$, is added to account for asymmetric conditions:

$$Nu = aRe_b^{0.8} Pr_b^c \left(\frac{T_w}{T_b}\right)^d \left(\frac{T_w}{\mid T_w - T_b \mid}\right)^{e\left(1-\frac{T_w}{T_m}\right)\frac{T_b}{T_w}} \tag{7.3}$$

The exponent of the Reynolds number is fixed to 0.8 because this value is widely used in similar conditions [277, 25, 23]. A term accounting for asymmetric heating conditions is added in the equation to reproduce the heat transfers at hot and cold walls. Notice that this term involves variables in the exponent. The singularity of the Nusselt number, encountered when the bulk temperature tends towards the cold wall temperature and explained in [308], is reproduced thanks to the difference of temperature at the denominator of the asymmetric group. The coefficients of the correlation (a, c, d and e) are optimized using a least-squares fit. The best-fitting correlation for the simulation results is:

$$Nu = 0.024 Re_b^{0.8} Pr_b^{0.4} \left(\frac{T_w}{T_b}\right)^{-0.9} \left(\frac{T_w}{\mid T_w - T_b \mid}\right)^{1.4\left(1-\frac{T_w}{T_m}\right)\frac{T_b}{T_w}} \tag{7.4}$$

In case of symmetric heating, the asymmetric term is equal to one and the expression can be simplified in:

$$Nu = 0.024 Re_b^{0.8} Pr_b^{0.4} \left(\frac{T_w}{T_b}\right)^{-0.9} \tag{7.5}$$

In accordance with the literature, the proposed correlation has a bigger multiplicative constant than the one proposed by Battista and Perkins [23] for square ducts. Indeed, channel flow experiments performed by Jo *et al.* [290] indicate that the correlation of Battista and Perkins [23] underestimates the heat transfer in this geometry. Furthermore, several studies show that the more the shape of the channel is flattened, the bigger the Nusselt number is [270, 298, 291]. The proposed correlation is investigated in the commonly encountered working conditions of heat exchangers and solar receivers.

- For symmetric conditions
  - ⋆ $12000 < Re_b < 177000$
  - ⋆ $0.47 < T_b/T_w < 0.99$
- For asymmetric conditions
  - ⋆ $10600 < Re_b < 145000$
  - ⋆ $1.1 < T_h/T_c < 2.0$

⋆ $0.63 < T_b/T_c < 0.95$

⋆ $0.44 < T_b/T_h < 0.85$

The wall temperatures range from 293 K to 1300 K. The fluid temperature varies from 342 K and 1237 K, Prandtl number is between 0.76 and 3.18, and heat fluxes are between 4 kW/m^2 and 578 kW/m^2.

7.2.4.2 Results of the proposed correlation

The proposed correlation is firstly assessed using the indicators described below. The relative error is defined in Eq. 7.6.

$$\epsilon_{Nu,i} = \frac{Nu_i^{correlation} - Nu_i^{LES}}{Nu_i^{LES}} \tag{7.6}$$

The determination coefficient is evaluated to assess the global revelancy of the correlation (Eq. 7.7).

$$R^2 = 1 - \frac{\sum_{i=1}^{N} \left(Nu_i^{LES} - Nu_i^{correlation}\right)^2}{\sum_{i=1}^{N} \left(Nu_i^{LES} - \overline{Nu^{LES}}\right)^2} \tag{7.7}$$

where $\overline{Nu^{LES}}$ is the average of the Nusselt numbers obtained with LES. The mean error and the standard deviation are calculated as follow (Eq. 7.8 and Eq.7.9).

$$Mean = \frac{1}{N} \sum_{i=1}^{N} \epsilon_{Nu,i} \tag{7.8}$$

where N is the number of results.

$$Std = \sqrt{\frac{1}{N} \sum_{i=1}^{N} \mid \epsilon_{Nu,i} - Mean \mid^2} \tag{7.9}$$

All the Nusselt numbers estimated with the proposed correlation have a relative error inferior to ±9.1 % and more than three-quarter of them are in the error bound ±5 %. The determination coefficient is 0.993. The mean error is 0.29 % and standard deviation is 4.1 %.

The Nusselt number obtained by the proposed correlation is plotted as a function of the Nusselt number calculated by numerical simulations in Fig. 7.4. The Nusselt numbers range from 20 to 705. High Nusselt number values are reached by the cold Nusselt number under asymmetric conditions when the bulk temperature is close to the cold wall temperature. As discussed above, all points are below the ±10 % error lines. For symmetric calculations, in most cases, the correlation slightly overestimates the Nusselt number. Indeed, the mean error is 1.6 %. For asymmetric conditions, points relative to hot and cold walls are equally spread out on either side of the 0 % error line.

Fig. 7.5 shows the error on the Nusselt number against various parameters of the simulations. The graphs are described from left to right. The effect of the bulk Reynolds number is observed on the first graph. For symmetric conditions, the biggest errors are obtained for small Reynolds numbers. In the case of asymmetric heating, the Nusselt number is underestimated at the cold wall for Reynolds numbers under 88000 and over-predicted for higher values. As for the hot wall, the accuracy of the correlation is enhanced for low Reynolds numbers. Indeed, for Reynolds

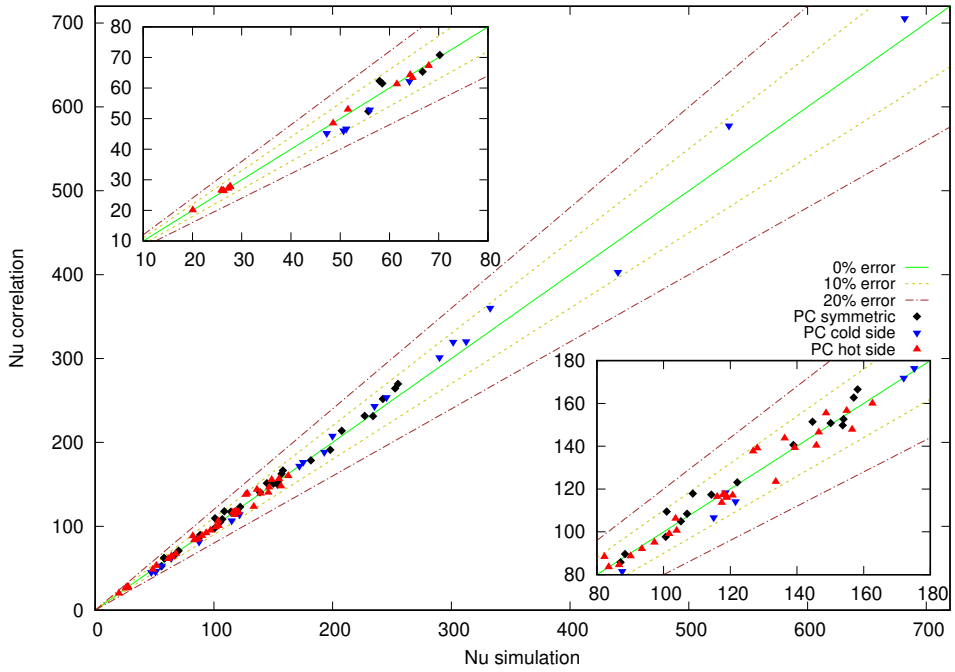

Figure 7.4 – Nusselt numbers obtained by the proposed correlation (PC) against Nusselt numbers calculated by Large Eddy Simulations.

numbers inferior to 80000, all points are below the ±5 % error bound. The standard deviation increases with the Reynolds number. The second graph presents the evolution of the error on the Nusselt number depending on the friction Reynolds number. For symmetric heating and cold wall, the tendencies are the same as in the first graph. For the hot side, no significant tendency is observed. In the third graph, the results are plotted against the ratio of bulk and cold wall temperatures. As explained in subsection 7.2.4.1, in the particular case where the bulk temperature is superior to the cold wall temperature (meaning that the fluid is cooled at the cold wall), this correlation is only able to predict the hot Nusselt number because of the singularity, described in [308], which occur at the cold wall. For that reason, some points corresponding to the hot side have a ratio of bulk and cold wall temperatures superior to 1. The fourth graph shows the error on the Nusselt number depending on the ratio of hot and cold wall temperatures. The evolution of the relative error seems to have no link with the temperature ratio.

A synthetic view of the result is proposed in Fig. 7.6. The errors on the Nusselt number are plotted as a function of the bulk Reynolds number and the ratio of bulk and cold wall temperatures. Points are colored according to the error on the Nusselt number. The same behaviors as those mentioned in the analysis of Fig. 7.5 are observed.

7.2.4.3 Comparison with selected correlations from the literature

In this section, the correlations of Jo *et al.* [290], Battista and Perkins [23], Gnielinski [26] and the proposed expression are compared. None of the expression existing in the literature is applicable in these conditions. However, the ones selected are the most promising due to their

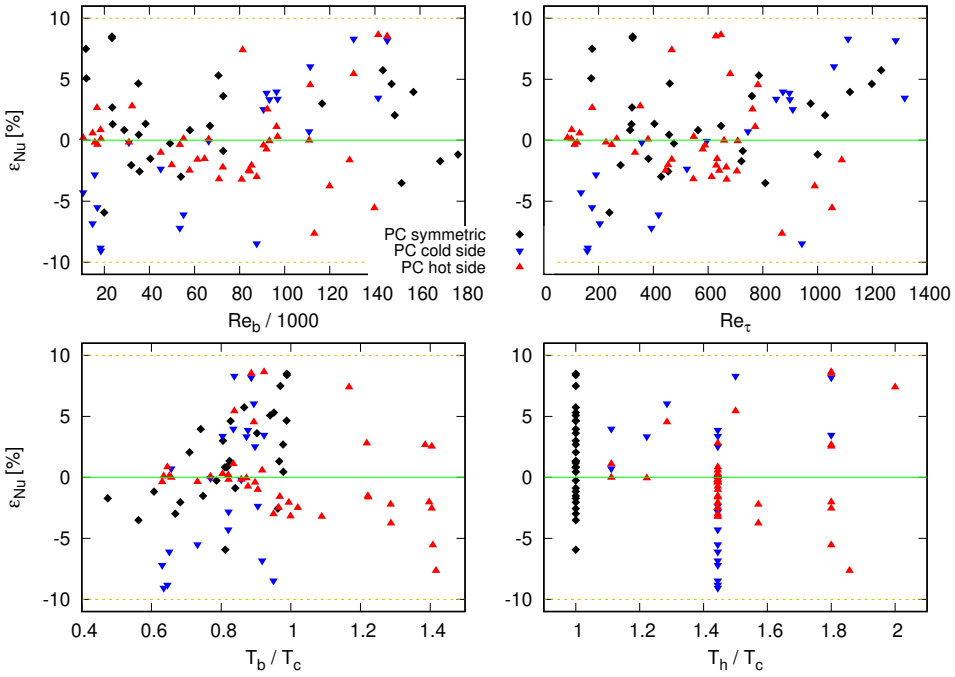

Figure 7.5 – From left to right, errors on the Nusselt number depending on the bulk Reynolds number, on the friction Reynolds number, on the ratio of bulk and cold wall temperatures and on the ratio of hot and cold wall temperatures.

Author	pro	cons
Jo *et al.* (2014)	turbulent channel flow	water
Gnielinski (1976)	turbulent air flow, wall temperature involved	circular tubes
Battista and Perkins (1970)	turbulent air flow, wall temperature involved	square ducts

Table 7.6 – Pro and cons of the selected correlations regarding the present study configuration.

validity domain and/or their formulation. Pro and cons, with regard to the present configuration, of these correlations are reported in Table 7.6.

The performances of the four correlations are compared, in Table 7.7, for simulations with symmetric heating only, with asymmetric heating only and for the entire data set. Coefficient of determination (R^2), Mean error, standard deviation (Std) as well as minimum and maximum values (Min and Max) in terms of error are specified. Min and Max values of respectively -2.3 % and 145.1 % indicate that the estimation of the correlation fluctuates between -2.3 % and 145.1 % error bounds. The results show that all the assessed correlations of the literature are more accurate when the heating conditions are symmetric which was expected since they are developed for this type of heating. The results of the correlation proposed by Jo *et al.* [290] do not show a good agreement with the simulations: overestimation of the Nusselt number in symmetric heating conditions and for the hot wall of asymmetric heating. The correlation of Battista and Perkins and the one of Gnielinski are quite accurate for symmetric heating (respectively $R^2 = 0.970$ and $R^2 = 0.963$). Gnielinski expression has a lower mean error than

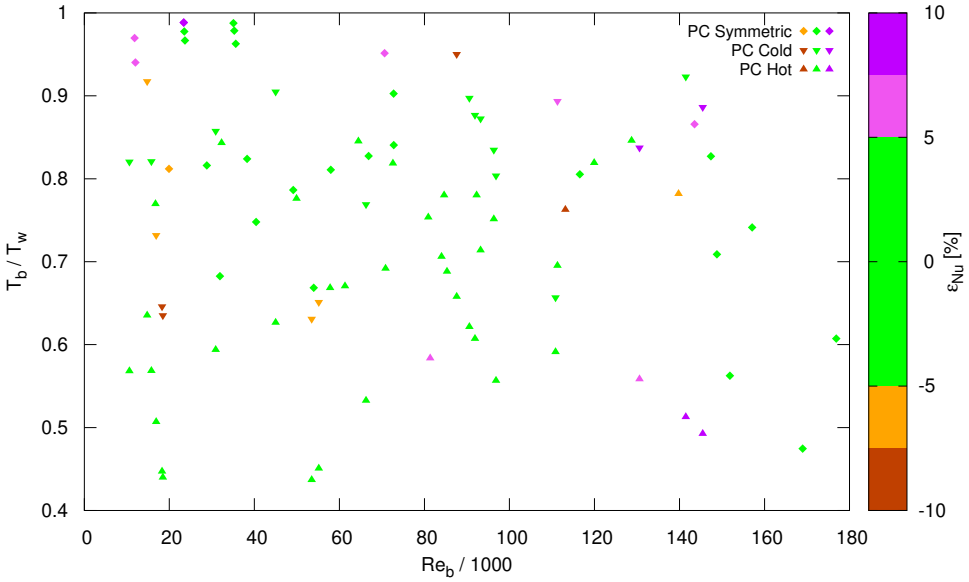

Figure 7.6 – Errors on the Nusselt number as a function of the bulk Reynolds number and the ratio of bulk and wall temperature.

the one of Battista and Perkins but a bigger standard deviation. Considering the asymmetric case, the two correlations have the same drawbacks: underestimation of the Nusselt number at the cold wall and overestimation at the hot wall. The expression proposed in this paper is the best of those studied here and agrees very well with the simulations. Indeed, it is accurate in both heating conditions in terms of R^2, mean error and standard deviation. Regarding the entire data set, the mean error is 0.3 %, the standard deviation is 4.1 % and the correlation provides prediction within ±9.1 % error.

Fig. 7.7 exposes the behavior of the four correlations. Nusselt numbers obtained with the correlation are plotted against Nusselt number obtained by simulations. The three correlations of the literature tend to overestimate the hot Nusselt number in asymmetric conditions and they underestimate the cold Nusselt number. The error committed at the hot side and in the case of symmetric heating seems to evolve in the same way: for the correlation proposed by Jo *et al.* [290], the error increases with the Nusselt number whereas for the two others, the deviation is independent of the Nusselt number. The underestimation observed for the three correlations of the literature is worsened with the increase of the Nusselt number. For the proposed correlation, Nusselt numbers relative to cold and hot walls are equally spread out over the 0 % error line which traduces the relevance of the term accounting for asymmetric heating. The errors committed by correlations are presented against the bulk Reynolds number in Fig. 7.8. In the symmetric conditions and hot side of the channel, the deviation of the Jo *et al.* [290] correlation increases with the Nusselt number. These results can be explained by the fact that this correlation has been developed for bulk Reynolds numbers below 50000. For the Nusselt number predicted by Jo *et al.* at the cold wall and the one estimated by the other correlations, there is no significant

Type of simulation	Correlations	R^2	Mean [%]	Std [%]	Min [%]	Max [%]
Symmetric	Jo	-1.670	36.14	34.9	-2.3	145.1
	Perkins	0.970	-7.41	2.9	-14.1	-0.3
	Gnielinski	0.963	3.67	5.7	-6.0	22.9
	PC	0.992	1.61	3.6	-5.8	8.6
Asymmetric cold side	Jo	0.658	-6.21	28.7	-48.7	68.2
	Perkins	0.239	-37.11	13.8	-64.3	9.0
	Gnielinski	0.298	-31.19	16.7	-63.4	2.4
	PC	0.990	-0.81	5.5	-9.1	8.3
Asymmetric hot side	Jo	-7.226	108.36	29.8	62.4	193.5
	Perkins	0.641	19.72	14.3	-6.2	51.3
	Gnielinski	0.180	36.27	12.3	10.2	63.9
	PC	0.991	-0.44	3.36	-7.7	8.6
Entire data set	Jo	-0.103	57.65	56.9	-48.7	193.5
	Perkins	0.519	-2.66	25.5	-64.3	51.3
	Gnielinski	0.518	9.70	29.6	-63.4	63.9
	PC	0.993	0.29	4.1	-9.1	8.6

Table 7.7 – Performances of the four correlations for symmetric heating, for cold and hot side of asymmetric heating conditions, and for all simulations.

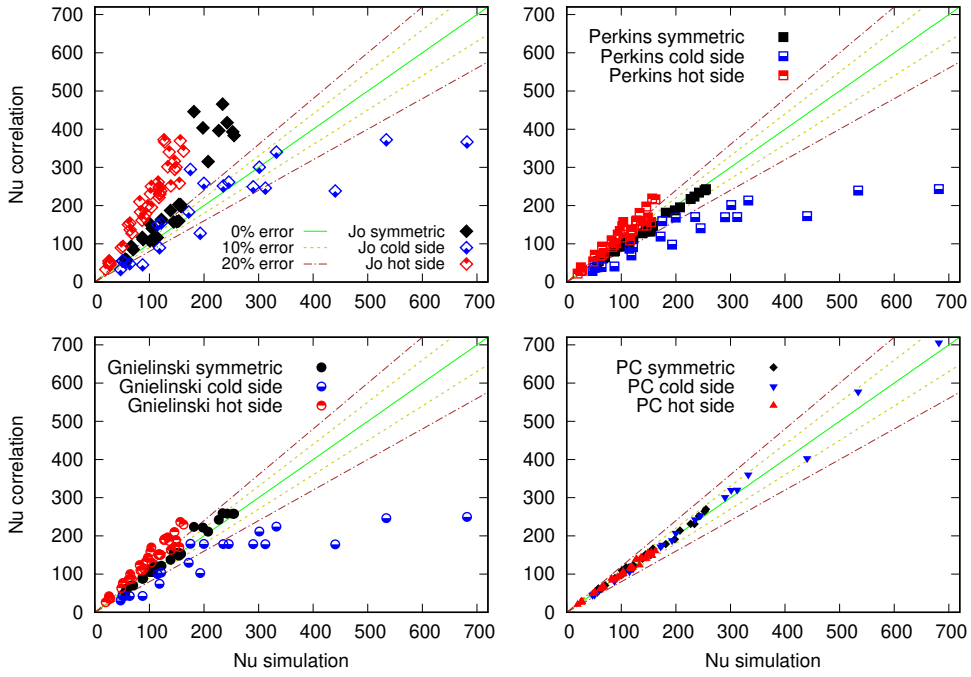

Figure 7.7 – Nusselt number obtained by correlations against Nusselt number calculated by simulations.

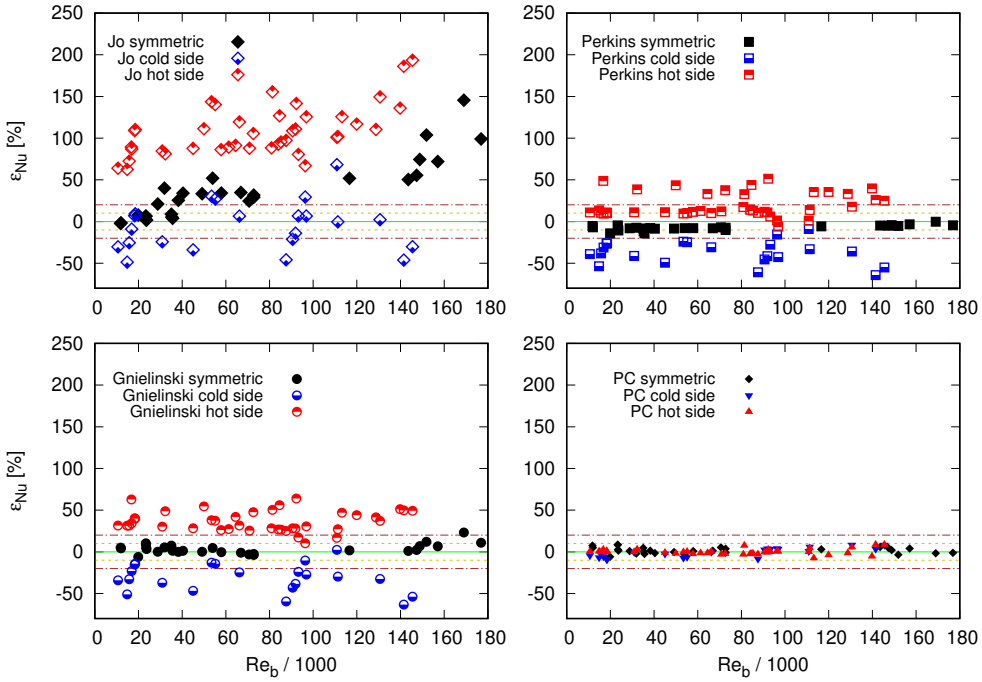

Figure 7.8 – Comparison of errors on the Nusselt number obtained by the four correlations depending on the bulk Reynolds number.

influence of the bulk Reynolds number on the error committed.

Fig. 7.9 shows the evolution of the gap in the Nusselt number against the ratio of bulk and cold wall temperatures for the selected correlations. In the symmetric case, the correlation suggested by Jo *et al.* [290] gradually overestimates the Nusselt number as the ratio of temperatures becomes small. The same behavior, at a lesser extent, is observed for the Gnielinski correlation. The expression proposed by Battista and Perkins is very mildly affected by the evolution of the temperature ratio. At the cold wall, the error increases with the ratio of temperatures for the three expressions of the literature. This is explained by the fact that when the bulk temperature tends toward the cold wall temperature, the Nusselt number skyrockets as shown in [308, 310]. This behavior of the Nusselt number at the cold wall is not considered by the existing correlations since they are developed for symmetric heating conditions. As a result, the heat transfer is significantly underestimated. The asymmetrical term involved in the proposed correlation permits reproducing this particular evolution of the Nusselt number. At the hot wall, the error committed by the correlation of Jo *et al.* [290] seems to be independent of the temperature ratio. However, for the expression of Battista and Perkins [23] and Gnielinski [26], the error is constant from $T_b/T_c = 0.63$ to $T_b/T_c = 1$ then it increases with the ratio of temperature. This tendency is not observed for the proposed correlation and its errors remain equally spread out over the 0 % error line and between the ± 10 % limit.

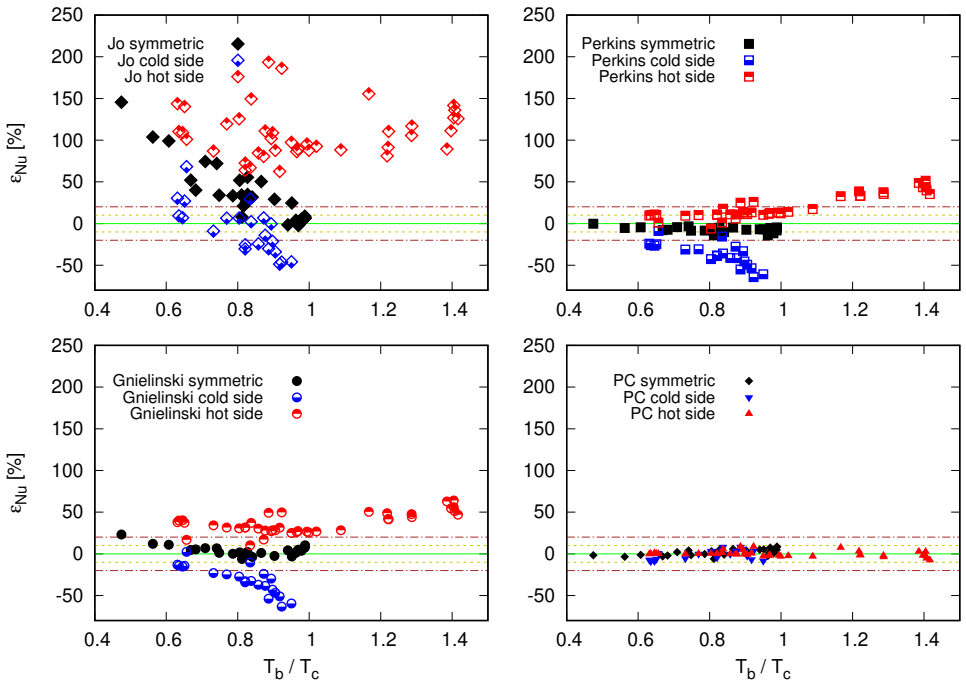

Figure 7.9 – Comparison of errors on the Nusselt number obtained by the four correlations depending on the ratio of bulk and cold wall temperatures.

7.2.5 Conclusions

In this paper, a review of heat transfer studies for tube and channel flows is proposed. Symmetrically and asymmetrically heated flows as well as one sided heated channel flows are presented. For the two geometries, the main correlations are summarized in tables. A graphical view of the applicable domain of correlations is proposed. It follows from this literature review that there is a lack of correlations for asymmetrically heated channels under turbulent flow conditions.

A new correlation for turbulent flows in symmetrically and asymmetrically heated channels is investigated using a Large Eddy Simulation database composed of more than 90 Nusselt number values. The simulations have been performed in a bi-periodic channel representing a channel with a small height compared to width. The domain covered by simulations is large (heat fluxes varying between 4 and 580 kW/m^2, bulk temperature ranging from 340 K to 1240 K and bulk Reynolds number from 10 600 to 177 000).

The Nusselt number obtained by the proposed expression is compared to three correlations of the literature which have been selected for their relative closeness with the studied configuration. The coefficient of determination, mean error and standard deviation between the estimation provided by correlations and the results of Large Eddy Simulations are calculated. Moreover, the error committed by correlations is plotted against various flow characteristics in order to analyze their behavior.

The evaluation of the turbulent heat transfer coefficient shows that the correlations of the literature tend to overestimate the Nusselt number at the hot side of asymmetrically heated channel independently of the temperature ratio. They, also, underestimate the heat transfer

at the cold side, especially when the bulk temperature is close to cold wall temperature. On the contrary, the proposed correlation is very accurate for both heating conditions and provides reliable predictions. Indeed, the coefficient of determination is 0.993, the mean error is 0.29 % and all the results obtained are below the 9.1 % error limit.

The term accounting for asymmetrical heating involves variables in exponent. To the authors' knowledge it is the first time that such a formulation is used to estimate heat transfer and its relevancy has been proved in this study. With a possible adjustment, this term may be added to other correlations to extend their domain of validity to asymmetric heating.

Acknowledgment

The authors gratefully acknowledge the CEA for the development of the TRUST platform. This work was granted access to the HPC resources of CINES under the allocation 2019-A0062A05099 and 2020-A0082A05099 made by GENCI. The authors also acknowledge the Occitania region for their funding of the thesis grant.

References

[2] S. Paolucci. "Filtering of Sound from the Navier-Stokes Equations." In: *NASA STI/Recon Technical Report N* 83 (1982).

[13] W. Rozema et al. "Minimum-Dissipation Models for Large-Eddy Simulation". In: *Physics of Fluids* 27.8 (2015), p. 085107.

[15] A. Leonard. "Energy Cascade in Large-Eddy Simulations of Turbulent Fluid Flows". In: *Advances in Geophysics*. Ed. by F. N. Frenkiel and R. E. Munn. Vol. 18. Turbulent Diffusion in Environmental Pollution. Elsevier, 1975, pp. 237–248.

[21] D. Dupuy, A. Toutant, and F. Bataille. "Study of the Large-Eddy Simulation Subgrid Terms of a Low Mach Number Anisothermal Channel Flow". In: *International Journal of Thermal Sciences* 135 (2019), pp. 221–234.

[23] E. Battista and H. C. Perkins. "Turbulent Heat and Momentum Transfer in a Square Duct with Moderate Property Variations". In: *International Journal of Heat and Mass Transfer* 13.6 (1970), pp. 1063–1065.

[24] A. P. Colburn. "A Method of Correlating Forced Convection Heat-Transfer Data and a Comparison with Fluid Friction". In: *International Journal of Heat and Mass Transfer* 7.12 (1964), pp. 1359–1384.

[25] F. W. Dittus and L. M. K. Boelter. "Heat Transfer in Automobile Radiators of the Tubular Type". In: *International Communications in Heat and Mass Transfer* 12.1 (1985), pp. 3–22.

[26] V. Gnielinski. "New Equations for Heat and Mass Transfer in Turbulent Pipe and Channel Flow". In: *Int. Chem. Eng.* 16.2 (1976), pp. 359–368.

[56] X. Daguenet-Frick et al. "Numerical Investigation of a Ceramic High-Temperature Pressurized-Air Solar Receiver". In: *Solar Energy* 90 (2013), pp. 164–178.

[59] J. Capeillère et al. "Thermomechanical Behavior of a Plate Ceramic Solar Receiver Irradiated by Concentrated Sunlight". In: *Solar Energy* 110 (2014), pp. 174–187.

[60] A. Colleoni, A. Toutant, and G. Olalde. "Simulation of an Innovative Internal Design of a Plate Solar Receiver: Comparison between RANS and LES Results". In: *Solar Energy* 105 (2014), pp. 732–741.

[61] Q. Li et al. "Micro-Channel Pressurized-Air Solar Receiver Based on Compact Heat Exchanger Concept". In: *Solar Energy* 91 (2013), pp. 186–195.

[69] W. Sutherland. "The Viscosity of Gases and Molecular Force". In: *The London, Edinburgh, and Dublin Philosophical Magazine and Journal of Science* 36.223 (1893), pp. 507–531.

[141] J. Smagorinsky. "General Circulation Experiments with the Primitive Equations". In: *Monthly Weather Review* 91.3 (1963), pp. 99–164.

[160] D. Dupuy, A. Toutant, and F. Bataille. "A Priori Tests of Subgrid-Scale Models in an Anisothermal Turbulent Channel Flow at Low Mach Number". In: *International Journal of Thermal Sciences* 145 (2019), p. 105999.

[162] J. W. Deardorff. "A Numerical Study of Three-Dimensional Turbulent Channel Flow at Large Reynolds Numbers". In: *Journal of Fluid Mechanics* 41.2 (1970), pp. 453–480.

[188] S. Serra, A. Toutant, and F. Bataille. "Thermal Large Eddy Simulation in a Very Simplified Geometry of a Solar Receiver". In: *Heat Transfer Engineering* 33.6 (2012), pp. 505–524.

[190] L. D. Dailey, N. Meng, and R. H. Pletcher. "Large Eddy Simulation of Constant Heat Flux Turbulent Channel Flow With Property Variations: Quasi-Developed Model and Mean Flow Results". In: *Journal of Heat Transfer* 125.1 (2003), pp. 27–38.

[211] J. M. Avellaneda, F. Bataille, and A. Toutant. "DNS of Turbulent Low Mach Channel Flow under Asymmetric High Temperature Gradient: Effect of Thermal Boundary Condition on Turbulence Statistics". In: *International Journal of Heat and Fluid Flow* 77 (2019), pp. 40–47.

[214] F. Aulery et al. "Spectral Analysis of Turbulence in Anisothermal Channel Flows". In: *Computers & Fluids*. A Special Issue in Honor of Cecil "Chuck" E. Leith 151 (2017), pp. 115–131.

[221] X. Daguenet-Frick et al. "Experimental Analysis of the Turbulent Flow Behavior of a Textured Surface Proposed for Asymmetric Heat Exchangers". In: *Flow, Turbulence and Combustion* 89.1 (2012), pp. 149–169.

[260] E. N. Sieder and G. E. Tate. "Heat Transfer and Pressure Drop of Liquids in Tubes". In: *Industrial & Engineering Chemistry* 28.12 (1936), pp. 1429–1435.

[261] H. Shi et al. "Numerical Study of Heat Transfer in Square Millimetric Zigzag Channels in the Laminar Flow Regime". In: *Chemical Engineering and Processing - Process Intensification* 144 (2019), p. 107624.

[262] R. K. Shah. "Laminar Flow Friction and Forced Convection Heat Transfer in Ducts of Arbitrary Geometry". In: *International Journal of Heat and Mass Transfer* 18.7 (1975), pp. 849–862.

[263] M. V. V. Mortean and M. B. H. Mantelli. "Nusselt Number Correlation for Compact Heat Exchangers in Transition Regimes". In: *Applied Thermal Engineering* 151 (2019), pp. 514–522.

[264] M. V. V. Mortean et al. "Thermal and Hydrodynamic Analysis of a Cross-Flow Compact Heat Exchanger". In: *Applied Thermal Engineering* 150 (2019), pp. 750–761.

[265] T.-M. Liou, C.-S. Wang, and H. Wang. "Nusselt Number and Friction Factor Correlations for Laminar Flow in Parallelogram Serpentine Micro Heat Exchangers". In: *Applied Thermal Engineering* 143 (2018), pp. 871–882.

[266] W. Qu and I. Mudawar. "Experimental and Numerical Study of Pressure Drop and Heat Transfer in a Single-Phase Micro-Channel Heat Sink". In: *International Journal of Heat and Mass Transfer* 45.12 (2002), pp. 2549–2565.

[267] Y. Sudo, M. Kaminaga, and H. Ikawa. "Combined Forced and Free Convective Heat Transfer Characteristics in Narrow Vertical Rectangular Channel Heated from Both Sides". In: *Journal of Nuclear Science and Technology* 24.5 (1987), pp. 355–364.

[268] J. Ma et al. "Experimental Studies on Single-Phase Flow and Heat Transfer in a Narrow Rectangular Channel". In: *Nuclear Engineering and Design* 241.8 (2011), pp. 2865–2873.

[269] R. W. Lyczkowski, C. W. Solbrig, and D. Gidaspow. "Forced Convection Heat Transfer in Rectangular Ducts—General Case of Wall Resistances and Peripheral Conduction for Ventilation Cooling of Nuclear Waste Repositories". In: *Nuclear Engineering and Design* 67.3 (1982), pp. 357–378.

[270] P.-S. Lee and S. V. Garimella. "Thermally Developing Flow and Heat Transfer in Rectangular Microchannels of Different Aspect Ratios". In: *International Journal of Heat and Mass Transfer* 49.17 (2006), pp. 3060–3067.

[271] Q. Li et al. "Compact Heat Exchangers: A Review and Future Applications for a New Generation of High Temperature Solar Receivers". In: *Renewable and Sustainable Energy Reviews* 15.9 (2011), pp. 4855–4875.

[272] J. W. Deardorff. "The Use of Subgrid Transport Equations in a Three-Dimensional Model of Atmospheric Turbulence". In: *Journal of Fluids Engineering* 95.3 (1973), pp. 429–438.

[273] D. G. Fox and D. K. Lilly. "Numerical Simulation of Turbulent Flows". In: *Reviews of Geophysics* 10.1 (1972), pp. 51–72.

[274] M. R. Rodríguez-Sánchez et al. "Development of a New Method to Estimate the Incident Solar Flux on Central Receivers from Deteriorated Heliostats". In: *Renewable Energy* 130 (2019), pp. 182–190.

[275] S. Whitaker. "Forced Convection Heat Transfer Correlations for Flow in Pipes, Past Flat Plates, Single Cylinders, Single Spheres, and for Flow in Packed Beds and Tube Bundles". In: *AIChE Journal* 18.2 (1972), pp. 361–371.

[276] B. S. Petukhov. "Heat Transfer and Friction in Turbulent Pipe Flow with Variable Physical Properties". In: *Advances in Heat Transfer*. Ed. by J. P. Hartnett and T. F. Irvine. Vol. 6. Elsevier, 1970, pp. 503–564.

[277] J. F. Barnes and J. D. Jackson. "Heat Transfer to Air, Carbon Dioxide and Helium Flowing through Smooth Circular Tubes under Conditions of Large Surface/Gas Temperature Ratio". In: *Journal of Mechanical Engineering Science* (2006), pp. 303–314.

[278] V. Gnielinski. "On Heat Transfer in Tubes". In: *International Journal of Heat and Mass Transfer* 63 (2013), pp. 134–140.

[279] D. Bertsche, P. Knipper, and T. Wetzel. "Experimental Investigation on Heat Transfer in Laminar, Transitional and Turbulent Circular Pipe Flow". In: *International Journal of Heat and Mass Transfer* 95 (2016), pp. 1008–1018.

[280] V. Gnielinski. "G1 Heat Transfer in Pipe Flow". In: *VDI Heat Atlas*. VDI-Buch. Berlin, Heidelberg: Springer, 2010, pp. 691–700. ISBN: 978-3-540-77877-6.

[281] D. Taler. "Simple Power-Type Heat Transfer Correlations for Turbulent Pipe Flow in Tubes". In: *Journal of Thermal Science* 26.4 (2017), pp. 339–348.

[282] S. C. R. Dennis, A. M. Mercer, and G. Poots. "Forced Heat Convection in Laminar Flow through Rectangular Ducts". In: *Quarterly of Applied Mathematics* 17.3 (1959), pp. 285–297.

[283] W. M. Kays and M. E. Crawford. *Convective Heat and Mass Transfer*. New York: McGraw-Hill, 1993. ISBN: 978-0-07-033721-3 978-0-07-112516-1.

[284] K. R. Perkins, K. W. Schade, and D. M. McEligot. "Heated Laminarizing Gas Flow in a Square Duct". In: *International Journal of Heat and Mass Transfer* 16.5 (1973), pp. 897–916.

[285] D. A. Campbell and H. C. Perkins. "Variable Property Turbulent Heat and Momentum Transfer for Air in a Vertical Rounded Corner Triangular Duct". In: *International Journal of Heat and Mass Transfer* 11.6 (1968), pp. 1003–1012.

[286] H. C. Perkins and P. Worsoe-Schmidt. "Turbulent Heat and Momentum Transfer for Gases in a Circular Tube at Wall to Bulk Temperature Ratios to Seven". In: *International Journal of Heat and Mass Transfer* 8.7 (1965), pp. 1011–1031.

[287] Y. Sudo et al. "Experimental Study of Differences in Single-Phase Forced-Convection Heat Transfer Characteristics between Upflow and Downflow for Narrow Rectangular Channel". In: *Journal of Nuclear Science and Technology* 22.3 (1985), pp. 202–212.

[288] Z. H. Liang et al. "Experimental Investigation on Flow and Heat Transfer Characteristics of Single-Phase Flow with Simulated Neutronic Feedback in Narrow Rectangular Channel". In: *Nuclear Engineering and Design* 248 (2012), pp. 82–92.

[289] C. Wang et al. "Forced Convection Heat Transfer and Flow Characteristics in Laminar to Turbulent Transition Region in Rectangular Channel". In: *Experimental Thermal and Fluid Science* 44 (2013), pp. 490–497.

[290] D. Jo et al. "Experimental Investigation of Convective Heat Transfer in a Narrow Rectangular Channel for Upward and Downward Flows". In: *Nuclear Engineering and Technology* 46.2 (2014), pp. 195–206.

[291] A. Ghione et al. "Assessment of Thermal–Hydraulic Correlations for Narrow Rectangular Channels with High Heat Flux and Coolant Velocity". In: *International Journal of Heat and Mass Transfer* 99 (2016), pp. 344–356.

[292] J. Ma et al. "Experimental Investigations on Single-Phase Heat Transfer Enhancement with Longitudinal Vortices in Narrow Rectangular Channel". In: *Nuclear Engineering and Design* 240.1 (2010), pp. 92–102.

[293] K. Stephan and P. Preußer. "Wärmeübergang Und Maximale Wärmestromdichte Beim Behältersieden Binärer Und Ternärer Flüssigkeitsgemische". In: *Chemie Ingenieur Technik* 51.1 (1979), pp. 37–37.

[294] R. Sun et al. "Experimental Study of Single-Phase Flow and Heat Transfer in Rectangular Channels under Uniform and Non-Uniform Heating". In: *Experimental Thermal and Fluid Science* 114 (2020), p. 110055.

[295] T.-S. Wang and M. K. Chyu. "Heat Convection in a 180-Deg Turning Duct with Different Turn Configurations". In: *Journal of Thermophysics and Heat Transfer* 8.3 (1994), pp. 595–601.

[296] Z. Qin and R. Pletcher. "Large Eddy Simulation of Turbulent Heat Transfer in a Rotating Square Duct". In: *International Journal of Heat and Fluid Flow* 27.3 (2006), pp. 371–390.

[297] N. Sato et al. "Numerical Investigation of the Effect of Prandtl Number on Heat Transfer in a Dimpled-Channel Flow". In: *International Journal of Heat and Fluid Flow* 68 (2017), pp. 139–150.

[298] L. Su et al. "Heat Transfer Characteristics of Thermally Developing Flow in Rectangular Microchannels with Constant Wall Temperature". In: *International Journal of Thermal Sciences* 155 (2020), p. 106412.

[299] W.-S. Fu et al. "Flow Downward Penetration of Vertical Parallel Plates Natural Convection with an Asymmetrically Heated Wall". In: *International Communications in Heat and Mass Transfer* 74 (2016), pp. 55–62.

[300] G. E. Lau et al. "Large-Eddy Simulation of Natural Convection in an Asymmetrically-Heated Vertical Parallel-Plate Channel: Assessment of Subgrid-Scale Models". In: *Computers & Fluids* 59 (2012), pp. 101–116.

[301] S. Taieb, L. Ali Hatem, and J. Balti. "Natural Convection in an Asymmetrically Heated Vertical Channel with an Adiabatic Auxiliary Plate". In: *International Journal of Thermal Sciences* 74 (2013), pp. 24–36.

[302] Y. Cherif et al. "Experimental and Numerical Natural Convection in an Asymmetrically Heated Double Vertical Facade". In: *International Journal of Thermal Sciences* 152 (2020), p. 106288.

[303] N. Kimouche et al. "Effect of Inclination Angle of the Adiabatic Wall in Asymmetrically Heated Channel on Natural Convection: Application to Double-Skin Façade Design". In: *Journal of Building Engineering* 12 (2017), pp. 171–177.

[304] B. Brangeon, P. Joubert, and A. Bastide. "Influence of the Dynamic Boundary Conditions on Natural Convection in an Asymmetrically Heated Channel". In: *International Journal of Thermal Sciences* 95 (2015), pp. 64–72.

[305] D. G. Osborne and F. P. Incropera. "Laminar, Mixed Convection Heat Transfer for Flow between Horizontal Parallel Plates with Asymmetric Heating". In: *International Journal of Heat and Mass Transfer* 28.1 (1985), pp. 207–217.

[306] C. Gau, Y. C. Jeng, and C. G. Liu. "An Experimental Study on Mixed Convection in a Horizontal Rectangular Channel Heated From a Side". In: *Journal of Heat Transfer* 122.4 (2000), pp. 701–707.

[307] T. H. Hwang, Y. Cai, and P. Cheng. "An Experimental Study of Forced Convection in a Packed Channel with Asymmetric Heating". In: *International Journal of Heat and Mass Transfer* 35.11 (1992), pp. 3029–3039.

[308] D. A. Nield. "Forced Convection in a Parallel Plate Channel with Asymmetric Heating". In: *International Journal of Heat and Mass Transfer* 47.25 (2004), pp. 5609–5612.

[309] J. Mitrović, B. Maletić, and B. S. Bačlić. "Some Peculiarities of the Asymmetric Graetz Problem". In: *International Journal of Engineering Science* 44.7 (2006), pp. 436–455.

[310] R. Repaka and V. V. Satyamurty. "Local and Average Heat Transfer in the Thermally Developing Region of an Asymmetrically Heated Channel". In: *International Journal of Heat and Mass Transfer* 53.9 (2010), pp. 1654–1665.

[311] A. V. Kuznetsov and D. A. Nield. "Forced Convection in a Channel Partly Occupied by a Bidisperse Porous Medium: Asymmetric Case". In: *International Journal of Heat and Mass Transfer* 53.23 (2010), pp. 5167–5175.

[312] P. van Male et al. "Heat and Mass Transfer in a Square Microchannel with Asymmetric Heating". In: *International Journal of Heat and Mass Transfer* 47.1 (2004), pp. 87–99.

[313] S. Torii and W.-J. Yang. "Effect of Heat Flux Ratio on Two-Dimensional Horizontal Channel Flow". In: *Journal of Thermophysics and Heat Transfer* 18.1 (2004), pp. 73–78.

[314] S. Serra et al. "High-Temperature Gradient Effect on a Turbulent Channel Flow Using Thermal Large-Eddy Simulation in Physical and Spectral Spaces". In: *Journal of Turbulence* 13 (2012), N49.

[315] A. Toutant and F. Bataille. "Turbulence Statistics in a Fully Developed Channel Flow Submitted to a High Temperature Gradient". In: *International Journal of Thermal Sciences* 74 (2013), pp. 104–118.

7.3 Conclusion of chapter 7

In this chapter, a state of the art of the existing heat transfer correlations has been carried out. It has shown that there is no expression applicable in the working conditions of gas-pressurized solar receivers. For that reason, the focus has been placed on the development of a simple tool that permits investigating the wall heat transfers in the desired conditions, namely a Reynolds number of approximately 10^5, hot and cold wall temperatures around respectively 1300 K and 900 K, and a thermodynamical pressure of about 10 bars. This correlation should help the achievement of feasibility studies and thus promote the implementation of this technology in the global energy mix. The present chapter is the last link of the multi-scale approach.

Heat transfer correlations also permit performing wall heat flux sensitivity analyzes [316, 317]. In chapter 8, the developed heat transfer correlation is used to quantify the propagation of the flow parameters uncertainties on the wall heat fluxes.

Chapter 8

Impact of asymmetrical heating on the uncertainty propagation of flow parameters on wall heat transfers in solar receivers

Contents

8.1 Introduction of chapter 8

This chapter aims to quantify the error propagation of the measurement or the calculation of the flow parameters on the wall heat fluxes. The study relies on the proposed heat transfer correlation and provides key information for the sizing of solar receivers. The heat transfer sensitivity analysis permits concreting the upstream researches carried out in part I. This chapter

contributes to answer to the overall problem of facilitating the development of the gas-pressurized solar power towers.

The operating conditions of gas-pressurized solar receiver are very complex. They involve an intense turbulence to enhance the wall heat transfers, a strong asymmetric heating of the fluid due to the fact that only one wall receives the concentrated solar radiation, and high levels of wall heat fluxes because of the strong temperature gradients between the fluid and the walls. For that reason, the accurate measurement or computation of the flow properties is complex and costly. Both methods induce uncertainties. Hence, the uncertainty propagation of the flow parameters on the wall heat fluxes should be quantified. A misestimation of the wall heat transfer could have severe consequences on the solar receiver lifetime and efficiency of the solar power tower.

8.2 Paper 4: Impact of asymmetrical heating on the uncertainty propagation of flow parameters on wall heat transfers in solar receivers

This section reproduces the paper of M. David, A. Toutant, and F. Bataille untitled Impact of asymmetrical heating on the uncertainty propagation of flow parameters on wall heat transfers in solar receivers and published in *Applied Thermal Engineering*.

Abstract

Uncertainties may skew the understanding of experiments or numerical simulations results. The impact of the flow parameters uncertainties of measurement on wall heat flux is investigated in a non-isothermal turbulent channel flow. A heat transfer correlation dedicated to gas-pressurized solar receivers of concentrated solar tower power is used. Both symmetric and asymmetric heating conditions are tested. A sensitivity study is performed. The effects of the wall and bulk temperatures are analyzed in a large bulk-to-wall temperature ratio range. The Guide to the expression of Uncertainty in Measurement (GUM) is applied and provides an analytical expression of the uncertainty propagation. Assuming the quasi-normality and quasi-linearity of the studied function, this method provides approximate results. The results obtained following the methodology described in the GUM are then compared to the direct computation of the wall heat flux with altered temperatures. The study shows a dependence of the high heat flux estimation to some temperature variations, highlighting the necessity of accurate measurements. This is particularly salient in the end region of the solar receiver, *i.e.* when the bulk and the wall temperature are close. The GUM produces very satisfying estimations in the symmetric conditions and quite satisfying estimations in the asymmetric conditions. This study shows that the accuracy of measurement devices should be adapted according to their location in the solar receiver.

8.2.1 Introduction

In applied engineering devices, there are many possible sources of uncertainty: measurement with finite instrument resolution, personal bias in reading analog instruments, inadequate knowledge of the effects of environmental conditions on the measurement [318]. The committed errors should be put into perspective with a sensitivity analysis. They may become very problematic when moving from principles to a functioning system. Indeed, while some devices are poorly affected by parameter variations, some are very sensitive to specific parameters. For example, in

gas turbines the wall temperature variation greatly affects the lifetime of the components: it is generally accepted that a variation of 20 K in the metal reduces the life of the components by 50% [319]. Uncertainties may skew the understanding of the results of experiments or numerical simulations. For that reason, several authors propose methods to bring uncertainties out. Some studies dealing with uncertainties in the fields of fluid mechanics and heat transfers are addressed below. Oliver *et al.* [320] address two major sources of uncertainty in statistics computed from Direct Numerical Simulation (DNS): finite sampling error and discretization error. They propose a systematic and unified approach to estimate these two uncertainty sources when resolving the Navier–Stokes equations. A Bayesian extension of the standard Richardson extrapolation that accounts for both statistical uncertainty and prior information is formulated. Phillips and Roy [321] investigate the accuracy of various Richardson extrapolation-based discretization error and uncertainty estimators for problems in computational fluid dynamics. The Richardson extrapolation consists in using two solutions on systematically refined grids to estimate the exact solution to partial differential equations. This method is only applicable when the grids are sufficiently fine. Carneval *et al.* [322] propose a stochastic method to predict heat transfer using Large Eddy Simulation (LES). It consists in coupling a classical uncertainty quantification to LES in a duct with pin fins. The authors demonstrate that the uncertainties related to the unknown conditions, named aleatoric uncertainties, and those related to the physical model, named epistemic uncertainties, are strongly interconnected. Menberg *et al.* [323] investigate three methods for sensitivity analysis in relation to dynamic, high-order, non-linear behavior and the level of uncertainty in building energy models. Prediction of uncertainties in heat transfer coefficient determination is a commonly studied topic. For instance, a large number of works addresses the uncertainty propagation when estimating the convection coefficients in a wide spectrum of convective heat transfer processes with the Wilson plot method. Uhía *et al.* [324] detail the application of the Guide to the expression of Uncertainty in Measurement (GUM) [318] for calculating the uncertainty associated with experimental heat transfer data obtained thanks to the Wilson plot method. They illustrate their work by applying the GUM to the specific process of condensation of R-134a on a horizontal smooth tube. The impact of the uncertainty of measurements is discussed on the basis of two normalized coefficients proposed by Coleman and Steele [325]: the uncertainty magnification factor (UMF) and the uncertainty percentage contribution (UPC). The effects of the temperature interference on the results obtained using the Wilson plot technique are also investigated by Wójs and Tietze [326]. The authors highlight the importance of using adequate experimental data to obtain reliable results.

The uncertainty propagation can be quantified with probabilistic and deterministic methods. The Monte Carlo approach rely on repeated random sampling. It is very commonly used in engineering [327, 328, 329, 330, 331, 332, 333]. The methodology has many advantages: it is a general and powerful technique that can be applied to non-linear problems. However, the computational cost of Monte Carlo simulation can easily become prohibitive [334]. Taler [335] details the calculation of the indirect measurement uncertainty using the rule formulated by Gauss for the uncertainty propagation. The non-linear least squares method used to estimate parameters and indirectly determined quantities are described and several examples of uncertainty determination of measured parameters involved in heat transfer correlations are presented. Functional expansion-based methods such as the arbitrary polynomial chaos expansion [336], Karhunen–Loève expansion [337], and Neumann expansion [338] can also be used for uncertainty quantification. The Guide to the expression of Uncertainty in Measurement (GUM) provides a local expansion-based method involving the Taylor expansions. It gives general rules for evaluating and expressing uncertainty in measurement that are intended to be applicable to a broad

spectrum of measurements. It is considered as a general cross-disciplinary standard, applicable to all fields. Furthermore, it produces an analytical expression of the error. The GUM framework assumes the quasi-linearity and the quasi-normality of the studied function. The linear approximation of the function has to be close to the function in the uncertainty range. The GUM method is particularly advantageous when dealing with reasonable input variability and outputs that do not express high non-linearity. For these reasons, this method is selected to study the sensitivity of the wall heat flux to flow parameters. The GUM framework is detailed in [318]. Studying convective heat transfer, Håkansson [339] notices some incoherence in the literature when regarding heat transfer coefficient values. Using the GUM, he points out that several methods used to determine the heat transfer coefficient are very dependent on the accuracy of measurements. This could be responsible for the various results obtained in the literature.

Heat transfer correlations are widely used in engineering field to estimate wall heat flux of complex devices such as automobile radiators [25], heat exchangers [340, 341, 342], and solar receivers of concentrated solar power tower [27]. Correlations allow the estimation of the heat transfer within, generally, 10% to 20% of error [27, 260, 268, 23, 278, 281]. This accuracy is usually acceptable for pre-dimensioning. However, it is necessary to consider the uncertainty of measurements and their propagation to estimate an error range associated with the heat flux prediction. Correlation may also be useful to quantify the heat transfer sensitivity to parameters. Table 8.1 gives the major results of some studies investigating uncertainty propagation.

To the author's knowledge, there is no study addressing wall heat flux sensitivity in the operating conditions of solar receivers. In this paper, a correlation developed for both symmetrically and asymmetrically heated turbulent channel flow is used to quantify the propagation of the uncertainties of the flow parameters on the wall heat fluxes. Firstly, the used correlation is presented in Section 8.2.2. The sensitivity of the heat fluxes to flow parameters is analyzed under symmetric heating conditions and in the working conditions of gas-pressurized solar receivers of concentrated solar power tower (Section 8.2.3). Then, in Section 8.2.4, the results obtained by the GUM applied to the correlation are compared to the direct computation of the wall heat fluxes with the same variations of the input parameters in both heating conditions. The entire applicable range of the correlation in terms of bulk-to-cold wall temperature is investigated.

8.2.2 Heat transfer correlation for turbulent channel flow

The correlation proposed by David *et al.* [27] aims to estimate the heat transfer in the working conditions of gas-pressurized solar receivers. This technology is still in the research stage. Numerous geometries are investigated in the literature including tubes [58], channels with vortex generators [59, 60], and thin channels [61, 56]. In the present study, we focus on this last type of gas-pressurized solar receiver. A bi-periodic channel is used to model the geometry. The correlation has been established thanks to 70 Thermal-Large Eddy Simulations, constituting a consequent and reliable database. In those simulations, the Navier-Stokes equations are solved under the low Mach number approximation. The coupling between velocity and temperature is considered. The thermal dilatation is taken into account. The density is linked to the temperature variations thanks to the ideal gas-law. The gravity force is not taken into account since its impact is negligible in the working conditions. Indeed, the Richardson number is about 10^{-5}. The correlation is obtained for fully developed flows. The simulations are performed in a bi-periodical channel. To lower the fluid temperature, a source term is introduced in the energy equation. It allows to maintain a constant bulk temperature. Hence, this temperature corresponds to the average of the fluid temperature along the wall-normal direction. The small

Table 8.1 – Major results of some literature papers dealing with uncertainty propagation.

Authors	Topic	Major results
Driscoll and Landrum [316]	Uncertainty on heat transfer correlations for fuel in copper tubing. They quantify the influence of uncertainties on the engine design.	The overall uncertainty on the Nusselt number can reach 36%. The magnitude of the uncertainty values and their impact on engine design parameters highlights the importance of mitigating the Nusselt number uncertainties.
Scariot *et al.* [317]	Influence of the uncertainty of measurements on the fluid temperature and enthalpy in carbon dioxide tube flow using heat transfer correlations.	Results shows that the uncertainty propagation is significantly influenced by the local conditions. They state that the difficulty to predict experimental data from correlations is due to the observed uncertainty amplification. In the worst case, the uncertainties on the enthalpy range from -7% to +15%, considering that the correlation has a 10% uncertainty under such conditions. These uncertainties are significantly increased if the accuracy of the correlation decreases.
Dimassi and Dehamni [343]	Experimental thermal analysis of a Trombe wall	Uncertainties of thermal heat fluxes can reach 4.8% despite small uncertainties on the temperature, velocity, radiation coefficient, and convection coefficient measurements.
Sciacchitano and Wieneke [344]	PIV uncertainty propagation	The uncertainty of the vorticity is estimated typically within 5–10% accuracy, time-averaged velocities are accurate within 5%. The Reynolds stresses are more difficult to estimate and the PIV gives a prediction within 10%.
Paudel and Hostikka [345]	Stochastic simulations of a compartment fire with Fire Dynamic Simulation.	The results show that the prediction uncertainty for both gas phase and solid phase temperature is accurate within 10%.
Zhao *et al.* [346]	Uncertainty and sensitivity analysis of flow parameters for transition models on hypersonic flows.	Uncertainties on heat flux and skin friction coefficient distribution, as well as uncertainties on the Stanton number, and the onset and length of the transition zone are investigated. The uncertainty results quantitatively verify that the transition zone is greatly sensitive to changes in flow parameters. The transition length and onset are estimated within 10% of uncertainty.

Table 8.2 – Applicable domain of the correlation.

Symmetric heating	Asymmetric heating
$12000 < Re_b < 177000$	$10600 < Re_b < 145000$
$0.47 < T_b/T_w < 0.99$	$1.1 < T_h/T_c < 2.0$
	$0.63 < T_b/T_c < 0.95$
	$0.44 < T_b/T_h < 0.85$

turbulent scales are not solved in LES. Their effects on bigger turbulent structures are considered thanks to the Anisotropic-Minimum-Dissipation (AMD) model. This model showed a good agreement with DNS in similar conditions [17, 145, 160]. The proposed correlation is given by:

$$Nu_w^{asy} = 0.024 Re_b^{0.8} Pr_b^{0.4} \left(\frac{T_w}{T_b}\right)^{-0.9} \left(\frac{T_w}{T_w - T_b}\right)^{1.4\left(1-\frac{T_w}{T_m}\right)\frac{T_b}{T_w}}, \tag{8.1}$$

with $T_m = (T_h + T_c)/2$.

A term accounting for asymmetric heating conditions is included in the equation to reproduce the heat transfers at both walls taking into account the respective effects of one on this other. This term involves flow parameters in the exponent. The singularity of the Nusselt number, observed when the bulk temperature (defined as the average fluid temperature) tends towards the cold wall temperature and explained by Nield in [308], is reproduced thanks to the difference of temperature at the denominator of the asymmetric group. This term, accounting for asymmetric condition, is equal to 1 in the case of symmetric heating conditions leading to the correlation presented below:

$$Nu_w^{sym} = 0.024 Re_b^{0.8} Pr_b^{0.4} \left(\frac{T_w}{T_b}\right)^{-0.9}. \tag{8.2}$$

The proposed correlation is studied in the commonly encountered working conditions of heat exchangers and solar receivers. The validity domain of the correlation in terms of Reynolds number and temperature ranges is given in Table 8.2. The wall temperatures vary from 293 K to 1300 K. The fluid temperature ranges from 342 K to 1237 K, Prandtl number is between 0.76 and 3.18, and heat fluxes vary from 4 kW/m^2 to 578 kW/m^2.

An overview of the point distribution is given in this paragraph. The values are given indifferently for both types of heating. The Reynolds number ranges from 10600 to 177000. 25 different values of Reynolds number are covered with a mean step of 6400. The Prandt number is between 0.76 and 3.18. The values taken by the Prandtl number are dependent of the temperatures. Most of the points are around 3.1, 2.6, 1, and 0.8. The hot wall temperature is between 586 K and 1300 K. The covered values are: 586 K, 700 K, 810 K, 900 K, 1100 K, and 1300 K. The cold wall temperature is between 293 K and 1300 K. It takes the following values: 293 K, 500 K, 700 K, 810 K, 900 K, 1100 K, and 1300 K. The bulk temperature is between 461 K and 1236 K. The range is homogeneously covered. There are several bulk temperature points in every 50 K interval.

The Nusselt numbers obtained with the correlation proposed by David *et al.* [27] are plotted against the Nusselt numbers obtained with the numerical simulations in Figure 8.1. The relative error on the Nusselt number is obtained as follows:

$$\epsilon_{Nu} = \frac{Nu_{cor} - Nu_{sim}}{Nu_{sim}}. \tag{8.3}$$

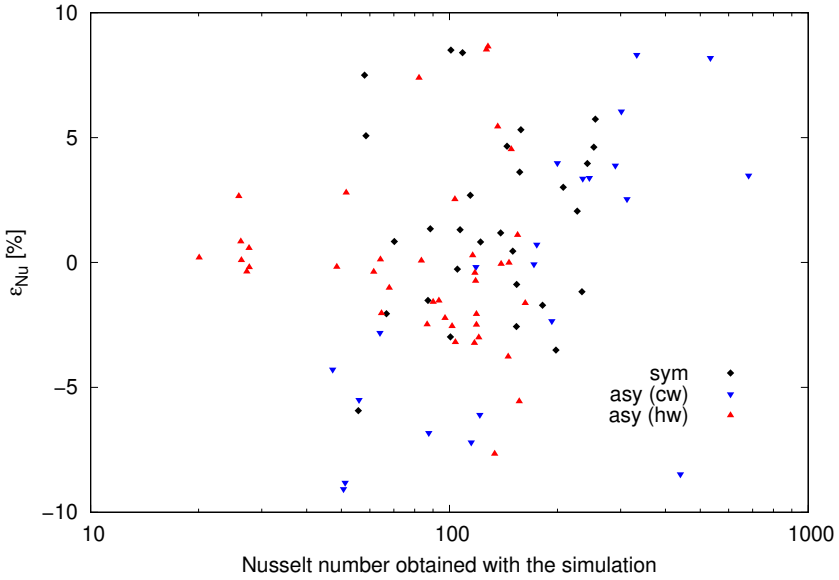

Figure 8.1 – Relative error on the Nusselt number obtained with the heat transfer correlation as function of the Nusselt number obtained by the simulation.

Black dots stand for the Nusselt number obtained under symmetric heating conditions. Red dots, respectively blue dots, account for the Nusselt obtained at the hot wall, respectively cold wall, under asymmetric heating conditions. The Nusselt number range is between 20 and 680. The results show that all the points are within the 10% error range. A detailed analysis of the data shows that more than three-quarters of the results are in the error bound 5%. The determination coefficient is 0.993. The mean error is 0.29% and the standard deviation is 4.1%.

In the following, the wall heat fluxes are computed using the Nusselt numbers obtained with the correlation thanks to equation presented below:

$$\phi_w = \frac{\lambda_w (T_w - T_b) Nu_w}{L}. \tag{8.4}$$

Figure 8.2 aims to give an overview of the wall heat flux behavior depending on the ratio between bulk temperature and the average of both wall temperatures in both heating conditions. It permits linking the heat flux uncertainties presented in Section 8.2.4 to the value of the reference heat flux. The Reynolds number and the wall temperatures used to obtain Figure 8.2 are those referenced in Table 8.3 for the symmetric heating case and those referenced in Table 8.5 for the asymmetric heating case. The bulk temperature varies between 700 K and 1100 K. Hence, this figure is valid for a fixed Reynolds number of 60 000 and fixed wall temperatures of 1100 K under symmetric heating condition or 900 K and 1300 K under asymmetric heating conditions. The wall heat fluxes are normalized with the following equation:

$$\phi^+ = \frac{\phi_w (T_b/T_m)}{\phi_{w,\ max}^{sym}}, \tag{8.5}$$

where $\phi_{w,\ max}^{sym}$ corresponds to the maximum wall heat flux obtained under symmetric heating and $\phi_{w,\ max}^{sym} = 198$ kW/m^2. This maximum wall heat flux obtained under symmetric heating is reached for a Reynolds number of 60 000, a Prandtl number of 0.87, a bulk temperature of

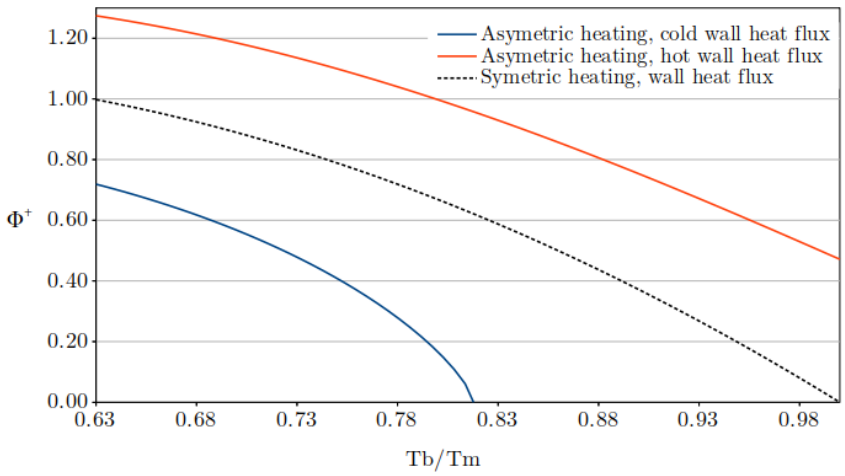

Figure 8.2 – Normalized wall heat fluxes as function of the ratio between bulk temperature and the average of both wall temperatures. The wall temperatures are 1300 K and 900 K in the case of asymmetric heating. They are of 1100 K in the case of symmetric heating. The bulk temperature and the Reynolds number are respectively 700 K and 60 000.

700 K, and wall temperature of 1100 K. The ratio T_b/T_m into brackets is a functional expression. The wall heat fluxes are decreasing with the increase of the temperature ratio. For the asymmetric case, the cold wall heat flux is rapidly diminishing and became equal to zero when the bulk and cold wall temperatures are the same. On the hot side, the normalized heat flux is slowly decreasing and reaches 0.45 for a ratio between bulk temperature and the average of both wall temperatures of 1. In the symmetric heating conditions, the wall heat flux is moderately diminishing.

8.2.3 Wall heat flux sensitivity

Studying the sensitivity of wall heat flux with a correlation is an interesting approach to highlight the influence of each parameter. It gives the measurement accuracy necessary to provide a reliable prediction of the wall heat fluxes. In the applicable domain of the correlation, the estimated wall heat flux sensitivity reflects the physic behavior. A high temperature sensitivity calculated with the correlation means that the physical wall heat flux is greatly impacted by this parameter. In Subsections 8.2.3.1 and 8.2.3.2, the wall heat flux is computed thanks to the direct application of the correlation. A routine is used to compute the reference wall heat flux and the altered wall heat flux thanks to the correlation. The altered wall heat flux is calculated by altering a single flow parameter from -10% to 10% of its reference value by step of 0.5%. For each step, the ratio between the reference and the altered wall heat flux is computed and reported in Figures 8.3 and 8.5.

8.2.3.1 Symmetric heating conditions

Firstly, the sensitivity of the wall heat fluxes is studied in symmetric heating condition. These conditions are summarized in Table 8.3.

Figure 8.3 exposes the error on the wall heat fluxes depending on the error committed on various flow parameters in the symmetric heating conditions presented in Table 8.3. The propaga-

Table 8.3 – Studied conditions in the symmetric heating case.

Re_b	Pr_b	T_h [K]	T_c [K]	T_b [K]
60 000	0.87	1100	1100	700

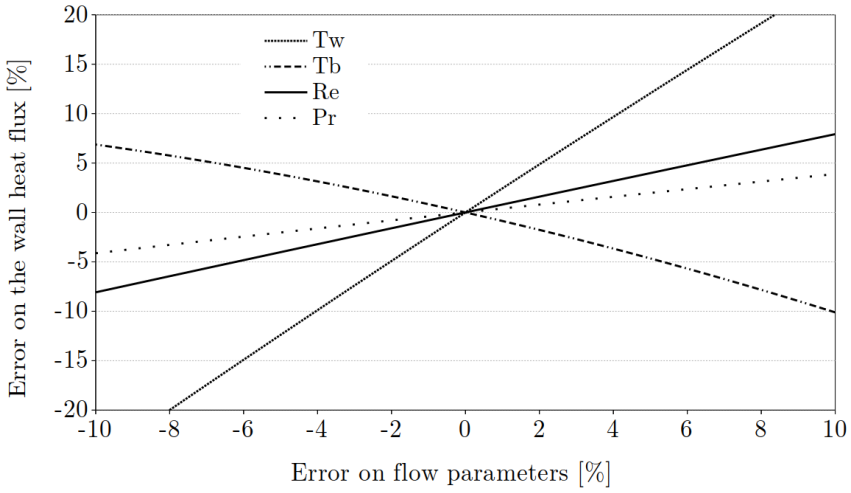

Figure 8.3 – Error on the wall heat fluxes depending on the error committed on various flow parameters for symmetric heating conditions. The results are obtained with the conditions listed in Table 8.3.

tion of the error committed on the measurements of the wall temperature, the bulk temperature, the Reynolds number, and the Prandtl number are studied. The error on the wall heat flux is computed as follows:

$$Err_\phi = \frac{\phi\left(Y_{alt}\right) - \phi\left(Y_{ref}\right)}{\phi\left(Y_{ref}\right)}, \tag{8.6}$$

where $Y_{alt} = Y_{ref} + x\%$ with x ranging between -10% and 10%. The errors on flow parameters are defined in the same way that the error on the wall heat flux and described by equation 8.2.3.1. All the temperatures are expressed in degree Kelvin. The results show that uncertainties on wall temperature are amplified. They induce an important error on the wall heat flux. The bulk temperature and Reynolds number estimations are less impacting but remain consequent. The wall heat flux error is mitigated when compared to the error on the Prandtl number. Indeed, the wall heat flux error is in the 5% error range. The ranking of the parameters in terms of influence is independent of the uncertainty of measurement.

Figure 8.4 presents the slope of the error propagation for uncertainties relative to the wall and bulk temperatures. The curves observed in Figure 8.3 are approximated by straight lines thanks to the generalized least-squares method. Four wall temperatures are investigated. The wall temperature increases from 700 K to 1300 K. In each case, the bulk temperature is 200 K below the wall temperature. The investigated cases are listed in Table 8.4 The error propagations concerning the Reynolds number and the Prandtl number are not affected by the thermal conditions that is why they are not plotted in this figure. The results show that the slope of the error propagation increases linearly with the wall temperature. In the studied cases, the slope of the error propagation corresponding to the wall temperature is higher than the slope of the

Table 8.4 – List of the tested cases in Figure 8.4.

T_w [K]	T_b [K]	T_b/T_w
700	500	0.71
900	700	0.78
1100	900	0.82
1300	1100	0.85

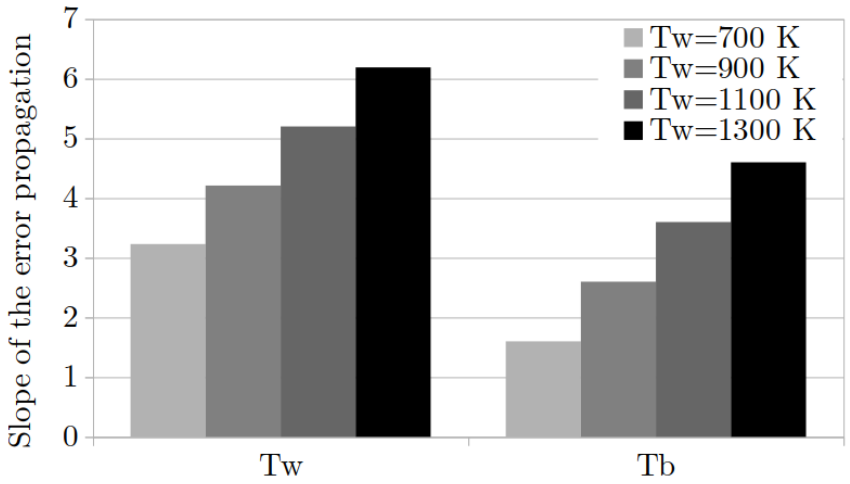

Figure 8.4 – Slope of the error propagation in absolute value for wall and bulk temperatures. Four wall temperatures are investigated, see Table 8.4. The bulk Reynolds number is 60 000 for all the tested cases.

error propagation of the bulk temperature.

8.2.3.2 Asymmetric heating conditions

The sensitivity of the wall heat fluxes is studied in the typical working conditions of gas-pressurized solar receivers [59]. Asymmetric heating is due to the fact that one wall is irradiated by the concentrated sunlight and the opposite wall is insulated on the exterior face of the solar receiver (the one which is in contact with ambient air). The flow temperature is increasing as the fluid moves forward. These conditions are summarized in Table 8.5. In the following, the insulated wall is denoted as the "cold wall" for practical reasons. Nonetheless, in this study and in classical working conditions of solar receiver, for a given axial distance from the inlet, the mean fluid temperature is lower than the insulated wall temperature. Indeed, the "cold wall" is indirectly heated by the concentrated sunlight thanks to the radiations of the hot wall.

The impact of the error, committed on various flow parameters, on the wall heat fluxes is plotted in Figure 8.5. The results are obtained in the working conditions discussed in Table 8.5. The bulk-to-cold wall temperature ratio is 0.78, reproducing the working conditions observed in the middle of the solar receiver [59]. As expected, the results show that the uncertainties on the cold wall temperature (respectively hot wall temperature), induce the biggest uncertainties on the cold wall heat flux (respectively hot wall heat flux). The cold wall heat flux is highly

Table 8.5 – Studied conditions in the asymmetric heating case.

Re_b	Pr_b	T_h [K]	T_c [K]	T_b [K]
60 000	0.87	1300	900	700

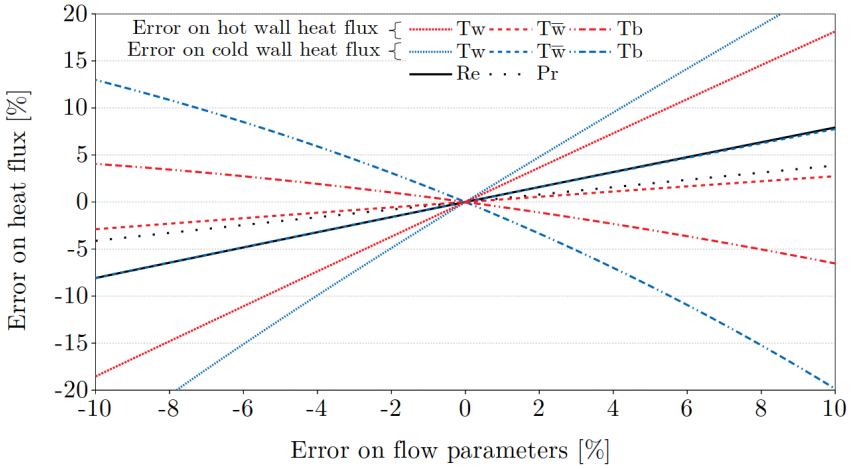

Figure 8.5 – Error on the wall heat fluxes depending on the error committed on various flow parameters. The results are obtained with the conditions listed in Table 8.5.

sensitive to the bulk temperature. The hot wall is less sensitive to the fluid temperature. These different behaviors are due to the asymmetric heating of the fluid. Since the bulk temperature is closer to the cold wall temperature than the hot wall temperature, the uncertainties are bigger when estimating the cold wall heat flux but they are associated with smaller heat transfers. The opposite wall temperatures also have an impact on the wall heat fluxes, even if it is much smaller than the effect of the concerned wall temperature. The propagation of the uncertainties on the bulk Reynolds number is similar to the propagation of the uncertainties on the hot wall temperature when studying the cold wall heat flux. The error committed on the Prandtl number has low impact on the heat flux prediction. For the four last discussed parameters and regarding the impact of the cold wall temperature on the hot wall heat flux, the propagation of the error on the heat flux is mitigated compared to the error on these parameters. For instance, an overestimation of the Reynolds number of 10% leads to an error of 8%. Notice that the propagation of bulk temperature uncertainties is not symmetric. An overestimation of 10% of the bulk wall temperature induces 20% of error on the cold heat flux, whereas an under-estimation of 10% of this temperature conducts to an error of 13% on the heat flux. The ranking of the parameters in terms of influence is independent of the uncertainty of measurement.

In Figure 8.6, the curves observed in Figure 8.5 are approximated by straight lines thanks to the generalized least-squares method. The slope of the heat flux error is computed for each flow parameter. The coefficient of determination is superior to 0.999 for all the parameters except the bulk temperature, for which it is 0.979 in the most unfavorable case. Three bulk temperatures, corresponding to three locations in the solar receiver, are investigated. The left graph displays the slope of the error propagation on the hot wall heat flux and the right graph gives information on the cold wall heat flux. The slope of the error propagation of the wall and bulk temperatures

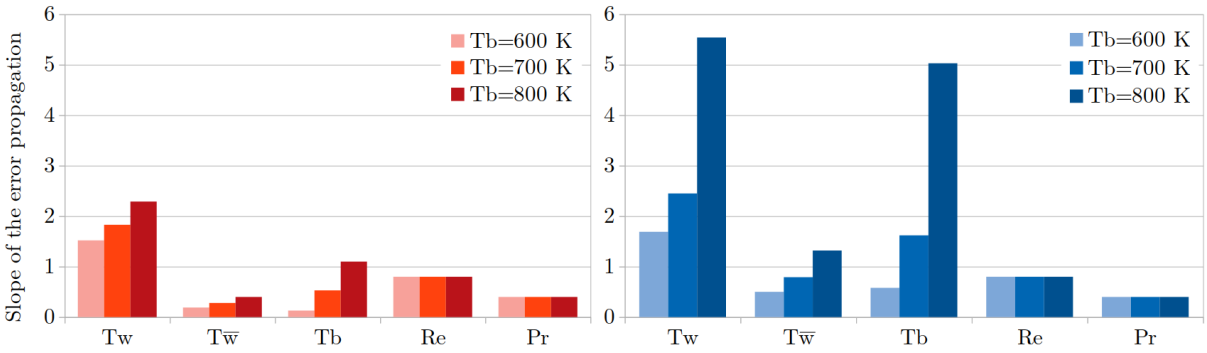

Figure 8.6 – Slope of the error propagation in absolute value for the five flow parameters. Three bulk temperatures are investigated. The bulk Reynolds number is 60 000 for all the tested cases and the wall temperatures are 1300 K and 900 K.

Table 8.6 – List of the tested cases in Figure 8.7.

T_h [K]	T_c [K]	T_b [K]	T_b/T_c
700	500	350	0.70
900	700	550	0.79
1100	900	750	0.83
1300	1100	950	0.86

increases with the bulk temperature. The errors of the Reynolds number and the Prandtl number are independent of the bulk temperature. As observed in Figure 8.5, the slope of the errors is bigger on the cold wall heat flux than on the hot wall heat flux. Furthermore, their increase soars when the bulk temperature becomes close to the cold wall temperature. So, the measurement of the flow parameter should be adapted to the location in the solar receiver in order to keep a constant uncertainty on the wall heat fluxes.

In Figure 8.7, four couples of wall temperatures are investigated. The hot wall temperature increase from 700 K to 1300 K. In each case, the cold temperature is 200 K below the hot wall temperature. The bulk temperature is chosen so that it is 250 K below the mean of hot and cold wall temperatures, see Table 8.6. The results show that the cold wall heat flux is more sensitive than the hot wall. The slope of the error propagation increases linearly with the temperatures as observed in Figure 8.4. The slope inclination of the error propagation of the bulk temperature steepen faster with the increase of the wall temperature than the one of the wall temperatures. This is particularly salient at the cold wall since for $T_h = 1300$ K and $T_c = 1100$ K the slope of the error propagation concerning the bulk temperature is almost as steep as the one concerning the wall temperature.

8.2.4 Propagation of temperature uncertainties

In this section, the propagation of the temperature uncertainties on the wall heat fluxes is analyzed with two methods. The computation of the propagation of uncertainties using the GUM method is compared to the results obtained by the direct computation of heat fluxes with altered temperature values. The uncertainty associated with the thermal conductivity has almost

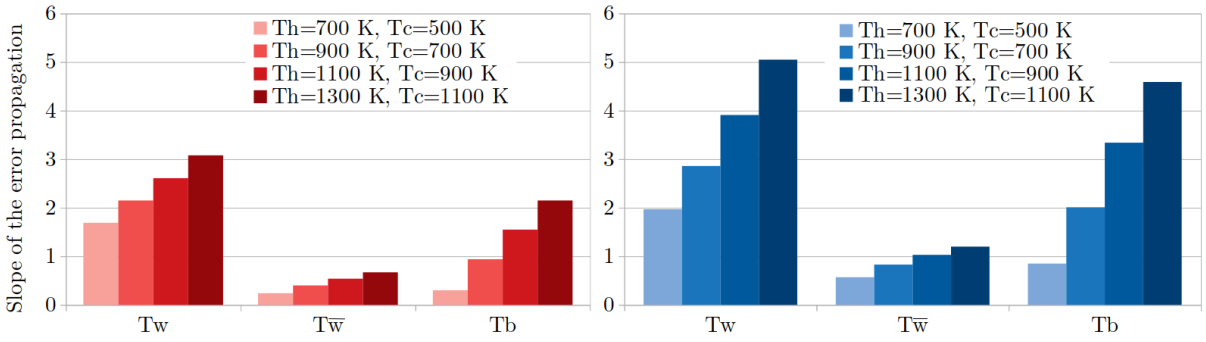

Figure 8.7 – Slope of the error propagation in absolute value for wall and bulk temperatures. Four couples of wall temperatures are investigated, see Table 8.6. The left, respectively right, graph concerns the hot, respectively cold, wall heat flux. The bulk Reynolds number is 60 000 for all the tested cases.

no influence on the results. It is then, neglected to simplify the equation. The uncertainties on the input variables are assumed to be uncorrelated. In the following, we consider the uncertainty of measurements on one parameter at a time and we only investigate the uncertainties relative to temperature.

8.2.4.1 Symmetric heating conditions

In the symmetric heating case, the Taylor series expansion of the simplified heat transfer correlation proposed by David *et al.* [27] is computed. The expression of the uncertainty propagation is given by:

$$\frac{\Delta\phi_{sym}}{\phi_{sym}} = \sqrt{A_{sym}^2 + B_{sym}^2 + C_{sym}^2 + D_{sym}^2}, \tag{8.7}$$

with

$$\begin{aligned}
A_{sym} &= \Delta Re_b \left(\frac{0.8}{Re_b}\right), \\
B_{sym} &= \Delta Pr_b \left(\frac{0.4}{Pr_b}\right), \\
C_{sym} &= \Delta T_b \left(\frac{0.9}{T_b} - \frac{1}{T_w - T_b}\right), \\
D_{sym} &= \Delta T_w \left(-\frac{0.9}{T_w} + \frac{1}{T_w - T_b}\right).
\end{aligned}$$

In Sections 8.2.4.1, and 8.2.4.1, the studied conditions are those described in Table 8.3, except for the bulk temperature which varies in order to cover the entire range of the correlation in terms of bulk-to-cold wall temperature ratio.

Uncertainties on the measurements of the wall temperature depending on the bulk-to-wall temperature ratio The uncertainties on the wall flux depending on the bulk-to-cold wall temperature ratio and the error of the measurements of the wall temperature are plotted in Figure 8.8. The top-left corner of the left graph is colored in black because, in this region, the altered cold wall temperature induces a bulk-to-altered wall temperature superior to 0.95 and is,

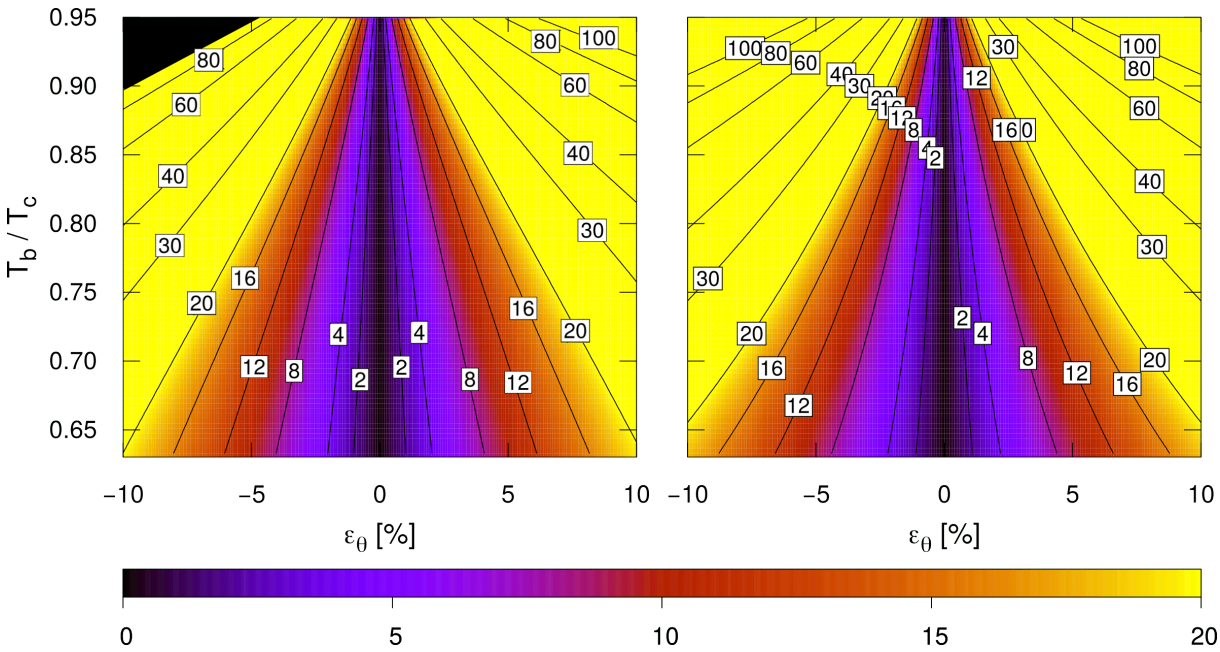

Figure 8.8 – Uncertainties on the wall flux depending on the bulk-to-cold wall temperature ratio and the error of the measurements of the wall temperatures in the case of symmetric heating conditions. The left graph shows the reference results, the right graph exposes the estimation produced by the GUM. The lines indicate the isovalues of error 2%, 4%, 8%, 12%, 16%, 20%, 30%, 40%, 60%, 80% and 100%.

then, out of the applicable domain of the correlation (even if the plotted bulk-to-reference wall temperature is inferior to 0.95). The wall heat fluxes, obtained by the direct computation of heat transfer correlation with the altered input wall temperature, are compared to the results obtained with the GUM. The reference wall heat flux errors are presented on the left side whereas the estimation provided by the GUM procedure is displayed on the right side. The results show the wall heat flux is strongly dependent on the wall temperature error of measurement. The shape of the lines indicates that the bigger the bulk temperature is, the more influential the error of measurement is. An under-estimation of the wall temperature leads to slightly higher uncertainty on the wall heat flux than an overestimation. The model provides an accurate estimation of the error on the entire validity domain of the correlation. Nevertheless, it is worth noting that the lines of isoerror predicted by the GUM are not linear. The error committed by the model increases with the inaccuracies of the measurement since it assumes the linearity of the studied function.

Uncertainties on the measurements of the bulk temperature depending on the bulk-to-wall temperature ratio The bulk temperature is also affected to the uncertainties of measurement. Figure 8.9 shows the uncertainties on the wall flux depending on the bulk-to-cold wall temperature ratio and the error of the measurements of the bulk temperature. The left graph exposes a strong asymmetric distribution of the error. Indeed, at a bulk-to-wall temperature ratio of 0.70, for the same value of uncertainty, an overestimation of 10% of the bulk temperature induces an error of 16% of the wall heat flux. An under-estimation in the same conditions leads to an error of 12%. This is due to the increase of the sensitivity of the wall heat

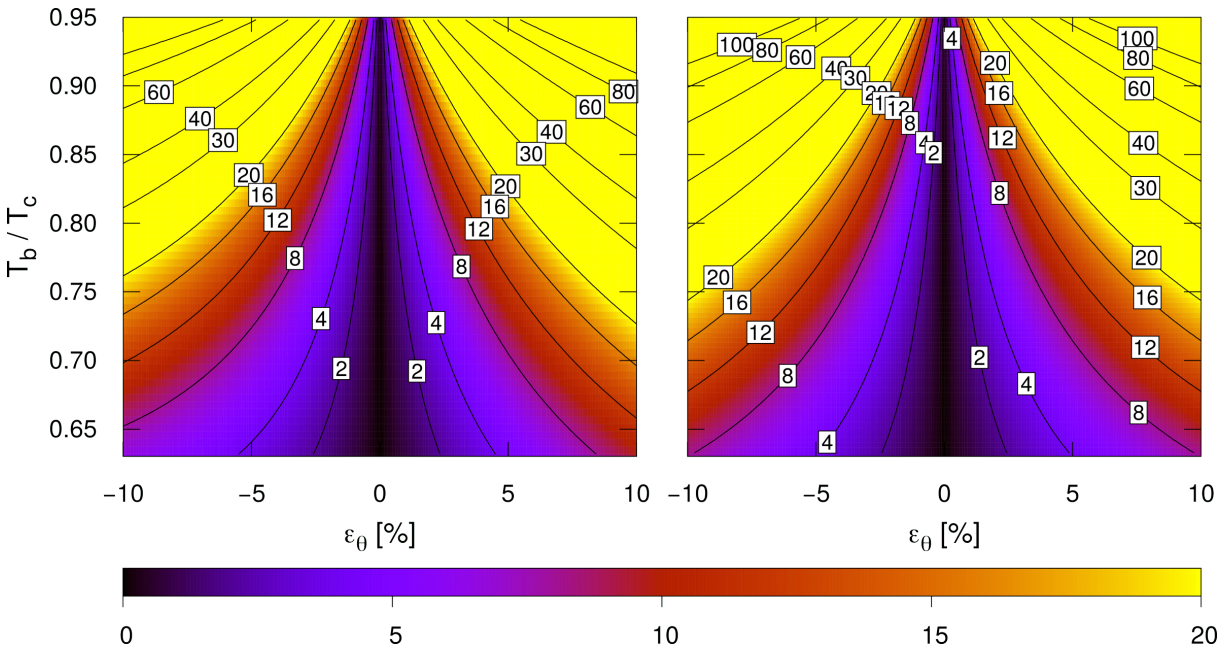

Figure 8.9 – Uncertainties on the wall flux depending on the bulk-to-cold wall temperature ratio and the error of the measurements of the bulk temperature in the case of symmetric heating conditions. The left graph shows the reference results, the right graph exposes the estimation produced by the GUM. The lines indicate the isovalues of error 2%, 4%, 8%, 12%, 16%, 20%, 30%, 40%, 60%, 80% and 100%.

flux to bulk temperature when the temperature difference between the wall and the fluid is low. On the right graph, the estimation of the uncertainties obtained with the Taylor expansion, does not capture this asymmetric behavior of the error propagation. However, the results obtained with the GUM procedure are satisfying since the obtained error is almost equal to the average of the under-estimation and overestimation. For small bulk-to-wall temperature ratios, *i.e.* near the entrance of the solar receiver, the wall heat flux is only slightly affected by the uncertainties on the bulk temperature.

8.2.4.2 Asymmetric heating conditions

Applying the Taylor series expansions to the heat transfer correlation of David *et al.* [27], the GUM provides the analytical expression of the uncertainty propagation exposed in the following equation:

$$\frac{\Delta\phi_{asy}}{\phi_{asy}} = \sqrt{A_{asy}^2 + B_{asy}^2 + C_{asy}^2 + D_{asy}^2 + E_{asy}^2}, \tag{8.8}$$

with

$$
\begin{aligned}
A_{asy} &= \Delta Re_b \left(\frac{0.8}{Re_b}\right), \\
B_{asy} &= \Delta Pr_b \left(\frac{0.4}{Pr_b}\right), \\
C_{asy} &= \Delta T_b \left(\frac{0.9}{T_b} + \frac{1.4}{T_w}\alpha\left(\gamma + \log(\beta)\right) - \frac{1}{T_w - T_b}\right), \\
D_{asy} &= \Delta T_w \left(-\frac{0.9}{T_w}\right) \\
&+ \Delta T_w \left(-1.4\alpha\frac{T_b}{T_w^2}\left(\gamma + \frac{\log(\beta)}{1 + \frac{1}{\delta} + \frac{\alpha}{\delta}}\right) + \frac{1}{T_w - T_b}\right), \\
E_{asy} &= \Delta T_{\overline{w}} \left(2.8\frac{T_b}{\left(T_w + T_{\overline{w}}\right)^2}\log(\beta)\right).
\end{aligned}
$$

where $\alpha = \left(T_{\overline{w}} - T_w\right) / \left(T_w + T_{\overline{w}}\right)$, $\beta = T_w/(T_w - T_b)$, $\gamma = T_b/(T_w - T_b)$, $\delta = (T_{\overline{w}} - T_w)/T_w$. The logarithm used here is the natural logarithm.

Note that, when the wall temperatures are close, the terms associated with the uncertainties on the bulk and wall temperatures tend towards the ones obtained in the symmetric heating case. Indeed, $(T_w - T_{\overline{w}}) \to 0$ induces $\alpha \to 0$ and $\delta \to 0$.

In Sections 8.2.4.2, and 8.2.4.2, the studied conditions are those described in Table 8.5, except for the bulk temperature which varies in order to cover the entire range of the correlation in terms of bulk-to-cold wall temperature ratio.

Uncertainties on the measurements of the wall temperatures depending on the location in the solar receiver The uncertainties on the wall fluxes depending on the bulk-to-cold wall temperature ratio and the error of the measurements of the wall temperatures are exposed in Figure 8.10. On the hot side, the maximum error is obtained for an under-estimation of the hot wall temperature of 10% and a bulk-to-wall temperature ratio of 0.95. It reaches an error of 26%. The results obtained for an under-estimation of the wall temperature are similar to those obtained for an overestimation. The isoerror lines show that the wall heat flux is not very affected by the bulk-to-wall temperature ratio, especially for small errors of temperature measurement. The model is slightly under-estimating the results traducing the non-linearity of the studied function. The uncertainty propagation is bigger at the cold wall than at the hot wall. Furthermore, the results are more sensitive to the bulk-to-wall temperature ratio. The uncertainty distribution is similar for under-estimation and overestimation of the wall temperature, as observed on the hot side. As for Figure 8.8, the results out of the applicable domain of the correlation, resulting from an under-estimation of the cold wall temperature, are masked thanks to a black triangle. It corresponds to a bulk-to-altered cold wall temperature superior to 0.95. In the case of asymmetric heating, the wall heat flux is affected by the opposite wall temperature. Figure 8.11 depicts the propagation of the wall temperature uncertainties on the opposed wall heat flux, *i.e.* the influence of the cold, respectively hot, wall temperature on the hot, respectively cold, wall heat flux (the black corner on the top-left graph masks the results out of the framework of the heat transfer correlation). The uncertainties on the hot wall heat flux are low since they remain below 5%. The model under-estimates the uncertainty propagation. The bottom graphs show that the cold wall heat flux is more impacted by the hot wall temperature

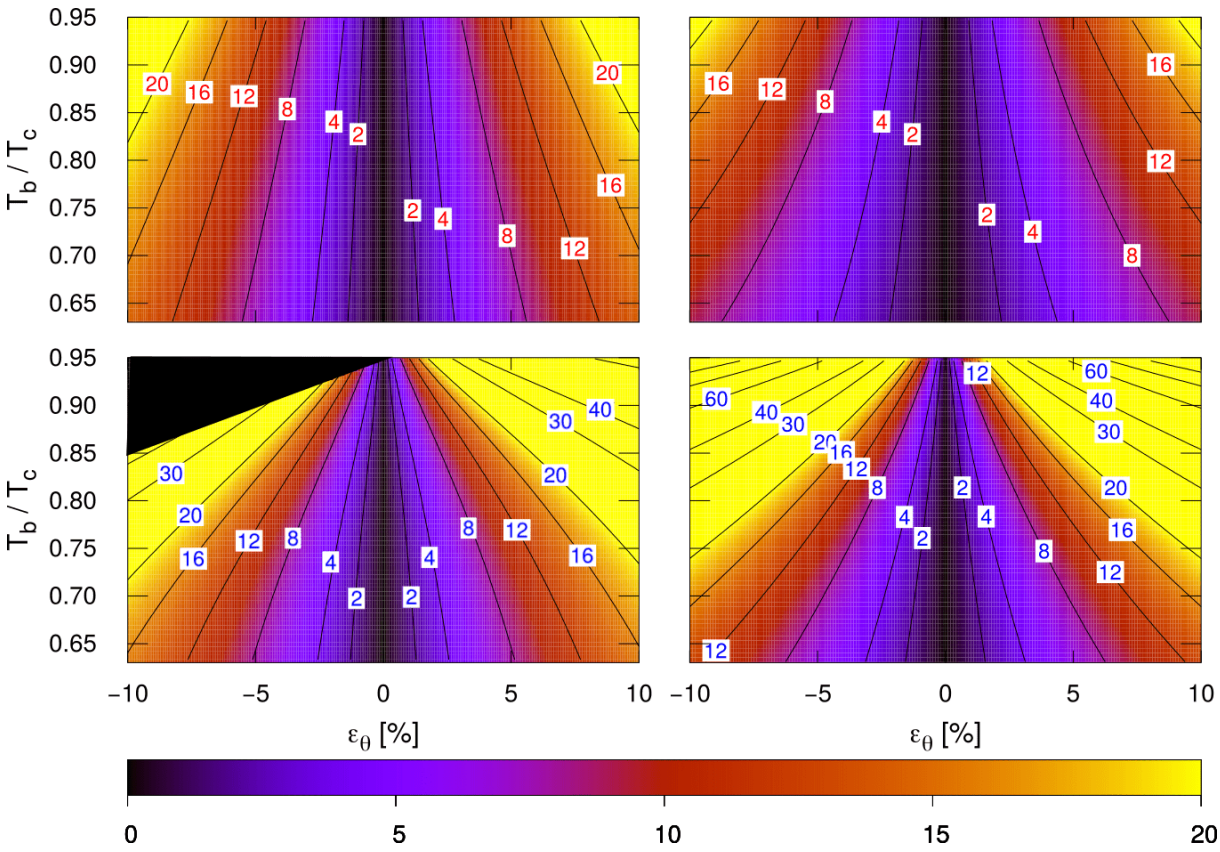

Figure 8.10 – Uncertainties on the wall fluxes depending on the bulk-to-cold wall temperature ratio and the error of the measurements of the wall temperatures in the case of asymmetric heating conditions. The left graphs show the reference results, the right graphs expose the estimations produced by the GUM. The results regarding the hot, respectively cold, wall heat flux are displayed on the two top, respectively bottom, graphs. The lines indicate the isovalues of error 2%, 4%, 8%, 12%, 16%, 20%, 30%, 40%, 60%, 80% and 100%.

than the hot wall heat flux by the cold wall temperature. Indeed, the errors reach 18% for the most unfavorable case. The Taylor series expansion significantly under-estimates the uncertainties when the bulk-to-cold wall temperature ratio is high (end of the solar receiver). This may be explained by the relatively strong non-linear dependence to the opposite wall temperature of the term accounting for asymmetric heating in the correlation.

Uncertainties on the measurements of the bulk temperature depending on the location in the solar receiver The accuracy of measurement of the bulk temperature is also impacting the wall heat flux estimation. The wall heat flux uncertainties are plotted as a function of the bulk-to-wall temperature ratio and the uncertainty of measurement of the bulk temperature in Figure 8.12. The results indicate that the hot wall heat flux is substantially less impacted by altered measurement of the bulk temperature than the cold wall heat flux. The GUM procedure provides a quite satisfying estimation of the uncertainties despite the non-normal distribution of the uncertainties on the wall heat fluxes. At the cold wall, an overestimation of the bulk temperature may result in a bulk-to-altered cold wall temperature ratio out of the application

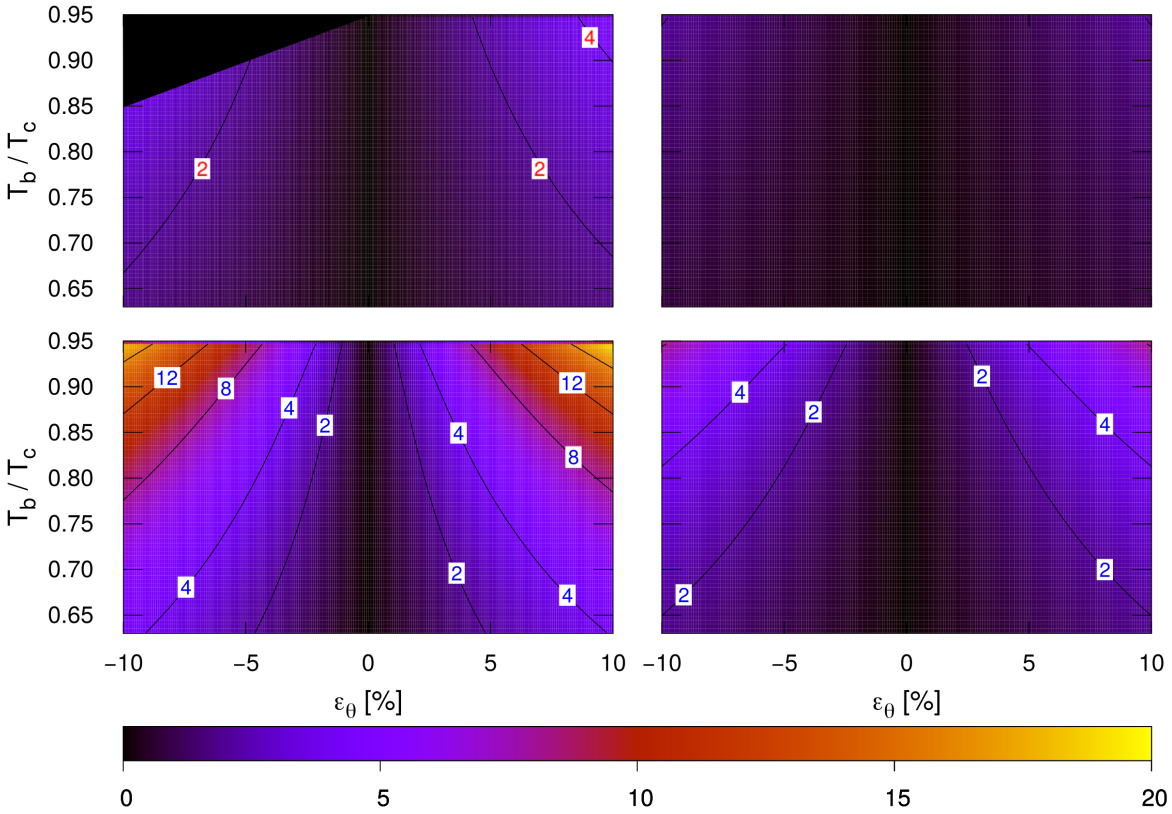

Figure 8.11 – Uncertainties on the wall fluxes depending on the bulk-to-cold wall temperature ratio and the error of the measurements of the opposed wall temperatures in the case of asymmetric heating conditions. The left graphs show the reference results, the right graphs expose the estimations produced by the GUM. The results regarding the hot, respectively cold, wall heat flux are displayed on the two top, respectively bottom, graphs. The lines indicate the isovalues of error 2%, 4%, 8%, 12%, 16%, 20%, 30%, 40%, 60%, 80% and 100%.

domain of the correlation (see the top-right corner of the bottom-left graph). For low bulk-to-cold wall temperature ratio, the uncertainty of measurement of the bulk temperature has little effect on the wall heat flux when compared to the uncertainties on the measurement of the wall (see Figure 8.10). However, the results are very sensitive to the bulk-to-wall temperature ratio, *i.e.* very sensitive to the location in the solar receiver: when this ratio is small, the uncertainty of measurement of the bulk temperature is not very impacting the wall heat flux. At the cold wall, when the bulk temperature is close to the cold wall temperature, the heat flux uncertainties become very high even for uncertainties of measurements below 5%. Note that these high uncertainties should be put into perspective with the relatively small wall heat flux associated.

8.2.4.3 Comparison of the uncertainties in both types of heating

The results presented in Subsections 8.2.4.1 and 8.2.4.2 show that, contrarily to what one might think, the biggest uncertainties are obtained in the case of symmetric heating. Reducing the wall temperature difference induces a more homogeneous uncertainty propagation on the wall heat fluxes but the propagation is amplified when compared to the case of asymmetric heating.

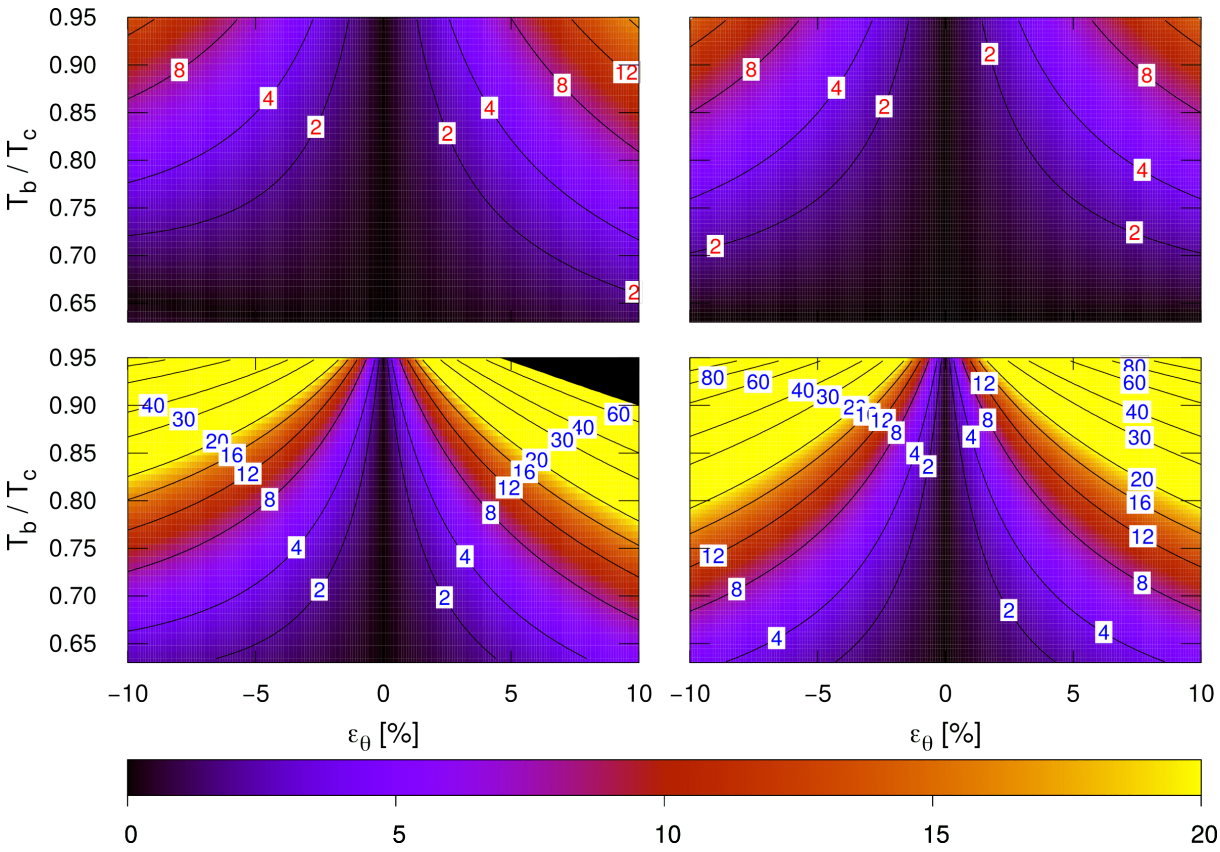

Figure 8.12 – Uncertainties on the wall fluxes depending on the bulk-to-cold wall temperature ratio and the error of the measurements of the bulk temperature in the case of asymmetric heating conditions. The left graphs show the reference results, the right graphs expose the estimations produced by the GUM. The results regarding the hot, respectively cold, wall heat flux are displayed on the two top, respectively bottom, graphs. The lines indicate the isovalues of error 2%, 4%, 8%, 12%, 16%, 20%, 30%, 40%, 60%, 80% and 100%.

Indeed, the term accounting for asymmetric heating, $(T_w/(T_w - T_b))^{1.4(1-(T_w/T_m))T_b/T_w}$, balances the effect of the term $(T_w/T_b)^{-0.9}$. The result is a mitigation of the wall heat flux dependence to wall and bulk temperature estimation under asymmetrical heating conditions.

8.2.5 Conclusion

In this study, the correlation proposed by David *et al.* [27] for asymmetrically heated turbulent channel flow has been used to investigate the sensitivity to flow parameters of the wall heat fluxes and the propagation of uncertainties depending on the location in the solar receiver.

The results obtained following the Guide to the expression of Uncertainty in Measurement, which used Taylor series expansion to provide an analytical expression of the uncertainty propagation, have been compared to the results obtained with the direct computation of the heat flux with altered flow parameters. The results presented in this study show that a low bulk-to-wall temperature ratio mitigates the influence of the bulk and wall temperatures on the wall heat fluxes. In the studied conditions, the impact of the bulk temperature on the wall heat fluxes is more influenced by the working condition than the wall temperatures. Progressing in the solar

receiver, the fluid temperature becomes closer to the wall temperatures. For relatively high values of the bulk-to-cold wall temperature ratio, the uncertainties on the bulk temperature become more influential than the uncertainties on the wall temperatures and are highly impacting the wall heat flux estimation. This means that it is possible to adapt the accuracy of measurement devices according to their location in the solar receiver.

A precise analysis shows that the asymmetric term induces a highly non-linear dependence of the wall heat flux to the bulk, wall, and opposite wall temperatures. In the case of inaccuracies in the measurement of the bulk temperature, the uncertainties on the wall heat flux are strongly asymmetrically distributed with regards to the 0% uncertainty line.

The expression of the heat transfer correlation used for asymmetric heating conditions involves an additional term to reproduce the heat transfers at both walls taking into account the respective effects of one on this other. Contrarily to what one might think, this new term tends to mitigate the wall heat flux dependence to bulk temperature estimation. The result is a lower wall heat flux sensitivity to wall and bulk temperatures in the case of asymmetric heating than in the case of symmetric heating.

The method described in the GUM gives very satisfying results in the studied symmetric heating conditions. Even though the effects of the opposite wall temperature on the wall heat flux are underestimated, the method produces quite accurate estimations in the asymmetric heating case.

Acknowledgements

This work was granted access to the HPC resources of CINES under the allocation 2020-A0082A05099 made by GENCI. The authors acknowledge PRACE for awarding them access to Joliot-Curie at GENCI@CEA, France (PRACE Project : 2020225398). The authors gratefully acknowledge the CEA for the development of the TRUST platform. The authors gratefully acknowledge the Occitania region for their funding of the thesis grant.

References

[17] D. Dupuy, A. Toutant, and F. Bataille. “A Posteriori Tests of Subgrid-Scale Models in an Isothermal Turbulent Channel Flow”. In: *Physics of Fluids* 31.4 (2019), p. 045105.

[23] E. Battista and H. C. Perkins. “Turbulent Heat and Momentum Transfer in a Square Duct with Moderate Property Variations”. In: *International Journal of Heat and Mass Transfer* 13.6 (1970), pp. 1063–1065.

[25] F. W. Dittus and L. M. K. Boelter. “Heat Transfer in Automobile Radiators of the Tubular Type”. In: *International Communications in Heat and Mass Transfer* 12.1 (1985), pp. 3–22.

[27] M. David, A. Toutant, and F. Bataille. “Numerical Development of Heat Transfer Correlation in Asymmetrically Heated Turbulent Channel Flow”. In: *International Journal of Heat and Mass Transfer* 164 (2021), p. 120599.

[56] X. Daguenet-Frick et al. “Numerical Investigation of a Ceramic High-Temperature Pressurized-Air Solar Receiver”. In: *Solar Energy* 90 (2013), pp. 164–178.

[58] W.-Q. Wang et al. “Coupled Optical and Thermal Performance of a Fin-like Molten Salt Receiver for the next-Generation Solar Power Tower”. In: *Applied Energy* 272 (2020), p. 115079.

[59] J. Capeillère et al. "Thermomechanical Behavior of a Plate Ceramic Solar Receiver Irradiated by Concentrated Sunlight". In: *Solar Energy* 110 (2014), pp. 174–187.

[60] A. Colleoni, A. Toutant, and G. Olalde. "Simulation of an Innovative Internal Design of a Plate Solar Receiver: Comparison between RANS and LES Results". In: *Solar Energy* 105 (2014), pp. 732–741.

[61] Q. Li et al. "Micro-Channel Pressurized-Air Solar Receiver Based on Compact Heat Exchanger Concept". In: *Solar Energy* 91 (2013), pp. 186–195.

[145] D. Dupuy, A. Toutant, and F. Bataille. "A Posteriori Tests of Subgrid-Scale Models in Strongly Anisothermal Turbulent Flows". In: *Physics of Fluids* 31.6 (2019), p. 065113.

[160] D. Dupuy, A. Toutant, and F. Bataille. "A Priori Tests of Subgrid-Scale Models in an Anisothermal Turbulent Channel Flow at Low Mach Number". In: *International Journal of Thermal Sciences* 145 (2019), p. 105999.

[260] E. N. Sieder and G. E. Tate. "Heat Transfer and Pressure Drop of Liquids in Tubes". In: *Industrial & Engineering Chemistry* 28.12 (1936), pp. 1429–1435.

[268] J. Ma et al. "Experimental Studies on Single-Phase Flow and Heat Transfer in a Narrow Rectangular Channel". In: *Nuclear Engineering and Design* 241.8 (2011), pp. 2865–2873.

[278] V. Gnielinski. "On Heat Transfer in Tubes". In: *International Journal of Heat and Mass Transfer* 63 (2013), pp. 134–140.

[281] D. Taler. "Simple Power-Type Heat Transfer Correlations for Turbulent Pipe Flow in Tubes". In: *Journal of Thermal Science* 26.4 (2017), pp. 339–348.

[308] D. A. Nield. "Forced Convection in a Parallel Plate Channel with Asymmetric Heating". In: *International Journal of Heat and Mass Transfer* 47.25 (2004), pp. 5609–5612.

[316] E. Driscoll and D. Landrum. "Uncertainty Analysis on Heat Transfer Correlations for RP-1 Fuel in Copper Tubing". In: *NTRS - NASA Technical Reports Server* (2004).

[317] V. K. Scariot, G. M. Hobold, and A. K. da Silva. "On the Sensitivity to Convective Heat Transfer Correlation Uncertainties in Supercritical Fluids". In: *Applied Thermal Engineering* 145 (2018), pp. 123–132.

[318] JCGM. *Evaluation of Measurement Data – Guide to the Expression of Uncertainty in Measurement*. https://www.bipm.org/en/publications/guides/gum.html. 2008.

[319] J. Han, S. Dutta, and S. V. Ekkad. *Gas Turbine Heat Transfer and Cooling Technology*. CRC Press - Taylor & Francis Group, 2012. ISBN: 978-0-429-10711-5.

[320] T. A. Oliver et al. "Estimating Uncertainties in Statistics Computed from Direct Numerical Simulation". In: *Physics of Fluids* 26.3 (2014), p. 035101.

[321] T. Phillips and C. Roy. "Richardson Extrapolation-Based Discretization Uncertainty Estimation for Computational Fluid Dynamics". In: *Journal of Fluids Engineering* 136 (2014), p. 121401.

[322] M. Carnevale et al. "Uncertainty Quantification: A Stochastic Method for Heat Transfer Prediction Using LES". In: *Journal of Turbomachinery* 135 (2013).

[323] K. Menberg, Y. Heo, and R. Choudhary. "Sensitivity Analysis Methods for Building Energy Models: Comparing Computational Costs and Extractable Information". In: *Energy and Buildings* 133 (2016), pp. 433–445.

[324] F. Uhía, A. Campo, and J. Fernández-Seara. "Uncertainty Analysis for Experimental Heat Transfer Data Obtained by the Wilson Plot Method: Application to Condensation on Horizontal Plain Tubes". In: *Thermal Science* 17 (2013).

[325] G. N. Coleman, J. Kim, and R. D. Moser. "A Numerical Study of Turbulent Supersonic Isothermal-Wall Channel Flow". In: *Journal of Fluid Mechanics* 305 (1995), pp. 159–183.

[326] K. Wójs and T. Tietze. "Effects of the Temperature Interference on the Results Obtained Using the Wilson Plot Technique". In: *Heat and Mass Transfer* 33.3 (1997), pp. 241–245.

[327] D. D. Clarke et al. "Sensitivity and Uncertainty Analysis of Heat-Exchanger Designs to Physical Properties Estimation". In: *Applied Thermal Engineering* 21.10 (2001), pp. 993–1017.

[328] J. C. Helton. "Uncertainty and Sensitivity Analysis Techniques for Use in Performance Assessment for Radioactive Waste Disposal". In: *Reliability Engineering & System Safety* 42.2 (1993), pp. 327–367.

[329] D. Rochman et al. "Efficient Use of Monte Carlo: Uncertainty Propagation". In: *Nuclear Science and Engineering* 177.3 (2014), pp. 337–349.

[330] J. Mazo et al. "Uncertainty Propagation and Sensitivity Analysis of Thermo-Physical Properties of Phase Change Materials (PCM) in the Energy Demand Calculations of a Test Cell with Passive Latent Thermal Storage". In: *Applied Thermal Engineering* 90 (2015), pp. 596–608.

[331] D. Colorado et al. "Hybrid Evaporator Model: Analysis under Uncertainty by Means of Monte Carlo Method". In: *Applied Thermal Engineering*. Optimisation of Cogeneration and Energy Intensive Processes, Heat Transfer Enhancement, Industrial Applications – PRES 11 43 (2012), pp. 148–152.

[332] L. M. Zhou, E. Zhao, and S. Ren. "Interval Element-Free Galerkin Method for Uncertain Mechanical Problems". In: *Advances in Mechanical Engineering* 10.1 (2018).

[333] T. Zhou, J. Yuan, and M. Li. "Simultaneously Estimate Solid- and Liquid-Phase Thermal Conductivities". In: *International Communications in Heat and Mass Transfer* 119 (2020), p. 104959.

[334] C. R. Á. da Silva Jr. and A. T. Beck. "Efficient Bounds for the Monte Carlo-Neumann Solution of Stochastic Thermo-Elasticity Problems". In: *International Journal of Solids and Structures* 58 (2015), pp. 136–145.

[335] D. Taler. "Assessment of the Indirect Measurement Uncertainty". In: *Numerical Modelling and Experimental Testing of Heat Exchangers*. Studies in Systems, Decision and Control. Springer International Publishing, 2019, pp. 373–448. ISBN: 978-3-319-91127-4.

[336] S. Oladyshkin and W. Nowak. "Data-Driven Uncertainty Quantification Using the Arbitrary Polynomial Chaos Expansion". In: *Reliability Engineering & System Safety* 106 (2012), pp. 179–190.

[337] H. Cho, D. Venturi, and G. E. Karniadakis. "Karhunen–Loève Expansion for Multi-Correlated Stochastic Processes". In: *Probabilistic Engineering Mechanics* 34 (2013), pp. 157–167.

[338] G. J. K. Tomy and K. J. Vinoy. "Neumann-Expansion-Based FEM for Uncertainty Quantification of Permittivity Variations". In: *IEEE Antennas and Wireless Propagation Letters* 19.4 (2020), pp. 561–565.

[339] A. Håkansson. "An Investigation of Uncertainties in Determining Convective Heat Transfer during Immersion Frying Using the General Uncertainty Management Framework". In: *Journal of Food Engineering* 263 (2019), pp. 424–436.

[340] S. G. Penoncello. *Thermal Energy Systems : Design and Analysis*. CRC Press - Taylor & Francis Group, 2015. ISBN: 978-0-429-17226-7.

[341] D. Taler. "Mathematical Modeling and Control of Plate Fin and Tube Heat Exchangers". In: *Energy Conversion and Management* 96 (2015), pp. 452–462.

[342] M. Trojan and D. Taler. "Thermal Simulation of Superheaters Taking into Account the Processes Occurring on the Side of the Steam and Flue Gas". In: *Fuel* 150 (2015), pp. 75–87.

[343] N. Dimassi and L. Dehmani. "Experimental Heat Flux Analysis of a Solar Wall Design in Tunisia". In: *Journal of Building Engineering* 8 (2016), pp. 70–80.

[344] A. Sciacchitano and B. Wieneke. "PIV Uncertainty Propagation". In: *Measurement Science and Technology* 27.8 (2016), p. 084006.

[345] D. Paudel and S. Hostikka. "Propagation of Model Uncertainty in the Stochastic Simulations of a Compartment Fire". In: *Fire Technology* 55.6 (2019), pp. 2027–2054.

[346] Y. Zhao et al. "Uncertainty and Sensitivity Analysis of Flow Parameters for Transition Models on Hypersonic Flows". In: *International Journal of Heat and Mass Transfer* 135 (2019), pp. 1286–1299.

8.3 Conclusion of chapter 8

In this chapter, a wall heat flux sensitivity analysis has been performed thanks to the proposed correlation in the typically encountered operating conditions of gas-pressurized solar receivers. It draws on the use of the proposed heat transfer correlation. The sensitivity analysis materializes the upstream works achieved in the multi-scale approach of this thesis and gives key information for the sizing of solar receivers.

The highly turbulent flow passing through the receiver is asymmetrically heated from both walls. These conditions complicate the measurement and the computation of the flow parameters. The study shows that the uncertainty propagation of the flow parameters on the wall heat flux sensitivity is very dependent on the studied conditions. The closer the fluid and wall temperatures are, in other words, the closer the studied conditions are to those encountered near the outlet of the fluid receiver, the higher the uncertainty propagation is. However, these uncertainties are associated with smaller wall heat flux intensities since the temperature difference between the wall and the fluid is reduced. This mitigates the importance that should be given to these uncertainties. Note that numerically, the estimation of the wall temperatures is slightly more costly at the cold wall (insulated wall) due to the higher turbulence levels in the vicinity of this wall when compared to the hot wall. However, the measurement of the temperature during an experiment is easier and more accurate at the insulated wall than at the irradiated wall. Indeed, at the cold wall, the measurement with a thermocouple placed in the exterior face of the wall is easily achieved. The measurement of the irradiated wall temperature requires to use an infrared camera and to precisely know the emissivity of the wall.

The Guide to the expression of the Uncertainty in Measurement (GUM) employs the Taylor series to provide an analytical expression of the error propagation. This method gives relatively

accurate estimations of the uncertainties on the wall heat fluxes as long as the non-linearities of the error propagation remain small or the errors on the flow parameters are low.

Quantifying the uncertainty propagation is needed for the development of the gas-pressurized solar receivers at the industrial scale and should strongly influence the sizing of this device and the tools used to estimate the wall heat fluxes.

Chapter 9

Conclusion of part II

In this part, the focus has been placed on heat transfers with the aim of providing simple tools to investigate wall heat fluxes in solar receivers. It relies on the assessment of the LES, which in turn draws on the DNS results, and represents the last link of the multi-scale approach performed in this thesis. In chapter 7, a heat transfer correlation has been developed in the typically encountered working conditions of gas-pressurized solar receivers. Chapter 8 was one step further toward the application by addressing the wall heat flux sensitivity to the flow parameters thanks to the proposed correlation.

A state of art has been performed and highlights that, to the author's knowledge, there is no heat transfer correlation applicable in asymmetrically heated turbulent channel flows. Nonetheless, three existing correlations have been tested. The results are good in the validity domain of those correlations but become unsatisfying in the asymmetric heating conditions. Indeed, the heat fluxes tend to be overestimated at the hot wall and underestimated at the cold wall. As no correlation found in the literature produces satisfying results in the operating conditions of the solar receivers, a heat transfer correlation has been established thanks to 70 large eddy simulations performed in channel with fixed wall temperatures. The correlation has been validated with direct numerical simulations and experimental data. The correlation is valid for both symmetric and asymmetric heating conditions. It involves a term specifically designed for the asymmetric heating conditions that becomes neutral if the flow heating is symmetric. The correlation permits estimating the Nusselt number of both walls within 10% of error thanks to five flow parameters. The coefficient of determination of the correlation is of 0.993 on the entire data set provided by the simulations. The applicable domain of the correlation covers large ranges of Reynolds numbers, temperatures and wall heat fluxes. Hence, it could be used to perform pre-sizing studies or wall heat flux sensitivity analyzes.

The gas-pressurized solar receiver is the place of very high heat fluxes and temperatures. The accurate prediction of the flow parameters is very complex in those extreme conditions but crucial to estimate the heat fluxes. For that reason, a wall heat flux sensitivity analysis has been carried out to quantify the influence of the different flow parameters. The proposed correlation is well adapted to perform this study since it reproduces the wall heat flux dependency to the flow parameters in its applicable domain. The results show that the uncertainties on the wall heat fluxes strongly depend on the studied conditions. The uncertainties substantially increased as the flow progresses in the solar receiver. However, this should be put into perspective with the reduction of the wall heat fluxes. The Taylor series have been applied to the correlation for the

purpose of providing an analytical expression of the uncertainty propagation on the wall heat flux. This method has been compared with the direct computation of the error propagation with the correlation. The results show that the Taylor series should only be used if the uncertainties on the flow parameters are low or if the temperature difference between the wall and the fluid is high.

Conclusions and perspectives

In the past few years, the Concentrated Solar Power (CSP) systems start to spread out around the world as an interesting technology of renewable energy conversion for large-scale production. Several types of concentrated solar power systems exist and they are at different stages of maturity. The concentrated solar power towers functioning with molten salt are the most mature of this category of CSP systems. However, this technology suffers from the limited temperature range induced by the use of molten salts which narrows the possible enhancement of the global system efficiency. Among the existing technologies that permit freeing the concentrated solar power tower from the limited operating temperature of the fluid transfer, the gas-pressurized systems seem promising. This technology is still at the research stage and requires further investigation to be competitive with the other sources of renewable energy.

The objective of this thesis has been to address the flows encountered in gas-pressurized solar receivers. These flows are highly turbulent and asymmetrically heated by the irradiated and the insulated walls of the absorber. The reached levels of temperature and heat transfers are great. The fluid passing through the receiver constitutes a low Mach number flow submitted to high-temperature variations. To investigate these flow features in different axial locations of solar receivers, the academic geometry of the bi-periodic channel has been selected.

The gas-pressurized solar receiver has dimensions of the order of one meter and it involves micro-metric turbulent scales. For that reason, a multi-scale approach has been performed during this thesis. In the first part, the focus has been placed on the numerical simulation of the flow and the modeling of the small turbulent scales using Direct Numerical Simulations (DNS) to assess Large Eddy Simulations (LES). In the second part, LES have been employed to develop a heat transfer correlation. Then, this correlation has been used to investigate the wall heat fluxes sensitivity. The conclusion of this thesis reminds the main results of this multi-scale approach. Firstly, the physic of the studied flows is described. Secondly, the LES are analyzed. Thirdly, the development of the heat transfer correlation is reported, and lastly, the wall heat flux sensitivity is investigated thanks to the correlation.

The flow has been investigated by solving the Navier-Stokes equations under the low Mach number approximation. This system of equations has been coupled with the ideal gas law to consider the thermal dilatation. The fluid properties variations have also been taken into account thanks to Sutherland's law. The channel flow has been studied in three thermal conditions keeping a friction Reynolds number around 950. Firstly, the simulations have been performed in isothermal conditions at a friction Reynolds number of about 950 which permits validating the DNS with reference data from the literature and to study the turbulence levels encountered in

solar receivers without the temperature influence. The results have shown the presence of very high Reynolds number effects characterized by a quasi-plateau of the velocity fluctuations in the meso layer of the logarithmic region. Then, the wall temperatures of the channel have been fixed to 900 K and 1300 K, which corresponds to the typically encountered wall temperatures of solar receivers. The results of the DNS have shown a strong coupling between the dynamic and the temperature. The fluid temperature is close to the average of the wall temperatures but not equal due to the property variations. These conditions are those that would be encountered in an infinitely long solar receiver. The temperature gradients induce wall-normal velocities that are directly linked to the wall heat fluxes. The latter are similar at both walls and reach 100 kW/m^2. Lastly, the conditions typically encountered in gas-pressurized solar receivers have been investigated. The mean fluid temperature has been lowered to 883 K thanks to the introduction of a source term in the energy equation. The wall-normal temperature profile reaches a minimum on the cold side of the channel. These new conditions induce asymmetric temperature gradients and thus asymmetric wall-normal velocities on both sides. The wall heat fluxes are oriented toward the center of the channel and are 64 kW/m^2 at the cold wall and 263 kW/m^2 at the hot wall. A comparison of the simulations in both anisothermal conditions has been performed. It appears that the fluctuation of heat flux-to-heat flux ratio is constant and equal to 0.43 at both walls of the two DNS. Instantaneous fields and density probability functions of wall heat fluxes have been analyzed. They highlight the existence of very high-frequency structures associated with the strongest wall heat fluxes and structures stretched in the direction of the flow. The most frequent wall heat fluxes are slightly below the mean wall heat flux. The DNS permit obtaining very accurate results but their computational cost is also very high. In order to perform simulations of entire modules of solar receivers, it is necessary to develop reliable turbulence models of LES.

Subgrid-scale models of large eddy simulations have been studied in the same three thermal conditions as the DNS. Functional, structural, and mixed subgrid-scale models, as well as no-model simulations, have been investigated with a two-step approach. Firstly, a global evaluation of the model performance has been carried out which permits testing a large number of models and obtain an overview of the results. Then, some simulations have been selected for a detailed analysis that consists in their assessment on the basis of first- and second-order statistics with DNS results. In the anisothermal conditions, the instantaneous fields and density probability functions of wall heat fluxes are also examined and the term associated with the density-velocity correlation is modeled in addition to the classically modeled velocity-velocity subgrid term. The numerical scheme effect for the discretization of the mass and momentum convection terms is investigated. The fourth-order accurate scheme used for the approximation of the momentum convection term provides better results on the velocity fluctuations than the second-order centered scheme. Regarding the mass convection term, the second-order centered scheme is advantageous for the estimation of the wall heat fluxes when compared to the third-order accurate Quick scheme. However, the second-order scheme does not impact the fluctuations of wall-normal velocity. This partial improvement suggests that the second-order-centered scheme modifies the turbulent structures obtained with DNS. The LES produce good results on the streamwise velocity and very good results on the correlation of streamwise and wall-normal velocity which is involved in the momentum balance. The peaks of velocity fluctuations observed around $y^+ = 15$ are overestimated by all the models. Focusing on the simulations performed with the Quick scheme, the LES tend to underestimate the wall heat fluxes and their color maps of wall heat flux are comparable to those obtained with the DNS but the very high-frequency structures are less present. The performance of the LES models depends on the thermal configuration. Indeed,

the high the temperature gradient is, the best the results are. The performance of the models between each other is weakly influenced by the heating conditions. Overall, the tensorial version of the AMD model seems to be the most effective of the tested models with the chosen numerical setup. Particularly, it is the only model that permits significantly reducing the overestimation of the velocity fluctuation peaks. Large eddy simulations are less costly than DNS and are applicable to entire modules but they remain a cumbersome approach. That is why they have been used to produce a simple expression that permits directly estimating the wall heat transfer.

The LES permits obtaining a quite reliable description of the flow behavior while requiring about 200 times less computational cost than DNS in the above studied conditions. Thanks to their reasonable cost, it has been possible to perform a large number of simulations to develop a heat transfer correlation applicable in the operating conditions of the gas-pressurized solar receivers. To the author's knowledge, the proposed expression is the only heat transfer correlation valid in turbulent channel flow asymmetrically heated. It produces an estimation of the Nusselt number within 10% error in a wide range of Reynolds numbers, wall temperatures, and fluid temperature. The correlation has a coefficient of determination of 0.993 with the points obtained thanks to the LES.

Performing sensitivity analysis is essential before moving from principles to practice. Indeed, in physical systems, uncertainties on the operating conditions are manifold. Quantifying the uncertainty propagation permits determining the accuracy needed for the measurement or the calculation of a specific parameter. In their validity domain, heat transfer correlations reproduce the evolution of the Nusselt number with the flow parameters. Hence, they are well adapted to investigate the wall heat flux sensitivity. The proposed correlation has been used to quantify the influence of the misestimation of the various flow parameters impacting the wall heat fluxes. The results show that, in the typically encountered working conditions of solar receivers, the wall heat fluxes are mainly influenced by the wall temperature and the fluid temperature. The Prandtl number and the opposite wall temperatures have a low impact on the wall heat flux sensitivity. The error committed on the wall heat fluxes when misestimating the Prandtl number or the Reynolds number does not depend on the working conditions. Nevertheless, the results suggest that the propagation of the error is significantly amplified as the fluid temperature tends towards the wall temperature. Note that this should be put into perspective with the caused reduction of the wall heat flux. An analytical expression of the uncertainty propagation has been obtained thanks to the Taylor series. It provides a satisfying approximation of the error committed on the wall heat flux as long as the uncertainty on the flow parameter is low and/or the gap between the mean fluid temperature and the wall temperature is significant.

The works carried out during this thesis offer various perspectives. Currently, the multigrid solver used to compute the dynamic pressure forces the cells of the mesh to be symmetric with regard to the plan defined by the streamwise and the spanwise directions. However, in the asymmetric heating conditions the friction Reynolds number is different at each wall. Hence, it could be interesting to improve the multigrid solver to permit the asymmetrisation of the absolute cell sizes from either side of the center plan for the purpose of discretizing the computational domain with the same normalized cell sizes on both sides. Furthermore, the TrioCFD code could be improved by increasing the order of accuracy of the numerical scheme in order to reduce the truncature error. For each studied line of research, perspectives arise.

Regarding the physic of the flow, it would be very interesting to deepen the investigation of instantaneous fields. Particularly, observing the link between the wall heat fluxes and the wall stresses could be helpful in the perspective of the optimization of the solar receiver [271].

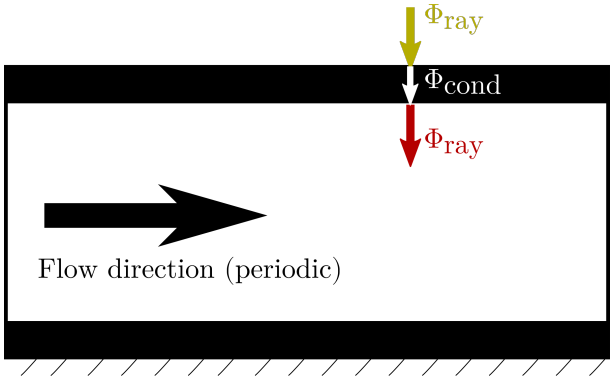

Figure 9.1 – Schematic view of the configuration taking into account the coupling between the fluid and the solid. The streamwise and spanwise directions are periodic. The black rectangles depict the solid and the white area between the two walls is the fluid.

Similarly, the visualization of the turbulent structure shapes and motions in the vicinity of the wall would be very useful to examine the coupling between the flow and the temperature. Spectral studies of the flows are commonly performed in the literature and would also be worthwhile in the present case [347, 214, 348] because the temperature gradient acts as a strong external force that modifies the turbulence properties. In order to get closer to the operating conditions of gas-pressurized solar receivers, it would be interesting to apply a heat flux on the hot wall of the channel, taking into account the conduction in the walls and the radiation between the hot wall and the cold one (conjugated heat transfers), as displayed in figure 9.1. Note that, the conductive heat flux is not equal to the radiative heat flux because of convective heat transfers. An adiabatic thermal boundary condition should be applied to the cold wall to simulate the insulation of the solar receiver.

Focusing on the LES, the simulations performed have shown that there is room for improvement. Since the numerical method and the subgrid-scale model efficiency are linked, the turbulence model enhancement is highly complex. The improvement of subgrid-scale models is a broad subject of research that gathers researchers from multiple domains. The good performances of the tensorial version of the AMD model encourage to pursue investigations on this approach. Among the current works, those of Streher *et al.* [12] seems very promising. It seems that their approach worth being tested in anisothermal conditions with few adaptations. More generally, in the achieved work, the mixed models do not produce the desired and forecast effects. It could be interesting to study them more in detail in order to implement a better association of functional and structural models. A large number of recent works uses the artificial intelligence to develop new subgrid-scale models [349, 350, 351]. The possibilities offered by artificial neural networks are huge and their use in the field of subgrid-scale modeling seems very promising [352]. Hence, it could be interesting to develop a new research line that involves artificial intelligence to investigate the turbulence models of LES in the operating conditions of solar receivers.

Lastly, in the perspective of the industrialization of the gas-pressurized solar power tower, it should be wise to carry conjugated heat transfer simulations by replacing the thermal boundary conditions from fixed wall temperatures to a distribution of heat flux on the hot wall of the receiver and considering the conductive transfer through the solid and the radiation of the hot wall on the insulated wall. Removing a periodicity direction could also help understanding the

spatial development of the observed quantities. Working at higher thermodynamical pressure permits increasing the fluid density and thus the quantity of energy carried out in a given volume. Some researches investigate thermodynamic cycles for solar receiver operating at a thermodynamical pressure of about 30 bar [353, 354]. Hence, performing simulations at this pressure level should also be interesting.

Appendices

Appendix A

Discretization of the temperature gradient at the walls

The order of accuracy of the numerical scheme used to compute the wall heat flux has been enhanced. The spatial temperature derivative is discretized with three points off-centered scheme:

$$\left.\frac{\partial T}{\partial y}\right|_w = \frac{(y_2 - y_w)(y_1 - y_w)}{(y_2 - y_1)} \left(T_2 \frac{1}{(y_2 - y_w)^2} - T_1 \frac{1}{(y_1 - y_w)^2} - T_w \frac{(y_1 - y_w)^2 - (y_2 - y_w)^2}{(y_1 - y_w)^2 (y_2 - y_w)^2} \right) \tag{A.1}$$

The validation of this implementation has been performed by carrying out a simulation in very simple conditions characterized by a null streamwise velocity and a thermal conductivity fixed to 0.06 W/(m K). The obtained temperature value of the fluid at the closest point from the wall has been compared with the analytical solution at the same computational time (0.067s). The results are given in Figure A.1.

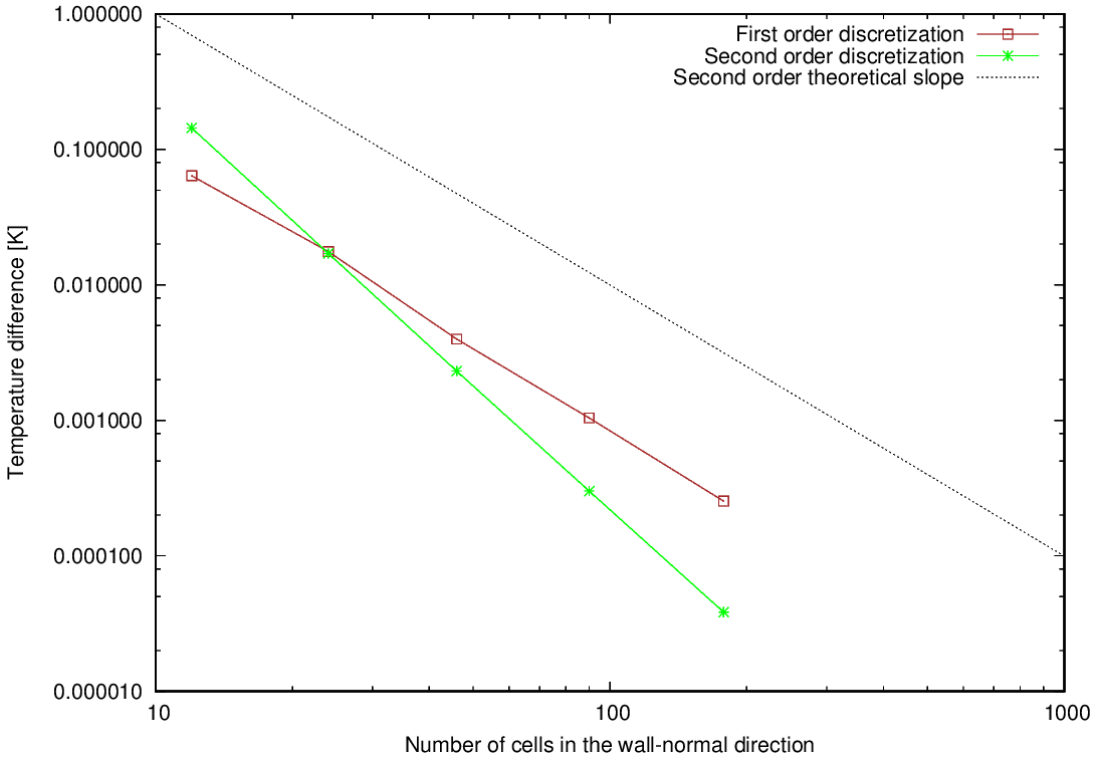

Figure A.1 – Difference between the temperature obtained with the simulation and the temperature obtained with the analytical solution as a function of the number of cells in the wall-normal direction.

Appendix B

Validation of the heat source

The heat source is added in the energy equation. Its implementation has been validated in a simple case corresponding to a null streamwise velocity. For the sake of simplicity the thermal conductivity has been fixed to 0.06 kW/m^2.

The energy equation gives:

$$\frac{\partial U_j}{\partial x_j} = -\frac{1}{\gamma P_0}\left[(\gamma-1)\left(\frac{\partial Q_j}{\partial x_j} - H_s\right) + \frac{\mathrm{d}P_0}{\mathrm{d}t}\right], \tag{B.1}$$

with the assumed hypothesis, it becomes:

$$\frac{\partial Q}{\partial y} = H_s, \tag{B.2}$$

where $Q = \lambda \partial T/\partial y$ the conductive heat flux in the 2-th direction. The temperature profile is obtained by integrating the expression and is:

$$T(y) = Ay^2 + By + C, \tag{B.3}$$

with $H_s = 5\mathrm{MW/m}^3$, $A = \frac{H_s}{2\lambda} = 4.17 \times 10^7$ K/m^2. B and C are determined with two boundary conditions:

$$\begin{cases} T(y=0) = 900\mathrm{K}, \\ T(y=0.0059692\mathrm{m}) = 1300\mathrm{K}, \end{cases} \tag{B.4}$$

leading to:

$$\begin{cases} C = 900 \text{ K}, \\ B = 181706 \text{ K/m}. \end{cases} \tag{B.5}$$

The results obtained with a simulation performed without turbulence model are compared to the obtained analytical solution in Figure B.1. The simulation perfectly fits the analytical solution which permits validating the implementation of the heat source.

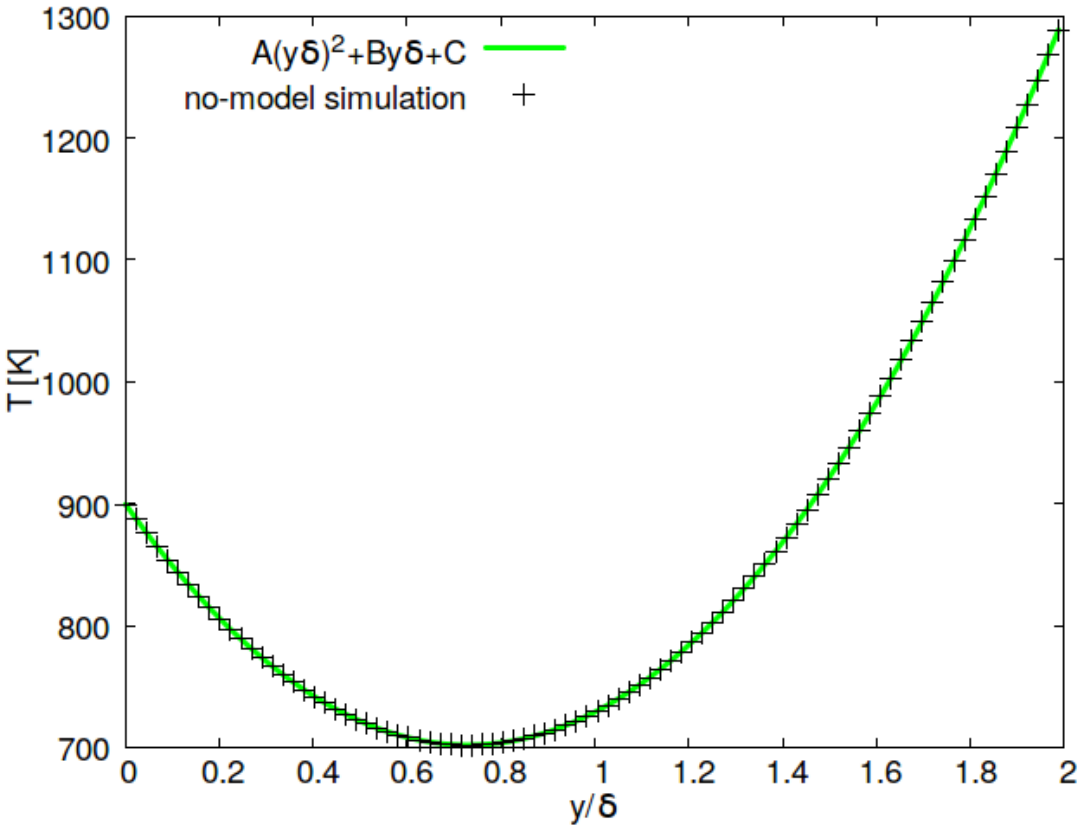

Figure B.1 – Validation of the heat source with an analytical solution. The source term is fixed to $H_s = 5\ MW/m^3$.

Appendix C

Initialization of the simulations

The simulations are initialized with profiles of velocities and temperature. Firstly, a LES without model is carried out, then, the obtained streamwise velocity and temperature profiles are interpolated with an eighth-degree polynomial which conserves the mass flow as well as the strong velocity gradient in the near wall regions, and produces oscillations that mimics the fluctuations of the flow. The spanwise velocity is set to 0 and the wall-normal velocity is initialized with a combination of sinusoidal disturbances. The normalized initialization profiles are given below:

$$\begin{cases} U^o(y^\times) = a_8 y^{\times 8} + a_7 y^{\times 7} + a_6 y^{\times 6} + a_5 y^{\times 5} + a_4 y^{\times 4} + a_3 y^{\times 3} + a_2 y^{\times 2} + a_1 y^\times + a_0 \\ W^o(y^\times) = 0 \\ V^o(x^\times, y^\times, z^\times) = \dfrac{4y^\times}{U_\tau^{mean}} \left(1 - y^\times\right) \\ \quad \left[sin\left(2\pi(x^\times - 1)\right) sin\left(2\pi z^\times\right) + sin\left(12\pi(x^\times - 1)\right) sin\left(8\pi z^\times\right) + sin\left(4\pi(x^\times - 1)\right) sin\left(16\pi z^\times\right)\right] \end{cases} \tag{C.1}$$

where $x_i^\times = x_i / L_i$ and $U_i^o = U_i / U_\tau^{mean}$. The coefficients $a_0, ..., a_8$ depend on the working conditions. They are listed in Table C.1. Figure C.1 gives a graphical representation of the wall-normal velocity initialization.

In the isothermal case, the temperature is fixed to 293 K. In the anisothermal case, the initialization depend on the value of the heat source. The inlet temperature profile is:

$$T^o(y^\times) = b_8 y^{\times 8} + b_7 y^{\times 7} + b_6 y^{\times 6} + b_5 y^{\times 5} + b_4 y^{\times 4} + b_3 y^{\times 3} + b_2 y^{\times 2} + b_1 y^\times + b_0, \tag{C.2}$$

where $T^o = T / T_\tau^{mean}$. The coefficients $b_0, ..., b_8$ depend on the working conditions. They are given in Table C.1.

Initialization profiles of the streamwise velocity and the temperature are given in Figures C.2 and C.3. The converged statistics plotted are those of the ILES.

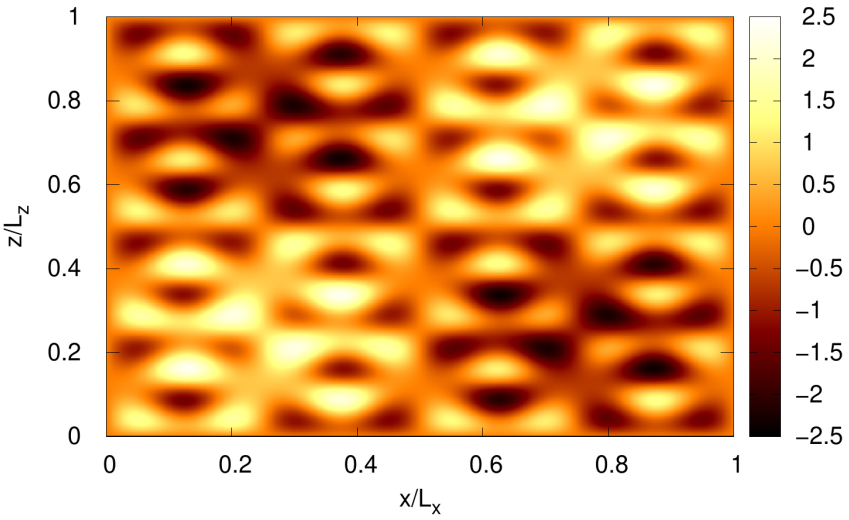

Figure C.1 – Initialization of the wall-normal velocity. The graph is plotted for $y = \delta$.

Table C.1 – Used values for the initialization of the streamwise velocity and the temperature profiles in the three studied conditions. X_i either accounts for a_i or b_i depending on the studied quantity.

Simulation name	ILES [ISO]	ILES [HT]	ILES [LT]	ILES [HT]	ILES [LT]
Coefficient	Initialization of the streamwise velocity			Initialization of the temperature	
X_8	-59535	-56486	-50755	39108	2419476
X_7	238145	225927	202959	165988	-9341630
X_6	-390982	-371007	-333183	-871772	14730952
X_5	339430	322280	289283	1357976	-12201865
X_4	-167259	-158966	-142584	-1020386	5684332
X_3	46643	44397	39768	404115	-1480098
X_2	-6937	-6619	-5913	-81999	203272
X_1	495.6	474.1	422.2	8148.2	-13251.6
X_0	5.55	5.31	4.88	3205.61	3045.81

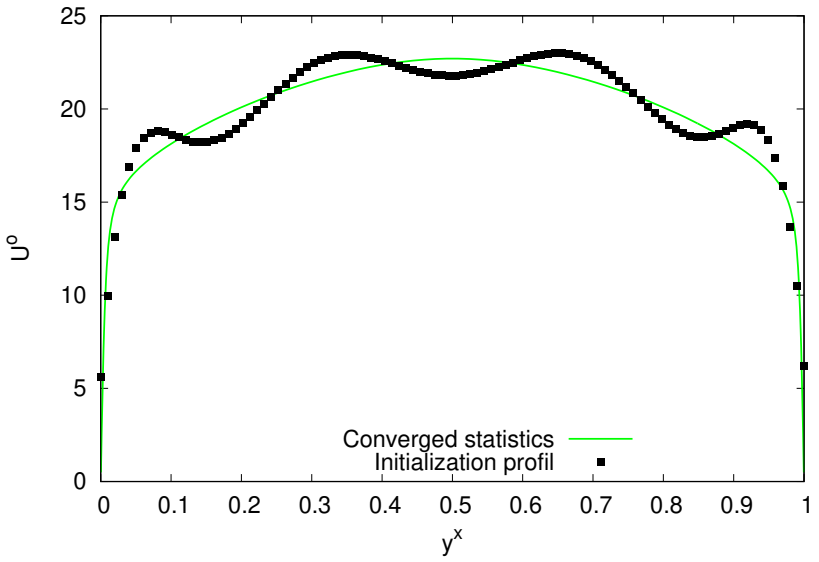

Figure C.2 – Initialization of the streamwise velocity for the isothermal conditions.

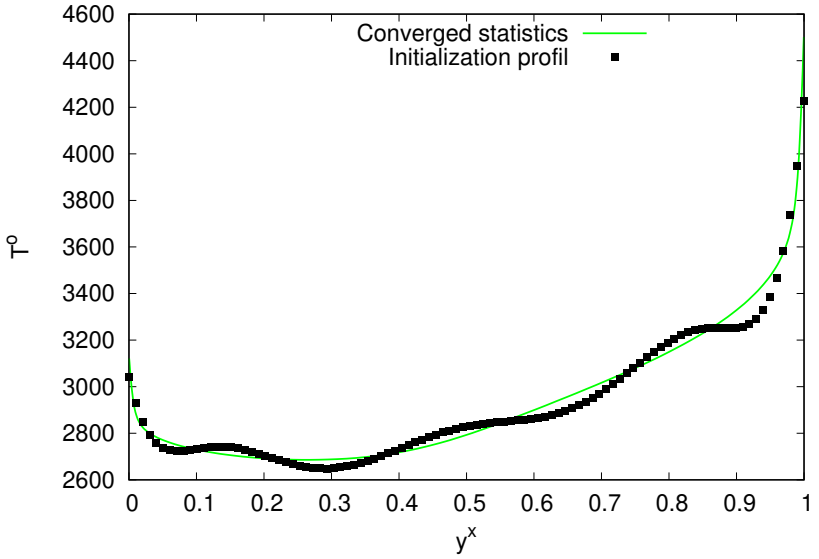

Figure C.3 – Initialization of the temperature for the anisothermal conditions with $H_s = 55$ MW/m^3.

Appendix D

Influence of the channel height and the thermodynamical pressure

In this appendix, the influence of the channel height and the thermodynamical pressure is investigated. In figure D.1, the results of two simulations performed with channel heights of 30 mm and 6 mm are presented. In figure D.2, the results of two simulations carried out with thermodynamical pressure of 1 bar and 10 bar are exhibited. Normalizing the quantities with the adapted values results in superposing the profiles.

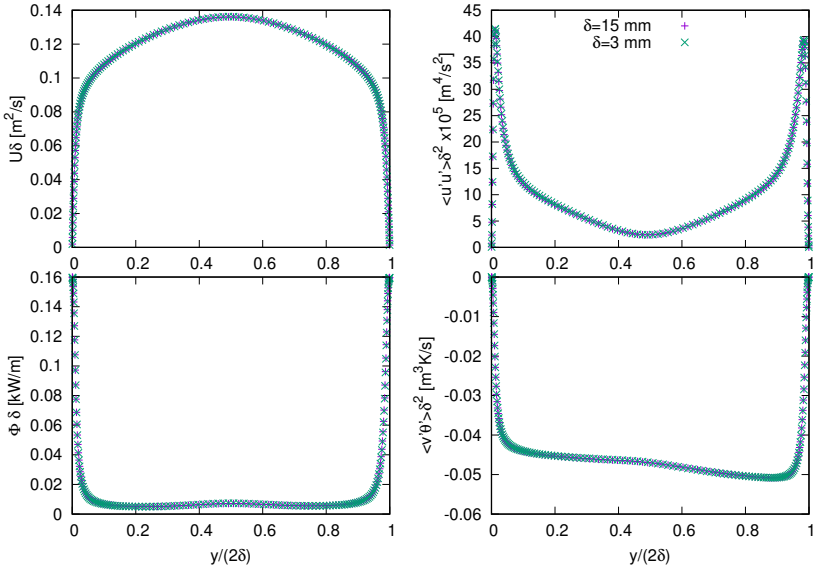

Figure D.1 – Influence of the channel height.

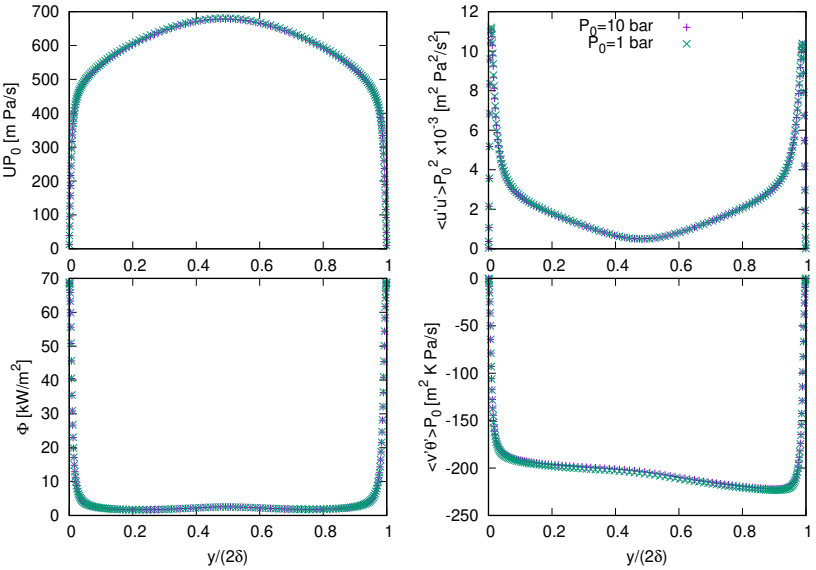

Figure D.2 – Influence of the thermodynamical pressure.

Appendix E

Computational cost

The anisothermal DNS have been performed on the supercomputer OCCIGEN while the isothermal DNS have been achieved on the supercomputer Irene SKL. The characteristics of the two supercomputer are given in table E.1.

A scalability test has been performed on the Irene SKL supercomputer. The objective is to determine how fast the efficiency decreases when the number of cores increases. The simulation "DNS [LT]", that contains 660 million of cells ($N_x \times N_y \times N_z = 1152 \times 746 \times 768$), has been run with 144, 288, 576, 1152, 2304 and 4608 cores. Figure E.1 presents computational cost needed to perform 200 time steps with different number of cores. Below 144 cores, the memory asked for saving fields of velocity is too important and the simulation cannot be realized that is why the graph start with 144 cores. Computational cost of calculation is growing with the number of cores from 243 hours with 144 cores to 741 hours for 4608 cores.

Table E.2 shows the characteristics of the simulations in terms of scalability. When the number of cores is 2 times higher the simulations are generally around 1.8 times faster (with ideal scalability simulation would be 2 times faster). We notice that calculation with 1152 cores is not as good as the others. For instance, it appears that the simulation with 2304 cores is 8.8 times faster than simulation with 144 cores and requires 2 times more computational cost than the one with 144 cores.

The DNS have been carried out on 2304 cores on two different supercomputers. Table E.3 gives the computational characteristics of the DNS. Notice that the electricity consumption and the economic cost of computing performed on the supercomputer OCCIGEN are the following: 9100 €/Mh and 16.3 MWh/Mh, 1 Mh correspond to one million of computational hours. The LES have been performed on 48 cores and their computational cost lies between 0.5% and 0.7%

Table E.1 – Characteristics of the used supercomputers.

Characteristic	OCCIGEN (Haswell)	Irene (SKL)
Processor	E5-2690V3 (2.6 GHz)	Intel Skylake 8168 (2,7 GHz)
Computational power [Pflop/s]	3.5	6.86
Memory per node [Go]	128	192
Memory type	DDR4-2133P-R	DDR4
Network attachment	Infiniband FDR 56 Gbit/s	Infiniband EDR

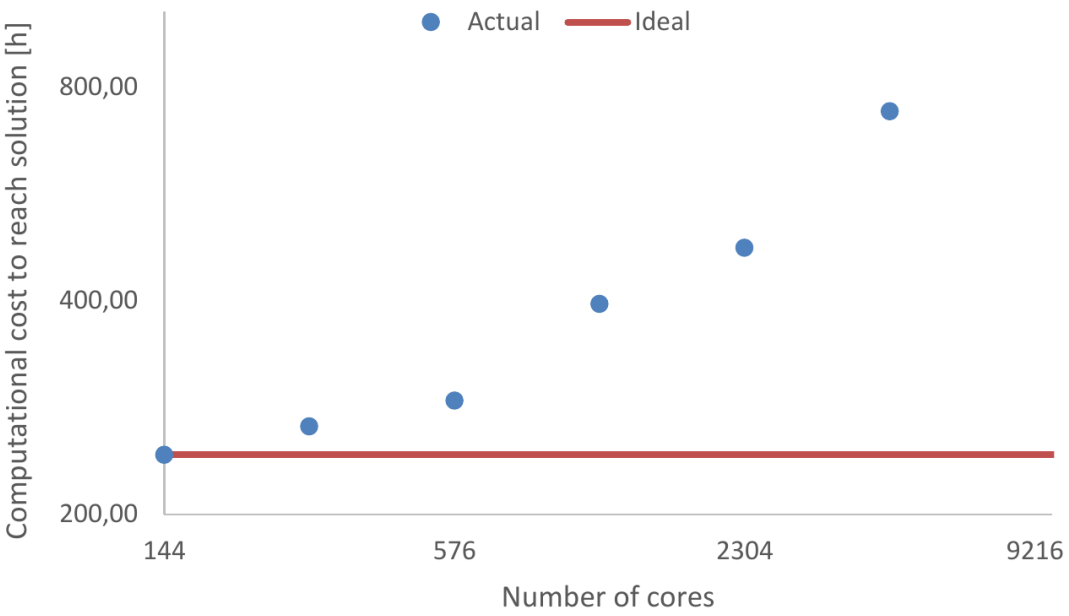

Figure E.1 – Time to reach solution as a function of the number of used cores.

Table E.2 – Characteristics of the time and cost of the simulations depending on the number of used cores.

Number of cores	144	288	576	1152	2304	4608
Number of cells per core	4595712	2297856	1148928	574464	287232	143616
Computational cost [h]	243.1	266.7	290	396.8	476.1	741.1
Number of cores / 144 cores	1	2	4	8	16	32
X time faster than simulation with 144 cores	1	1.8	3.5	5.1	8.8	13.7
X time faster than simulation with 2 times less cores	?	1.8	1.9	1.5	1.7	1.8
X times more costly	1	1.1	1.2	1.6	2.0	3.0

of the DNS cost depending on the model used.

Table E.3 – Computational characteristics of the DNS for the last run of 24 hours and total computational cost.

Supercomputer	Irene SKL	OCCIGEN	
Simulation	DNS [ISO]	DNS [HT]	DNS [LT]
Secondes/time step	2.446	2.352	2.320
Solvers/time step	12	18	18
Secondes/solver	0.037	0.011	0.009
Iterations/solver	58.476	95.401	88.667
Communications avg [% of total time]	52.1	32.7	31.7
Network latency benchmark [s]	1.2×10^{-4}	2.6×10^{-5}	4.3×10^{-5}
Network bandwidth max [MB/s]	542.175	894.391	951.958
Total network traffic [MB/time step]	622935	870256	869015
Avg waiting time [% of total time]	23.0	10.1	7.7
Total computational cost [h]	2.5×10^{6}	3.8×10^{6}	4.5×10^{6}

Appendix F

Numerical setting and mean values of the direct numerical simulations

Three Direct Numerical Simulations (DNS) are performed in a bi-periodical channel of 3 mm height. The first is denoted DNS [iso], is carried out in isothermal conditions, and is used to validate the numerical method with the DNS of Hoyas and Jiménez [10]. The streamwise volume force, $f = 908$ kg/m^2/s^2, permits obtaining the desired friction Reynolds number of 930. The two others aim to represent various axial locations in the solar receiver and are performed with the same streamwise volume force, $f = 15350$ kg/m^2/s^2, leading to similar mean friction Reynolds number of about 800. The two DNS are differentiated by the introduction of a volume heat source, H_s in the energy equation. The DNS carried out without heat source is denoted DNS [HT] (for High fluid Temperature) because its bulk temperature is above the cold wall temperature. The other DNS, denoted DNS [LT] (for Low fluid Temperature) is performed with an heat source of $H_s = 55$ MW/m^3 resulting in a bulk temperature lower than the cold wall temperature. The computational domain and the number of grid points are the same for the three simulations and are respectively: $\mathrm{L_x} \times \mathrm{L_y} \times \mathrm{L_z} = 4\pi\delta \times 2\delta \times 4/3\pi\delta$ and $\mathrm{N_x} \times \mathrm{N_y} \times \mathrm{N_z} = 1152 \times 748 \times 768$.

Table F.1 summaries the mean values obtained after the convergence of the statistics for the three simulations.

Table F.1 – Mean values of the performed direct numerical simulations

	isothermal conditions	anisothermal conditions	
Heat source, MW/m^3	$H_s = 0$	$H_s = 0$	$H_s = 55$
Simulation name	DNS [iso]	DNS [HT]	DNS [LT]
Mass flow, kg/s	8.50×10^{-3}	1.64×10^{-2}	1.98×10^{-2}
Thermodynamic pressure, Pa	$1.00 \times 10^{+6}$	$9.93 \times 10^{+5}$	$1.06 \times 10^{+6}$
Bulk velocity $U_b = \frac{1}{2\delta}\int_0^{2\delta} \overline{U}_x dy$, m/s	$9.54 \times 10^{+0}$	$7.97 \times 10^{+1}$	$7.22 \times 10^{+1}$
Bulk temperature $T_b = \frac{1}{2\delta}\int_0^{2\delta} \overline{T} dy$, K	$2.93 \times 10^{+2}$	$1.09 \times 10^{+3}$	$8.83 \times 10^{+2}$
Bulk density $\rho_b = \frac{1}{2\delta}\int_0^{2\delta} \overline{\rho} dy$, kg/m^3	$1.19 \times 10^{+1}$	$2.76 \times 10^{+0}$	$3.66 \times 10^{+0}$
Bulk dynamic viscosity $\mu_b = \frac{1}{2\delta}\int_0^{2\delta} \overline{\mu} dy$, Pa s	1.81×10^{-5}	4.38×10^{-5}	3.85×10^{-5}
Bulk kinematic viscosity $\nu_b = \frac{1}{2\delta}\int_0^{2\delta} \overline{\nu} dy$, m^2/s	1.52×10^{-6}	1.59×10^{-5}	1.06×10^{-5}
Bulk thermal conductivity $\lambda_b = \frac{1}{2\delta}\int_0^{2\delta} \overline{\lambda} dy$, W/(m K)	2.39×10^{-2}	5.79×10^{-2}	5.09×10^{-2}
Bulk Reynolds number $Re_b = 4\delta\rho_b U_b/\mu_b$	$7.48 \times 10^{+4}$	$6.00 \times 10^{+4}$	$8.19 \times 10^{+4}$
Bulk Mach number $Ma = U_b/\sqrt{\gamma r T_b}$	2.78×10^{-2}	1.20×10^{-1}	1.21×10^{-1}
Centerline streamwise velocity $U_{x,\mathrm{centre}}$, m/s	$1.08 \times 10^{+1}$	$9.05 \times 10^{+1}$	$8.16 \times 10^{+1}$
Centerline wall-normal velocity $U_{y,\mathrm{centre}}$, m/s	∅	-2.77×10^{-2}	2.82×10^{-2}
Centerline temperature T_{centre}, K	$2.93 \times 10^{+2}$	$1.09 \times 10^{+3}$	$8.55 \times 10^{+2}$
Cold friction velocity $U_{\tau,c}$, m/s	4.74×10^{-1}	$3.79 \times 10^{+0}$	$3.64 \times 10^{+0}$
Cold friction temperature $T_{\tau,c}$, K	∅	$6.25 \times 10^{+0}$	$-4.07 \times 10^{+0}$
Cold density ρ_c, kg/m^3	$1.19 \times 10^{+1}$	$3.34 \times 10^{+0}$	$3.58 \times 10^{+1}$
Cold friction Reynolds number $Re_{\tau,c} = \rho_c U_{\tau,c}\delta/\mu_c$	$9.30 \times 10^{+2}$	$9.68 \times 10^{+2}$	$9.96 \times 10^{+2}$
Cold dynamic viscosity μ_c, Pa s	1.81×10^{-5}	3.90×10^{-5}	3.90×10^{-5}
Cold wall temperature T_c, K	$2.93 \times 10^{+2}$	$9.00 \times 10^{+2}$	$9.00 \times 10^{+2}$
Cold wall heat flux $\Phi_c = \left\lvert\lambda_c(\partial_y \overline{T})_c\right\rvert$, W/m^2	∅	$9.84 \times 10^{+4}$	$6.37 \times 10^{+4}$
Cold wall RMS of heat flux $\Phi_{RMS,c}$, W/m^2	∅	$4.20 \times 10^{+4}$	$2.70 \times 10^{+4}$
Cold wall shear stress $\tau_c = \mu_c(\partial_y \overline{U}_x)_c$, Pa	$2.68 \times 10^{+0}$	$4.80 \times 10^{+1}$	$4.73 \times 10^{+1}$
Hot friction velocity $U_{\tau,h}$, m/s	4.75×10^{-1}	$4.38 \times 10^{+0}$	$4.17 \times 10^{+0}$
Hot density ρ_h, kg/m^3	$1.19 \times 10^{+1}$	$2.32 \times 10^{+0}$	$2.48 \times 10^{+1}$
Hot friction temperature $T_{\tau,h}$, K	∅	$7.80 \times 10^{+0}$	$2.11 \times 10^{+1}$
Hot dynamic viscosity μ_h, Pa s	1.81×10^{-5}	4.85×10^{-5}	4.85×10^{-5}
Hot friction Reynolds number $Re_{\tau,h} = \rho_h U_{\tau,h}\delta/\mu_h$	$9.32 \times 10^{+2}$	$6.25 \times 10^{+2}$	$6.37 \times 10^{+2}$
Hot wall temperature T_h, K	$2.93 \times 10^{+2}$	$1.30 \times 10^{+3}$	$1.30 \times 10^{+3}$
Hot wall heat flux $\Phi_h = \left\lvert\lambda_h(\partial_y \overline{T})_h\right\rvert$, W/m^2	∅	$9.84 \times 10^{+4}$	$2.63 \times 10^{+5}$
Hot wall RMS of heat flux $\Phi_{RMS,h}$, W/m^2	∅	$4.20 \times 10^{+4}$	$1.13 \times 10^{+5}$
Hot wall shear stress $\tau_h = \mu_h(\partial_y \overline{U}_x)_h$, Pa	$2.69 \times 10^{+0}$	$4.45 \times 10^{+1}$	$4.32 \times 10^{+1}$
Mean friction Reynolds number $Re_\tau = \frac{1}{2}(Re_{\tau,c} + Re_{\tau,h})$	$9.31 \times 10^{+2}$	$7.96 \times 10^{+2}$	$8.16 \times 10^{+2}$
Mean wall heat flux $\Phi = \frac{1}{2}(\Phi_c + \Phi_h)$, W/m^2	∅	$9.84 \times 10^{+4}$	$1.63 \times 10^{+5}$
Mean wall shear stress $\tau = \frac{1}{2}(\tau_c + \tau_h)$, Pa	$2.68 \times 10^{+0}$	$4.63 \times 10^{+1}$	$4.53 \times 10^{+1}$

Appendix G

Skin frictions and pressure drops

With the aim of improving the competitiveness of the gas-pressurized solar receivers the wall heat transfer should be maximized in order to increase the fluid temperature as high as the used materials can endure it. This permits increasing the heat-to-power conversion efficiency of the thermodynamic cycle. However, the pressure drops should remain as low as possible to maintain the fluid pressure. In gas-pressurized solar receivers, the acceptable pressure drops are below 5% of the total pressure. In the studied conditions, the thermodynamic pressure being 10 bar, the pressure drops should not exceed 50 000 Pa.

The linear pressure drops are computed thanks to the skin friction coefficient, C_f:

$$\Delta P = \frac{C_f \rho_b U_b^2}{2 D_h}, \tag{G.1}$$

with D_h the hydraulic diameter. The skin friction coefficient is defined by the following expression:

$$C_f = \frac{2\tau_w}{\rho_b U_b^2}, \tag{G.2}$$

where

$$\tau_w = \rho_b U_\tau^2 = \mu_w \left.\frac{\partial U}{\partial y}\right|_w \tag{G.3}$$

The Dean correlation [355] permit estimating the friction coefficient in the isothermal conditions thanks to the following equation:

$$C_f^{Dean} = 0.073 Re_m^{-0.25}, \tag{G.4}$$

where $Re_m = 2\delta U_b/\nu_b$. The skin friction coefficient obtained by the Dean correlation are compared to those obtained by the DNS in Table G.1. The relative error between the results is computed as follows:

$$\epsilon_w^{Dean-DNS} = \frac{C_{f,w}^{Dean} - C_{f,w}^{DNS}}{C_{f,w}^{DNS}} \tag{G.5}$$

The pressure drops are computed in Table G.2, taking the average of the wall skin frictions in the anisothermal case.

Table G.1 – Skin friction obtained by the various DNS.

Studied conditions	$C_{f,c}^{DNS}$	$C_{f,h}^{DNS}$	$\epsilon_c^{Dean-DNS}$ [%]	$\epsilon_h^{Dean-DNS}$ [%]
ISO	4.9551×10^{-03}	4.9551×10^{-03}	5.93	5.93
HT	5.4765×10^{-03}	5.0738×10^{-03}	1.30	9.34
LT	4.9673×10^{-03}	4.5318×10^{-03}	3.32	13.25

Table G.2 – Pressure drops obtained by the various DNS.

Simulation name	ΔP [Pa/m]
DNS [ISO]	225
DNS [HT]	3875
DNS [LT]	3790

Using the Dean correlation and the definition of the skin friction coefficient, it is possible to link the friction Reynolds number to the bulk Reynolds number:

$$\begin{cases} C_f^{Dean} = 0.073 Re_m^{-0.25}, \\ C_f = \dfrac{2\tau_w}{\rho U_b^2}. \end{cases} \tag{G.6}$$

where

$$Re_m = \frac{2\delta U_b}{\nu_b}. \tag{G.7}$$

Defining the bulk Reynolds number as:

$$Re_b = \frac{4\delta U_b}{\nu_b}, \tag{G.8}$$

and, the friction Reynolds number as:

$$Re_\tau = \frac{U_\tau \delta}{\nu_w}. \tag{G.9}$$

We obtain:

$$Re_\tau = 0.05162 Re_b^{7/8}. \tag{G.10}$$

For the anisothermal case, Bellec *et al.* [196] suggest to compute the skin friction correlation proposed by Dean with a modified bulk Reynolds number defined as follows:

$$Re_{bw} = Re_b \frac{\rho\left(\frac{Tw+Tb}{2}\right)}{\rho\left(T_w\right)}. \tag{G.11}$$

Hence, in the anisothermal case, the Dean correlation written in terms of friction Reynolds number gives:

$$Re_\tau = 0.05162 Re_{bw}^{7/8}. \tag{G.12}$$

The results of the Dean correlation and those of the adjustements proposed by Bellec *et al.* [196] for the estimation of the friction Reynolds numbers are listed in Table G.3. Note that the Dean correlation permits estimating the mean friction Reynolds number with accuracy as long as the heat source is null. The error committed for the "ISO", "HT", and "LT" conditions are respectively of 2.03%, −1.74%, and 25.85%.

Table G.3 – Results of the adjustements proposed by Bellec *et al.* for the estimation of the friction Reynolds numbers.

Simulation name	$\epsilon^{Bellec}_{Re_{\tau,c}}$	$\epsilon^{Bellec}_{Re_{\tau,h}}$
ISO	2.03	2.03
HT	−3.31	5.61
LT	0.67	8.98

Appendix H

Comparison of direct numerical simulation wall-normal profiles

In this appendix, the wall-normal profiles of DNS first- and second-order statistics are investigated. The plotted results belong to the three DNS performed during this thesis (DNS [ISO], DNS [HT], DNS[LT]) and the DNS of Dupuy *et al.* [145] performed at a mean friction Reynolds number of 180 and 395. Figures H.1, H.2, and H.3 present the classically scaled profiles.

The results obtained with the $(^o)$ scaling are given in figures H.4, H.5, and H.6. The "$(^o)$" scaling is performed as follows: $y^o = yRe_\tau^{mean}/\delta$, $U_i^o = U_i/U_\tau^{mean}$, $\langle R_{ij}\rangle^o = \langle R_{ij}\rangle / \left(U_\tau^{mean}\right)^2$, $T^o = (T_w - T)/T_\tau^{mean}$, and $\langle R_{\theta\theta}\rangle^o = \langle R_{\theta\theta}\rangle / \left(T_\tau^{mean}\right)^2$. ^{mean} denote the averaging of the values obtained at both walls.

The results obtained with the semi-local scaling are given in figures H.7, H.8, and H.9. The semi-local scaling, denoted "(*)", involves the mean local fluid properties instead of the fluid properties at the wall [248]. The normalized quantities are: $y^* = yU_{\tau,\,w}^*/\overline{\nu}(y)$, $U_i^* = U_i/U_{\tau,\,w}^*$, $\langle R_{ij}\rangle^* = \langle R_{ij}\rangle / \left(U_{\tau,\,w}^*\right)^2$, $T^* = T/T_{\tau,\,w}^*$, $\langle R_{i\theta}\rangle^* = \langle R_{i\theta}\rangle / \left(U_{\tau,\,w}^* T_{\tau,\,w}^*\right)$, $\langle R_{\theta\theta}\rangle^* = \langle R_{\theta\theta}\rangle / \left(T_{\tau,\,w}^*\right)^2$, with, $U_{\tau,\,w}^* = \sqrt{\mu_w/\overline{\rho}(y)\partial U/\partial y}$ and $T_{\tau,\,w}^* = \overline{\rho}(y) / \left(\rho_w C_p U_{\tau,\,w}^*\right)$

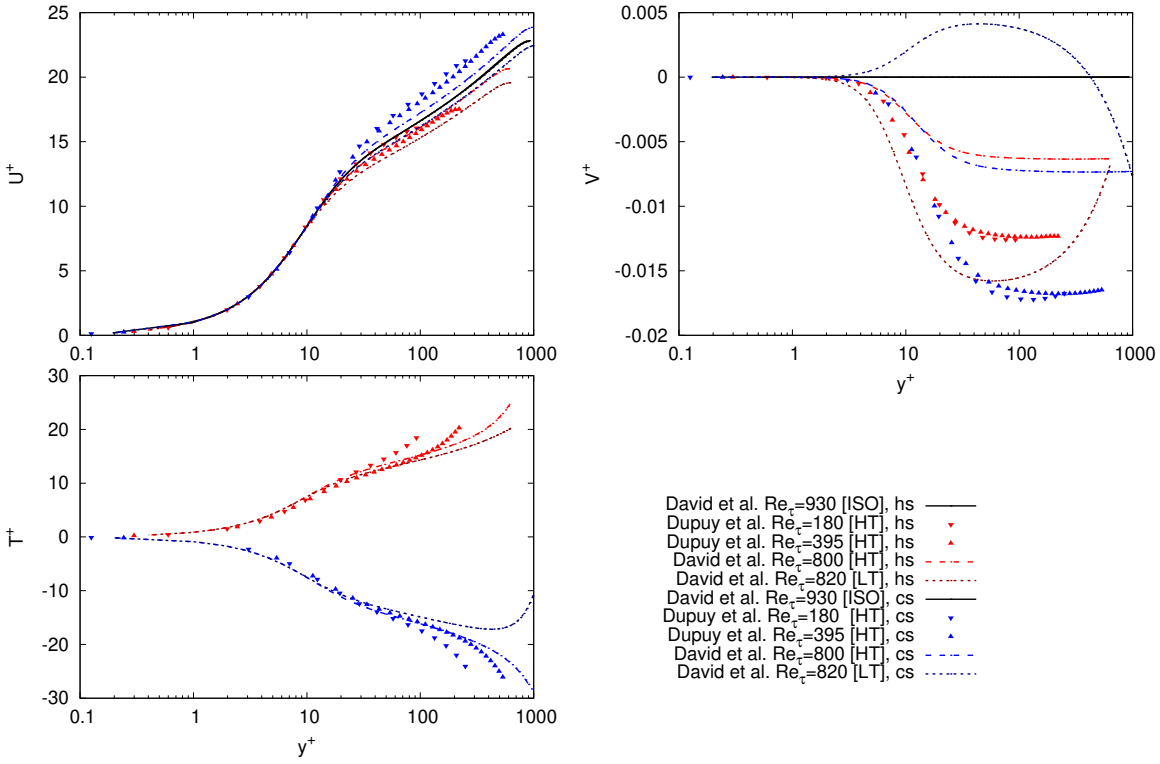

Figure H.1 – Wall-normal profile of classically scaled streamwise velocity, spanwise velocity, and temperature of DNS.

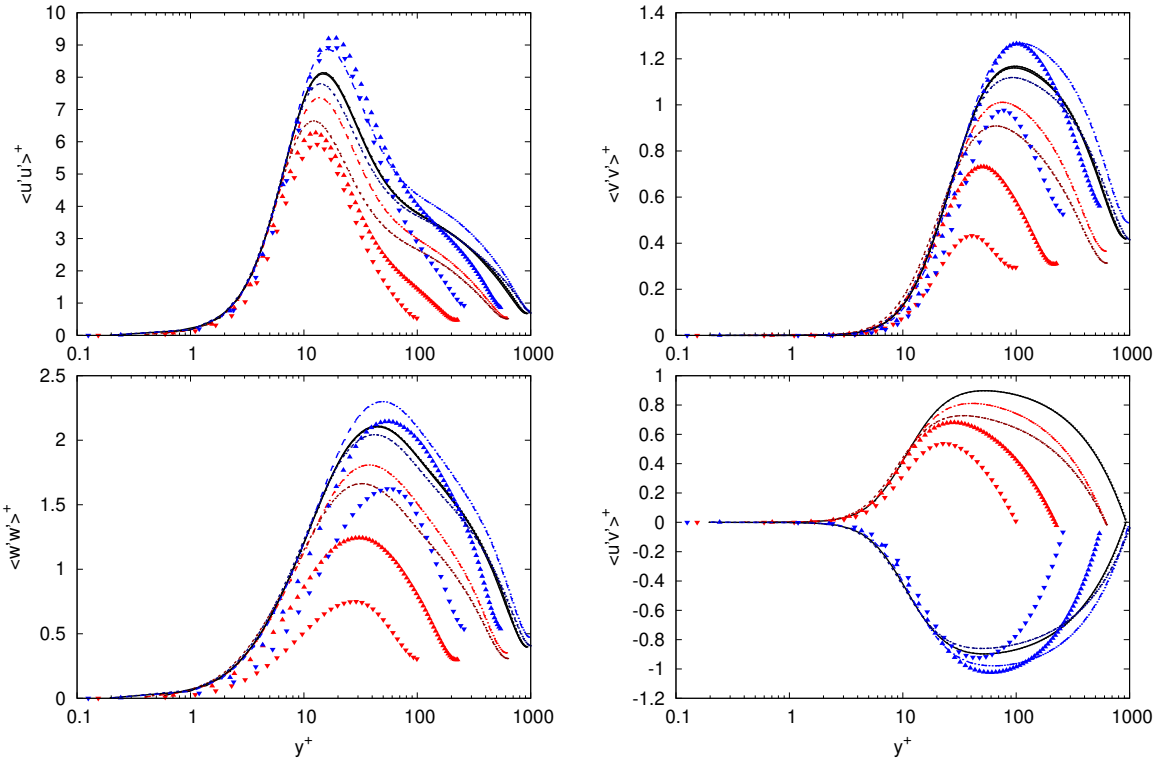

Figure H.2 – Wall-normal profile of classically scaled velocity correlations of DNS.

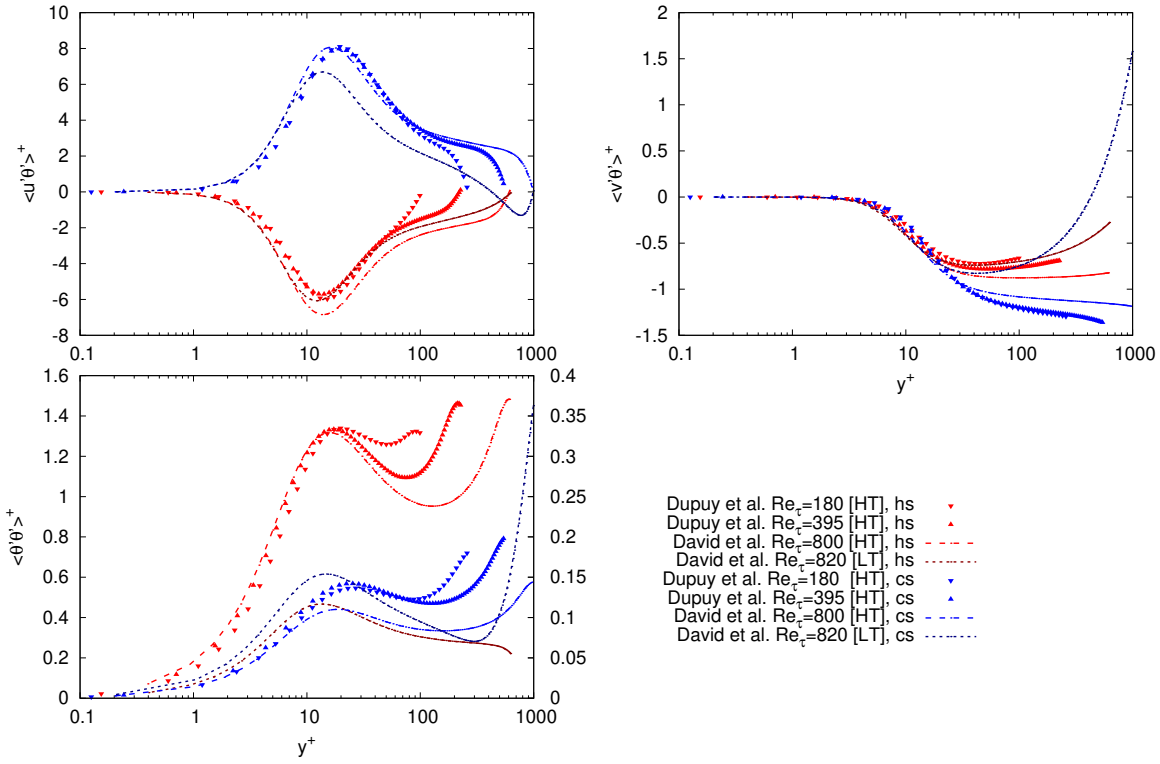

Figure H.3 – Wall-normal profile of classically scaled velocity-temperature correlations and temperature covariances of DNS.

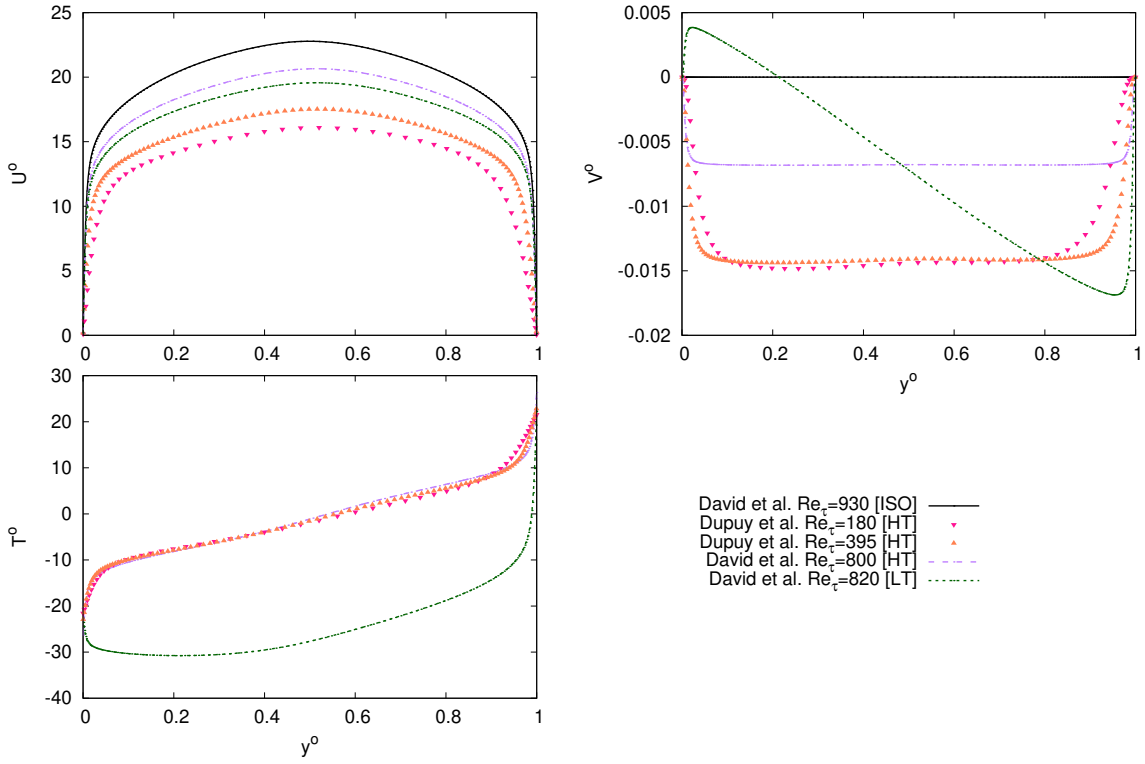

Figure H.4 – Wall-normal profile of (^{o}) scaled streamwise velocity, spanwise velocity, and temperature of DNS.

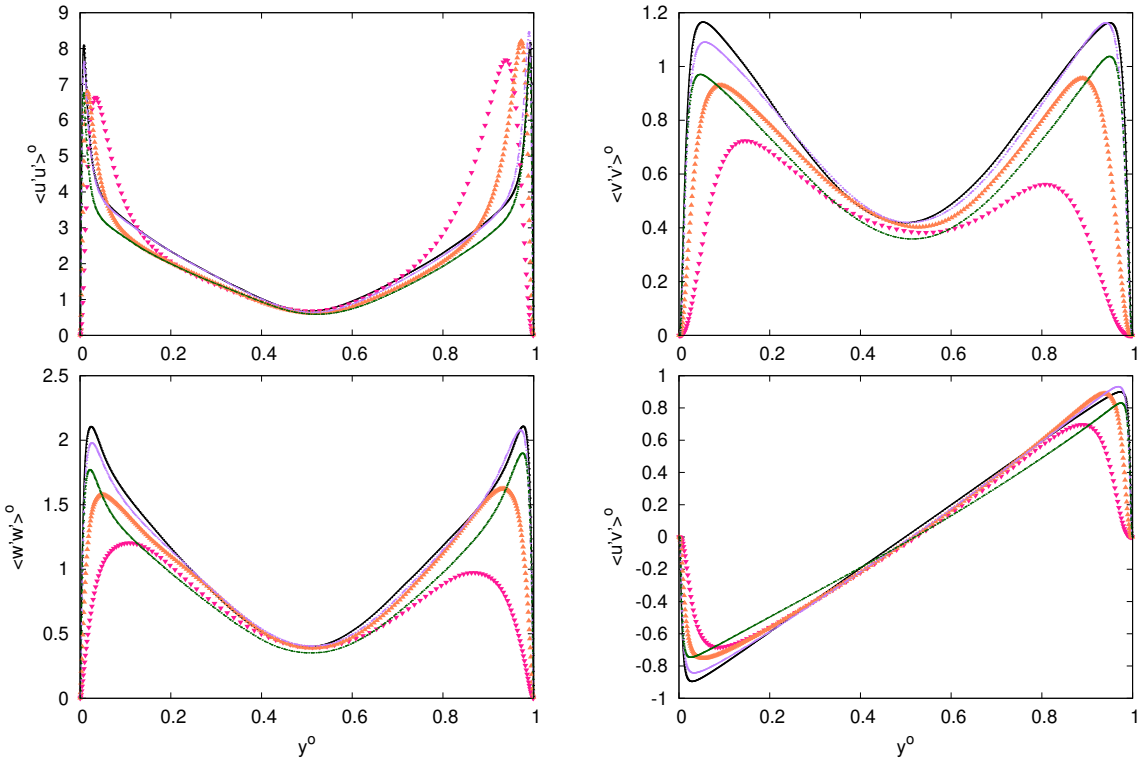

Figure H.5 – Wall-normal profile of (^{o}) scaled velocity correlations of DNS.

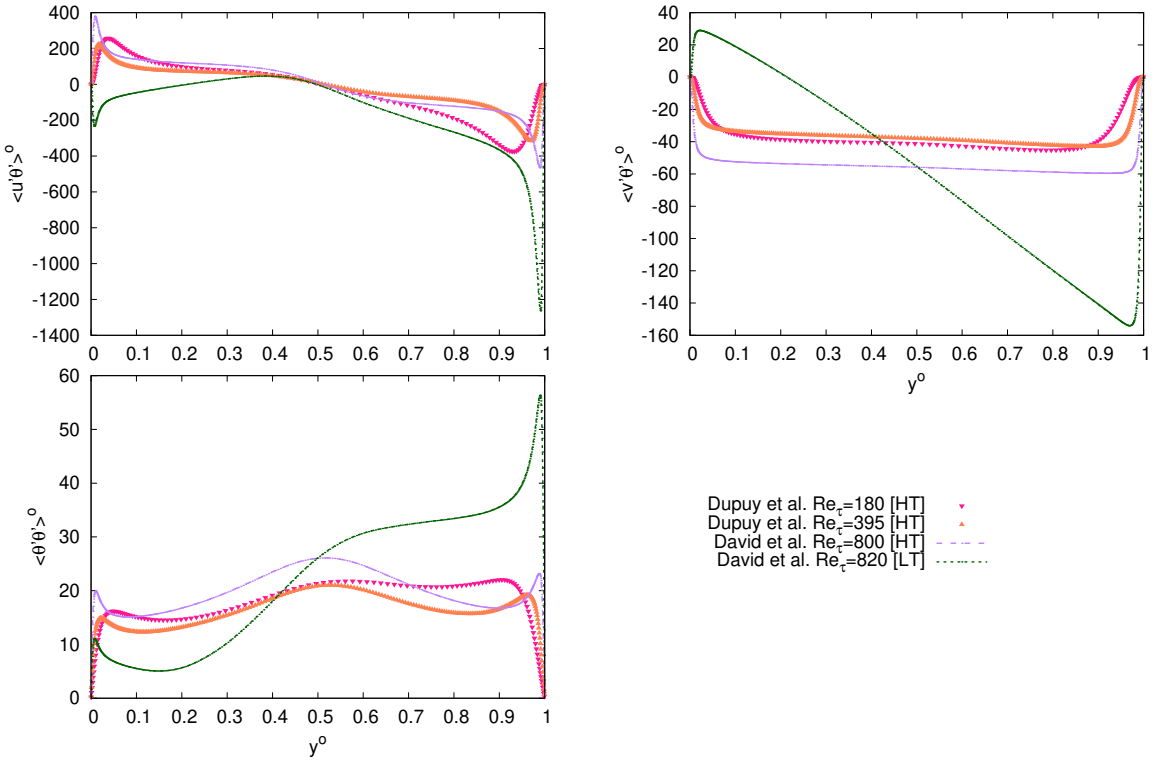

Figure H.6 – Wall-normal profile of (^{o}) scaled velocity-temperature correlations and temperature covariances of DNS.

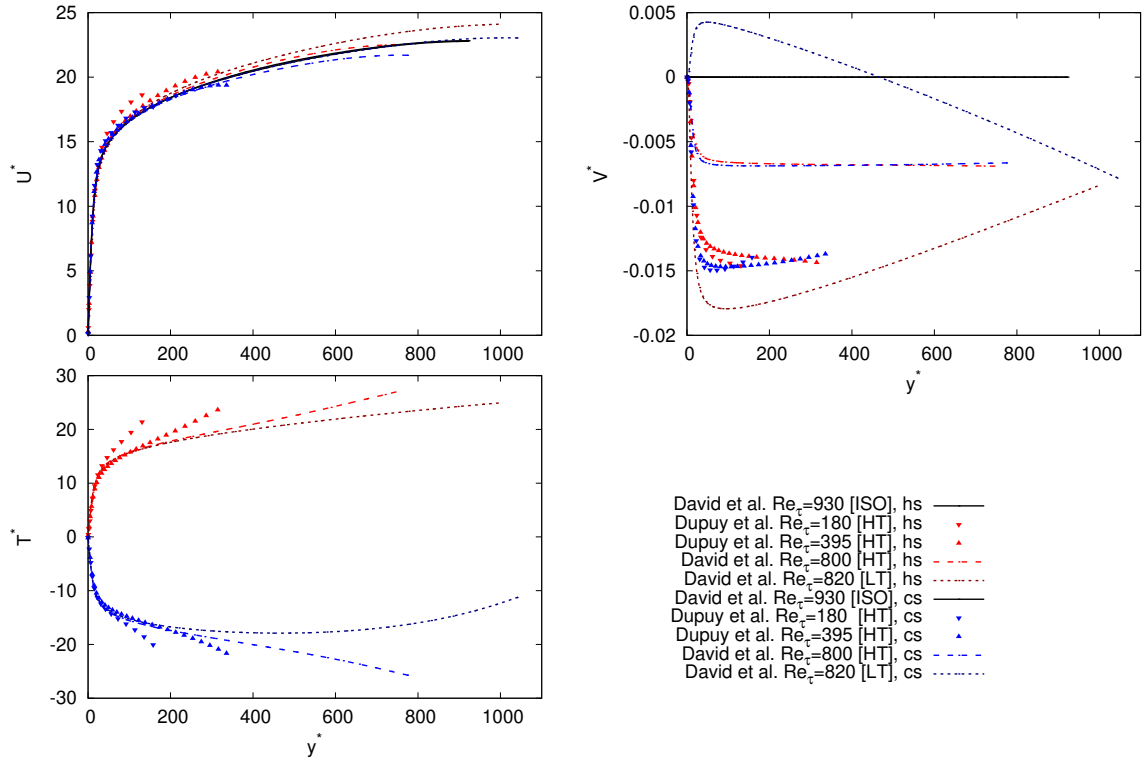

Figure H.7 – Wall-normal profile of semi-locally scaled streamwise velocity, spanwise velocity, and temperature of DNS.

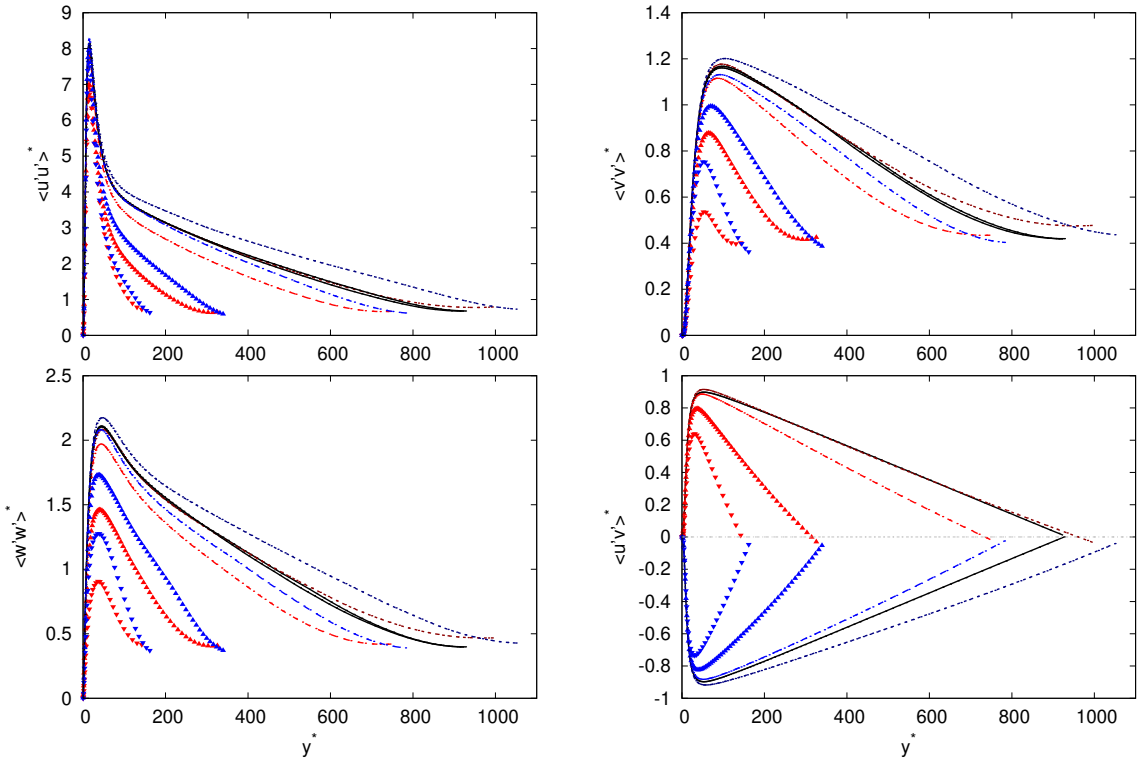

Figure H.8 – Wall-normal profile of semi-locally scaled velocity correlations of DNS.

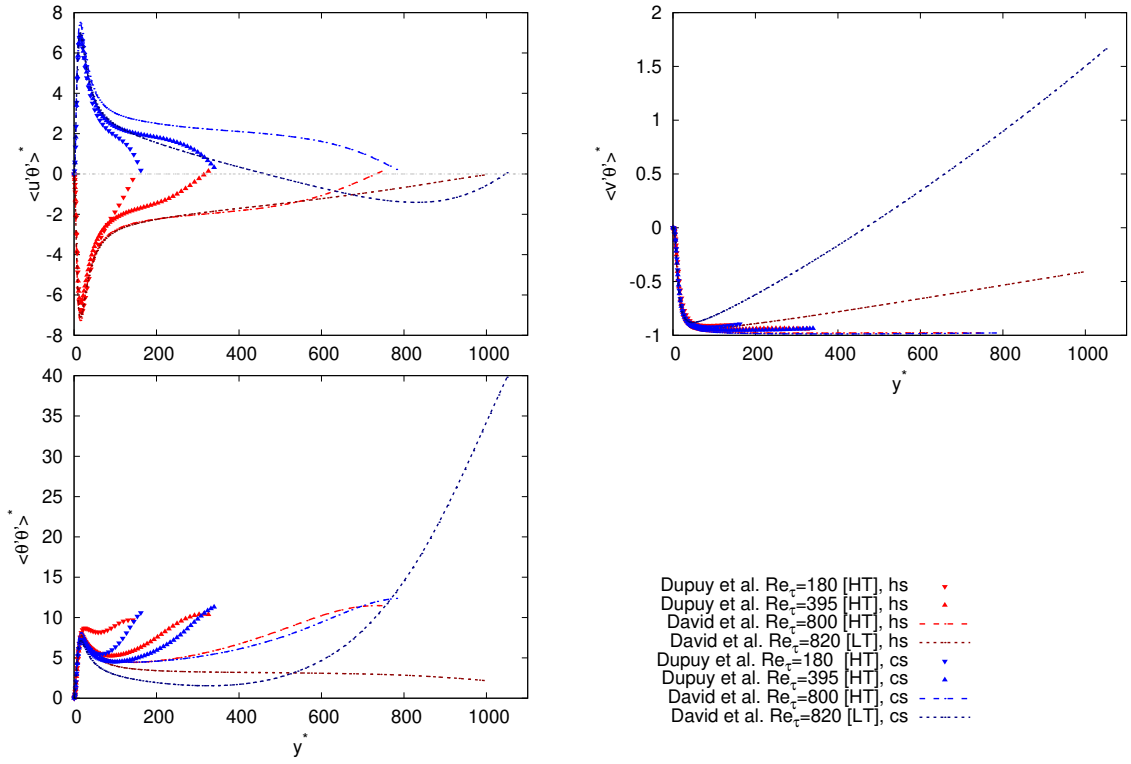

Figure H.9 – Wall-normal profile of semi-locally scaled velocity-temperature correlations and temperature covariances of DNS.

Appendix I

Correction applied to the Nusselt numbers obtained with large eddy simulations

The heat transfer correlation has been developed thanks to LES performed with the AMD model and with a constant absolute mesh size. Part I has shown that the LES tend to underestimate the wall heat fluxes and thus the Nusselt numbers when compared to the DNS. For that reason, the Nusselt numbers obtained with the LES have been corrected before been used to develop the correlation. The correction consists in weighting the Nusselt number by a term depending on the local mesh resolution:

$$Nu_w^{LES,cor} = Nu_w^{LES}\left[1 - \upsilon_w \frac{\Delta x_w^{+,LES} - \Delta x_w^{+,DNS}}{\Delta x_w^{+,DNS}}\right], \tag{I.1}$$

with

$$\begin{cases} \upsilon_c = -0.0245, \\ \upsilon_h = -0.0130. \end{cases} \tag{I.2}$$

In the case where the LES local mesh size is equal to the DNS local mesh size, the Nusselt number are identical. Note that, the values of υ_w are only valid in the case where the mesh resolution in the spanwise direction is two times finer than the mesh resolution in the spanwise direction, the mesh in the wall-normal direction having very little influence as long as the first point is in the linear region of the viscous sublayer [171]. Furthermore, the coefficients of correction also depend on the used turbulence model, the AMD model in the present case.

Figure I.1 shows the Nusselt number obtained with LES, corrected LES, and DNS depending on the friction Reynolds number. The results show that the proposed correction permits compensating the underestimation of the LES.

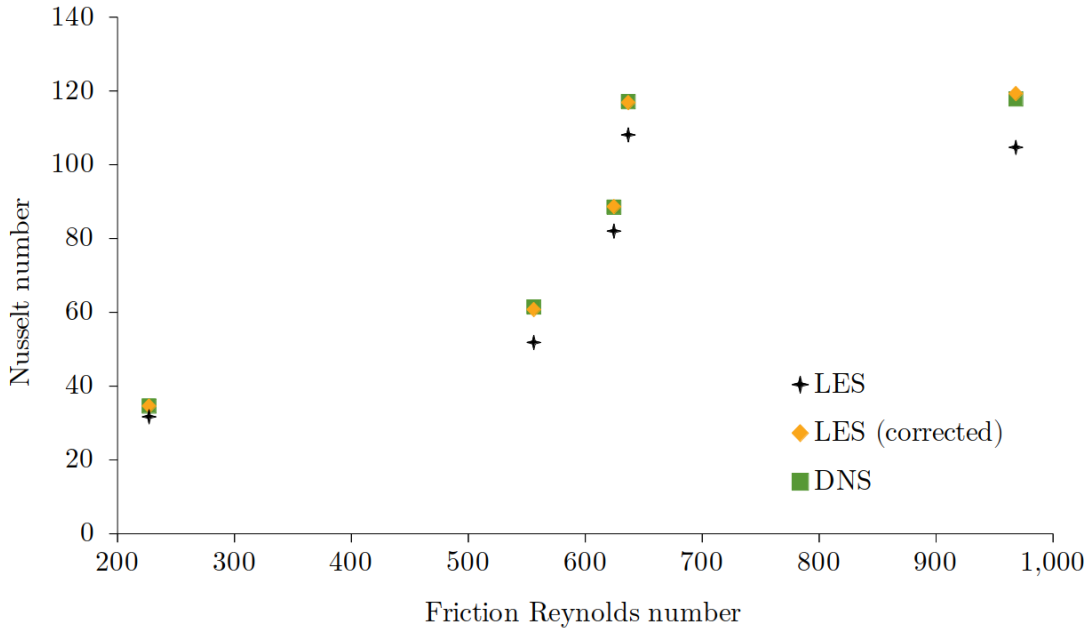

Figure I.1 – Nusselt number obtained with LES, corrected LES, and DNS as a function of the friction Reynolds number.

Complete References

[1] IEA. *World Energy Balances: Overview*. Tech. rep. Paris, 2020.

[2] S. Paolucci. "Filtering of Sound from the Navier-Stokes Equations." In: *NASA STI/Recon Technical Report N* 83 (1982).

[3] C. Calvin, O. Cueto, and P. Emonot. "An object-oriented approach to the design of fluid mechanics software". In: *ESAIM: Mathematical Modelling and Numerical Analysis - Modélisation Mathématique et Analyse Numérique* 36.5 (2002), pp. 907–921.

[4] F. Nicoud. "Conservative High-Order Finite-Difference Schemes for Low-Mach Number Flows". In: *Journal of Computational Physics* 158.1 (2000), pp. 71–97.

[5] J. H. Williamson. "Low-Storage Runge-Kutta Schemes". In: *Journal of Computational Physics* 35.1 (1980), pp. 48–56.

[6] B. P. Leonard. "A Stable and Accurate Convective Modelling Procedure Based on Quadratic Upstream Interpolation". In: *Computer Methods in Applied Mechanics and Engineering* 19.1 (1979), pp. 59–98.

[7] R. D. Moser, J. Kim, and N. N. Mansour. "Direct numerical simulation of turbulent channel flow up to Reτ=590". In: *Physics of Fluids* 11.4 (1999), pp. 943–945.

[8] A. W. Vreman and J. G. M. Kuerten. "Comparison of Direct Numerical Simulation Databases of Turbulent Channel Flow at Reτ = 180". In: *Physics of Fluids* 26.1 (2014), p. 015102.

[9] M. Lee and R. D. Moser. "Direct Numerical Simulation of Turbulent Channel Flow up To". In: *Journal of Fluid Mechanics* 774 (2015), pp. 395–415.

[10] S. Hoyas and J. Jiménez. "Reynolds Number Effects on the Reynolds-Stress Budgets in Turbulent Channels". In: *Physics of Fluids* 20.10 (2008), p. 101511.

[11] G. S. Winckelmans, H. Jeanmart, and D. Carati. "On the Comparison of Turbulence Intensities from Large-Eddy Simulation with Those from Experiment or Direct Numerical Simulation". In: *Physics of Fluids* 14.5 (2002), pp. 1809–1811.

[12] L. B. Streher et al. "Mixed Modeling for Large-Eddy Simulation: The Single-Layer and Two-Layer Minimum-Dissipation-Bardina Models". In: *AIP Advances* 11.1 (2021), p. 015002.

[13] W. Rozema et al. "Minimum-Dissipation Models for Large-Eddy Simulation". In: *Physics of Fluids* 27.8 (2015), p. 085107.

[14] F. Nicoud and F. Ducros. "Subgrid-Scale Stress Modelling Based on the Square of the Velocity Gradient Tensor". In: *Flow, Turbulence and Combustion* 62.3 (1999), pp. 183–200.

[15] A. Leonard. "Energy Cascade in Large-Eddy Simulations of Turbulent Fluid Flows". In: *Advances in Geophysics*. Ed. by F. N. Frenkiel and R. E. Munn. Vol. 18. Turbulent Diffusion in Environmental Pollution. Elsevier, 1975, pp. 237–248.

[16] J. Bardina, J. Ferziger, and W. Reynolds. "Improved Subgrid-Scale Models for Large-Eddy Simulation". In: *13th Fluid and PlasmaDynamics Conference*. Fluid Dynamics and Co-Located Conferences. American Institute of Aeronautics and Astronautics, 1980.

[17] D. Dupuy, A. Toutant, and F. Bataille. "A Posteriori Tests of Subgrid-Scale Models in an Isothermal Turbulent Channel Flow". In: *Physics of Fluids* 31.4 (2019), p. 045105.

[18] T. Wei and W. W. Willmarth. "Reynolds-Number Effects on the Structure of a Turbulent Channel Flow". In: *Journal of Fluid Mechanics* 204 (1989), pp. 57–95.

[19] M. P. Schultz and K. A. Flack. "Reynolds-Number Scaling of Turbulent Channel Flow". In: *Physics of Fluids* 25.2 (2013), p. 025104.

[20] J. Yao and F. Hussain. "Turbulence Statistics and Coherent Structures in Compressible Channel Flow". In: *Physical Review Fluids* 5.8 (2020), p. 084603.

[21] D. Dupuy, A. Toutant, and F. Bataille. "Study of the Large-Eddy Simulation Subgrid Terms of a Low Mach Number Anisothermal Channel Flow". In: *International Journal of Thermal Sciences* 135 (2019), pp. 221–234.

[22] M. Abkar, H. J. Bae, and P. Moin. "Minimum-Dissipation Scalar Transport Model for Large-Eddy Simulation of Turbulent Flows". In: *Physical Review Fluids* 1.4 (2016), p. 041701.

[23] E. Battista and H. C. Perkins. "Turbulent Heat and Momentum Transfer in a Square Duct with Moderate Property Variations". In: *International Journal of Heat and Mass Transfer* 13.6 (1970), pp. 1063–1065.

[24] A. P. Colburn. "A Method of Correlating Forced Convection Heat-Transfer Data and a Comparison with Fluid Friction". In: *International Journal of Heat and Mass Transfer* 7.12 (1964), pp. 1359–1384.

[25] F. W. Dittus and L. M. K. Boelter. "Heat Transfer in Automobile Radiators of the Tubular Type". In: *International Communications in Heat and Mass Transfer* 12.1 (1985), pp. 3–22.

[26] V. Gnielinski. "New Equations for Heat and Mass Transfer in Turbulent Pipe and Channel Flow". In: *Int. Chem. Eng.* 16.2 (1976), pp. 359–368.

[27] M. David, A. Toutant, and F. Bataille. "Numerical Development of Heat Transfer Correlation in Asymmetrically Heated Turbulent Channel Flow". In: *International Journal of Heat and Mass Transfer* 164 (2021), p. 120599.

[28] *Combien Suis-Je Un Esclavagiste ? – Jean-Marc Jancovici*. https://jancovici.com/transition-energetique/l-energie-et-nous/combien-suis-je-un-esclavagiste/.

[29] N. Shykinov, R. Rulko, and D. Mroz. "Importance of Advanced Planning of Manufacturing for Nuclear Industry". In: *Management and Production Engineering Review* 7.2 (2016), pp. 42–49.

[30] AIE. *Les chiffres clés de l'énergie dans le monde*. https://www.connaissancedesenergies.org/les-chiffres-cles-de-lenergie-dans-le-monde-170926. 26 sept. 2017 - 12:00.

[31] *Technology Roadmap - Concentrating Solar Power*. Tech. rep. Paris: IEA, 2010.

[32] I. 2021. *Renewable Power Generation Costs in 2020*. Tech. rep. Abu Dhabi: International Renewable Energy, 2021.

[33] W. Fuqiang et al. "Progress in Concentrated Solar Power Technology with Parabolic Trough Collector System: A Comprehensive Review". In: *Renewable and Sustainable Energy Reviews* 79 (2017), pp. 1314–1328.

[34] J. R. Williams. "41 - SOLAR POWER". In: *Solar Energy Conversion*. Ed. by A. E. Dixon and J. D. Leslie. Pergamon, 1979, pp. 1129–1136. ISBN: 978-0-08-024744-1.

[35] A. Luzzi and K. Lovegrove. "Solar Thermal Power Generation". In: *Encyclopedia of Energy*. Ed. by C. J. Cleveland. New York: Elsevier, 2004, pp. 669–683. ISBN: 978-0-12-176480-7.

[36] S. A. Kalogirou. "Chapter 10 - Solar Thermal Power Systems". In: *Solar Energy Engineering (Second Edition)*. Ed. by S. A. Kalogirou. Boston: Academic Press, 2014, pp. 541–581. ISBN: 978-0-12-397270-5.

[37] R. Sullivan and J. Abplanalp. *Visibility and Visual Characteristics of the Ivanpah Solar Electric Generating System Power Tower Facility*. Tech. rep. Argonne National Laboratory, 2015.

[38] C. Singer, S. Giuliano, and R. Buck. "Assessment of Improved Molten Salt Solar Tower Plants". In: *Energy Procedia*. Proceedings of the SolarPACES 2013 International Conference 49 (2014), pp. 1553–1562.

[39] A. Caraballo et al. "Molten Salts for Sensible Thermal Energy Storage: A Review and an Energy Performance Analysis". In: *Energies* 14.4 (2021), p. 1197.

[40] S. Dieckmann et al. "LCOE Reduction Potential of Parabolic Trough and Solar Tower CSP Technology until 2025". In: *AIP Conference Proceedings* 1850.1 (2017), p. 160004.

[41] G. Flamant et al. "A New Heat Transfer Fluid for Concentrating Solar Systems: Particle Flow in Tubes". In: *Energy Procedia*. Proceedings of the SolarPACES 2013 International Conference 49 (2014), pp. 617–626.

[42] T. Neises and C. Turchi. "A Comparison of Supercritical Carbon Dioxide Power Cycle Configurations with an Emphasis on CSP Applications". In: *Energy Procedia*. Proceedings of the SolarPACES 2013 International Conference 49 (2014), pp. 1187–1196.

[43] J. Pacio et al. "Liquid Metals as Efficient Coolants for High-Intensity Point-Focus Receivers: Implications to the Design and Performance of Next-Generation CSP Systems". In: *Energy Procedia*. Proceedings of the SolarPACES 2013 International Conference 49 (2014), pp. 647–655.

[44] M. Sedighi et al. "Design of High-Temperature Atmospheric and Pressurised Gas-Phase Solar Receivers: A Comprehensive Review on Numerical Modelling and Performance Parameters". In: *Solar Energy* 201 (2020), pp. 701–723.

[45] C. K. Ho. "Advances in Central Receivers for Concentrating Solar Applications". In: *Solar Energy*. Progress in Solar Energy Special Issue: Concentrating Solar Power (CSP) 152 (2017), pp. 38–56.

[46] M. A. Reyes-Belmonte et al. "Optimization of an Integrated Solar Combined Cycle". In: *AIP Conference Proceedings* 2033.1 (2018), p. 210012.

[47] P. Breeze. "Chapter 13 - Solar Power". In: *Power Generation Technologies (Third Edition)*. Ed. by P. Breeze. Newnes, 2019, pp. 293–321. ISBN: 978-0-08-102631-1.

[48] *Principe - PEGASE*. https://www.promes.cnrs.fr/index.php?page=pegase-informations.

[49] L. Mercatelli et al. "Ultra-Refractory Diboride Ceramics for Solar Plant Receivers". In: *Energy Procedia*. Proceedings of the SolarPACES 2013 International Conference 49 (2014), pp. 468–477.

[50] V. R. Patil et al. "Experimental Testing of a Solar Air Cavity-Receiver with Reticulated Porous Ceramic Absorbers for Thermal Processing at above 1000 C". In: *Solar Energy* 214 (2021), pp. 72–85.

[51] B. J. Geurts, A. Rouhi, and U. Piomelli. "Recent Progress on Reliability Assessment of Large-Eddy Simulation". In: *Journal of Fluids and Structures* 91 (2019), p. 102615.

[52] J. Meyers, B. J. Geurts, and P. Sagaut. "A Computational Error-Assessment of Central Finite-Volume Discretizations in Large-Eddy Simulation Using a Smagorinsky Model". In: *Journal of Computational Physics* 227.1 (2007), pp. 156–173.

[53] S. Singh, D. You, and S. T. Bose. "Large-Eddy Simulation of Turbulent Channel Flow Using Explicit Filtering and Dynamic Mixed Models". In: *Physics of Fluids* 24.8 (2012), p. 085105.

[54] B. G. Miller. *Clean Coal Engineering Technology*. Second. Amsterdam ; Boston: Butterworth-Heinemann Inc, 2016. ISBN: 978-0-12-811365-3.

[55] M. A. Silva-Pérez. "17 - Solar Power Towers Using Supercritical CO2 and Supercritical Steam Cycles, and Decoupled Combined Cycles". In: *Advances in Concentrating Solar Thermal Research and Technology*. Ed. by M. J. Blanco and L. R. Santigosa. Woodhead Publishing Series in Energy. Woodhead Publishing, 2017, pp. 383–402. ISBN: 978-0-08-100516-3.

[56] X. Daguenet-Frick et al. "Numerical Investigation of a Ceramic High-Temperature Pressurized-Air Solar Receiver". In: *Solar Energy* 90 (2013), pp. 164–178.

[57] C. K. Ho and B. D. Iverson. "Review of High-Temperature Central Receiver Designs for Concentrating Solar Power". In: *Renewable and Sustainable Energy Reviews* 29 (2014), pp. 835–846.

[58] W.-Q. Wang et al. "Coupled Optical and Thermal Performance of a Fin-like Molten Salt Receiver for the next-Generation Solar Power Tower". In: *Applied Energy* 272 (2020), p. 115079.

[59] J. Capeillère et al. "Thermomechanical Behavior of a Plate Ceramic Solar Receiver Irradiated by Concentrated Sunlight". In: *Solar Energy* 110 (2014), pp. 174–187.

[60] A. Colleoni, A. Toutant, and G. Olalde. "Simulation of an Innovative Internal Design of a Plate Solar Receiver: Comparison between RANS and LES Results". In: *Solar Energy* 105 (2014), pp. 732–741.

[61] Q. Li et al. "Micro-Channel Pressurized-Air Solar Receiver Based on Compact Heat Exchanger Concept". In: *Solar Energy* 91 (2013), pp. 186–195.

[62] H. Goldstein, C. Poole, and J. Safko. "Classical Mechanics, 3rd Ed." In: *American Journal of Physics* 70.7 (2002), pp. 782–783.

[63] I. Newton et al. *Sir Isaac Newton's Mathematical principles of natural philosophy, and his System of the world*. Berkeley: University of California Press, 1962. ISBN: 978-0-520-00928-8 978-0-520-00929-5.

[64] R. Clausius. "Ueber Die Bewegende Kraft Der Wärme Und Die Gesetze, Welche Sich Daraus Für Die Wärmelehre Selbst Ableiten Lassen". In: *Annalen der Physik* 155.3 (1850), pp. 368–397.

[65] G. G. Stokes. "On the Theories of the Internal Friction of Fluids in Motion, and of the Equilibrium and Motion of Elastic Solids". In: *Transactions of the Cambridge Philosophical Society* 8 (1880).

[66] J. Fourier. *Mémoire Sur La Propagation de La Chaleur Dans Les Corps Solides*. Nouveau Bulletin des Sciences de la Société Philomathique de Paris. 1807.

[67] E. Garnier, N. Adams, and P. Sagaut. *Large Eddy Simulation for Compressible Flows*. Springer. Berlin, 2009.

[68] E. Clapeyron. "Memoire Sur La Puissance Motrice de La Chaleur". In: *Journal de l'Ecole Polytechnique* 14, cahier 23 (1834), pp. 153–190.

[69] W. Sutherland. "The Viscosity of Gases and Molecular Force". In: *The London, Edinburgh, and Dublin Philosophical Magazine and Journal of Science* 36.223 (1893), pp. 507–531.

[70] J. Salat et al. "Experimental and Numerical Investigation of Turbulent Natural Convection in a Large Air-Filled Cavity". In: *International Journal of Heat and Fluid Flow*. Selected Papers from the 4th International Symposium on Turbulence Heat and Mass Transfer 25.5 (2004), pp. 824–832.

[71] S. Xin, P. Le Quéré, and O. Daube. "Natural Convection in a Differentially Heated Horizontal Cylinder: Effects of Prandtl Number on Flow Structure and Instability". In: *Physics of Fluids* 9 (1997), pp. 1014–1033.

[72] J. Leray. "Sur le mouvement d'un liquide visqueux emplissant l'espace". In: *Acta Mathematica* 63.1 (1934), pp. 193–248.

[73] B. Desjardins et al. "Incompressible Limit for Solutionsof the Isentropic Navier–Stokes Equationswith Dirichlet Boundary Conditions". In: *Journal de Mathématiques Pures et Appliquées* 78.5 (1999), pp. 461–471.

[74] E. Feireisl, B. J. Jin, and A. Novotný. "Relative Entropies, Suitable Weak Solutions, and Weak-Strong Uniqueness for the Compressible Navier–Stokes System". In: *Journal of Mathematical Fluid Mechanics* 14.4 (2012), pp. 717–730.

[75] T. Kato. "StrongLp-Solutions of the Navier-Stokes Equation inRm, with Applications to Weak Solutions". In: *Mathematische Zeitschrift* 187.4 (1984), pp. 471–480.

[76] H.-O. Bae and B. J. Jin. "Temporal and Spatial Decays for the Navier–Stokes Equations". In: *Proceedings of the Royal Society of Edinburgh Section A: Mathematics* 135.3 (2005), pp. 461–478.

[77] A. M. Jaffe. "The Millennium Grand Challenge in Mathematics". In: *Not.Amer.Math.Soc.* 53.6 (2006), pp. 652–660.

[78] C. Bailly and G. Comte-Bellot. *Turbulence*. Experimental Fluid Mechanics. Springer International Publishing, 2015. ISBN: 978-3-319-16159-4.

[79] A. J. Chorin. "Numerical Solution of the Navier-Stokes Equations". In: *Mathematics of Computation* 22.104 (1968), pp. 745–762.

[80] R. Témam. "Sur l'approximation de la solution des équations de Navier-Stokes par la méthode des pas fractionnaires (I)". In: *Archive for Rational Mechanics and Analysis* 32.2 (1969), pp. 135–153.

[81] C.-W. Tsang and C. Rutland. "Effects of Numerical Schemes on Large Eddy Simulation of Turbulent Planar Gas Jet and Diesel Spray". In: *SAE International Journal of Fuels and Lubricants* 9.1 (2016), pp. 149–164.

[82] N. N. Mansour et al. "Improved Methods for Large Eddy Simulations of Turbulence". In: *Turbulent Shear Flows I*. Ed. by F. Durst et al. Berlin, Heidelberg: Springer, 1979, pp. 386–401. ISBN: 978-3-642-46395-2.

[83] F. Gao and E. E. O'Brien. "A Large-eddy Simulation Scheme for Turbulent Reacting Flows". In: *Physics of Fluids A: Fluid Dynamics* 5.6 (1993), pp. 1282–1284.

[84] B. Vreman, B. Geurts, and H. Kuerten. "Comparison of Numerical Schemes in Large-Eddy Simulation of the Temporal Mixing Layer". In: *International journal for numerical methods in fluids* 22.4 (1996), pp. 297–312.

[85] B. Perot. "Conservation Properties of Unstructured Staggered Mesh Schemes". In: *Journal of Computational Physics* 159.1 (2000), pp. 58–89.

[86] K. Mahesh, G. Constantinescu, and P. Moin. "A Numerical Method for Large-Eddy Simulation in Complex Geometries". In: *Journal of Computational Physics* 197.1 (2004), pp. 215–240.

[87] P. Lenaers. "A New High-Order Method for Direct Numerical Simulations of Turbulent Wall-Bounded Flows". Thesis. Stockholm: KTH Royal Institute of Technology, 2014.

[88] R. Vinuesa et al. "Convergence of Numerical Simulations of Turbulent Wall-Bounded Flows and Mean Cross-Flow Structure of Rectangular Ducts". In: *Meccanica* 51.12 (2016), pp. 3025–3042.

[89] M. Chapman. "FRAM—Nonlinear Damping Algorithms for the Continuity Equation". In: *Journal of Computational Physics* 44 (1981), pp. 84–103.

[90] R. Courant, K. Friedrichs, and H. Lewy. "On the Partial Difference Equations of Mathematical Physics". In: *IBM Journal of Research and Development* 11.2 (1967), pp. 215–234.

[91] D. Dupuy. "Analyse et Modélisation de l'interaction Entre Thermique et Turbulence Dans Les Récepteurs Solaires à Haute Température." Thesis. Perpignan, 2018.

[92] S. M. Salim et al. "Numerical Simulation of Atmospheric Pollutant Dispersion in an Urban Street Canyon: Comparison between RANS and LES". In: *Journal of Wind Engineering and Industrial Aerodynamics* 99.2 (2011), pp. 103–113.

[93] T. van Hooff, B. Blocken, and Y. Tominaga. "On the Accuracy of CFD Simulations of Cross-Ventilation Flows for a Generic Isolated Building: Comparison of RANS, LES and Experiments". In: *Building and Environment* 114 (2017), pp. 148–165.

[94] L. Temmerman, B. Tartinville, and C. Hirsch. "URANS Investigation of the Transonic M219 Cavity". In: *Progress in Hybrid RANS-LES Modelling*. Ed. by S. Fu et al. Notes on Numerical Fluid Mechanics and Multidisciplinary Design. Berlin, Heidelberg: Springer, 2012, pp. 471–481. ISBN: 978-3-642-31818-4.

[95] M. M. Amiri et al. "URANS Investigation of the Interaction between the Free Surface and a Shallowly Submerged Underwater Vehicle at Steady Drift". In: *Applied Ocean Research* 84 (2019), pp. 192–205.

[96] J. García et al. "A Second-Generation URANS Model (STRUCT-ϵ) Applied to Simplified Freight Trains". In: *Journal of Wind Engineering and Industrial Aerodynamics* 205 (2020), p. 104327.

[97] P. R. Spalart et al. "A New Version of Detached-Eddy Simulation, Resistant to Ambiguous Grid Densities". In: *Theoretical and Computational Fluid Dynamics* 20.3 (2006), p. 181.

[98] P. R. Spalart. "Detached-Eddy Simulation". In: *Annual Review of Fluid Mechanics* 41.1 (2009), pp. 181–202.

[99] I. Celik et al. "Assessment Measures for URANS/DES/LES: An Overview with Applications". In: *Journal of Turbulence* 7 (2006), N48.

[100] M. Lesieur, O. Métais, and P. Comte. *Large-Eddy Simulations of Turbulence*. Cambridge ; New York: Cambridge University Press, 2005. ISBN: 978-0-521-78124-4.

[101] P. Sagaut. *Large Eddy Simulation for Incompressible Flows: An Introduction*. Third. Scientific Computation. Berlin Heidelberg: Springer-Verlag, 2006. ISBN: 978-3-540-26344-9.

[102] L. Berselli, T. Iliescu, and W. J. Layton. *Mathematics of Large Eddy Simulation of Turbulent Flows*. Scientific Computation. Berlin Heidelberg: Springer-Verlag, 2006. ISBN: 978-3-540-26316-6.

[103] U. Piomelli, G. N. Coleman, and J. Kim. "On the Effects of Nonequilibrium on the Subgrid-Scale Stresses". In: *Physics of Fluids* 9.9 (1997), pp. 2740–2748.

[104] A. N. Kolmogorov et al. "The Local Structure of Turbulence in Incompressible Viscous Fluid for Very Large Reynolds Numbers". In: *Proceedings of the Royal Society of London. Series A: Mathematical and Physical Sciences* 434.1890 (1991), pp. 9–13.

[105] N. A. Adams and S. Hickel. "Implicit Large-Eddy Simulation: Theory and Application". In: *Advances in Turbulence XII*. Ed. by B. Eckhardt. Springer Proceedings in Physics. Berlin, Heidelberg: Springer, 2009, pp. 743–750. ISBN: 978-3-642-03085-7.

[106] K. Chow and P. Moin. "A Further Study of Numerical Errors in Large-Eddy Simulations". In: *Elsevier* (2002), pp. 1–15.

[107] J. Meyers, B. J. Geurts, and M. Baelmans. "Database Analysis of Errors in Large-Eddy Simulation". In: *Physics of Fluids* 15.9 (2003), pp. 2740–2755.

[108] B. J. Geurts. "Analysis of Errors Occurring in Large Eddy Simulation". In: *Philosophical Transactions of the Royal Society A: Mathematical, Physical and Engineering Sciences* 367.1899 (2009), pp. 2873–2883.

[109] A. Lozano-Durán and H. J. Bae. "Error Scaling of Large-Eddy Simulation in the Outer Region of Wall-Bounded Turbulence". In: *Journal of Computational Physics* 392 (2019), pp. 532–555.

[110] D. Carati. "Time Filtering in Large Eddy Simulations". In: *Proceedings of the Summer Program*. Vol. 2000. 2000, pp. 263–270.

[111] P. Sagaut. "On the Use of Time-Dependent Filters for Large-Eddy Simulation". In: *ESAIM: Proceedings* 10 (2001), pp. 1–7.

[112] F. van der Bos and B. J. Geurts. "Commutator Errors in the Filtering Approach to Large-Eddy Simulation". In: *Physics of Fluids* 17.3 (2005), p. 035108.

[113] S. B. Pope. *Turbulent Flows*. Cambridge: Cambridge University Press, 2000. ISBN: 978-0-521-59886-6.

[114] G. S. Winckelmans et al. "Explicit-Filtering Large-Eddy Simulation Using the Tensor-Diffusivity Model Supplemented by a Dynamic Smagorinsky Term". In: *Physics of Fluids* 13.5 (2001), pp. 1385–1403.

[115] T. S. Lund. "The Use of Explicit Filters in Large Eddy Simulation". In: *Computers & Mathematics with Applications*. Turbulence Modelling and Simulation 46.4 (2003), pp. 603–616.

[116] J. Mathew et al. "An Explicit Filtering Method for Large Eddy Simulation of Compressible Flows". In: *Physics of Fluids* 15.8 (2003), pp. 2279–2289.

[117] S. T. Bose, P. Moin, and D. You. "Grid-Independent Large-Eddy Simulation Using Explicit Filtering". In: *Physics of Fluids* 22.10 (2010), p. 105103.

[118] U. Piomelli, A. Rouhi, and B. J. Geurts. "A Grid-Independent Length Scale for Large-Eddy Simulations". In: *Journal of Fluid Mechanics* 766 (2015), pp. 499–527.

[119] P. J. Mason and N. S. Callen. "On the Magnitude of the Subgrid-Scale Eddy Coefficient in Large-Eddy Simulations of Turbulent Channel Flow". In: *Journal of Fluid Mechanics* 162 (1986), pp. 439–462.

[120] S. Ghosal. "An Analysis of Numerical Errors in Large-Eddy Simulations of Turbulence". In: *Journal of Computational Physics* 125.1 (1996), pp. 187–206.

[121] A. Muschinski. "A Similarity Theory of Locally Homogeneous and Isotropic Turbulence Generated by a Smagorinsky-Type LES". In: *Journal of Fluid Mechanics* 325 (1996), pp. 239–260.

[122] N. Park, J. Y. Yoo, and H. Choi. "Discretization Errors in Large Eddy Simulation: On the Suitability of Centered and Upwind-Biased Compact Difference Schemes". In: *Journal of Computational Physics* 198.2 (2004), pp. 580–616.

[123] M. Lesieur and P. Comte. "Favre Filtering and Macro-Temperature in Large-Eddy Simulations of Compressible Turbulence". In: *Comptes Rendus de l'Académie des Sciences - Series IIB - Mechanics* 329.5 (2001), pp. 363–368.

[124] A. J. Favre. *The Equations of Compressible Turbulent Gases*. Tech. rep. AD0622097. Aix-Marseille univ (France) Inst de mécanique statistiques de la turbulence, 1965. Chap. Technical Reports.

[125] A. J. Favre. "Statistical Equations of Turbulent Gases." In: *Problems of Hydrodynamics and Continuum Mechanics* (1969), pp. 231–266.

[126] A. Favre. "Turbulence: Space-time Statistical Properties and Behavior in Supersonic Flows". In: *The Physics of Fluids* 26.10 (1983), pp. 2851–2863.

[127] S. Ghosal and P. Moin. "The Basic Equations for the Large Eddy Simulation of Turbulent Flows in Complex Geometry". In: *Journal of Computational Physics* 118.1 (1995), pp. 24–37.

[128] O. V. Vasilyev, T. S. Lund, and P. Moin. "A General Class of Commutative Filters for LES in Complex Geometries". In: *Journal of Computational Physics* 146.1 (1998), pp. 82–104.

[129] D. Razafindralandy, A. Hamdouni, and M. Oberlack. "Analysis and Development of Subgrid Turbulence Models Preserving the Symmetry Properties of the Navier–Stokes Equations". In: *European Journal of Mechanics - B/Fluids* 26.4 (2007), pp. 531–550.

[130] C. G. Speziale et al. "The Subgrid-scale Modeling of Compressible Turbulence". In: *The Physics of Fluids* 31.4 (1988), pp. 940–942.

[131] M. H. Silvis, R. A. Remmerswaal, and R. Verstappen. "Physical Consistency of Subgrid-Scale Models for Large-Eddy Simulation of Incompressible Turbulent Flows". In: *Physics of Fluids* 29.1 (2017), p. 015105.

[132] T. Kajishima and T. Nomachi. "One-Equation Subgrid Scale Model Using Dynamic Procedure for the Energy Production". In: *Journal of Applied Mechanics* 73.3 (2005), pp. 368–373.

[133] S. Krajnović and L. Davidson. "A Mixed One-Equation Subgrid Model for Large-Eddy Simulation". In: *International Journal of Heat and Fluid Flow* 23.4 (2002), pp. 413–425.

[134] Y. Fang and S. Menon. "A Two-Equation Subgrid Model for Large-Eddy Simulation of High Reynolds Number Flows". In: *44th AIAA Aerospace Sciences Meeting and Exhibit*. American Institute of Aeronautics and Astronautics, 2012.

[135] F. Gallerano, E. Pasero, and G. Cannata. "A Dynamic Two-Equation Sub Grid Scale Model". In: *Continuum Mechanics and Thermodynamics* 17.2 (2005), pp. 101–123.

[136] J. Ferziger and D. Leslie. "Large Eddy Simulation - A Predictive Approach to Turbulent Flow Computation". In: *4th Computational Fluid Dynamics Conference*. American Institute of Aeronautics and Astronautics, 2012.

[137] J. Boussinesq. *Essai sur la théorie des eaux courantes*. Impr. nationale, 1877.

[138] F. G. Schmitt. "About Boussinesq's Turbulent Viscosity Hypothesis: Historical Remarks and a Direct Evaluation of Its Validity". In: *Comptes Rendus Mécanique*. Joseph Boussinesq, a Scientist of Bygone Days and Present Times 335.9 (2007), pp. 617–627.

[139] A. Yoshizawa. "Statistical Theory for Compressible Turbulent Shear Flows, with the Application to Subgrid Modeling". In: *The Physics of Fluids* 29.7 (1986), pp. 2152–2164.

[140] M. Pino Martín, U. Piomelli, and G. Candler. "Subgrid-Scale Models for Compressible Large-Eddy Simulations". In: *Theoretical and Computational Fluid Dynamics* 13.5 (2000), pp. 361–376.

[141] J. Smagorinsky. "General Circulation Experiments with the Primitive Equations". In: *Monthly Weather Review* 91.3 (1963), pp. 99–164.

[142] M. Germano et al. "A Dynamic Subgrid-scale Eddy Viscosity Model". In: *Physics of Fluids A: Fluid Dynamics* 3.7 (1991), pp. 1760–1765.

[143] P. Sagaut, E. Montreuil, and O. Labbé. "Assessment of Some Self-Adaptive SGS Models for Wall Bounded Flows". In: *Aerospace Science and Technology* 3.6 (1999), pp. 335–344.

[144] G. Aubard et al. "Comparison of Subgrid-Scale Viscosity Models and Selective Filtering Strategy for Large-Eddy Simulations". In: *Flow, Turbulence and Combustion* 91.3 (2013), pp. 497–518.

[145] D. Dupuy, A. Toutant, and F. Bataille. "A Posteriori Tests of Subgrid-Scale Models in Strongly Anisothermal Turbulent Flows". In: *Physics of Fluids* 31.6 (2019), p. 065113.

[146] S. N. Gadde, A. Stieren, and R. J. A. M. Stevens. "Large-Eddy Simulations of Stratified Atmospheric Boundary Layers: Comparison of Different Subgrid Models". In: *Boundary-Layer Meteorology* 178.3 (2021), pp. 363–382.

[147] J. Meyers and P. Sagaut. "Evaluation of Smagorinsky Variants in Large-Eddy Simulations of Wall-Resolved Plane Channel Flows". In: *Physics of Fluids* 19.9 (2007), p. 095105.

[148] S. Malik et al. "Shear Improved Smagorinsky Model for Large Eddy Simulation of Flow in a Stirred Tank with a Rushton Disk Turbine". In: *Chemical Engineering Research and Design*. The 15th European Conference on Mixing 108 (2016), pp. 69–80.

[149] A. W. Vreman. "An Eddy-Viscosity Subgrid-Scale Model for Turbulent Shear Flow: Algebraic Theory and Applications". In: *Physics of Fluids* 16.10 (2004), pp. 3670–3681.

[150] F. Nicoud et al. "Using Singular Values to Build a Subgrid-Scale Model for Large Eddy Simulations". In: *Physics of Fluids* 23.8 (2011), p. 085106.

[151] S. Ryu and G. Iaccarino. "A Subgrid-Scale Eddy-Viscosity Model Based on the Volumetric Strain-Stretching". In: *Physics of Fluids* 26.6 (2014), p. 065107.

[152] R. Verstappen. "An Eddy-Viscosity Model Based on the Invariants of the Rate-of-Strain Tensor". In: *Direct and Large-Eddy Simulation VIII*. Ed. by H. Kuerten et al. ERCOFTAC Series. Dordrecht: Springer Netherlands, 2011, pp. 83–88. ISBN: 978-94-007-2482-2.

[153] F. X. Trias et al. "Building Proper Invariants for Eddy-Viscosity Subgrid-Scale Models". In: *Physics of Fluids* 27.6 (2015), p. 065103.

[154] R. A. Clark, J. H. Ferziger, and W. C. Reynolds. "Evaluation of Subgrid-Scale Models Using an Accurately Simulated Turbulent Flow". In: *Journal of Fluid Mechanics* 91.1 (1979), pp. 1–16.

[155] H. Lu and F. Porté-Agel. "A Modulated Gradient Model for Large-Eddy Simulation: Application to a Neutral Atmospheric Boundary Layer". In: *Physics of Fluids* 22.1 (2010), p. 015109.

[156] K. Horiuti. "A New Dynamic Two-Parameter Mixed Model for Large-Eddy Simulation". In: *Physics of Fluids* 9.11 (1997), pp. 3443–3464.

[157] B. Vreman, B. Geurts, and H. Kuerten. "On the Formulation of the Dynamic Mixed Subgrid-scale Model". In: *Physics of Fluids* 6.12 (1994), pp. 4057–4059.

[158] Y. M. Lee et al. "Assessment of Two-Parameter Mixed Models for Large Eddy Simulations of Transitional and Turbulent Flows". In: *Journal of Mechanical Science and Technology* 34.2 (2020), pp. 727–743.

[159] K. Horiuti. "Backward Scatter of Subgrid-Scale Energy in Wall-Bounded and Free Shear Turbulence". In: *Journal of the Physical Society of Japan* 66.1 (1997), pp. 91–107.

[160] D. Dupuy, A. Toutant, and F. Bataille. "A Priori Tests of Subgrid-Scale Models in an Anisothermal Turbulent Channel Flow at Low Mach Number". In: *International Journal of Thermal Sciences* 145 (2019), p. 105999.

[161] N. S. Ghaisas and S. H. Frankel. "A Priori Evaluation of Large Eddy Simulation Subgrid-Scale Scalar Flux Models in Isotropic Passive-Scalar and Anisotropic Buoyancy-Driven Homogeneous Turbulence". In: *Journal of Turbulence* 15.2 (2014), pp. 88–121.

[162] J. W. Deardorff. "A Numerical Study of Three-Dimensional Turbulent Channel Flow at Large Reynolds Numbers". In: *Journal of Fluid Mechanics* 41.2 (1970), pp. 453–480.

[163] U. Schumann. "Subgrid Scale Model for Finite Difference Simulations of Turbulent Flows in Plane Channels and Annuli". In: *Journal of Computational Physics* 18.4 (1975), pp. 376–404.

[164] U. Piomelli et al. "New Approximate Boundary Conditions for Large Eddy Simulations of Wall-bounded Flows". In: *Physics of Fluids A: Fluid Dynamics* 1.6 (1989), pp. 1061–1068.

[165] I. Marusic, G. J. Kunkel, and F. Porté-Agel. "Experimental Study of Wall Boundary Conditions for Large-Eddy Simulation". In: *Journal of Fluid Mechanics* 446 (2001), pp. 309–320.

[166] S. T. Bose and G. I. Park. "Wall-Modeled Large-Eddy Simulation for Complex Turbulent Flows". In: *Annual Review of Fluid Mechanics* 50.1 (2018), pp. 535–561.

[167] F. Nicoud et al. "Large Eddy Simulation Wall-Modeling Based on Suboptimal Control Theory and Linear Stochastic Estimation". In: *Physics of Fluids* 13.10 (2001), pp. 2968–2984.

[168] D. Chung and D. I. Pullin. "Large-Eddy Simulation and Wall Modelling of Turbulent Channel Flow". In: *Journal of Fluid Mechanics* 631 (2009), pp. 281–309.

[169] J. Xu et al. "Wall-Modeled Large Eddy Simulation of Turbulent Channel Flow at High Reynolds Number Using the von Karman Length Scale". In: *Theoretical and Computational Fluid Dynamics* 30.6 (2016), pp. 565–577.

[170] D. Chapman. "Computational Aerodynamics Development and Outlook". In: *AIAA Journal* 17 (1979), pp. 1293–1313.

[171] S. Rezaeiravesh and M. Liefvendahl. "Effect of Grid Resolution on Large Eddy Simulation of Wall-Bounded Turbulence". In: *Physics of Fluids* 30 (2018).

[172] T. Iliescu and P. F. Fischer. "Large Eddy Simulation of Turbulent Channel Flows by the Rational Large Eddy Simulation Model". In: *Physics of Fluids* 15.10 (2003), pp. 3036–3047.

[173] C. Winkler and S. L. Rani. "Evaluation of Subgrid Scale Kinetic Energy Models in Large Eddy Simulations of Turbulent Channel Flow". In: *International Journal of Numerical Methods for Heat & Fluid Flow* 16.2 (2006), pp. 226–239.

[174] S. T. Bose, P. Moin, and D. You. "Grid-Independent Large-Eddy Simulation Using Explicit Filtering". In: *Physics of Fluids* 22.10 (2010), p. 105103.

[175] F. Kremer and C. Bogey. "Large-Eddy Simulation of Turbulent Channel Flow Using Relaxation Filtering: Resolution Requirement and Reynolds Number Effects". In: *Computers and Fluids* 116 (2015), pp. 17–28.

[176] M. O. Deville and T. B. Gatski. *Mathematical Modeling for Complex Fluids and Flows*. Berlin, Heidelberg: Springer Berlin Heidelberg, 2012. ISBN: 978-3-642-25294-5 978-3-642-25295-2.

[177] H. Reichardt. "Vollständige Darstellung der turbulenten Geschwindigkeitsverteilung in glatten Leitungen". In: *ZAMM - Journal of Applied Mathematics and Mechanics / Zeitschrift für Angewandte Mathematik und Mechanik* 31.7 (1951), pp. 208–219.

[178] Y. Cheng et al. "Large Eddy Simulations of Spray Combustion Instability in an Aero-Engine Combustor at Elevated Temperature and Pressure". In: *Aerospace Science and Technology* 108 (2021), p. 106329.

[179] J. C. Ong et al. "Large-Eddy Simulation of n-Dodecane Spray Flame: Effects of Nozzle Diameters on Autoignition at Varying Ambient Temperatures". In: *Proceedings of the Combustion Institute* 38.2 (2021), pp. 3427–3434.

[180] A. d'Adamo, C. Iacovano, and S. Fontanesi. "Large-Eddy Simulation of Lean and Ultra-Lean Combustion Using Advanced Ignition Modelling in a Transparent Combustion Chamber Engine". In: *Applied Energy* 280 (2020), p. 115949.

[181] S. Srivastava and F. Jaberi. "Large Eddy Simulations of Complex Multicomponent Diesel Fuels in High Temperature and Pressure Turbulent Flows". In: *International Journal of Heat and Mass Transfer* 104 (2017), pp. 819–834.

[182] S. Jogee, B. V. S. S. S. Prasad, and K. Anupindi. "Large-Eddy Simulation of Non-Isothermal Flow over a Circular Cylinder". In: *International Journal of Heat and Mass Transfer* 151 (2020), p. 119426.

[183] T. Lu et al. "Large-Eddy Simulations (LES) of Temperature Fluctuations in a Mixing Tee with/without a Porous Medium". In: *International Journal of Heat and Mass Transfer* 53.21 (2010), pp. 4458–4466.

[184] T. Lu, D. Attinger, and S. M. Liu. "Large-Eddy Simulations of Velocity and Temperature Fluctuations in Hot and Cold Fluids Mixing in a Tee Junction with an Upstream Straight or Elbow Main Pipe". In: *Nuclear Engineering and Design* 263 (2013), pp. 32–41.

[185] J. .-.-B. Chapelier and G. Lodato. "A Spectral-Element Dynamic Model for the Large-Eddy Simulation of Turbulent Flows". In: *Journal of Computational Physics* 321 (2016), pp. 279–302.

[186] M. Terracol, P. Sagaut, and C. Basdevant. "A Time Self-Adaptive Multilevel Algorithm for Large-Eddy Simulation". In: *J. Comput. Phys.* 184.2 (2003), pp. 339–365.

[187] Y. M. Lee et al. "Assessment of Two-Parameter Mixed Models for Large Eddy Simulations of Transitional and Turbulent Flows". In: *Journal of Mechanical Science and Technology* 34.2 (2020), pp. 727–743.

[188] S. Serra, A. Toutant, and F. Bataille. "Thermal Large Eddy Simulation in a Very Simplified Geometry of a Solar Receiver". In: *Heat Transfer Engineering* 33.6 (2012), pp. 505–524.

[189] C. Brun et al. "Large Eddy Simulation of Compressible Channel Flow". In: *Theoretical and Computational Fluid Dynamics* 22.3 (2008), pp. 189–212.

[190] L. D. Dailey, N. Meng, and R. H. Pletcher. "Large Eddy Simulation of Constant Heat Flux Turbulent Channel Flow With Property Variations: Quasi-Developed Model and Mean Flow Results". In: *Journal of Heat Transfer* 125.1 (2003), pp. 27–38.

[191] E. Lenormand, P. Sagaut, and L. T. Phuoc. "Large eddy simulation of subsonic and supersonic channel flow at moderate Reynolds number". In: *International Journal for Numerical Methods in Fluids* 32.4 (2000), pp. 369–406.

[192] S. Hickel and N. A. Adams. "On Implicit Subgrid-Scale Modeling in Wall-Bounded Flows". In: *Physics of Fluids* 19.10 (2007), p. 105106.

[193] W.-P. Wang and R. H. Pletcher. "On the Large Eddy Simulation of a Turbulent Channel Flow with Significant Heat Transfer". In: *Physics of Fluids* 8.12 (1996), pp. 3354–3366.

[194] P. Moin et al. "A Dynamic Subgrid-scale Model for Compressible Turbulence and Scalar Transport". In: *Physics of Fluids A: Fluid Dynamics* 3.11 (1991), pp. 2746–2757.

[195] B. Lessani and M. V. Papalexandris. "Numerical Study of Turbulent Channel Flow with Strong Temperature Gradients". In: *International Journal of Numerical Methods for Heat & Fluid Flow* 18.3/4 (2008). Ed. by A. J. Nowak and R. A. Białecki, pp. 545–556.

[196] M. Bellec, A. Toutant, and G. Olalde. "Large Eddy Simulations of Thermal Boundary Layer Developments in a Turbulent Channel Flow under Asymmetrical Heating". In: *Computers & Fluids*. A Special Issue in Honor of Cecil "Chuck" E. Leith 151 (2017), pp. 159–176.

[197] S. M. Yahya, S. F. Anwer, and S. Sanghi. "Turbulent Forced Convective Flow in an Anisothermal Channel". In: *International Journal of Thermal Sciences* 88 (2015), pp. 84–95.

[198] S. Serra et al. "Asymmetric Reverse Transition Phenomenon in Internal Turbulent Channel Flows Due to Temperature Gradients". In: *International Journal of Thermal Sciences* 159 (2021), p. 106463.

[199] C. Meneveau and J. Katz. "Scale-Invariance and Turbulence Models for Large-Eddy Simulation". In: *Annual Review of Fluid Mechanics* 32.1 (2000), pp. 1–32.

[200] B. Kosović, D. I. Pullin, and R. Samtaney. "Subgrid-Scale Modeling for Large-Eddy Simulations of Compressible Turbulence". In: *Physics of Fluids* 14.4 (2002), pp. 1511–1522.

[201] S. Hickel, N. A. Adams, and J. A. Domaradzki. "An Adaptive Local Deconvolution Method for Implicit LES". In: *J. Comput. Phys.* 213.1 (2006), pp. 413–436.

[202] S. Vashishtha et al. "Large Eddy Simulation of Hydrodynamic Turbulence Using Renormalized Viscosity". In: *Physics of Fluids* 31.6 (2019), p. 065102.

[203] K. Horiuti. "The Role of the Bardina Model in Large Eddy Simulation of Turbulent Channel Flow". In: *Physics of Fluids A: Fluid Dynamics* 1.2 (1989), pp. 426–428.

[204] S. Stolz, N. A. Adams, and L. Kleiser. "An Approximate Deconvolution Model for Large-Eddy Simulation with Application to Incompressible Wall-Bounded Flows". In: *Physics of Fluids* 13.4 (2001), pp. 997–1015.

[205] B. J. Geurts and F. van der Bos. "Numerically Induced High-Pass Dynamics in Large-Eddy Simulation". In: *Physics of Fluids* 17.12 (2005), p. 125103.

[206] A. Keating et al. "A Priori and a Posteriori Tests of Inflow Conditions for Large-Eddy Simulation". In: *Physics of Fluids* 16.12 (2004), pp. 4696–4712.

[207] M. V. Papalexandris. "On the Applicability of Stokes' Hypothesis to Low-Mach-Number Flows". In: *Continuum Mechanics and Thermodynamics* 32.4 (2020), pp. 1245–1249.

[208] P. Sagaut. *Large Eddy Simulation for Incompressible Flows*. 3ème. Springer, 1998.

[209] R. Akhavan et al. "Subgrid-Scale Interactions in a Numerically Simulated Planar Turbulent Jet and Implications for Modelling". In: *Journal of Fluid Mechanics* 408 (2000), pp. 83–120.

[210] C. Meneveau and J. Katz. "Conditional Subgrid Force and Dissipation in Locally Isotropic and Rapidly Strained Turbulence". In: *Physics of Fluids* 11.8 (1999), pp. 2317–2329.

[211] J. M. Avellaneda, F. Bataille, and A. Toutant. "DNS of Turbulent Low Mach Channel Flow under Asymmetric High Temperature Gradient: Effect of Thermal Boundary Condition on Turbulence Statistics". In: *International Journal of Heat and Fluid Flow* 77 (2019), pp. 40–47.

[212] S. K. Lele. "Compact Finite Difference Schemes with Spectral-like Resolution". In: *Journal of Computational Physics* 103.1 (1992), pp. 16–42.

[213] A. Toutant. "Numerical Simulations of Unsteady Viscous Incompressible Flows Using General Pressure Equation". In: *Journal of Computational Physics* 374 (2018), pp. 822–842.

[214] F. Aulery et al. "Spectral Analysis of Turbulence in Anisothermal Channel Flows". In: *Computers & Fluids*. A Special Issue in Honor of Cecil "Chuck" E. Leith 151 (2017), pp. 115–131.

[215] J. A. Domaradzki and N. A. Adams. "Direct Modelling of Subgrid Scales of Turbulence in Large Eddy Simulations". In: *Journal of Turbulence* 3 (2002), N24.

[216] V. Boutrouche et al. "Influence of the Turbulence Model for Channel Flows with Strong Transverse Temperature Gradients". In: *International Journal of Heat and Fluid Flow* 70 (2018), pp. 79–103.

[217] A. V. Johansson and P. M. Wikström. "DNS and Modelling of Passive Scalar Transport in Turbulent Channel Flow with a Focus on Scalar Dissipation Rate Modelling". In: *Flow, Turbulence and Combustion* 63.1 (2000), p. 223.

[218] N. Silin et al. "Hydrodynamic Transition Delay in Rectangular Channels under High Heat Flux". In: *Annals of Nuclear Energy* 37.4 (2010), pp. 615–620.

[219] Z. Wang et al. "Numerical Study on Laminar-Turbulent Transition Flow in Rectangular Channels of a Nuclear Reactor". In: *Frontiers in Energy Research* 8 (2020).

[220] M. M. Sorour and Z. A. Mottaleb. "Performances of Channel-Type Flat-Plate Solar Energy Air-Heaters". In: *Applied Energy* 18.1 (1984), pp. 1–13.

[221] X. Daguenet-Frick et al. "Experimental Analysis of the Turbulent Flow Behavior of a Textured Surface Proposed for Asymmetric Heat Exchangers". In: *Flow, Turbulence and Combustion* 89.1 (2012), pp. 149–169.

[222] A. Colleoni et al. "Optimization of Winglet Vortex Generators Combined with Riblets for Wall/Fluid Heat Exchange Enhancement". In: *Applied Thermal Engineering* 50.1 (2013), pp. 1092–1100.

[223] J. Kim, P. Moin, and R. Moser. "Turbulence Statistics in Fully Developed Channel Flow at Low Reynolds Number". In: *Journal of Fluid Mechanics* 177 (1987), pp. 133–166.

[224] O. Cabrit and F. Nicoud. "DNS of a Periodic Channel Flow with Isothermal Ablative Wall". In: *Direct and Large-Eddy Simulation VII*. Ed. by V. Armenio, B. Geurts, and J. Fröhlich. ERCOFTAC Series. Springer Netherlands, 2010, pp. 33–39. ISBN: 978-90-481-3652-0.

[225] Y. Morinishi, S. Tamano, and K. Nakabayashi. "Direct Numerical Simulation of Compressible Turbulent Channel Flow between Adiabatic and Isothermal Walls". In: *Journal of Fluid Mechanics* 502 (2004), pp. 273–308.

[226] J. C. D. Álamo et al. "Scaling of the Energy Spectra of Turbulent Channels". In: *Journal of Fluid Mechanics* 500 (2004), pp. 135–144.

[227] S. Hoyas and J. Jiménez. "Scaling of the Velocity Fluctuations in Turbulent Channels up to Reτ=2003". In: *Physics of Fluids* 18.1 (2006), p. 011702.

[228] H. Kawamura, H. Abe, and Y. Matsuo. "DNS of Turbulent Heat Transfer in Channel Flow with Respect to Reynolds and Prandtl Number Effects". In: *International Journal of Heat and Fluid Flow* 20.3 (1999), pp. 196–207.

[229] M. David, A. Toutant, and F. Bataille. "Investigation of Thermal Large-Eddy Simulation Approaches in a Highly Turbulent Channel Flow Submitted to Strong Asymmetric Heating". In: *Physics of Fluids* 33.4 (2021), p. 045104.

[230] Y. Zhiyin. "Large-Eddy Simulation: Past, Present and the Future". In: *Chinese Journal of Aeronautics* 28.1 (2015), pp. 11–24.

[231] F. Nicoud and F. Ducros. "Subgrid-Scale Stress Modelling Based on the Square of the Velocity Gradient Tensor". In: *Flow, Turbulence and Combustion* 62.3 (1999), pp. 183–200.

[232] M. Kim et al. "Assessment of the Wall-Adapting Local Eddy-Viscosity Model in Transitional Boundary Layer". In: *Computer Methods in Applied Mechanics and Engineering* 371 (2020), p. 113287.

[233] H. Kobayashi. "The Subgrid-Scale Models Based on Coherent Structures for Rotating Homogeneous Turbulence and Turbulent Channel Flow". In: *Physics of Fluids* 17.4 (2005), p. 045104.

[234] O. Métais and M. Lesieur. "Spectral Large-Eddy Simulation of Isotropic and Stably Stratified Turbulence". In: *Journal of Fluid Mechanics* 239 (1992), pp. 157–194.

[235] B. Aupoix. "Subgrid Scale Models for Homogeneous Anisotropic Turbulence". In: *Direct and Large Eddy Simulation of Turbulence: Proceedings of the EUROMECH Colloquium No. 199, München, FRG, September 30 to October 2, 1985*. Ed. by U. Schumann and R. Friedrich. Notes on Numerical Fluid Mechanics. Wiesbaden: Vieweg+Teubner Verlag, 1986, pp. 37–66. ISBN: 978-3-663-00197-3.

[236] H. Lu and C. J. Rutland. "Structural Subgrid-Scale Modeling for Large-Eddy Simulation: A Review". In: *Acta Mechanica Sinica* 32.4 (2016), pp. 567–578.

[237] R. Anderson and C. Meneveau. "Effects of the Similarity Model in Finite-Difference LES of Isotropic Turbulence Using a Lagrangian Dynamic Mixed Model". In: *Flow, Turbulence and Combustion* 62.3 (1999), pp. 201–225.

[238] R. Akhavan et al. "Subgrid-Scale Interactions in a Numerically Simulated Planar Turbulent Jet and Implications for Modelling". In: *Journal of Fluid Mechanics* 408 (2000), pp. 83–120.

[239] C. Meneveau and J. Katz. "Scale-Invariance and Turbulence Models for Large-Eddy Simulation". In: *Annual Review of Fluid Mechanics* 32.1 (2000), pp. 1–32.

[240] S. Serra et al. "High-Temperature Gradient Effect on a Turbulent Channel Flow Using Thermal Large-Eddy Simulation in Physical and Spectral Spaces". In: *Journal of Turbulence* 13 (2012), N49.

[241] T. M. Eidson. "Numerical Simulation of the Turbulent Rayleigh–Bénard Problem Using Subgrid Modelling". In: *Journal of Fluid Mechanics* 158 (1985), pp. 245–268.

[242] A. Rasam, G. Brethouwer, and A. V. Johansson. "An Explicit Algebraic Model for the Subgrid-Scale Passive Scalar Flux". In: *Journal of Fluid Mechanics* 721 (2013), pp. 541–577.

[243] B.-C. Wang et al. "A General Dynamic Linear Tensor-Diffusivity Subgrid-Scale Heat Flux Model for Large-Eddy Simulation of Turbulent Thermal Flows". In: *Numerical Heat Transfer, Part B: Fundamentals* 51.3 (2007), pp. 205–227.

[244] B.-C. Wang et al. "A Complete and Irreducible Dynamic SGS Heat-Flux Modelling Based on the Strain Rate Tensor for Large-Eddy Simulation of Thermal Convection". In: *International Journal of Heat and Fluid Flow*. Revised and Extended Papers from the 5th Conference in Turbulence, Heat and Mass Transfer 28.6 (2007), pp. 1227–1243.

[245] B.-C. Wang et al. "New Dynamic Subgrid-Scale Heat Flux Models for Large-Eddy Simulation of Thermal Convection Based on the General Gradient Diffusion Hypothesis". In: *Journal of Fluid Mechanics* 604 (2008), pp. 125–163.

[246] S.-H. Peng and L. Davidson. "On a Subgrid-Scale Heat Flux Model for Large Eddy Simulation of Turbulent Thermal Flow". In: *International Journal of Heat and Mass Transfer* 45.7 (2002), pp. 1393–1405.

[247] F. Ries et al. "A Wall-Adapted Anisotropic Heat Flux Model for Large Eddy Simulations of Complex Turbulent Thermal Flows". In: *Flow, Turbulence and Combustion* 106.2 (2021), pp. 733–752.

[248] A. Patel et al. "Semi-Local Scaling and Turbulence Modulation in Variable Property Turbulent Channel Flows". In: *Physics of Fluids* 27.9 (2015), p. 095101.

[249] A. Toutant and F. Bataille. "Turbulence Statistics in a Fully Developed Channel Flow Submitted to a High Temperature Gradient". In: *International Journal of Thermal Sciences* 74 (2013), pp. 104–118.

[250] A. Patel, B. J. Boersma, and R. Pecnik. "Scalar Statistics in Variable Property Turbulent Channel Flows". In: *Physical Review Fluids* 2.8 (2017), p. 084604.

[251] M. Lesieur. *Turbulence in Fluids*. Third. Fluid Mechanics and Its Applications. Springer Netherlands, 1997. ISBN: 978-94-010-9018-6.

[252] F. Kremer and C. Bogey. "Large-Eddy Simulation of Turbulent Channel Flow Using Relaxation Filtering: Resolution Requirement and Reynolds Number Effects". In: *Computers & Fluids* 116 (2015), pp. 17–28.

[253] L. Wang et al. "Large Eddy Simulation of Turbulent Heat Transfer in a Non-Isothermal Channel: Effects of Temperature-Dependent Viscosity and Thermal Conductivity". In: *International Journal of Thermal Sciences* 146 (2019), p. 106094.

[254] A. Bejan. "Fundamental Principles". In: *Convection Heat Transfer*. Fourth. John Wiley & Sons, Ltd, 2013. Chap. 1, pp. 1–29. ISBN: 978-1-118-67162-7.

[255] C. Balaji, B. Srinivasan, and S. Gedupudi. "Chapter 6 - Natural Convection". In: *Heat Transfer Engineering*. Ed. by C. Balaji, B. Srinivasan, and S. Gedupudi. Academic Press, 2021, pp. 173–198. ISBN: 978-0-12-818503-2.

[256] E. D. Siggia. "High Rayleigh Number Convection". In: *Annual Review of Fluid Mechanics* 26.1 (1994), pp. 137–168.

[257] C. Balaji, B. Srinivasan, and S. Gedupudi. "Chapter 5 - Forced Convection". In: *Heat Transfer Engineering*. Ed. by C. Balaji, B. Srinivasan, and S. Gedupudi. Academic Press, 2021, pp. 121–171. ISBN: 978-0-12-818503-2.

[258] J. H. Lienhard V. "Heat Transfer in Flat-Plate Boundary Layers: A Correlation for Laminar, Transitional, and Turbulent Flow". In: *Journal of Heat Transfer* 142.6 (2020).

[259] A. Žukauskas. "Heat Transfer from Tubes in Crossflow". In: *Advances in Heat Transfer*. Ed. by J. P. Hartnett and T. F. Irvine. Vol. 8. Elsevier, 1972, pp. 93–160.

[260] E. N. Sieder and G. E. Tate. "Heat Transfer and Pressure Drop of Liquids in Tubes". In: *Industrial & Engineering Chemistry* 28.12 (1936), pp. 1429–1435.

[261] H. Shi et al. "Numerical Study of Heat Transfer in Square Millimetric Zigzag Channels in the Laminar Flow Regime". In: *Chemical Engineering and Processing - Process Intensification* 144 (2019), p. 107624.

[262] R. K. Shah. "Laminar Flow Friction and Forced Convection Heat Transfer in Ducts of Arbitrary Geometry". In: *International Journal of Heat and Mass Transfer* 18.7 (1975), pp. 849–862.

[263] M. V. V. Mortean and M. B. H. Mantelli. "Nusselt Number Correlation for Compact Heat Exchangers in Transition Regimes". In: *Applied Thermal Engineering* 151 (2019), pp. 514–522.

[264] M. V. V. Mortean et al. "Thermal and Hydrodynamic Analysis of a Cross-Flow Compact Heat Exchanger". In: *Applied Thermal Engineering* 150 (2019), pp. 750–761.

[265] T.-M. Liou, C.-S. Wang, and H. Wang. "Nusselt Number and Friction Factor Correlations for Laminar Flow in Parallelogram Serpentine Micro Heat Exchangers". In: *Applied Thermal Engineering* 143 (2018), pp. 871–882.

[266] W. Qu and I. Mudawar. "Experimental and Numerical Study of Pressure Drop and Heat Transfer in a Single-Phase Micro-Channel Heat Sink". In: *International Journal of Heat and Mass Transfer* 45.12 (2002), pp. 2549–2565.

[267] Y. Sudo, M. Kaminaga, and H. Ikawa. "Combined Forced and Free Convective Heat Transfer Characteristics in Narrow Vertical Rectangular Channel Heated from Both Sides". In: *Journal of Nuclear Science and Technology* 24.5 (1987), pp. 355–364.

[268] J. Ma et al. "Experimental Studies on Single-Phase Flow and Heat Transfer in a Narrow Rectangular Channel". In: *Nuclear Engineering and Design* 241.8 (2011), pp. 2865–2873.

[269] R. W. Lyczkowski, C. W. Solbrig, and D. Gidaspow. "Forced Convection Heat Transfer in Rectangular Ducts—General Case of Wall Resistances and Peripheral Conduction for Ventilation Cooling of Nuclear Waste Repositories". In: *Nuclear Engineering and Design* 67.3 (1982), pp. 357–378.

[270] P.-S. Lee and S. V. Garimella. "Thermally Developing Flow and Heat Transfer in Rectangular Microchannels of Different Aspect Ratios". In: *International Journal of Heat and Mass Transfer* 49.17 (2006), pp. 3060–3067.

[271] Q. Li et al. "Compact Heat Exchangers: A Review and Future Applications for a New Generation of High Temperature Solar Receivers". In: *Renewable and Sustainable Energy Reviews* 15.9 (2011), pp. 4855–4875.

[272] J. W. Deardorff. "The Use of Subgrid Transport Equations in a Three-Dimensional Model of Atmospheric Turbulence". In: *Journal of Fluids Engineering* 95.3 (1973), pp. 429–438.

[273] D. G. Fox and D. K. Lilly. "Numerical Simulation of Turbulent Flows". In: *Reviews of Geophysics* 10.1 (1972), pp. 51–72.

[274] M. R. Rodríguez-Sánchez et al. "Development of a New Method to Estimate the Incident Solar Flux on Central Receivers from Deteriorated Heliostats". In: *Renewable Energy* 130 (2019), pp. 182–190.

[275] S. Whitaker. "Forced Convection Heat Transfer Correlations for Flow in Pipes, Past Flat Plates, Single Cylinders, Single Spheres, and for Flow in Packed Beds and Tube Bundles". In: *AIChE Journal* 18.2 (1972), pp. 361–371.

[276] B. S. Petukhov. "Heat Transfer and Friction in Turbulent Pipe Flow with Variable Physical Properties". In: *Advances in Heat Transfer*. Ed. by J. P. Hartnett and T. F. Irvine. Vol. 6. Elsevier, 1970, pp. 503–564.

[277] J. F. Barnes and J. D. Jackson. "Heat Transfer to Air, Carbon Dioxide and Helium Flowing through Smooth Circular Tubes under Conditions of Large Surface/Gas Temperature Ratio". In: *Journal of Mechanical Engineering Science* (2006), pp. 303–314.

[278] V. Gnielinski. "On Heat Transfer in Tubes". In: *International Journal of Heat and Mass Transfer* 63 (2013), pp. 134–140.

[279] D. Bertsche, P. Knipper, and T. Wetzel. "Experimental Investigation on Heat Transfer in Laminar, Transitional and Turbulent Circular Pipe Flow". In: *International Journal of Heat and Mass Transfer* 95 (2016), pp. 1008–1018.

[280] V. Gnielinski. "G1 Heat Transfer in Pipe Flow". In: *VDI Heat Atlas*. VDI-Buch. Berlin, Heidelberg: Springer, 2010, pp. 691–700. ISBN: 978-3-540-77877-6.

[281] D. Taler. "Simple Power-Type Heat Transfer Correlations for Turbulent Pipe Flow in Tubes". In: *Journal of Thermal Science* 26.4 (2017), pp. 339–348.

[282] S. C. R. Dennis, A. M. Mercer, and G. Poots. "Forced Heat Convection in Laminar Flow through Rectangular Ducts". In: *Quarterly of Applied Mathematics* 17.3 (1959), pp. 285–297.

[283] W. M. Kays and M. E. Crawford. *Convective Heat and Mass Transfer*. New York: McGraw-Hill, 1993. ISBN: 978-0-07-033721-3 978-0-07-112516-1.

[284] K. R. Perkins, K. W. Schade, and D. M. McEligot. "Heated Laminarizing Gas Flow in a Square Duct". In: *International Journal of Heat and Mass Transfer* 16.5 (1973), pp. 897–916.

[285] D. A. Campbell and H. C. Perkins. "Variable Property Turbulent Heat and Momentum Transfer for Air in a Vertical Rounded Corner Triangular Duct". In: *International Journal of Heat and Mass Transfer* 11.6 (1968), pp. 1003–1012.

[286] H. C. Perkins and P. Worsoe-Schmidt. "Turbulent Heat and Momentum Transfer for Gases in a Circular Tube at Wall to Bulk Temperature Ratios to Seven". In: *International Journal of Heat and Mass Transfer* 8.7 (1965), pp. 1011–1031.

[287] Y. Sudo et al. "Experimental Study of Differences in Single-Phase Forced-Convection Heat Transfer Characteristics between Upflow and Downflow for Narrow Rectangular Channel". In: *Journal of Nuclear Science and Technology* 22.3 (1985), pp. 202–212.

[288] Z. H. Liang et al. "Experimental Investigation on Flow and Heat Transfer Characteristics of Single-Phase Flow with Simulated Neutronic Feedback in Narrow Rectangular Channel". In: *Nuclear Engineering and Design* 248 (2012), pp. 82–92.

[289] C. Wang et al. "Forced Convection Heat Transfer and Flow Characteristics in Laminar to Turbulent Transition Region in Rectangular Channel". In: *Experimental Thermal and Fluid Science* 44 (2013), pp. 490–497.

[290] D. Jo et al. "Experimental Investigation of Convective Heat Transfer in a Narrow Rectangular Channel for Upward and Downward Flows". In: *Nuclear Engineering and Technology* 46.2 (2014), pp. 195–206.

[291] A. Ghione et al. "Assessment of Thermal–Hydraulic Correlations for Narrow Rectangular Channels with High Heat Flux and Coolant Velocity". In: *International Journal of Heat and Mass Transfer* 99 (2016), pp. 344–356.

[292] J. Ma et al. "Experimental Investigations on Single-Phase Heat Transfer Enhancement with Longitudinal Vortices in Narrow Rectangular Channel". In: *Nuclear Engineering and Design* 240.1 (2010), pp. 92–102.

[293] K. Stephan and P. Preußer. "Wärmeübergang Und Maximale Wärmestromdichte Beim Behältersieden Binärer Und Ternärer Flüssigkeitsgemische". In: *Chemie Ingenieur Technik* 51.1 (1979), pp. 37–37.

[294] R. Sun et al. "Experimental Study of Single-Phase Flow and Heat Transfer in Rectangular Channels under Uniform and Non-Uniform Heating". In: *Experimental Thermal and Fluid Science* 114 (2020), p. 110055.

[295] T.-S. Wang and M. K. Chyu. "Heat Convection in a 180-Deg Turning Duct with Different Turn Configurations". In: *Journal of Thermophysics and Heat Transfer* 8.3 (1994), pp. 595–601.

[296] Z. Qin and R. Pletcher. "Large Eddy Simulation of Turbulent Heat Transfer in a Rotating Square Duct". In: *International Journal of Heat and Fluid Flow* 27.3 (2006), pp. 371–390.

[297] N. Sato et al. "Numerical Investigation of the Effect of Prandtl Number on Heat Transfer in a Dimpled-Channel Flow". In: *International Journal of Heat and Fluid Flow* 68 (2017), pp. 139–150.

[298] L. Su et al. "Heat Transfer Characteristics of Thermally Developing Flow in Rectangular Microchannels with Constant Wall Temperature". In: *International Journal of Thermal Sciences* 155 (2020), p. 106412.

[299] W.-S. Fu et al. "Flow Downward Penetration of Vertical Parallel Plates Natural Convection with an Asymmetrically Heated Wall". In: *International Communications in Heat and Mass Transfer* 74 (2016), pp. 55–62.

[300] G. E. Lau et al. "Large-Eddy Simulation of Natural Convection in an Asymmetrically-Heated Vertical Parallel-Plate Channel: Assessment of Subgrid-Scale Models". In: *Computers & Fluids* 59 (2012), pp. 101–116.

[301] S. Taieb, L. Ali Hatem, and J. Balti. "Natural Convection in an Asymmetrically Heated Vertical Channel with an Adiabatic Auxiliary Plate". In: *International Journal of Thermal Sciences* 74 (2013), pp. 24–36.

[302] Y. Cherif et al. "Experimental and Numerical Natural Convection in an Asymmetrically Heated Double Vertical Facade". In: *International Journal of Thermal Sciences* 152 (2020), p. 106288.

[303] N. Kimouche et al. "Effect of Inclination Angle of the Adiabatic Wall in Asymmetrically Heated Channel on Natural Convection: Application to Double-Skin Façade Design". In: *Journal of Building Engineering* 12 (2017), pp. 171–177.

[304] B. Brangeon, P. Joubert, and A. Bastide. "Influence of the Dynamic Boundary Conditions on Natural Convection in an Asymmetrically Heated Channel". In: *International Journal of Thermal Sciences* 95 (2015), pp. 64–72.

[305] D. G. Osborne and F. P. Incropera. "Laminar, Mixed Convection Heat Transfer for Flow between Horizontal Parallel Plates with Asymmetric Heating". In: *International Journal of Heat and Mass Transfer* 28.1 (1985), pp. 207–217.

[306] C. Gau, Y. C. Jeng, and C. G. Liu. "An Experimental Study on Mixed Convection in a Horizontal Rectangular Channel Heated From a Side". In: *Journal of Heat Transfer* 122.4 (2000), pp. 701–707.

[307] T. H. Hwang, Y. Cai, and P. Cheng. "An Experimental Study of Forced Convection in a Packed Channel with Asymmetric Heating". In: *International Journal of Heat and Mass Transfer* 35.11 (1992), pp. 3029–3039.

[308] D. A. Nield. "Forced Convection in a Parallel Plate Channel with Asymmetric Heating". In: *International Journal of Heat and Mass Transfer* 47.25 (2004), pp. 5609–5612.

[309] J. Mitrović, B. Maletić, and B. S. Bačlić. "Some Peculiarities of the Asymmetric Graetz Problem". In: *International Journal of Engineering Science* 44.7 (2006), pp. 436–455.

[310] R. Repaka and V. V. Satyamurty. "Local and Average Heat Transfer in the Thermally Developing Region of an Asymmetrically Heated Channel". In: *International Journal of Heat and Mass Transfer* 53.9 (2010), pp. 1654–1665.

[311] A. V. Kuznetsov and D. A. Nield. "Forced Convection in a Channel Partly Occupied by a Bidisperse Porous Medium: Asymmetric Case". In: *International Journal of Heat and Mass Transfer* 53.23 (2010), pp. 5167–5175.

[312] P. van Male et al. "Heat and Mass Transfer in a Square Microchannel with Asymmetric Heating". In: *International Journal of Heat and Mass Transfer* 47.1 (2004), pp. 87–99.

[313] S. Torii and W.-J. Yang. "Effect of Heat Flux Ratio on Two-Dimensional Horizontal Channel Flow". In: *Journal of Thermophysics and Heat Transfer* 18.1 (2004), pp. 73–78.

[314] S. Serra et al. "High-Temperature Gradient Effect on a Turbulent Channel Flow Using Thermal Large-Eddy Simulation in Physical and Spectral Spaces". In: *Journal of Turbulence* 13 (2012), N49.

[315] A. Toutant and F. Bataille. "Turbulence Statistics in a Fully Developed Channel Flow Submitted to a High Temperature Gradient". In: *International Journal of Thermal Sciences* 74 (2013), pp. 104–118.

[316] E. Driscoll and D. Landrum. "Uncertainty Analysis on Heat Transfer Correlations for RP-1 Fuel in Copper Tubing". In: *NTRS - NASA Technical Reports Server* (2004).

[317] V. K. Scariot, G. M. Hobold, and A. K. da Silva. "On the Sensitivity to Convective Heat Transfer Correlation Uncertainties in Supercritical Fluids". In: *Applied Thermal Engineering* 145 (2018), pp. 123–132.

[318] JCGM. *Evaluation of Measurement Data – Guide to the Expression of Uncertainty in Measurement*. https://www.bipm.org/en/publications/guides/gum.html. 2008.

[319] J. Han, S. Dutta, and S. V. Ekkad. *Gas Turbine Heat Transfer and Cooling Technology*. CRC Press - Taylor & Francis Group, 2012. ISBN: 978-0-429-10711-5.

[320] T. A. Oliver et al. "Estimating Uncertainties in Statistics Computed from Direct Numerical Simulation". In: *Physics of Fluids* 26.3 (2014), p. 035101.

[321] T. Phillips and C. Roy. "Richardson Extrapolation-Based Discretization Uncertainty Estimation for Computational Fluid Dynamics". In: *Journal of Fluids Engineering* 136 (2014), p. 121401.

[322] M. Carnevale et al. "Uncertainty Quantification: A Stochastic Method for Heat Transfer Prediction Using LES". In: *Journal of Turbomachinery* 135 (2013).

[323] K. Menberg, Y. Heo, and R. Choudhary. "Sensitivity Analysis Methods for Building Energy Models: Comparing Computational Costs and Extractable Information". In: *Energy and Buildings* 133 (2016), pp. 433–445.

[324] F. Uhía, A. Campo, and J. Fernández-Seara. "Uncertainty Analysis for Experimental Heat Transfer Data Obtained by the Wilson Plot Method: Application to Condensation on Horizontal Plain Tubes". In: *Thermal Science* 17 (2013).

[325] G. N. Coleman, J. Kim, and R. D. Moser. "A Numerical Study of Turbulent Supersonic Isothermal-Wall Channel Flow". In: *Journal of Fluid Mechanics* 305 (1995), pp. 159–183.

[326] K. Wójs and T. Tietze. "Effects of the Temperature Interference on the Results Obtained Using the Wilson Plot Technique". In: *Heat and Mass Transfer* 33.3 (1997), pp. 241–245.

[327] D. D. Clarke et al. "Sensitivity and Uncertainty Analysis of Heat-Exchanger Designs to Physical Properties Estimation". In: *Applied Thermal Engineering* 21.10 (2001), pp. 993–1017.

[328] J. C. Helton. "Uncertainty and Sensitivity Analysis Techniques for Use in Performance Assessment for Radioactive Waste Disposal". In: *Reliability Engineering & System Safety* 42.2 (1993), pp. 327–367.

[329] D. Rochman et al. "Efficient Use of Monte Carlo: Uncertainty Propagation". In: *Nuclear Science and Engineering* 177.3 (2014), pp. 337–349.

[330] J. Mazo et al. "Uncertainty Propagation and Sensitivity Analysis of Thermo-Physical Properties of Phase Change Materials (PCM) in the Energy Demand Calculations of a Test Cell with Passive Latent Thermal Storage". In: *Applied Thermal Engineering* 90 (2015), pp. 596–608.

[331] D. Colorado et al. "Hybrid Evaporator Model: Analysis under Uncertainty by Means of Monte Carlo Method". In: *Applied Thermal Engineering*. Optimisation of Cogeneration and Energy Intensive Processes, Heat Transfer Enhancement, Industrial Applications – PRES 11 43 (2012), pp. 148–152.

[332] L. M. Zhou, E. Zhao, and S. Ren. "Interval Element-Free Galerkin Method for Uncertain Mechanical Problems". In: *Advances in Mechanical Engineering* 10.1 (2018).

[333] T. Zhou, J. Yuan, and M. Li. "Simultaneously Estimate Solid- and Liquid-Phase Thermal Conductivities". In: *International Communications in Heat and Mass Transfer* 119 (2020), p. 104959.

[334] C. R. Á. da Silva Jr. and A. T. Beck. "Efficient Bounds for the Monte Carlo-Neumann Solution of Stochastic Thermo-Elasticity Problems". In: *International Journal of Solids and Structures* 58 (2015), pp. 136–145.

[335] D. Taler. "Assessment of the Indirect Measurement Uncertainty". In: *Numerical Modelling and Experimental Testing of Heat Exchangers*. Studies in Systems, Decision and Control. Springer International Publishing, 2019, pp. 373–448. ISBN: 978-3-319-91127-4.

[336] S. Oladyshkin and W. Nowak. "Data-Driven Uncertainty Quantification Using the Arbitrary Polynomial Chaos Expansion". In: *Reliability Engineering & System Safety* 106 (2012), pp. 179–190.

[337] H. Cho, D. Venturi, and G. E. Karniadakis. "Karhunen–Loève Expansion for Multi-Correlated Stochastic Processes". In: *Probabilistic Engineering Mechanics* 34 (2013), pp. 157–167.

[338] G. J. K. Tomy and K. J. Vinoy. "Neumann-Expansion-Based FEM for Uncertainty Quantification of Permittivity Variations". In: *IEEE Antennas and Wireless Propagation Letters* 19.4 (2020), pp. 561–565.

[339] A. Håkansson. "An Investigation of Uncertainties in Determining Convective Heat Transfer during Immersion Frying Using the General Uncertainty Management Framework". In: *Journal of Food Engineering* 263 (2019), pp. 424–436.

[340] S. G. Penoncello. *Thermal Energy Systems : Design and Analysis*. CRC Press - Taylor & Francis Group, 2015. ISBN: 978-0-429-17226-7.

[341] D. Taler. "Mathematical Modeling and Control of Plate Fin and Tube Heat Exchangers". In: *Energy Conversion and Management* 96 (2015), pp. 452–462.

[342] M. Trojan and D. Taler. "Thermal Simulation of Superheaters Taking into Account the Processes Occurring on the Side of the Steam and Flue Gas". In: *Fuel* 150 (2015), pp. 75–87.

[343] N. Dimassi and L. Dehmani. "Experimental Heat Flux Analysis of a Solar Wall Design in Tunisia". In: *Journal of Building Engineering* 8 (2016), pp. 70–80.

[344] A. Sciacchitano and B. Wieneke. "PIV Uncertainty Propagation". In: *Measurement Science and Technology* 27.8 (2016), p. 084006.

[345] D. Paudel and S. Hostikka. "Propagation of Model Uncertainty in the Stochastic Simulations of a Compartment Fire". In: *Fire Technology* 55.6 (2019), pp. 2027–2054.

[346] Y. Zhao et al. "Uncertainty and Sensitivity Analysis of Flow Parameters for Transition Models on Hypersonic Flows". In: *International Journal of Heat and Mass Transfer* 135 (2019), pp. 1286–1299.

[347] C. Cambon, D. Jeandel, and J. Mathieu. "Spectral Modelling of Homogeneous Non-Isotropic Turbulence". In: *Journal of Fluid Mechanics* 104 (1981), pp. 247–262.

[348] M. Lee and R. D. Moser. "Spectral Analysis of the Budget Equation in Turbulent Channel Flows at High Reynolds Number". In: *Journal of Fluid Mechanics* 860 (2019), pp. 886–938.

[349] C. Xie et al. "Artificial Neural Network Mixed Model for Large Eddy Simulation of Compressible Isotropic Turbulence". In: *Physics of Fluids* 31.8 (2019), p. 085112.

[350] Z. Yuan, C. Xie, and J. Wang. "Deconvolutional Artificial Neural Network Models for Large Eddy Simulation of Turbulence". In: *Physics of Fluids* 32.11 (2020), p. 115106.

[351] J. Park and H. Choi. "Toward Neural-Network-Based Large Eddy Simulation: Application to Turbulent Channel Flow". In: *Journal of Fluid Mechanics* 914 (2021).

[352] K. Duraisamy. "Perspectives on Machine Learning-Augmented Reynolds-Averaged and Large Eddy Simulation Models of Turbulence". In: *Physical Review Fluids* 6.5 (2021), p. 050504. arXiv: 2009.10675.

[353] J. Karni et al. "A High-Pressure Window for Volumetric Solar Receivers". In: *Journal of Solar Energy Engineering-transactions of The Asme - J SOL ENERGY ENG* 120 (1998), pp. 101–107.

[354] P. Poživil et al. "A Pressurized Air Receiver for Solar-Driven Gas Turbines". In: *Energy Procedia*. Proceedings of the SolarPACES 2013 International Conference 49 (2014), pp. 498–503.

[355] R. B. Dean. "Reynolds Number Dependence of Skin Friction and Other Bulk Flow Variables in Two-Dimensional Rectangular Duct Flow". In: *Journal of Fluids Engineering* 100.2 (1978), pp. 215–223.

Simulation and modeling of flows in gas-pressurized solar receivers

Abstract: The solar receiver is a key component of solar power towers operating with pressurized gas. It ensures the conversion of the concentrated solar radiation into fluid heating. The solar receiver flow is characterized by intense turbulence, high temperatures, and strong asymmetric fluid heating. The academic geometry of the bi-periodical channel is selected to investigate the flow physics. The Navier-Stokes equations are solved under the low Mach number hypothesis. A multi-scale approach is carried out and aims to produce information and tools that will aid the industrial development of solar power towers. The detailed levels of study feed the more macroscopic levels. At the local scale, Direct Numerical Simulations are performed to deepen the knowledge of the complex flows encountered in solar receivers. The results highlight the presence of high Reynolds number phenomena and the strong coupling between the dynamic and the temperature. At the intermediate scale, Large Eddy Simulations are achieved. The subgrid terms associated with the velocity-velocity and the velocity-density correlations are modeled. *A posteriori* tests are carried out in three different study conditions thanks to the results of the Direct Numerical Simulations. For each configuration, a large number of models is assessed thanks to a global approach then some are selected for more detailed analyzes. At the macroscopic scale, a heat transfer correlation is developed thanks to the results of Large Eddy Simulations. It fulfills a gap in the literature and permits, notably, estimating the heat fluxes in asymmetrical heating conditions. This correlation is then used to study the wall heat flux sensitivity to the flow parameters.

Keywords: tubulence, strong heat flux, solar energy, Direct Numerical Simulation, Large Eddy Simulation, modeling, anisothermal channel flow, low Mach number, heat transfer correlation, uncertainty propagation, multi-scale approach

Simulation et modélisation des écoulements dans les récepteurs solaires à gaz sous-pression

Résumé : Le récepteur solaire est un élément clé des centrales à tour fonctionnant à gaz sous-pression. Il assure la conversion du rayonnement solaire concentré en chauffage du fluide caloporteur. L'écoulement au sein du récepteur est caractérisé par une turbulence intense, des hauts niveaux de température ainsi qu'un fort chauffage asymétrique du fluide. La géométrie académique du canal plan bi-périodique est choisie pour étudier la physique de l'écoulement. Les équations de Navier-Stokes sont résolues sous l'hypothèse des bas nombres de Mach. Une approche multi-échelle est menée et vise à fournir des informations et des outils qui faciliteront le développement industriel des centrales à tour. Les niveaux d'études correspondant à des descriptions détaillées renseignent les niveaux de description plus macroscopique. À l'échelle locale, des Simulations Numériques Directes sont effectuées pour approfondir la compréhension des écoulements complexes rencontrés dans les récepteurs solaires. Les résultats mettent en évidence la présence de phénomènes caractéristiques des hauts nombres de Reynolds et d'un fort couplage entre la dynamique et la température. À l'échelle intermédiaire, des Simulations des Grandes Échelles sont menées. Les termes de sous-maille associés aux corrélations vitesse-vitesse et vitesse-masse volumique sont modélisés. Des tests *a posteriori* sont effectués par comparaison avec les résultats des Simulations Numériques Directes dans trois conditions d'étude différentes. Pour chaque configuration, un grand nombre de modèles est évalué grâce à une approche globale

puis quelques-uns sont sélectionnés pour des analyses plus approfondies. À l'échelle macroscopique, une corrélation permettant d'estimer les transferts de chaleur est développée grâce aux résultats des Simulations des Grandes Échelles. Elle comble un manque dans la littérature et permet, notamment, d'estimer le flux de chaleur dans des conditions de chauffage asymétrique. Cette corrélation est ensuite utilisée pour étudier la sensibilité des flux de chaleur pariétaux aux paramètres de l'écoulement.

Mots-clés : turbulence, forts flux, énergie solaire, Simulation Numérique Directe, Simulation des Grandes Échelles, modélisation, canal plan anisotherme, bas nombre de Mach, corrélation de transfert de chaleur, propagation d'incertitude, approche multi-échelle